RAPID HAPTIC PERCEPTION USING FORCE AND THERMAL SENSING

A Dissertation
Presented to
The Academic Faculty

By

Tapomayukh Bhattacharjee

In Partial Fulfillment
of the Requirements for the Degree
Doctor of Philosophy in Robotics

Department of Biomedical Engineering
Georgia Institute of Technology and Emory University

August 2017

RAPID HAPTIC PERCEPTION USING FORCE AND THERMAL SENSING

Approved by:

Prof. Charles C. Kemp, Advisor
Dept. of Biomedical Engineering
Georgia Institute of Technology and Emory University

Prof. James M. Rehg
School of Interactive Computing
Georgia Institute of Technology

Prof. Lena H. Ting
Dept. of Biomedical Engineering
Georgia Institute of Technology and Emory University

Prof. C. Karen Liu
School of Interactive Computing
Georgia Institute of Technology

Prof. Henrik I. Christensen
Dept. of Computer Science and Engineering
UC San Diego

Date Approved: July 10, 2017

Often the hands will solve a mystery that the intellect has struggled with in vain

Carl G. Jung

To my parents and my wife

ACKNOWLEDGMENTS

First and foremost, I thank my mother Minakshi Bhattacharjee, and my father Tapojyoti Bhattacharjee, for their unending and unconditional love and support throughout my life and career. Coming from one of the remotest parts of India, I would not be where I am today without their strong belief and trust in me. I must also thank my wife Natalia, who has been an amazing life-partner throughout. She is the nicest person there is and has been an unyielding pillar of support throughout the ups and downs of my PhD career. Her unparalleled accommodating and understanding nature always motivated me to push through during the tough times.

I must thank my advisor, Prof. Charlie Kemp, who was kind enough to give me an opportunity to join the Healthcare Robotics Lab for my PhD. Charlie always gave me the freedom to work in my areas of interest and I have immensely enjoyed the technical brainstorming sessions with him. I am always amazed by his communication and presentation skills and the insights and perspectives he brings into a problem. As his student, I have learned that being able to come up with simple approaches to solving complex problems with an eye on applying it in real-world problems is the key to making an impact in the society.

I am also thankful to my committee members, Prof. Jim Rehg, Prof. Lena Ting, Prof. Karen Liu, and Prof. Henrik Christensen for giving me the time amongst their busy schedule to continuously provide constructive feedback on my work. I gratefully acknowledge the funding support from DARPA's Maximum Mobility and Manipulation (M3) program, Contract W911NF-11-1-603, for the initial years of my PhD. I need to especially thank Prof. Lena Ting for giving me the freedom to work on my haptic perception research though it did not perfectly align with the proposed goals of the NSF Emerging Frontiers in Research and Innovation (EFRI) 1137229 which funded the later years of my Ph. D.

Being a member of the Healthcare Robotics Lab was one of the most rewarding expe-

riences I have ever had. This work would not be complete without the help from Joshua Wade, Ashwin Shenoi, Haoping Bai, Haofeng Chen and Linda Komnang Liezu. As a member of the lab, I also had the opportunity to interact very closely with and learn from some of the smartest robotics minds like Advait Jain, Tiffany Chen, Marc Killpack, Travis Deyle, Hai Nguyen, Kelsey Hawkins, Phillip Grice, Daehyung Park, Ariel Kapusta, Henry Clever, Zackory Erickson and many other colleagues.

Finally, I would like to thank my countless friends at Georgia Tech and outside who helped me settle when I first arrived in the US and made my life in Atlanta enjoyable and easy. I also thank my MS and undergraduate advisors and friends who have continuously guided me to this point and introduced me to the wonderful and fascinating world of robotics and haptics. After all, as Jacob Bronowski says, 'The hand is the cutting edge of the mind'.

TABLE OF CONTENTS

LIST OF TABLES

LIST OF FIGURES

SUMMARY

Tactile sensing can enable a robot to infer properties of its surroundings. Recent research has focused on robots that haptically perceive the world through exploratory behaviors that occur over tens of seconds. During manipulation, many opportunities arise for robots to gather information about the environment from brief ($\leq$ 2 seconds) contact due to simple motions (e.g., linear). The goal of our work was to enable robots to infer haptic properties under these conditions using force and thermal sensing.

We used a data-driven approach with various machine learning methods. Key challenges were obtaining adequate haptic data for training and developing methods that performed well on haptic data that differed from the training data due to common real-world phenomena. For example, haptic sensory signals vary significantly due to the robot, including its velocity, stiffness, and sensor temperature.

To collect suitable data, we used a variety of platforms, including simplified robots, handheld human-operated devices, and a mobile robot. We also generated synthetic data with physics-based models. Through careful empirical evaluation, we identified machine learning methods that better handled common signal variations. We also used physics-based models to characterize common perceptual ambiguities and predict the performance of data-driven methods. Overall, our research demonstrates the feasibility of robots inferring haptic properties from brief contact with objects in human environments. By using force and thermal sensing, our methods rapidly recognized materials, detected when objects moved, detected contact with people, and inferred other properties of the robots surroundings.

CHAPTER 1
HAPTIC CLASSIFICATION AND RECOGNITION OF OBJECTS USING A TACTILE SENSING FOREARM

1.1 Research Summary

In this paper, we demonstrate data-driven inference of mechanical properties of objects using a tactile sensor array (skin) covering a robot's forearm. We focus on the mobility (sliding vs. fixed), compliance (soft vs. hard), and identity of objects in the environment, as this information could be useful for efficient manipulation and search. By using the large surface area of the forearm, a robot could potentially search and map a cluttered volume more efficiently, and be informed by incidental contact during other manipulation tasks. Our approach tracks a contact region on the forearm over time in order to generate time series of select features, such as the maximum force, contact area, and contact motion. We then process and reduce the dimensionality of these time series to generate a feature vector to characterize the contact. Finally, we use the k-nearest neighbor algorithm (k-NN) to classify a new feature vector based on a set of previously collected feature vectors. Our results show a high cross-validation accuracy in both classification of mechanical properties and object recognition. In addition, we analyze the effect of taxel resolution, duration of observation, feature selection, and feature scaling on the classification accuracy.

1.2 Introduction

Autonomous manipulation in cluttered environmnets is a difficult problem due to the possibility of unavoidable contact with obstacles. Haptic technology can serve as a useful tool for enabling effective manipulation. A robot could utilize haptic information obtained from its interaction with objects in the environment to maneuver itself through clutter.

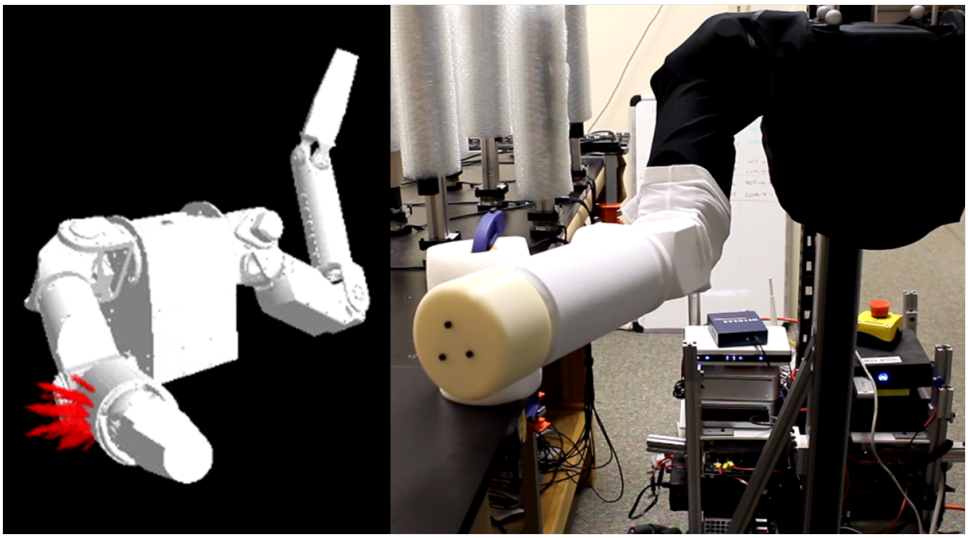

Figure 1.1: *Force data from forearm skin sensor mounted on the robot, Cody. The forearm came into contact with a cylindrical object made of polystyrene foam, while trying to reach a goal configuration. The red arrows show the forces acting on the skin.*

While doing so, knowledge of the mechanical properties of an object, such as its mobility, compliance, weight and surface properties like friction could be especially useful. Such information is not only useful for efficient manipulation but can also be used to haptically search for and recognize an object. By using the large surface area of the forearm, a robot could potentially search and map a cluttered volume more efficiently than if it only uses its hand.

Note that non-contact sensing modalities, such as cameras and laser scanners, are not always effective for manipulation in clutter. Such sensors have limited ability to infer mechanical properties [1, 2]. Humans rely heavily on their sense of touch for manipulation tasks and can even manipulate objects using only tactile information [3]. Visually similar objects or environments can have very different mechanical properties. For example, compliant leaves can be pushed aside without generating large forces. At the same time, if there is something fixed and rigid occluded by the leaves, such as a branch or a concealed object, then the total system or contact behavior can become quite rigid. Likewise, when searching for an object of interest in rubble with only non-contact sensing, it may be hard to distinguish between things that are stuck and those that can be pushed or pulled aside. *Hence,*

estimating the mobility of an object could be highly valuable for manipulation. However, mobility estimation studies using haptic sensing are lacking.

In this paper, we specifically address the mobility-based classification problem and also estimate object compliance characteristics using haptic sensing techniques during manipulation tasks. The rest of the paper is arranged as follows. In Section 1.3, we review the related work in this domain. Section 1.4 describes the approach that we have used in tackling the problem of haptic data based classification and recognition of environmental objects. In Section 1.5, we present the results of applying our algorithm in real-life experimental situations and analyze the effects of various conditions on the performance of our algorithm. In Section 1.6, we present conclusions from our work.

1.3 Related Work

Object categorization, based on their various characteristics for specific tasks, has been dealt with extensively in previous studies. Researchers have addressed the problem of object categorization based on the objects' various characteristics such as material, shape and functional properties using single or multiple sensor modalities as given below.

1.3.1 Material Property based Classification

Previous work on material property classification is perhaps the most closely related work to our approach. Although we do not explicitly model material properties, the features we extract from the interactions between the robot arm and environmental objects are a direct consequence of these material properties which affect the interaction dynamics. Drimus et al. [4] classify rigid and deformable objects based on haptic feedback from a novel tactile sensor using flexible piezoresistive rubber. They represent tactile information from a palpation procedure as a time-series of features, and use k-nearest neighbor classifier to categorize the objects [4]. This is the most similar prior work of which we are aware. *However, in addition to classifying compliant and rigid objects, we also classify fixed versus*

movable objects. This classification could be important in cluttered environments because the mobility of an object coupled with its compliance suggests how much force needs to be applied to either change its state for effective manipulation, or give up. Moreover, our method does not employ an exploratory / probing procedure used explicitly for classification as in [4]. Instead, our method extracts the required features through general contact during a stereotyped reaching motion. This scenario is more representative of incidental contact that could occur with the forearm during a manipulation task. Also, the features extracted in our method correspond with physical quantities whereas the features in [4] are tactile array images. The tactile images do not have a clear interpretation with respect to an object's mechanical properties. This makes it difficult to understand the underlying dynamics of the factors which might contribute in the haptic object classification.

Sukhoy et al. investigate the use of a vibrotactile sensor for surface texture recognition using a Support Vector Machine (SVM) classifier [5]. Ho and Jones develop a thermal display for simulating the thermal cues associated with making contact with various materials of different properties [6]. Kim and Kesavadas present a methodology for estimating the material properties of objects by an active tapping procedure [7]. Takamuku et al. use a simplified version of an artificial skin with strain gauges and PVDF films and estimate the material properties of objects with the help of exploratory procedures like tapping and squeezing [8]. Hosoda and Iwase [9] use a Bionic hand and utilize its hand compliance to grip an object to obtain haptic data. They use a recurrent neural network to classify objects based on learned haptic cues from dynamic interactions [9].

Frank et al. [10, 11] address the problem of determining the elasticity properties of deformable objects by minimizing the difference between the actual deformed surface of an object and its corresponding finite element model. They use a 3D registration technique based on point clouds obtained from a depth camera for this purpose. Ueda et al. [12] also address the issue of extracting rheological properties of deformable objects based on haptic vision. They monitor the surface deformation of an object by exerting a known

contact force and then observe how the object returns to its original shape after the contact force is withdrawn. Nizar et al. [13] address the problem of the classification of material type and surface properties by developing a sensor which uses a lightweight plunger probe to detect surface properties. They also used an optical mouse sensor to obtain surface images and used a Radial Basis Function Neural Network for classification. Platt et al. [14] use proprioceptive and load-based tactile information to localize features such as a bump, a snap and a grommet embedded in flexible materials like a fabric. They claim that using both tactile and proprioceptive data results in a gain in the localization performance. Matheus and Dollar [15] estimate the static friction between different object-surface pairs while sliding a variety of objects which affects the mobility of an object on a specific surface.

1.3.2 Shape based Classification

Kikuuwe and Yoshikawa use impedance perception schemes to extract information on the local properties of object surfaces and categorize objects into two classes such as flat and convex cylindrical surfaces [16]. Schneider et al. [17] use touch sensors installed in the fingertips of a manipulation robot to get low-resolution intensity images obtained from multiple grasping interactions. They apply a bag-of-words approach and unsupervised clustering techniques to categorize objects using only the haptic feedback [17]. Allen et al. use superquadric primitives for model-based haptic object recognition and perform object recognition using the similarity between the parameters of the recovered superquadrics [18]. Caselli et al. also use volumetric models for dynamic integration of geometric information with haptic exploration data and formulate the problem as a match-to-sample scheme using the recovered model features [19]. Faldella et al. utilize an unsupervised Kohonen self-organizing feature map for performing a match-to-sample classification of 3-D objects using a volumetric model called a wrapping polyhedron [20]. Pezzementi et al. view tactile sensor readings as images and apply PCA techniques to identify the principal

components of identified features, and then cluster them as well as build per-class histograms as a class characteristic [21]. Gorges et al. [22] additionally include some passive joints in the tactile sensor system of their robot hand so that the tactile sensor conforms to the object shape during interaction which could help to acquire more information for shape reconstruction. They use Self-Organizing Maps (SOMs) for identifying the haptic key features and use a Bayes Classifier to classify the objects based on their features [22].

1.3.3 Functional Property based Classification

Sinapov et al. use acoustic properties of objects during specific interaction schemes to classify the objects and the behavioral interactions performed with them such as grasping, shaking, dropping, pushing and tapping behaviors on 36 different household objects [23]. Berquist et al. monitor the changes in the joint torques of a robot while it performs five exploratory procedures such as lift, shake, crush, drop, and push on several objects and show that the robot can learn to recognize objects solely on the basis of proprioceptive information [24]. Griffith et al. use multiple exploratory behaviors and employ clustering techniques for categorizing containers and non-containers by extracting visual and acoustic features from its interaction with objects and then employing unsupervised clustering techniques to form several categorizations [25]. Sinapov et al. also combine proprioceptive and auditory feedback and use a behavior-grounded relational classification model to recognize categories of household objects [26].

1.4 Methods

We used supervised machine learning to analyze data from a skin sensor covering the forearm of a humanoid robot named 'Cody'. Our goal was to classify an object that the robot has not previously interacted with as being in one of four categories: *Rigid-Fixed*, 2) *Rigid-Movable*, 3) *Soft-Fixed*, and 4) *Soft-Movable*. We also used the same methods to haptically identify a specific object that the robot has previously interacted with. In Sections 1.5.2

and 1.5.3 we show the effects of the spatial resolution of the taxels, and the duration of the haptic interaction, on the classification accuracy. Section 1.5.4 shows the effect of different feature scaling schemes on the performance of the algorithm while Section 1.5.5 highlights the importance of the individual features for both classification and recognition purposes.

1.4.1 Experimental Setup

The experimental setup for our data collection is described below.

The Robot 'Cody'

Cody, as shown in Fig. 1.1, is a statically stable mobile manipulator weighing roughly 160 kg. The components of the robot are: Meka A1 arms, a Segway omni-directional base and a Festo 1-D.O.F. linear actuator. The arms consist of two 7-D.O.F. anthropomorphic arms with series elastic actuators. When we control these arms, each joint simulates a low-stiffness visco-elastic torsional spring. We control the robot's arms by changing the equilibrium angles of these simulated springs over time.

Cody has a force sensitive skin across its entire forearm. Meka Robotics and the Georgia-Tech Healthcare Robotics Lab developed the forearm tactile skin sensor, which is based on Stanfords capacitive sensing technology, as described in Ulmen et al. [27]. The skin consists of a capacitive pressure-sensor array. We refer to the elements of this array as taxels (tactile pixels). There are 384 taxels on the entire skin which are distributed into a 24 X 16 array with each taxel being 9 mm X 9 mm in size. The array of taxels reports the estimated force applied to each taxel at 100 Hz.

Data Collection

For our experiments, we used a set of 18 objects, shown in Fig. 1.2. We selected large objects that have mostly uniform material properties and vary widely in their mass, friction, and compliance. For each object, we collected haptic data by commanding the same

Figure 1.2: *Set of objects.*

equilibrium point trajectory for the arm and recording the sensor readings from the taxels of the forearm skin at approximately 100 Hz.

We labeled each of these objects as soft or rigid. We considered pillow-like materials, foam, bubble-wrap, and vegetation to be soft, and all other objects to be rigid. For objects that could be pushed aside by the robot's motion, we also fixed them with a clamp or a heavy weight, so that we could have both movable and fixed conditions. We collected a dataset of 5 trials for each of the 18 different objects, 10 of them in both fixed and movable conditions, 4 of them in only fixed conditions and the remaining 4 in movable conditions. Fig. 1.3 shows three images from one trial of the robot interacting with a plant. It also shows the data from the forearm sensor, visualized as an image.

1.4.2 Preprocessing, Feature Selection, and Dimensionality Reduction

We recorded data from the forearm taxel array at a 100 Hz sampling rate. We truncated this time series data to begin at the estimated onset of contact between the robot and the object. We then represented the data at every time step as a gray-scale image, as shown in Fig. 1.3. We converted this image to a binary image representing the taxels in contact by applying

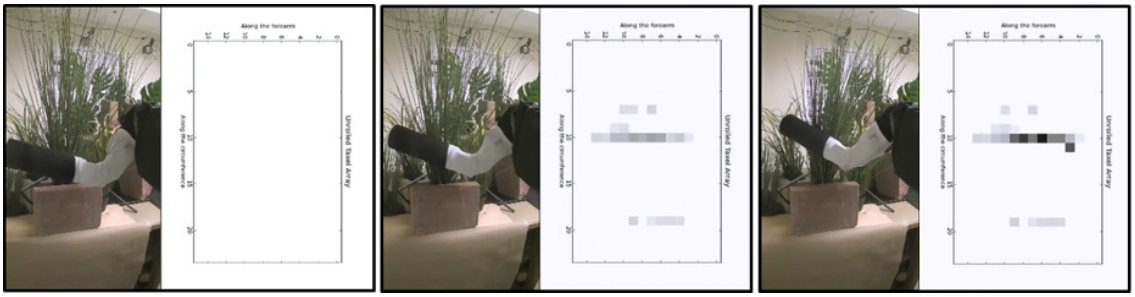

Figure 1.3: *Sequence of images that illustrate our data collection for our experiments on inferring mechanical properties of objects (foliage). Each image shows a picture of the robot Cody, and a visualization of the data from the forearm skin sensor as a 24X16 image (dark pixels correspond to larger forces). The leftmost picture shows a non-contact situation, the middle one corresponds to the situation just after the onset of contact while the rightmost picture shows the situation when the robot has pushed the foliage to the maximum extent consistent with its motion-limits.*

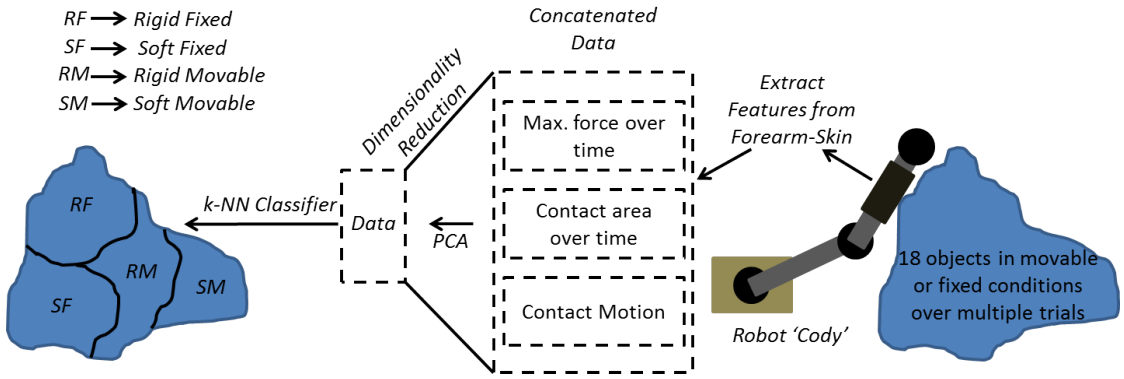

Figure 1.4: *Schematic representation of the Experimental Protocol.*

a threshold to each taxel. Note that this hand-tuned threshold was not same for all objects. This was done to account for some of the more rigid or coarser objects for which a covering was put over the otherwise bare skin-sensor to ensure its safety. Then, we computed connected components to segment the contact regions. For the connected component with the largest area, we computed three features. Figure 1.4 depicts the complete experimental protocol.

Fig. 1.5 shows the three features. The first feature was the maximum force that the robot applied to the object at every time step. Second, we estimated the area of the contact between the arm and the object as the number of taxels in the connected component. Third,

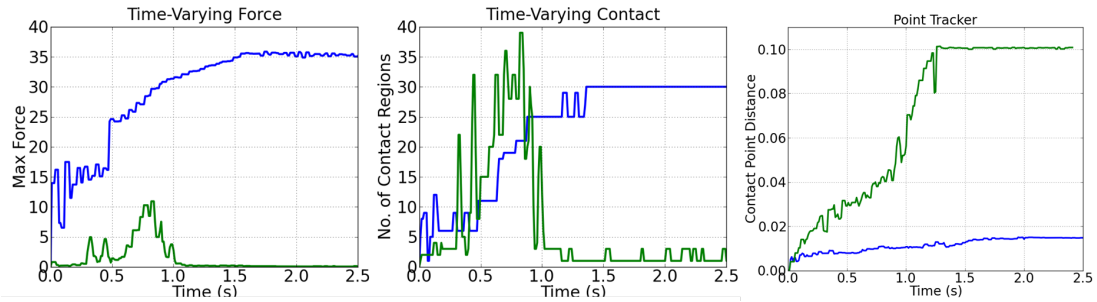

Figure 1.5: *Example of the three features that we computed from the data from the forearm skin sensor and used for classification of object properties. The leftmost picture shows the maximum force over time (in Newtons), the middle one shows the contact area over time while the rightmost picture shows the contact motion (in meters). The green lines are the features for a movable object while the blue lines are the features for a fixed object.*

we estimated the distance the 3D position of the centroid of the connected component traveled in the world frame from its 3D position at the onset of contact. We assumed that the robot's torso did not move throughout the trials and used the forward kinematics from the robot's torso to the contact location center on the robot's forearm to estimate the 3D positions and distance. We expected these three features to be informative about the object's softness and movability. For example, with increasing force applied to a soft, fixed object, we would expect the contact area to increase. Likewise, we would expect the 3D position of the contact to travel when encountering movable and soft objects. When making contact with a rigid and fixed object, we would expect the maximum force to go up.

We created 40 element vectors for each of the feature time-series by uniformly subsampling the 100 Hz measurements. We then concatenated the resulting vectors of maximum force, number of taxels in the contact region, and motion of the centroid of the contact region to form a feature vector of length 120 for each trial considering the first 1.2 s time-window after the onset of contact. To reduce the influence of noise and overfitting, we computed a low dimensional representation of the data with principal component analysis (PCA) before classification with a k-nearest neighbor classifier (k-NN). In our classification experiments, we used a maximum of 20 principal components for dimensionality reduction.

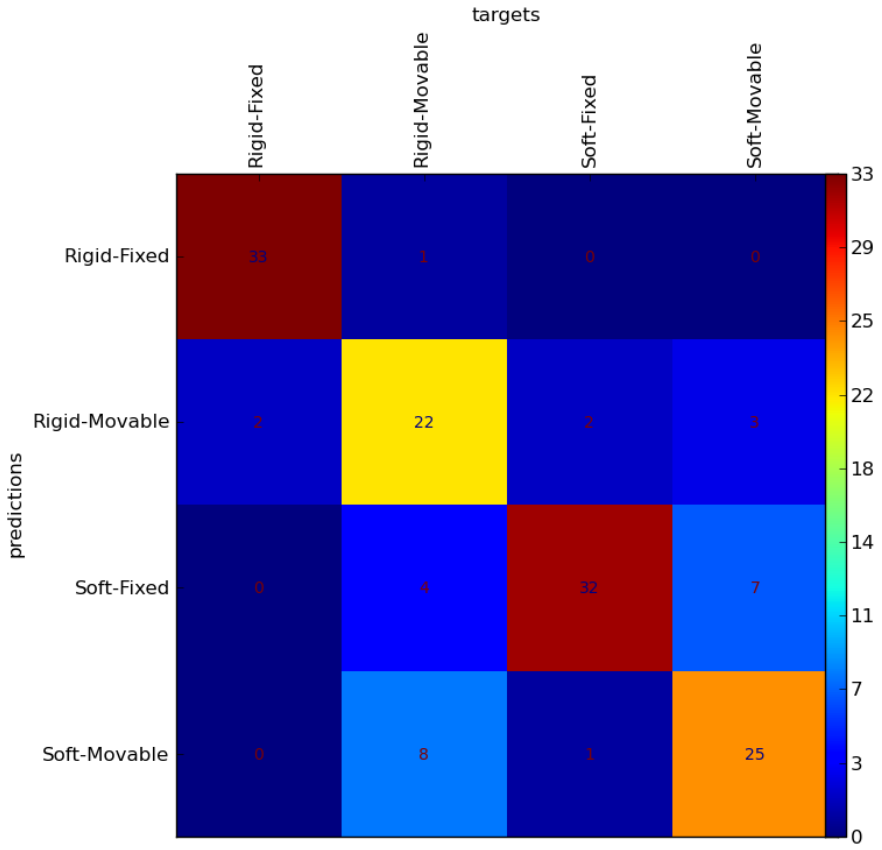

Figure 1.6: *Classification into 4-categories.*

1.5 Results and Discussion

1.5.1 Classification Results

We used a k-NN classifier to test the classification accuracy for two different classification problems. In each case, we picked the number of principal components and the value for k by performing a grid search over these two parameters and picking the values associated with the highest leave-one-out cross-validation accuracy.

Fig. 1.6 shows the confusion matrix for the classification into four categories: 1) *Rigid-Fixed*, 2) *Rigid-Movable*, 3) *Soft-Fixed*, and 4) *Soft-Movable*. The classification accuracy was 80% with k = 2 and dimensionality 20. Many of the classification errors were between

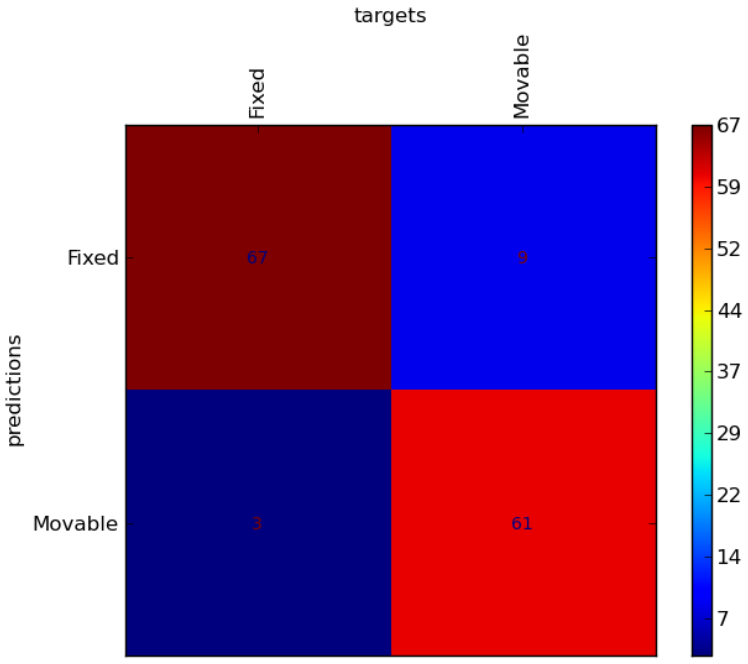

Figure 1.7: *Classification into 2-categories.*

the *Rigid-Movable* and *Soft-Movable* classes.

Fig. 1.7 shows the confusion matrix for a two category classification problem where we used the data to classify an object as either fixed or movable. The classification accuracy was 91.43% with k = 4 and dimensionality 3.

Fig. 1.8 shows the confusion matrix for recognizing the specific object that the robot interacted with. The classification accuracy was 72.14% with k = 1 and dimensionality 7.

The next subsections analyze the effect of various conditions, parameters and features on the classification and recognition accuracy.

1.5.2 Effect of Taxel Resolution

We performed the four category classification experiment and the object recognition experiment for different spatial resolutions of the taxels.

Table 1.1 shows the leave-one-out cross-validation accuracy, the values for the number

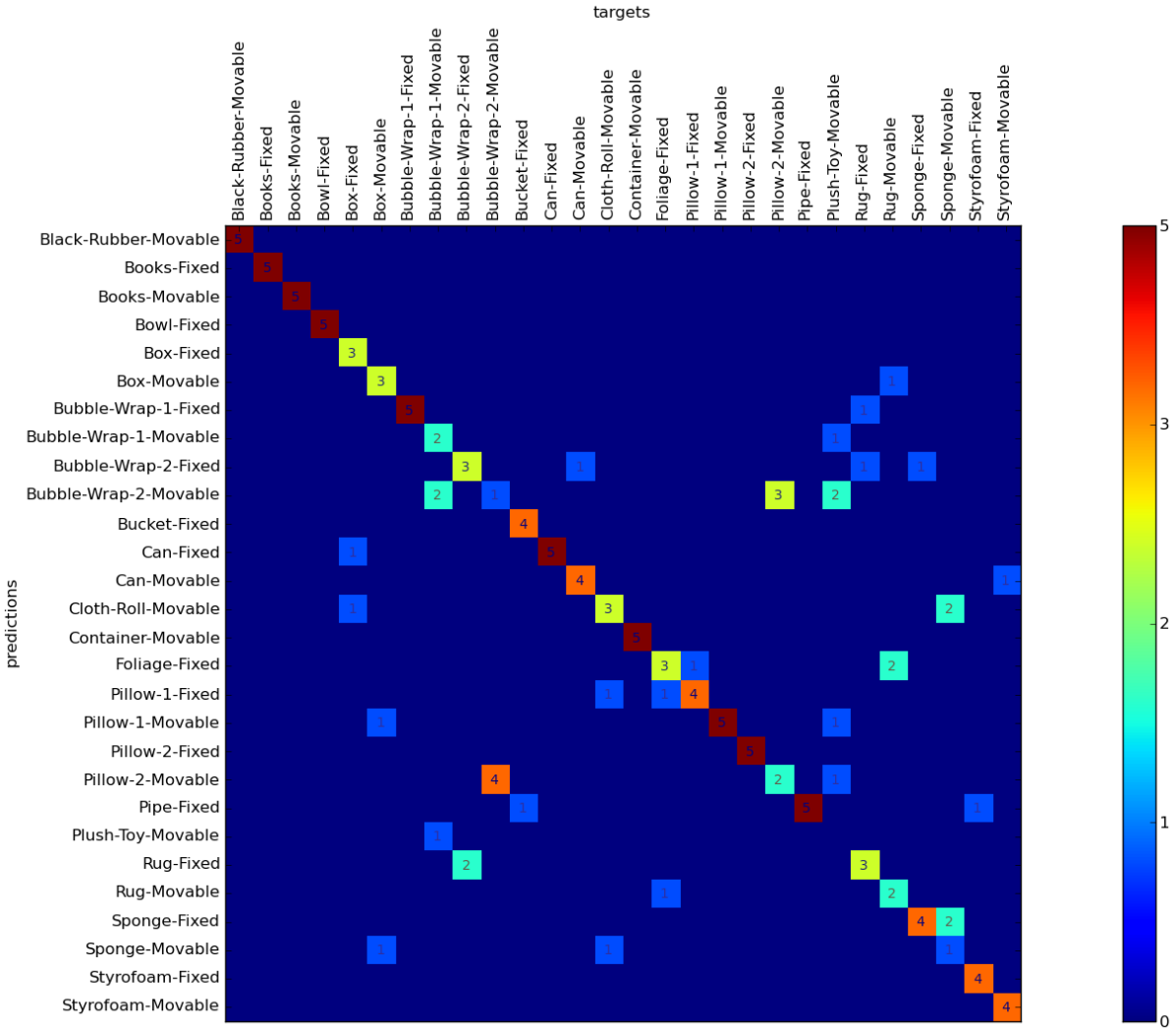

Figure 1.8: *Object Recognition.*

Table 1.1: Effect of Taxel Resolution.

Taxels/m	Classification Parameters	Classification Accuracy	Recognition Parameters	Recognition Accuracy
1	k = 3,PCs = 10	64.29%	k = 1,PCs = 14	57.14%
2	k = 5,PCs = 6	67.14%	k = 1,PCs = 5	58.57%
7	k = 14,PCs = 19	65.71%	k = 1,PCs = 4	57.14%
28	k = 8,PCs = 11	71.43%	k = 1,PCs = 7	63.57%
112	k = 2,PCs = 20	80%	k = 1,PCs = 7	72.14%

of neighbors and the dimensionality of the subspace that resulted in the highest accuracy for each taxel resolution. Fig. 1.9 shows the best classification accuracy that we obtained for the different resolutions. Compared to 1 taxel/meter, 112 taxel/meter resolution improved the classification accuracy by 24.44% for the four category classification problem and by 25.01% for object recognition.

1.5.3 Effect of Time Window

We also investigated the effect of varying the time-window of the sensor data on the classification accuracy. To do this, we used the same methods, except that we uniformly sampled 40 measurements of each feature type over a shorter time-window. Fig. 1.10 shows that a shorter time-window of 0.8 seconds resulted in substantially lower classification accuracy. This is unfortunate, since faster estimation could improve the robot's efficiency. Estimation over shorter periods of time might be possible with faster motions. Note that for our experiments the robot forearm joint velocity was around 0.35 rad/s prior to contact . Other measurements, such as higher frequency tactile information and different modalities, such as shear force and temperature, might enable more rapid estimation. For example, the surface texture of an object could potentially be sensed soon after initial contact. On the other hand, determining whether or not an object will slide depends on the applied force. So, we would expect that there would be some delay as the force applied by the robot ramps up and potentially overcomes static friction. For an object to be considered movable in our experiments, it needed to be moved by the robot's stereotyped motion.

1.5.4 Effect of Feature Scaling

Researchers often argue that proper scaling of different feature vectors might be necessary for high performance [28]. To analyze this aspect, we employed several scaling schemes to our original data, which were in units of taxels (contact region area), Newtons (maximum force), and Meters (displacement of the contact region center), to see how the performance was affected by the choice of scaling function. We used four different scaling methods as described by Eqs. 1.1-1.5 denoted as Methods I to V respectively. Methods I to IV given by Eqs. 1.1-1.4 scale all three features within a uniform range. However, Method V, given by Eq. 1.5 scales up the contact motion feature to the range of the other two features such as contact area and maximum force. We tested this since both the contact area and maximum force features are in a comparable range of values while the values for the contact motion feature were much smaller as seen from Fig. 1.5.

$$S_f = (f - mean(f)) \,/\, \max(f) \tag{1.1}$$

$$S_f = (f) \,/\, \max(f) \tag{1.2}$$

$$S_f = (f - mean(f)) \tag{1.3}$$

$$S_f = (f - mean(f)) \,/ Std\_dev(f) \tag{1.4}$$

$$\forall f \in \{Max.\ Force, Contact\ Area, Contact\ Motion\}$$

The results of the 4-category, 2-category classification accuracy and object recognition

Table 1.2: Effect of Feature Scaling.

Scheme	No Scaling	Method-I	Method-II	Method-III	Method-IV	Method-V
Classification into 4 categories	80%	66.43%	67.86%	75%	61.43%	82.14%
Classification into 2 categories	91.43%	92.14%	92.14%	87.14%	92.86%	90.71%
Object Recognition	72.14%	65%	67.86%	62.86%	62.14%	70.71%

performance, with feature scaling, are given in Table 1.2.

$$S_{f_{contact\_motion}} = \frac{f_{contact\_motion} * \max(f)}{\max(f_{contact\_motion})} \tag{1.5}$$

$$\forall f \in \{Max.\ Force, Contact\ Area\}$$

Results from Table 1.2 show that Method V has the highest 4-category classification accuracy while Method I and II have the highest 2-category classification accuracy. The highest object recognition performance was obtained using the original units without additional scaling. Also, the accuracy enhancement for classification algorithm was negligible compared to the unscaled feature based results. None of the scaling schemes showed a consistent increase in accuracy for all the object classification and recognition cases when compared to the unscaled data. Overall, scaling the original units did not have clear benefits.

1.5.5 Effect of Different Features

Lastly, we analyzed the effect of individual features and their combinations on the performance of the classification and object recognition tasks. We implemented the algorithm with different combinations of features for both 4-category and 2-category classification schemes as well as object recognition scheme. Table 1.3 shows the cross-validation accuracy.

Table 1.3 shows that using both maximum force and contact area features gave better overall performance. The addition of contact motion feature did not improve the perfor-

Table 1.3: Classification and Recognition Accuracy with Combinations of Different Features.

Scheme	Features	Maximum Force	Contact Area	Contact Motion
4-Category Classification Accuracy	Maximum Force	81.43%	80%	75.71%
	Contact Area	80%	73.57%	72.86%
	Contact Motion	75.71%	72.86%	60%
2-Category Classification Accuracy	Maximum Force	90%	91.43%	84.29%
	Contact Area	91.43%	90%	89.29%
	Contact Motion	84.29%	89.29%	82.14%
Object Recognition Accuracy	Maximum Force	64.29%	72.14%	66.43%
	Contact Area	72.14%	56.43%	60%
	Contact Motion	66.43%	60%	49.29%

mance considerably. If only one feature was to be used, the probable choice would be to use the maximum force over time feature. Also, the choice of a particular feature had little effect on the performance of the 2-category classification scheme. The lack of influence due to the motion feature may be due to the robot's stereotyped motion. Although the robot's compliance resulted in different contact motion over time, the motions resulted from the same controller commands over time, and thus had a form of temporal consistency.

1.6 Conclusion

In this paper, we developed an object classification and recognition algorithm using haptic information obtained from interactions of a tactile sensing forearm with environment objects. Our algorithm classified objects into one of the four categories: *Rigid-Fixed*, 2) *Rigid-Movable*, 3) *Soft-Fixed*, and 4) *Soft-Movable*. We extracted features such as time-trends of maximum force, contact area and contact motion from the haptic interactions and preprocessed those to show the information from the onset of contact. We computed a low-dimensional representation of the data using Principal component analysis and used a Nearest Neighbor classifier for classification and recognition purposes. Results showed that the classification and recognition algorithms worked well. We studied the effect of the skin-sensor resolution on the performance of the algorithm. It showed that the skin-sensor

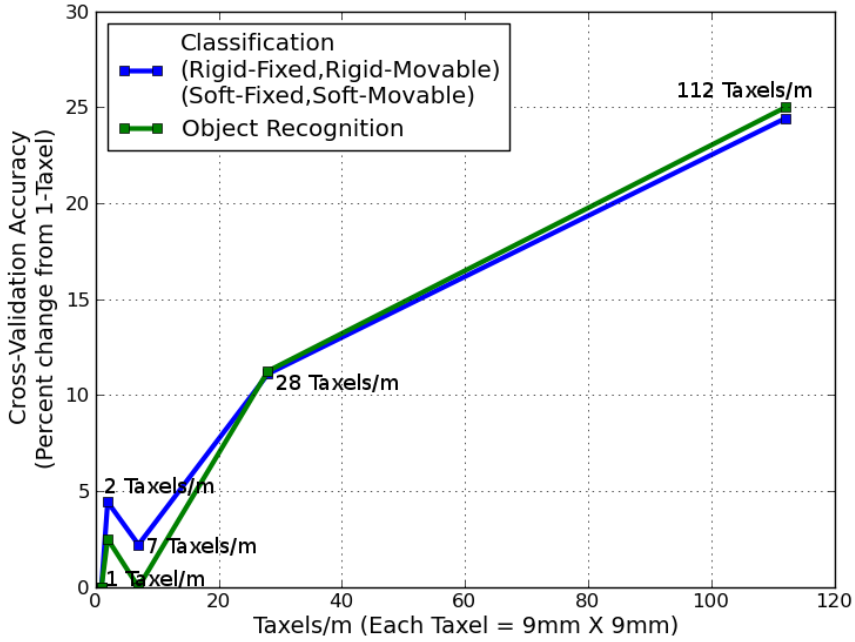

Figure 1.9: *Effect of Taxel Resolution on Cross-Validation Accuracy.*

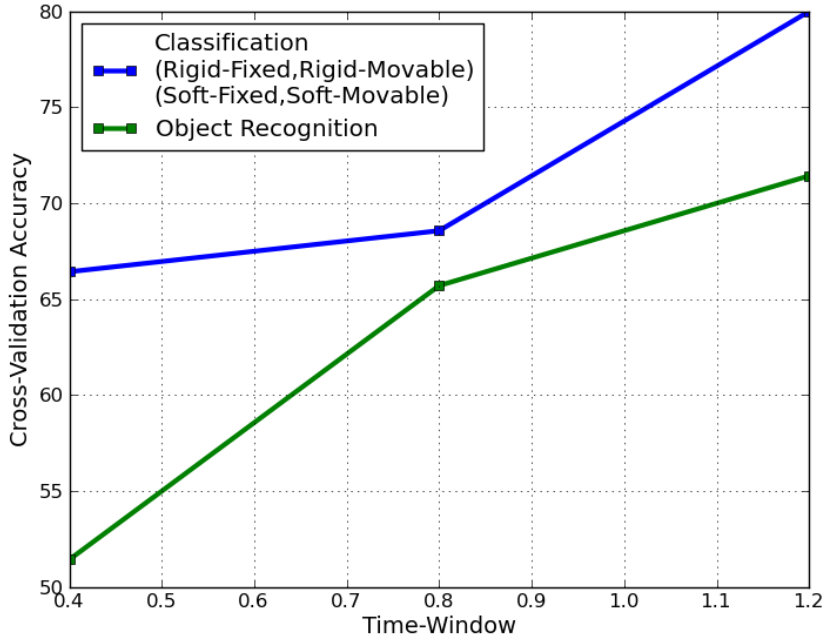

Figure 1.10: *Effect of Time-Window on Cross-Validation Accuracy.*

with higher resolution (384 taxels) enhanced the performance of the algorithm compared to 1 taxel resolution. We also analyzed the effects of time-window of haptic interaction, feature-scaling, and selection of specific features on the overall performance. These studies could provide useful intuitions on the various aspects of this task at hand and might serve as valuable guidelines for our future work in this domain.

CHAPTER 2
INFERRING OBJECT PROPERTIES WITH A TACTILE SENSING ARRAY GIVEN VARYING JOINT STIFFNESS AND VELOCITY

2.1 Research Summary

Whole-arm tactile sensing enables a robot to sense contact and infer contact properties across its entire arm. Within this paper, we demonstrate that using data-driven methods, a humanoid robot can infer mechanical properties of objects from contact with its forearm during a simple reaching motion. A key issue is the extent to which the performance of data-driven methods can generalize to robot actions that differ from those used during training. To investigate this, we developed an idealized physics-based lumped element model of a robot with a compliant joint making contact with an object. Using this physics-based model, we performed experiments with varied robot, object and environment parameters. We also collected data from a tactile-sensing forearm on a real robot as it made contact with various objects during a simple reaching motion with varied arm velocities and joint stiffnesses. The robot used one nearest neighbor classifiers (1-NN), hidden Markov models (HMMs), and long short-term memory (LSTM) networks to infer two object properties (hard vs. soft and moved vs. unmoved) based on features of time-varying tactile sensor data (maximum force, contact area, and contact motion). We found that, in contrast to 1-NN, the performance of LSTMs (with sufficient data availability) and multivariate HMMs successfully generalized to new robot motions with distinct velocities and joint stiffnesses. Compared to single features, using multiple features gave the best results for both experiments with physics-based models and a real-robot.

2.2 Introduction

Manipulation in unstructured environments with high clutter is difficult due to a variety of factors, including uncertainty about the state of the world, a lack of non-contact trajectories, and reduced visibility for line-of-sight sensors [29]. Tactile sensing is well-matched to these challenges, since it benefits from contact and uses sensors that move with the manipulator into the clutter. When contact occurs with tactile sensors, the robot has an opportunity to acquire information. By fully covering the robot's manipulator with tactile sensors, the robot is likely to have more opportunities to acquire useful information through contact. However, with a typical serial manipulator, a robot cannot independently control the pose of each of the sensors. In addition, contact may not be anticipated.

Within this paper, we address the problem of haptic perception based on contact [30–32] with a tactile-sensing forearm on a humanoid robot. The time varying signals from a tactile sensing array depend on the robot's actions, including the joint stiffnesses and joint velocities of the robot. A key problem for data-driven approaches is how to infer object properties based on these signals when the robot's actions are different from those used during training. In other words, after a robot has learned about an object using one action, it would ideally be able to infer the same properties of the object when making contact with it using a different action. In this paper, we consider an example of this type of problem. *Specifically, we focus on a robot inferring object properties with a tactile sensing array when the robot's joint stiffness and joint velocity differ from those used during training.*

The type of action we consider in this work is a short compliant movement of a robot's forearm akin to movements that occur during reaching. Figure 2.1 shows one such example when the robot, Cody, came into contact with a cylindrical object made of polystyrene foam, while trying to reach a goal configuration. We intentionally do not have the robot use exploratory behaviors, and instead investigate inference from short duration contact (i.e., 5 s and 1.2 s). Our choice of action is inspired by the potential for robots to infer

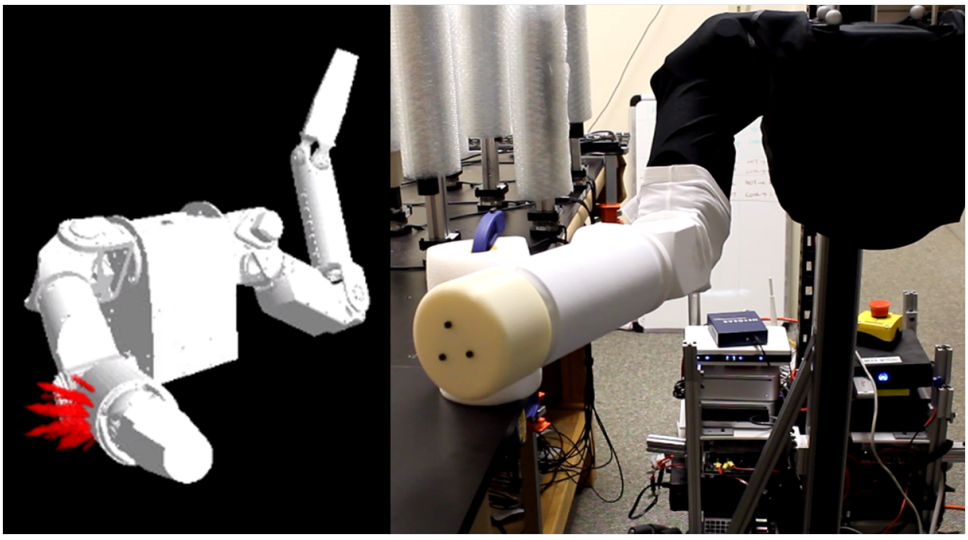

Figure 2.1: *Force data from forearm skin sensor mounted on the robot, Cody. The forearm came into contact with a cylindrical object made of polystyrene foam, while trying to reach a goal configuration. The red arrows show the forces acting on the skin.*

useful properties of the world based on *incidental contact*. By incidental contact, we mean contact that is not central to the robot's current actions and may occur unexpectedly or unintentionally.[1] For example, while manipulating in cluttered environments, incidental contact is more likely to occur and can be common with some approaches to robot control [29, 33, 34]. Incidental contact will typically not involve active exploration and interrogation of the contact, since the robot will be directing its resources elsewhere [31, 32]. Each such contact event is an opportunity for sensing. Unlike deliberate probing, during which the robot has more control over its actions to optimize its sensing, the sensing is opportunistic during these motions and contact events can be brief and simple, which could make inference challenging.

2.2.1 Opportunities and Challenges of Haptic Perception

Inferring mechanical properties of objects from contact could be beneficial in a number of ways. For example, we have shown that haptically recognizing leaves vs. trunk while a robot reaches into artificial foliage can be used to haptically map the environment and

[1] This description supersedes our previous descriptions from [31] and [32].

plan paths to goals [31, 32]. Rather than recognizing a particular object type, detecting an object's properties could be informative in novel environments. Detecting that an object has *moved* due to a robot's actions might be used by the robot to make better decisions, such as moving the object away in order to access a new location, or avoiding the object, so as not to alter the environment further. Likewise, detecting that an object is *hard* or *soft* has implications for the robot's ability to compress the object and the consequences of collisions with the object.

One of the challenges of haptics is that sensing depends on action. For example, haptic perception of surface roughness depends on contact speed [35] and contact force [36]. Many existing tactile systems use carefully controlled exploratory behaviors to reduce variability of the actions and gather information about the object (See Section 2.3). The signals produced from a robot's tactile sensors depend on the mechanics of both the object and the robot. Physical interaction depends on the dynamics of impact between a robot and an object. For example, *depending upon how stiff or compliant a robot is or how fast a robot moves, the physical interaction will vary.* As such, a key issue for data-driven approaches to tactile perception of contact is the extent to which the performance of perceptual classifiers can generalize when a robot's actions differ from those used to collect training data.

Classifying an object based on its compliance or mobility can become challenging when robot joint stiffness or velocity changes. For example, interaction forces are a function of the robot joint stiffness as well as object stiffness. The forces generated by contact between a stiff robot and a hard object is not the same as the forces generated by contact between a compliant robot and a hard object. Hence, perceiving an object as hard/soft is challenging if the robot stiffness changes, because it is difficult to distinguish the interaction between a stiff robot and a soft object and a compliant robot and a hard object. Similarly, it may be difficult to determine if an object has moved based on tactile sensing if the robot actions change. A movement in the robot's arm after contact can be due to the actual movement of the object (e.g. sliding motion) or because of the compliance in the structure of the object

(the robot arm pushes into the object and the object deforms). A compliant robot moving with a low velocity could push into a soft object resulting in robot arm movement after initial contact, which could be similar to the actual movement of a hard object (without any deformation) generated by a stiff robot impacting with a high velocity. In this work, we focus on addressing these challenges by:

- classifying an object into one of the four categories: 1) *Hard-Unmoved* (HU), 2) *Hard-Moved* (HM), 3) *Soft-Unmoved* (SU), and 4) *Soft-Moved* (SM), and
- investigating the potential of data-driven methods to generalize the performance of haptic perception to different robot conditions such as robot stiffness and velocity used to collect training data.

2.2.2 Methods

We used univariate and multivariate HMMs as well as long short-term memory (LSTM) networks to infer object properties (Section 2.4) and compared the results with 1-NN used in our previous work [30]. In Section 2.5, we present an idealized physics-based lumped element model of a robot with a compliant joint making contact with an object. Using this model, we performed experiments with physics-based simulations of varied robot, object, and environment parameters in Section 2.6. In Section 2.7, we present experiments with a real robot for which we varied the robot arm's velocity and joint stiffness to values distinct from those used during training. Our multivariate HMM-based method performed well in experiments with both physics-based simulations (Section 2.6.5) and with a real robot (Section 2.7.5) for classifying objects into the four categories. Our LSTM networks performed better when a larger amount of data was available with the physics-based simulation compared to experiments with the real robot. Section 2.8 discusses the methods and their limitations and Section 2.9 provides the conclusion of our work.

2.3 Related Work

Object categorization is a well studied task. In this work, we focus on inferring properties of objects based on haptic sensing. Although there have been multiple studies on haptics-based compliance discrimination, most have used specific exploratory behaviors using end effectors to extract information from the environment. Lederman and Klatzky discussed in detail the various factors and exploratory behaviors that humans use for inferring haptic properties of objects [37]. However, studies of discrimination tasks using information from incidental contact with large-area tactile sensing are lacking. Also, studies on inferring properties of objects and *generalizing the performance across various conditions such as robot stiffnesses and velocities* are rare.

Researchers have also used haptics and tactile sensing to infer properties of the world for purposes other than categorizing objects. Silvera-Tawil et al. presented a comprehensive review of state-of-the-art methods in tactile sensing for robots in socially interactive scenarios [38]. Wu et al. used tactile arrays for recognizing human intended directions in two dimensions using support vector machine classifiers (SVMs) [39]. Muscari et al. developed algorithms for reconstructing force and shape distributions using capacitive tactile sensing arrays [40]. Hughes et al. presented a soft robotic artificial skin for texture recognition and localization [41]. Javaid et al. used pressure sensors to classify human activities during assistive tasks to help older adults [42]. Matheus and Dollar used a load cell and a custom-built device to infer static friction properties of some 'Objects of Daily Living' [15]. Boonvisut and Çavuşoglu used exploratory behaviors and vision to collect deformation data for identifying boundary constraints of deformable objects required to estimate soft tissue properties [43]. Researchers have used tactile sensors to classify events such as slips between fingertips and objects and slips between objects and external surfaces [44–46]. Researchers have also used haptic sensing for texture perception [5, 47, 48], tactile servoing [49], contour following [50], and human-robot collaborative tasks [51, 52].

In the following subsections, we review the existing literature that addresses object categorization using haptics.

2.3.1 Material Property Based Classification

In this work, we do not explicitly model material properties, but the features that we extract from the interactions between the robot arm and environmental objects are a direct consequence of material properties. Drimus et al. classified hard and deformable objects based on haptic feedback from a novel tactile sensor consisting of a flexible, piezo-resistive rubber [4]. They represented tactile information from a palpation procedure as a time series of features and used a k-nearest-neighbor (k-NN) classifier to categorize the objects [4]. Our classification scheme considers both compliance and mobility characteristics and uses information from incidental contact sensed with large-area tactile sensors.

Chu et al. presented research that uses discrete HMMs to construct a feature vector of likelihoods and used binary SVM classifiers to classify those vectors and automatically assign 24 adjectives to 60 objects [53]. In contrast to our work, their research focused on classifying data using both static and dynamic features from four deliberate exploratory procedures with sophisticated BioTac [54] robotic fingers from *Syntouch*.

Kaboli et al. used multi-modal tactile features to distinguish texture and weight of objects using sliding and non-sliding exploratory behaviors [55]. Kim and Kesavadas presented a method for estimating the material properties of objects (steel, aluminum, wood, silicon rubber) using an active tapping procedure [7]. Takamuku et al. estimated the hardness properties of objects through tapping and squeezing behaviors [8]. Hosoda and Iwase obtained haptic data using a bionic hand to grip an object. They used a recurrent neural network to classify objects based on haptic cues learned from dynamic interactions [9]. Nizar et al. classified the material type and surface properties by developing a sensor that used a lightweight plunger probe to detect surface properties. They also used an optical mouse sensor to obtain surface images and implemented a radial basis function neural network

for classification [13]. Liarokapis et al. used random forests to classify size and stiffness of objects as well as distinguish object types using a single force closure grasp with an underactuated robotic hand and force sensors [56]. Schmitz et al. used power grasping of objects and multiple modalities for object recognition with deep learning [57]. Kiwatthana and Kaitwanidvilai used system identification and K-means clustering techniques to classify different cans using proprioceptive feedback [58]. Hoelscher et al. used BioTac fingers and Schunk F/T sensors with multiple classifiers and feature extraction methods for object recognition. They concluded that simple, dimensionally-reduced features performed better than more elaborate features [59].

In summary, although there have been many studies on material property based classification, most have focused on carefully controlled specific exploratory behaviors using the robot's end-effector. These studies have not looked at whether the classification performance can generalize to different robot behaviors.

2.3.2 Shape Based Classification

Many researchers have either used tactile images from touch sensors or analyzed object shape deformation behaviors for object categorization. Schneider et al. applied a "bag-of-words" approach and unsupervised clustering techniques to categorize objects [17]. Pezzementi et al. identified the principal components of features, then clustered them, and constructed per-class histograms as a class characteristic [21]. Gorges et al. introduced passive joints in the hand for better adaptibility to different object shapes and used a Bayes classifier to classify the objects [22]. Babu et al. used 'C4.5' algorithm to generate a decision tree and a naive Bayes classifier to categorize shapes of objects using a tactile sensor array [60].

Other researchers have analyzed deformation behavior to classify objects. They have used vision and haptic sensors [61, 62] or finite element models [10, 11] and volumetric models such as superquadrics [18], polyhedral models [19] or wrapping polyhedra [20].

To summarize, shape based classification methods have used tactile images or defor-

mation behaviors to classify objects after exploring or grasping them using multi-fingered robot hands. Again, most of these studies used exploratory behaviors and have not looked at whether the performance can generalize to different robot behaviors used to collect training data.

2.3.3 Functional Property Based Classification

This group of studies focused on functional property based classification or classification based on how objects behave when they are moved. Sinapov et al. used the acoustic properties of objects during specific interaction schemes and the behavioral interactions performed with them, such as grasping, shaking, dropping, pushing, and tapping, to classify 36 different household objects [23]. Berquist et al. monitored the changes in the joint torques of a robot while it performed five exploratory procedures — lifting, shaking, crushing, dropping, and pushing — on several objects and demonstrated that the robot could learn to recognize objects based solely on the joint-torque information [24]. Jain et al. used data-driven object centric models to haptically recognize specific doors as well as classes of doors (refrigerator vs. kitchen cabinet) [63]. Griffith et al. used multiple exploratory behaviors and employed clustering techniques to categorize containers and non-containers. After extracting visual and acoustic features from interactions with objects, they employed unsupervised clustering techniques to form several categories [25]. Sinapov et al. combined proprioceptive and auditory feedback and used a behavior-grounded relational classification model to recognize categories of household objects [26]. Sinapov and Stoytchev extended their previous work by using auditory, proprioceptive, and visual modalities to cluster novel and unlabeled objects for object individuation based on the robot's sensorimotor experience of handling those novel objects [64].

To summarize, functional property based classification methods have used multimodal feedback from robot behaviors and actions to distinguish between different object categories. But, similar to other work, most of them used exploratory behaviors and have not

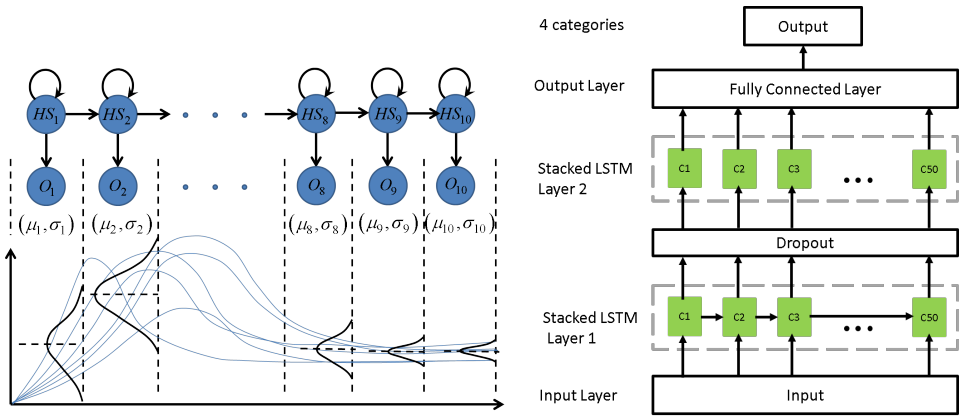

Figure 2.2: *Schematic of a left-right HMM with 10 states. The observations are modeled using Gaussian distributions (Left). Schematic of a Stacked LSTM network with 50 cells in each layer, dropout in between, and a fully connected layer as the output layer (Right).*

looked at if the results can generalize to different robot behaviors.

2.4 Data-Driven Methods

For this work, we chose hidden Markov models and long short-term memory (LSTM) networks as our data-driven methods to infer object properties from contact. To compare our results, we used k-nearest neighbors from our previous work [30] as the baseline data-driven method.

Hidden Markov Models

Hidden Markov models (HMMs) have a long history of success for classifying time series such as human speech [65]. HMMs are known to have rich mathematical structure for modeling non-stationary signals and can work effectively in practical applications [65]. In this study, we used HMMs to classify an object as being in one of four categories: 1) *Hard-Unmoved* (HU), 2) *Hard-Moved* (HM), 3) *Soft-Unmoved* (SU), and 4) *Soft-Moved* (SM).

A hidden Markov model (HMM) is a state-based data modeling tool that assumes the states are hidden and the system is a Markov process. The hidden states (HS_i) are inferred using observations (O_t) at time t. The components of an HMM include N, the number of

states in the model; $\mathbf{A}$, the state transition probabilities; $\mathbf{B}$, the observation probabilities; and π, the initial state probabilities. We use notation from [65]. Equation (2.1) shows the HMM model (λ). Eq. (2.2) shows the state transition probabilities.

$$\lambda = (\mathbf{A}, \mathbf{B}, \pi) \tag{2.1}$$

$$\mathbf{A} = \{a_{ij}\} = \{P\left(x_t = HS_j | x_{t-1} = HS_i\right)\},\ 1 \leq i,\ j \leq N, \tag{2.2}$$

where i, j are state indexes and

$$\begin{aligned} a_{ij} &\geq 0, \\ \sum_{j=1}^{N} a_{ij} &= 1 \end{aligned} \tag{2.3}$$

Note, for a left-right HMM, as time increases, the state index increases or stays the same. Therefore, there is an additional constraint given by

$$a_{ij} = 0,\ j < i \tag{2.4}$$

Eq. (2.5) represents the initial state probabilities.

$$\pi = \{\pi_i\} = \{P\left(x_1 = HS_i\right)\},\ 1 \leq i \leq N \tag{2.5}$$

For a discrete HMM with M distinct observation symbols, eq. (2.6) shows the obser-

vation probabilities.

$$\mathbf{B} = \{b_j(k)\} = \{P(O_t = v_k | x_t = HS_j)\},\ 1 \leq j \leq N, \quad 1 \leq k \leq M, \tag{2.6}$$

where $\mathbf{V} = \{v_1, v_2, ..., v_M\}$ are the individual symbols. However, for a continuous HMM with observation vector $\mathbf{O}$ and multivariate Gaussian emissions with mean vector $\boldsymbol{\mu}$ and covariance matrix $\mathbf{U}$, eq. (2.7) shows the emission probabilities.

$$\begin{aligned} \mathbf{B} = \{b_j(\mathbf{O})\} &= \{P(\mathbf{O} | x_t = HS_j)\} \\ &= \left\{\mathcal{N}\left[\mathbf{O}, \boldsymbol{\mu}_j, \mathbf{U}_j\right]\right\}, \\ &\quad 1 \leq j \leq N \end{aligned} \tag{2.7}$$

Figure 2.2 (Left) shows the schematic of one left-right HMM with $N = 10$ states.

2.4.1 Long Short-Term Memory Networks

Long short-term memory (LSTM) networks have been successfully used for modeling time-series in many applications such as machine translation, generating cursive writing, and speech recognition [66–68]. For mathematical details, please refer to [69], where this was first introduced. LSTMs have also been successfully used for haptic perception such as, to estimate forces during robot-assisted dressing simulations [70], and during robot-assisted surgery [71]. Note, Gao et al. [72] used LSTMs for haptic perception using visual and tactile features but the performance was lower compared to other deep-learning methods.

For our applications, we use an LSTM structure inspired by Gers et al. [73] in which each memory cell has an input gate, a forget gate, and an output gate. The specific structure that we used for our haptic classification tasks consists of 2 layers with 50 cells each. To

reduce overfitting, we also added a dropout layer in between the two layers, which helps in regularization [74]. We added a fully connected output layer. Section 2.6.4 shows the details of the implementation. The LSTM has a total of 31,004 parameters. The 31,004 parameters correspond to the weights of the stacked LSTM layers, the individual cells, as well as the fully connected layer for the 4-category classification output.

Figure 2.2 (Right) shows the schematic of the LSTM structure.

2.5 Physics-Based Model

We modeled contact between a tactile-sensing robot forearm and an object using a lumped element model. We developed a physics-based model that can model the mechanics of a variety of robot-object physical interaction phenomena. In this work, the tactile-sensing robot arm moves by actuating its shoulder joint towards a goal angle. The arc formed by the contact point during the motion is approximately a straight line for small angle movements and a large radius. We modeled the robot arm's motion at the contact point as a linear movement. We modeled the object as a deformable object and the contact surface as flat.

2.5.1 Robot and Object Model

We modeled the robot's arm trajectory using equilibrium point control [75]. Figure 2.3 (Left) shows a robot-arm of mass m_{arm} making contact with an object of mass m_{obj}. x_{arm} is the position of the robot-arm, x_{obj} is the position of the object, and x_{uobj} is the position of the undeformed object. During contact, if δ_{obj} is the object deformation, note that

$$x_{obj} = x_{arm} = x_{uobj} + \delta_{obj}, \tag{2.8}$$

otherwise, if the arm is not in contact with the object,

$$x_{obj} = x_{uobj} > x_{arm}, \tag{2.9}$$

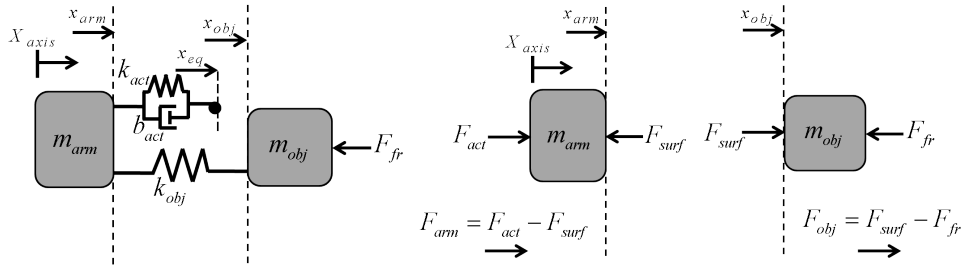

Figure 2.3: *Lumped element model of our system at the onset of contact between the robot-arm and the object (Left). Free-body diagrams of the robot-arm and object in contact (Right).*

x_{eq} is the equilibrium point of the actuator spring with stiffness k_{act} and actuator damping b_{act}. k_{obj} is the object stiffness. F_{fr} is the frictional force between the object and the environment.

Figure 2.3 (Right) shows free-body diagrams for the system depicted in Fig. 2.3 (Left). F_{act} is the force applied on the robot-arm by the actuator, F_{surf} is the force applied by the robot-arm to the surface of the object when in contact. F_{arm} and F_{obj} are the net forces acting on the robot-arm and the object respectively.

The force applied by the actuator to the robot-arm, F_{act} is given by eq. (2.10).

$$F_{act} = k_{act}\left(x_{eq} - x_{arm}\right) + b_{act}\left(\dot{x}_{eq} - \dot{x}_{arm}\right), \tag{2.10}$$

The net force on the arm, F_{arm}, is therefore calculated as in eq. (2.11).

$$F_{arm} = F_{act} - F_{surf}, \tag{2.11}$$

The net force on the object, F_{obj}, is given by eq. (2.12).

$$F_{obj} = F_{surf} - F_{fr}, \tag{2.12}$$

We model the joint as frictionless. Hence, the position of the robot-arm can be calculated by eq. (2.13), where $\dot{x}_{0_{arm}}$ is the initial velocity and $x_{0_{arm}}$ is the initial position of the

arm.

$$\begin{aligned} \dot{x}_{arm} &= \int \left(F_{arm}/m_{arm}\right) dt + \dot{x}_{0_{arm}}, \\ x_{arm} &= \int \dot{x}_{arm} dt + x_{0_{arm}}, \end{aligned} \tag{2.13}$$

The position of the undeformed object is calculated using eq. (2.14), where $\dot{x}_{0_{obj}}$ is the initial velocity and $x_{0_{obj}}$ is the initial position of the undeformed object.

$$\begin{aligned} \dot{x}_{uobj} &= \int \left(F_{obj}/m_{obj}\right) dt + \dot{x}_{0_{obj}}, \\ x_{uobj} &= \int \dot{x}_{uobj} dt + x_{0_{obj}}, \end{aligned} \tag{2.14}$$

F_{surf} is calculated using eq. (2.15),

$$F_{surf} = k_{obj} \left(x_{arm} - x_{uobj}\right), \tag{2.15}$$

Please note that the frictional force F_{fr} is calculated differently depending on whether the object is moving or not as shown in eq. (2.16). If the applied force overcomes static friction, the object starts moving. μ_s and μ_k are the coefficients of static and kinetic friction, respectively and $g = 9.81$ m/s^2.

$$F_{fr} = \begin{cases} F_{surf},\ stationary \\ \mu_s \left(m_{obj} g\right),\ just\ before\ motion \\ \mu_k \left(m_{obj} g\right),\ in\ motion \end{cases} \tag{2.16}$$

2.5.2 Contact Area Model

For an object in the shape of a cube with edge length L_{obj}, and surface area A_{obj}, let us assume that due to a robot-arm's applied force F_{surf}, there is a positive axial compression given by ΔL_{obj} in the x-direction (See Fig. 2.4). Let the cube be made up of a homogeneous material with Poisson's ratio ν_{obj} [76] and due to the applied force, let the elongations in

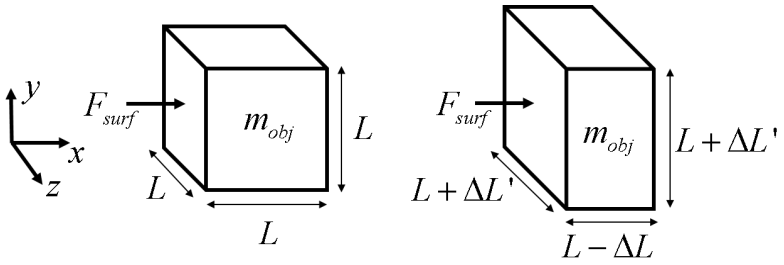

Figure 2.4: *Due to applied force in x-direction, an object undergoes axial compression. This results in elongation in the other orthogonal axes directions, thus increasing the surface contact area proportional to the object material's Poisson's ratio.*

the y and z-directions be $\Delta L'_{obj}$. Before deformation, the surface area is given by,

$$A = L^2, \tag{2.17}$$

After deformation, the surface area becomes

$$A' = (L + \Delta L')^2, \tag{2.18}$$

Therefore, the increase in the surface area, due to the applied force, becomes

$$\Delta A = A' - A = (L + \Delta L')^2 - L^2, \tag{2.19}$$

which leads to

$$\frac{\Delta A}{A} = \left(1 + \frac{\Delta L'}{L}\right)^2 - 1. \tag{2.20}$$

Let the strains in x, y, and z-axis due to the applied force F_{surf} be given by $d\epsilon_x = \frac{dx}{x}$, $d\epsilon_y = \frac{dy}{y}$, and $d\epsilon_z = \frac{dz}{z}$ respectively. We assume that when the object is compressed, the transverse strain is positive.

$$\nu_{obj} = -\frac{d\varepsilon_y}{d\varepsilon_x} = -\frac{d\varepsilon_z}{d\varepsilon_x} \tag{2.21}$$

Therefore, using the above relations, we have from [77]

$$\left(1 - \frac{\Delta L}{L}\right)^{-\nu_{obj}} = \left(1 + \frac{\Delta L'}{L}\right). \tag{2.22}$$

Combining eqs. (2.22) and (2.20), we have

$$\frac{\Delta A}{A} = \left(1 - \frac{\Delta L}{L}\right)^{-2\nu_{obj}} - 1, \tag{2.23}$$

Therefore, due to the applied force and resultant deformation, the new surface area is given by

$$A' = A + \Delta A = A\left(1 - \frac{\Delta L}{L}\right)^{-2\nu_{obj}}, \tag{2.24}$$

where $\Delta L = \frac{F_{surf}}{k_{obj}}$.

2.6 Experiments with Physics-Based Simulations

Using our physics-based model from Section 2.5, we generated simulated data and used the data for our experiments. The simulations with the physics-based model enabled us to generate data with a wide variety of robot, object, and environment conditions, which would be challenging with experiments with a real robot (Section 2.7). We focused on whether our algorithms could classify objects into four different categories and whether the classification performance could generalize to robots having varying mechanical characteristics. By *varying mechanical characteristics*, we mean motion of the robot in which the robot arm's joint stiffness and velocity are varied.

2.6.1 Experimental Setup

We modeled the objects as cubes of 10 different volumes. We varied the volumes of the cubes linearly. The edge-length varied from $l_{obj} = 0.01$ m to $l_{obj} = 0.2$ m. We chose 13 different materials to model the objects for our simulations. We chose materials represen-

Table 2.1: Material Selection for Simulations.

General Material	Common Objects	Young's Modulus (E) [87, 92] [98, 99] N/m^2	Density (ρ_{obj}) [87, 92] [93–96] kg/m^3	Friction Coefficients [78–91]				Ratio (ν)* [97] [100] [101]
				Wood Surface		Glass Surface		
				Static (μ_s)	Kinetic (μ_k)	Static (μ_s)	Kinetic (μ_k)	
ABS Plastic	Beverage containers	1.60E+09	1110.00	0.5	0.4	0.3	0.25	0.41
Glass	Beverage containers	6.25E+10	2250.00	0.17	0.14	0.95	0.35	0.2
Pine Wood	Furniture	1.68E+10	520.00	0.5	0.364	0.36	0.14	0.38
Ceramic	Counter Tops	7.00E+10	2250.00	0.5	0.4	0.42	0.35	0.18
Steel	Appliances	2.00E+11	7850.00	0.61	0.35	0.13	0.12	0.27
Polymer Foam	Mattresses	2.50E+05	54.00	0.12	0.11	0.37	0.3	0.27
Light Foam	Pillows	3.30E+04	16.00	0.12	0.11	0.37	0.3	0.28
Soft Foam	Seat Cushions	1.00E+04	48.06	0.12	0.11	0.55	0.5	0.30
Open Cell Foam	Sponges	2.20E+04	72.08	0.12	0.11	0.55	0.5	0.30
Natural Rubber	Footwear	2.00E+06	925.00	0.9	0.7	0.87	0.7	0.50
Neoprene Rubber	Clothing and Bags	1.35E+06	1240.00	0.9	0.7	0.87	0.7	0.49
Fat (Tissues)	Human Body	1.90E+03	919.60	0.91	0.6	0.45	0.3	0.41
Muscle (Thigh)	Human Body	1.28E+04	1060.00	0.91	0.6	0.45	0.3	0.30

*Ratio = Poisson's Ratio

tative of everyday household objects and the human body (See Table 2.1). We calculated the mass of the object, m_{obj}, using eq. (2.25), where ρ_{obj} is the density of the object. To calculate the friction coefficients, we modeled the objects resting on two kinds of surfaces made of wood and glass found on commonly used table tops (See Table 2.1).

We labeled objects as hard if the calculated stiffness (k_{obj}) was greater than $100,000$ N/m which is the stiffness of a medium-stiff environment [102]. Note, stiffness is a property

of object structure as well as its material and is distinct from the Young's modulus of a material which is a material property. For example, a flat thin rectangular block of plastic and a long slender cylindrical plastic bottle may have same Young's modulus (both are made of plastic, assuming the material is homogeneous) but they may have completely different stiffness due to different structural properties. If the calculated stiffness of the object (k_{obj}) was less than or equal to $100,000$ N/m, we labeled it as 'Soft' (See Section 2.8 for more detailed discussion on the 'hardness' of an object). We labeled objects as 'Moved' or 'Unmoved' based on whether x_{obj} was greater than 0 or equal to 0, respectively, at the end of the simulation. We ran simulations with the physics-based model for 5s. The mass of the robot, m_{arm}, was 1.167 kg based on the model of the forearm of the robot 'Cody' used in our experiments. During the simulations, the robot-arm model came in contact with objects in the shape of a cube of various edge-lengths. Each object of mass m_{obj} is made up of a single material from Table 2.1.

$$m_{obj} = \rho_{obj} {l_{obj}}^3 \tag{2.25}$$

For each object, we calculated the stiffness as

$$k_{obj} = 2 l_{obj} E_{obj}, \tag{2.26}$$

where E_{obj} is the Young's modulus of the material of the object. We derived eq. (2.26) for an object under both cantilever and axial loading.

2.6.2 Experimental Procedure

For the experiments, we simulated the robot moving using varying stiffness and velocity. Specifically, we trained the algorithms with three of the four possible combinations of stiffness and velocity conditions (low-velocity-low-stiffness, low-velocity-high-stiffness, high-velocity-low-stiffness, and high-velocity-high-stiffness) and tested with the other combina-

tion to find out how well the results generalized to different robot conditions. We repeated this procedure for each of the four conditions and reported the mean classification accuracy for all the conditions. We set the robot's stiffness (k_{act}) to a low value (543 N/m) or a high value (2050 N/m) based on the stiffness values identified in [103] and the velocity ($\dot{x}_{arm}$) to a low value (0.005 m/s) or a high value (0.02 m/s). These values correspond with the values used in our experiments with a real robot in Section 2.7.2. We set the damping (b_{act}) based on a critically damped system as given in eq. (2.27).

$$b_{act} = 2\eta\sqrt{k_{act}m_{arm}}, \tag{2.27}$$

where $\eta = 1$ is the damping ratio of a critically-damped system [104].

Data Collection

The simulated robot made contact with a set of solid cube objects (See Section 2.6.1) made of materials given in Table 2.1 while performing a simple, goal-directed reaching motion as shown in Section 2.5.1. We simulated the robot-object interactions on both a wooden and a glass table. We simulated the robot movement using an equilibrium-point control similar to that of our experiments with the real robot. We actuated the simulated robot by commanding a goal location and the robot moved according to a PD controller. The final goal location was inside the object.

Our algorithm classified the objects into the four categories 'Hard-Unmoved', 'Hard-Moved', 'Soft-Unmoved', and 'Soft-Moved'. There were 1835 simulation trials with 544 'Hard-Unmoved', 365 'Hard-Moved', 496 'Soft-Unmoved' and 430 'Soft-Moved' trials. Note that for each of the trials in which an object moved, we fixed it to generate one additional 'Unmoved' trial, similar to our experiments with the real robot.

Preprocessing and Feature Selection

We truncated the data to begin at the estimated onset of contact (whenever the force exceeds $0\ N$) between the robot and the object. We collected three time-varying features at each time-instant for $5\ s$ at 100 Hz. Our 'force' feature is F_{surf} (See Section 2.5.1), 'contact area' feature is A' (See Section 2.5.2), and 'motion' feature is x_{arm} (See Section 2.5.1). Note, if the robot loses contact with the object at any time-instant ($F_{surf} = 0$), A' becomes A. However, to match the scenario of experiments with the real robot (See Section 2.7.2), we make the 'contact area' feature 0 for those time-instants during preprocessing. We expected these three features (force, contact area, and motion) to be informative about the object's softness and mobility. These features are similar to the features selected in our experiments with a real-robot (See Section 2.7.2).

The frequency of the signal from tactile sensing forearm on the real robot is 100 Hz. We modeled an analog-to-digital anti-aliasing filter for the tactile sensing forearm using a low-pass Butterworth filter of order 6 and cut-off frequency of 200 Hz. We also modeled the tactile sensing forearm noise as Gaussian with zero mean and a signal-to-noise ratio of 0.5% for force measurements and zero mean and a signal-to-noise ratio of 0.05% for contact area measurements. We modeled the joint encoder noise as Gaussian with zero mean and a signal-to-noise ratio of 0.05%. The signal-to-noise ratio (SNR) values correspond with the sensor resolution values on the real robot and we used eq. (2.28) to compute them

$$SNR = \frac{\sigma^2_{signal}}{\sigma^2_{noise}}. \tag{2.28}$$

2.6.3 Implementation

We performed the simulations in MATLAB/Simulink with the 'ode15s (stiff/NDF)' solver [105] of maximum order '5' using the 'Variable-step' solver type and the 'Full perturbation' Jacobian method as well as the 'Adaptive' zero-crossing option. The resultant simulation

trials are of variable length due to the 'Variable-step' solver type. To make each simulation trial a vector of uniform length, first, we interpolated the data to a very high sampling rate of 100,000 Hz. Then, we applied a low-pass Butterworth filter to the signal. Finally, we resampled the data to 100 Hz to match the frequency of the tactile sensing forearm, and added Gaussian noise to match sensor noise.

We implemented continuous univariate and multivariate HMMs as well as LSTMs to model the temporal trends of features for different categories of objects. We modeled each of these four object categories: *Hard-Unmoved*, *Hard-Moved*, *Soft-Unmoved*, and *Soft-Moved*, using an HMM for each category ($\lambda_{HU}, \lambda_{HM}, \lambda_{SU}, \lambda_{SM}$).

We used the GHMM toolkit [106] to model the HMMs and implemented them in Python. We trained the models with the standard Baum-Welch algorithm, which uses expectation maximization. For testing, we ran the Viterbi algorithm which estimates the maximum likelihood with which a model can describe a given test data. These are standard methods for modeling sequential data (see [65] for details). We ran the Viterbi algorithm on the given test data for each of the trained HMM models and assigned the category associated with the model that returned the highest likelihood.

For LSTMs, we used the 'Keras' library [107] with the 'Theano' backend [108]. We trained our model for 10 epochs and used a batch-size of 5.

For comparison purposes, we implemented a one nearest neighbor classifier (1-NN) using the scikit-learn package [109] in Python. We used PCA to reduce the dimensionality of the concatenated features similar to [30]. We used the Amazon EC2 cloud computing service [110] to run the experiments on a c3.4xlarge system (high performance compute-optimized instances) with 30 GB of memory, 16 vCPUs and multiple c4.8xlarge systems with 60 GB of memory, 32 vCPUs. All of the systems were 64-bit Ubuntu 14.04 Linux platforms.

2.6.4 Algorithm Parameters

For the univariate and multivariate HMMs, we analyzed the performance with 10 states. We set a uniform prior to all the states and initialized the emission matrix with Gaussian distributions with means and standard deviations obtained from the training data. For multivariate HMMs using multiple features (force, area, and/or motion), we used a spherical covariance matrix for initialization. Also, for multivariate HMMs, we scaled each feature (f) to a scaled feature (S_f) according to eq. (2.29) to normalize the values.

$$S_f = (f - \text{mean}(f)) / \text{std}(f) \tag{2.29}$$

For LSTMs, we initialized the parameters with a uniform distribution, used 'softsign' activation functions for the hidden layers, and 'softmax' activation function [107] for the fully connected output layer. Our dropout probability was 0.2. We used 'RMSprop' [107] as the optimizer and 'categorical_crossentropy' [107] as our loss function because our task is a classification task. We used the 'MinMaxScaler' function [107] to scale multivariate features for LSTMs.

To compare this with our previous work [30], we used 1-NN. Before using 1-NN, we applied principal component analysis (PCA) representing more than 95% variance in the training data to reduce the dimensionality as described in our previous work [30]. We used PCA to reduce the effect of noise. As with the HMMs, we used eq. (2.29) to scale the multivariate features for 1-NNs.

2.6.5 Results

As seen in Table 2.2, multivariate HMMs with contact force and motion as the features performed the best (82.13%) when compared to our previous method, 1-NN [30], which failed to generalize (best performance was 64.58% with area and motion features) across different robot-arm stiffnesses and velocities. Univariate HMMs also failed to generalize.

LSTMs showed the best performance with force, area, and motion features (80.46%).

Note that, multivariate features with HMMs and LSTMs showed better performance compared to univariate features. Fig. 2.5 shows the confusion matrix from multivariate HMMs with force and motion features. The algorithm classified 'Hard-Unmoved' category well. But, there is some confusion between 'Soft-Moved', 'Soft-Unmoved' and 'Hard-Moved' categories. Section 2.8 summarizes a possible reason for this.

Table 2.2: Summary of Algorithm Performance for Simulations (Ranked based on Performance). Note 'f' = force, 'a' = contact area, and 'm' = motion feature.

Algorithm	Features	Ranked Accuracy (%)
HMM	f + m	**82.13**
LSTM	f + m + a	78.02
LSTM	m + a	70.64
LSTM	m	68.64
LSTM	f + m	66.73
LSTM	f + a	64.68
1-NN	m	64.41
1-NN	m + a	62.72
HMM	f + m + a	59.34
LSTM	f	58.52
HMM	m	57.87
1-NN	a	57.6
HMM	m + a	48.01
1-NN	f + m	40.93
1-NN	f	40.71
1-NN	f + m + a	40.54
1-NN	f + a	40.44
HMM	a	39.4
HMM	f	39.07
HMM	f + a	36.89
LSTM	a	36.17
Majority Classifier		29.65
Random Guess		25.0

2.7 Experiments with a Real Robot

We also performed a set of experiments with a real robot. Similar to our experiments with the physics-based models in Section 2.6, our experiments with the real robot varied arm

Figure 2.5: *Classification into four categories using multivariate HMMs with 10 states for experiments with physics-based models. The figure shows the result with force and motion features from the robot moving in varying motion. The numbers in the figure represent the number of trials.*

stiffness and velocity.

2.7.1 Experimental Setup

We used the robot, Cody, for our experiments. Cody, as shown in Fig. 2.1, is a statically stable (wheeled) mobile humanoid robot weighing approximately 160 kg. The components of the humanoid robot are: two Meka A1 arms, a Segway omni-directional base and a Festo 1-DOF (degree of freedom) linear actuator for a spine to adjust the torso height. The two seven-DOF anthropomorphic arms contain series elastic actuators. When we control these arms, each joint simulates a low-stiffness, visco-elastic, torsion spring. We control the robot's arms by changing the equilibrium angles of these simulated springs.

Cody has a force-sensitive skin covering its forearm. Meka Robotics and the Georgia Tech Healthcare Robotics Lab developed the forearm tactile skin sensor, which is based on Stanford's capacitive sensing technology, as described by Ulmen et al. [27]. The skin

consists of a capacitive pressure-sensor array. We refer to the elements of this array as taxels (tactile pixels). There are 384 taxels on the entire skin, and these are distributed in a 24 x 16 array, with each taxel being 9 mm x 9 mm in size. The array of taxels reports the measured force applied to each taxel at 100 Hz.

2.7.2 Experimental Procedure

We conducted experiments to determine whether the performance of our algorithm could perform well on data collected with different robot arm stiffness and velocity than the training data. For the experiments, we selected two velocity settings, low = 5 deg/s and high = 20 deg/s, and two arm stiffness settings, low = 2.01 Nm/rad and high = 20.1 Nm/rad.

Data Collection

The robot made contact with a set of objects on a wooden table while performing a simple, goal-directed reaching motion. We actuated the robot's shoulder joint only and it pushed into soft and hard objects in moved and unmoved conditions with varied arm stiffness (compliance) and velocities. We performed experiments with the eight objects shown in Fig. 2.8 (seven in both moved and unmoved conditions, one [heavy iron bucket] in the unmoved condition only). We selected large objects that have mostly uniform material properties and vary widely in their mass, friction, and stiffness. We actuated the robot's shoulder joint by commanding a goal angle in the joint space. The robot arm tried to reach the goal using a joint PD controller. We selected the final goal angle in joint space such that the equivalent point in the Cartesian space was inside the object. Thus, the robot would come in contact with the object before reaching the goal. When the robot incidentally came in contact with the object, it pushed against it and tried to reach the goal as shown in Fig. 2.6. For each object, we collected haptic data by commanding the same goal angle for the arm and recording the sensor readings from the taxels of the forearm skin at approximately 100 Hz.

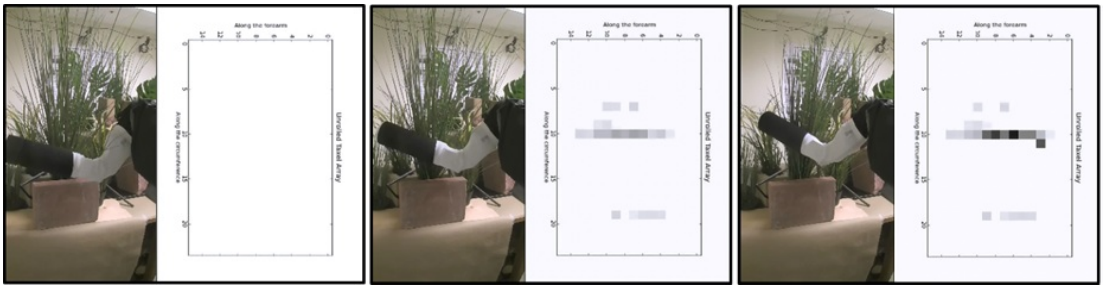

Figure 2.6: *Sequence of images that illustrates the data collection for our experiments on inferring mechanical properties of objects (foliage). Each image shows a picture of the robot Cody and a visualization of the data from the forearm skin sensor as a 24 x 16 image (darker pixels correspond to larger forces). The leftmost picture shows a non-contact situation, the middle picture corresponds to the situation just after the onset of contact, and the rightmost picture shows the situation when the robot has pushed the foliage.*

We labeled each of these objects as either soft or hard. For objects that could be pushed aside by the robot's motion, we fixed them with a clamp or a heavy weight so that we could obtain both moved and unmoved conditions. We repeated the experiments for four trials with each of the stiffness and velocity settings. We collected data for a total of 240 trials ((7 objects x 2 stiffness x 2 velocities x 2 conditions x 4 trials) + (1 object x 2 stiffness x 2 velocities x 1 condition x 4 trials)). Each object category had 60 trials. Our experiments with the heavy iron bucket were only with the unmoved condition because it could not be moved by the robot's motion.

Preprocessing and Feature Selection

After recording the time-series data using the forearm taxel array, we truncated them to begin at the estimated onset of contact between the robot and object. We estimated the onset of contact whenever the force exceeded a threshold. We represented the data at every time step as a gray-scale image, as shown in Fig. 2.6. We converted this image to a binary image, representing the taxels in contact by applying a threshold to each taxel. We used two thresholds. One threshold (0.01 N) was for objects which were less likely to harm the robot-arm. For the other set of objects, we used a larger threshold (0.1 N) to account for the extra covering that we put over the skin sensor to prevent damage to the skin. This is

equivalent to biasing the skin sensor. Then, we computed the connected components on the binary image to segment the contact regions. For the connected component with the largest area, we computed three features.

Figure 2.7 depicts the feature collection procedure. The first feature is the maximum force (F_{max}) measured by a taxel in the contact region at each time step. This is analogous to measuring the highest pressure. In our Initial tests, the maximum force performed better than total force (F_{total}) or mean force (F_{mean}).

For the second feature, we estimated the area of contact (a) between the arm and object (contact region) as the number of taxels in the connected component.

For the third feature, we estimated the distance that the centroid of the connected component traveled in the world frame from its position at the onset of contact (d). We held the robot's torso fixed throughout the trials and used the forward kinematics from the robot's torso to the center of the contact location on the robot's forearm to estimate the 3D positions and distance traveled.

Similar to the experiments with physics-based models, we expected these three features to be informative about the object's softness and mobility. For example, with increasing force applied to a soft, unmoved object, we would expect the contact area to increase. Likewise, we would expect the 3D position of the contact area to travel when encountering moved and soft objects. When making contact with a hard and unmoved object, we would expect the maximum force to increase. Our algorithms used the values of maximum force, the number of taxels in the contact region, and the contact motion for each trial during the first 1.2s time window after the onset of contact.

2.7.3 Implementation

We implemented HMMs, LSTMs, and 1-NN similar to our experiments with physics-based models in Section 2.6.3. We performed experiments with the real robot using a 32-bit Ubuntu 10.04 system with 8 CPU(s) and Intel(R) Core(TM) i7-2600 CPU processor with

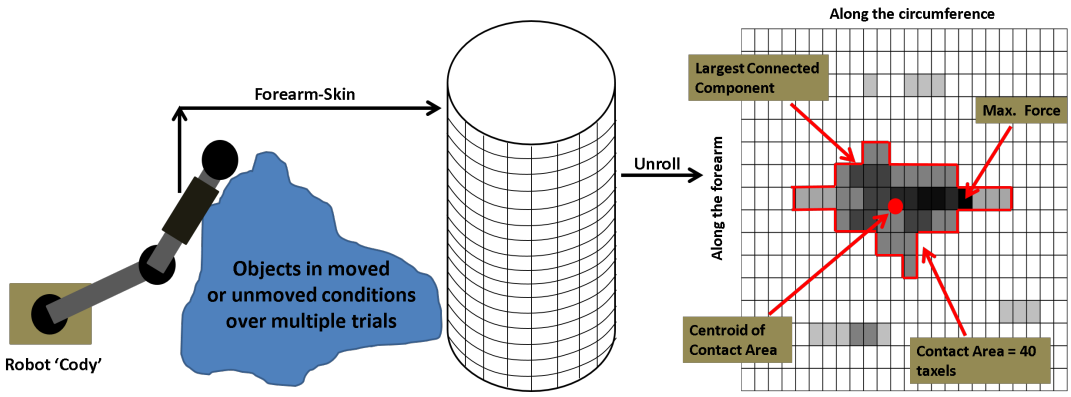

Figure 2.7: *Schematic representation of the experimental protocol.*

3.40 GHz. We used Python to send commands to the robot's real-time PC using ROS-Diamondback [111].

2.7.4 Algorithm Parameters

We used 10 states for the univariate and multivariate HMMs. We set a uniform prior for all states and initialized the emission matrix with Gaussian distributions with means and standard deviations obtained from the data.

For LSTMs, similar to experiments with physics-based models, we initialized the parameters with a uniform distribution, and used the same structure, scaling function, activation functions and dropout probability.

To compare this with our previous work [30], we extracted the features and converted them to a low-dimensional representation of these feature vectors using PCA. We used a dimensionality of three which represented greater than 95% of the variance in the data.

Also, we used the same evaluation procedure as in the experiments with the physics-based model (Section 2.6.4). We trained on three conditions of robot stiffness and velocity and tested on one. We repeated this procedure for each of the four conditions. For multivariate HMMs, we scaled each feature (f) to a scaled feature (S_f) according to eq. (8.1) to normalize the values.

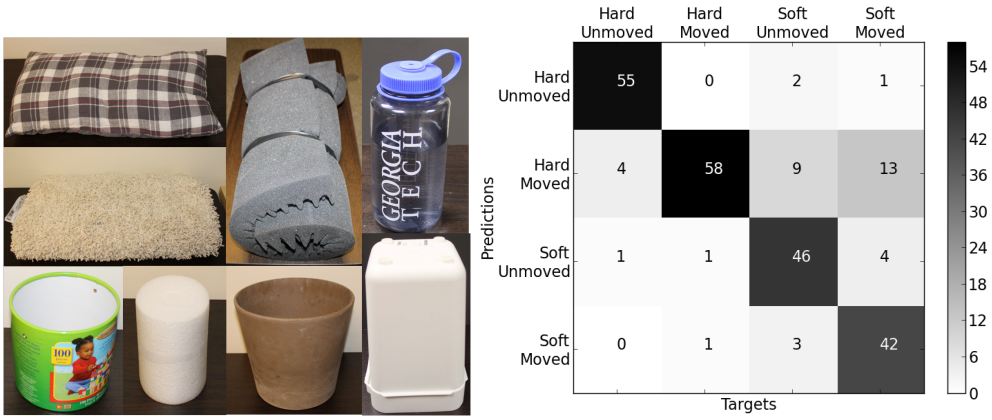

Figure 2.8: *Set of objects for experiments with variable motion (Left). Classification into four categories using multivariate HMMs for experiments using the robot 'Cody'. The figure shows the results with force, area, and motion features from the robot moving with varying stiffness and velocity. The numbers in the figure represent the number of trials (Right).*

2.7.5 Results

We used both univariate HMMs, multivariate HMMs, and LSTMs for classification to model the temporal trends of all combinations of the three feature vectors: maximum force (F_{max}), contact area (a) and contact motion (d). Table 2.3 presents the results for classification into four categories: 1) *Hard-Unmoved*, 2) *Hard-Moved*, 3) *Soft-Unmoved*, and 4) *Soft-Moved*. Our previous method (from [30]) performed poorly, and the highest accuracy was only 37.92% with a single feature (motion) and only 35% with three features (force, area, and motion) using a dimensionality of three. Note that 12 trials could not be captured up until the time window of 1.2 s because of the varying velocity conditions. In those cases, we extrapolated the data with the mean value for that particular trial to obtain a consistent time window of 1.2 s. With HMMs using a single feature (force or area), the accuracy improved only slightly to 40.41%. However, using multivariate HMMs, the accuracy improved to 83.75% with all three features. This provides evidence that multivariate HMMs can be used to generalize the data-driven inference results to testing data that differ from training data due to varying robot conditions. Fig. 2.8 (Right) shows the resulting confusion matrix. From the figure, we see that some 'Soft-Moved' and 'Soft-Unmoved' trials

were categorized as 'Hard-Moved'. However, the algorithm categorized 'Hard-Moved' and 'Hard-Unmoved' categories well. Note, the results with LSTMs did not perform well. With access to more data, LSTMs might match the better results we obtained with physics-based models shown in Section 2.6.5.

Table 2.3: Summary of Algorithm Performance for Experiments (Ranked based on Performance). Note 'f' = force, 'a' = contact area, and 'm' = motion feature.

Algorithm	Features	Ranked Accuracy (%)
HMM	f + m + a	**83.75**
HMM	f + m	71.25
HMM	m + a	60.41
HMM	f + a	52.08
LSTM	f + m	43.33
LSTM	f	40.42
HMM	f	40.41
HMM	a	40.41
LSTM	f + a	40.0
1-NN	f + a	39.17
LSTM	a	39.17
1-NN	m	37.92
LSTM	f + m + a	35.83
1-NN	f + m + a	35.0
LSTM	m + a	34.58
HMM	m	32.5
LSTM	m	31.67
1-NN	m + a	28.33
1-NN	f	27.5
1-NN	a	26.25
1-NN	f + m	25.42
Majority Classifier		25.0
Random Guess		25.0

2.8 Discussion and Limitations

Our data and models will be available publicly as a part of our 'Open-Access-Haptic-Database (OAHD)'. From the overall results, we learned that:

- It is feasible to use data-driven methods to infer object properties from contact during a reaching motion,

- Classification results using HMMs and LSTMs (with sufficient data availability) with multiple features can generalize well to different robot behaviors, such as robot-arm stiffness and arm velocity used to collect training data.

We used the physics-based model to do experiments with objects with a wide-variety of stiffnesses. Collecting haptic data from robots touching real-world objects is challenging. The physics-based model we used in this work can help collect data from a wide variety of objects and robot settings (varied robot stiffnesses, velocities etc.) by leveraging the widely available material properties in online databases. In addition to collecting the real-world data, the results from our physics-based model matched quite well with the results from our real-world data. For example, for both the experiments with physics-based models as well as the real-robot, we note that there is confusion between 'hard-moved', 'soft-unmoved' and 'soft-moved' categories. This is probably because, given the features we have, the algorithm finds it difficult to disambiguate between sliding motion in hard objects and motion due to deformation of soft objects.

Note that for our experiments with the real robot using multivariate HMMs, there was very little confusion between hard and soft objects in the 'Unmoved' condition. However, for experiments with the physics-based models, there was some confusion between hard objects and soft objects. This could be because objects in the hard category for the experiments with the real robot were much stiffer than objects in the soft category. We used a compression spring to compress the objects used in the real-robot experiment and found that the soft objects had stiffnesses ranging between $630\ N/m$ to $1500\ N/m$ whereas the hard objects had stiffnesses ranging between $8000\ N/m$ to $100,000\ N/m$ and above. This is not the case for experiments with the physics-based models. We experimented with a wide variety of stiffnesses and used a stiffness threshold of $100,000\ N/m$ that differentiated hard and soft categories. Thus, the stiffnesses of the objects in the hard and soft categories were much closer (e.g. our simulation labeled an object with stiffness $100,100\ N/m$ as hard but labeled an object with stiffness $99,900\ N/m$ as soft) for experiments with the

physics-based models and this led to more confusion.

For our experiments with physics-based models, we used stiffness as a criterion for labeling objects as hard or soft. In material sciences community, 'hardness' is defined as a measure of how resistant an object is to deformation when a compressive force is applied [112, 113]. We are interested in forces only in the elastic deformation range of a material and for elastic deformation ranges, this highly correlates with stiffness of an object [112, 113] which is a function of the object material as well as structural properties. This is related to deformation of the object, as stiffness is monotonically related to deformation. Similarly, we labeled the objects for experiments with the real robot depending on how an object deforms in macroscopic scale due to applied forces. The human labeling of hard vs. soft objects for experiments with the real robot was coarse. However, note that when consistent force was applied, all the objects labeled soft showed larger macroscopic deformation when compared to objects labeled hard.

Finally, we intentionally made the problem harder by not giving the perceptual classifiers information about the robot's joint stiffness or arm velocity. This is because robots might not have good stiffness estimates for all contact locations on their bodies. Likewise, robots might have uncharacterized compliant coverings or components like soft robots. Similarly, accurate velocity estimates may not be attainable. Also, although the performance with LSTMs (with sufficient data) and multivariate HMMs generalized well to new robot behaviors used to collect training data, there are some limitations to the results presented here. In this work, our objective was to see if our algorithms can infer haptic properties using simple motions (e.g. linear) without haptic exploratory behaviors. Note that many motions are locally linear and therefore, this simple type of motion may be applicable in many scenarios. However, there are many factors which are relevant to real-world incidental contact like the impact dynamics, non-ideal contact (partial, non-normal) due to different robot trajectories and object shapes and sizes etc. In this paper, we focused on two aspects — 'stiffness' and 'velocity'— which affect the way contact occurs. Other aspects

of non-ideal contact merit consideration in the future.

2.9 Conclusion

We developed algorithms to infer object properties using haptic information obtained from contact between a robot's tactile sensing forearm and objects in the robot's environment. We showed that using our algorithms and relevant tactile sensing features, haptic inference can be generalized to data collected using different robot-arm velocities and stiffnesses. Our algorithms classified objects into four categories: 1) *Hard-Unmoved*, 2) *Hard-Moved*, 3) *Soft-Unmoved*, and 4) *Soft-Moved*.

We developed an idealized physics-based model and generated simulated data under varying robot stiffness and velocity. We also performed experiments with a real robot. We used univariate and multivariate HMMs and long short-term memory (LSTM) networks to classify objects under these conditions and compared the results with our previous method of PCA + 1-NN [30]. Our results showed that HMMs are a useful tool to model robot-object interactions. Multivariate HMMs consistently performed better in all cases with varying robot velocity and compliance parameter values and outperformed our previous technique using PCA + 1-NN [30] (See Fig. 2.2 and Table 2.3). With the availability of more data, the classification performance using LSTMs can also generalize to data collected using different robot actions. Also, for HMMs and LSTMs, classification results using a combination of relevant features such as force, area, and motion generalize better than using single features.

CHAPTER 3

RAPID CATEGORIZATION OF OBJECT PROPERTIES FROM INCIDENTAL CONTACT WITH A TACTILE SENSING ROBOT ARM

3.1 Research Summary

We demonstrate that data-driven methods can be used to rapidly categorize objects encountered through incidental contact on a robot arm. Allowing incidental contact with surrounding objects has benefits during manipulation such as increasing the workspace during reaching tasks. The information obtained from such contact, if available online, can potentially be used to map the environment and help in manipulation tasks. In this paper, we address this problem of online categorization using incidental contact during goal-oriented motion. In cluttered environments, the detailed internal structure of clutter can be difficult to infer, but the environment type is often apparent. In a randomized cluttered environment of known object types and "outliers", our approach uses Hidden Markov Models to capture the dynamic robot-environment interactions and to categorize objects based on the interactions. We combined leaf and trunk objects to create artificial foliage as a test environment. We collected data using a skin-sensor on the robot's forearm while it reached into clutter. Our algorithm classifies the objects rapidly with low computation time and few data-samples. Using a taxel-by-taxel classification approach, we can successfully categorize simultaneous contacts with multiple objects and can also identify outlier objects in the environment based on the prior associated with an object's likelihood in the given environment.

3.2 Introduction

Rapid identification of haptic properties of objects in unknown environments during exploration or navigation is a difficult problem. Our method extracts information from incidental contacts and simultaneously comprehends the incoming data. The information obtained from such contact can be used to map the environment by categorizing object properties from the robot-environment interactions. This can potentially help in manipulation tasks and in the exploration of unknown environments. Allowing incidental contact with surrounding objects while maneuvering through a cluttered environment has many benefits such as an increase in the robot's workspace. By '*incidental contact*', we mean any contact that occurs unintentionally while performing a goal-directed manipulation tasks. In this study, we address this issue of rapid categorization of objects conditioned on the environment.

Our approach uses hidden Markov models (HMMs) and considers the likelihood of finding particular object types in an environment to classify dynamic robot-environment interactions. We extend our previous work [30] on object classification by implementing HMMs to model these interactions for rapid online categorization. We generalize our algorithm to non-stereotyped motions. Our new algorithm allows multiple simultaneous contacts and has the capability to identify outlier objects. Inferences based on the likelihood of finding an object in a given environment use little training data for identifying specific objects and isolating outliers. For our experiments, we used the 7 DoF arm of the humanoid mobile manipulator, Cody, as shown in Fig. 3.1. As an example of a cluttered environment with known object types and unknown configuration, we created artificial foliage consisting of combinations of leaf and trunk objects. A common scenario is shown in Fig. 3.1 in which the robot is making simultaneous incidental contacts on its forearm (forearm skin sensor) and end-effector (our developed flipper with tactile sensing described in Section 3.5.1) with multiple objects. Only the forearm sensors are used to perform ob-

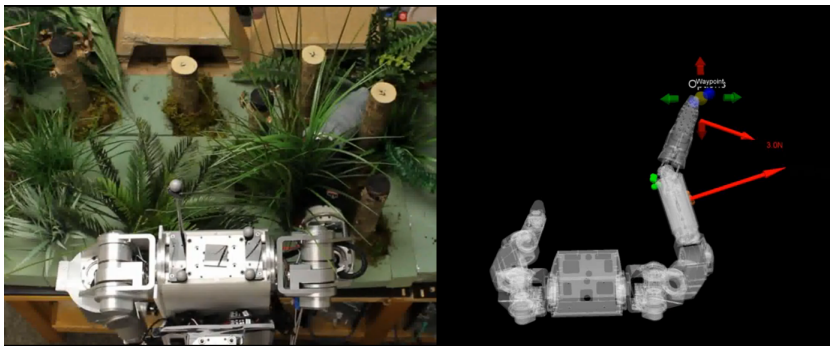

Figure 3.1: *(Left) A mobile humanoid robot, Cody, reaching into clutter while making simultaneous contact with multiple objects; (Right) Rapid categorization of Leaf and Trunk categories while the robot is reaching into clutter. The taxels categorized as leaves are marked with green dots (on the left side of forearm) while the brown dots show the trunk (on the right side of forearm).*

ject categorization. We provided the robot-arm with goals in its workspace, and it used model-predictive control (MPC) [114] to limit contact forces while navigating towards the goals.

We organize the remainder of the paper as follows. In Section 3.3, we review related work in this domain. Section 3.4 describes our approach of categorization of objects conditioned on the robots environment. In Section 3.5, we describe our experimental procedure in detail and in Section 3.5.5, we present experimental results for this algorithm and analyze the accuracy in various conditions. In Section 3.7, we present the conclusions from our work.

3.3 Related Work

Categorization of haptic properties of objects is an extensively explored field (refer [30] for a detailed literature review). Our focus in this study is online classification of objects from incidental contact, on which there are few related previous studies. Our previous work included categorization from incidental contact during goal-directed movements [30] but it was implemented for stereotyped motion of the robot-arm and was not generalized to multiple contacts. In addition, the categorization was done offline and the algorithm required

Figure 3.2: *(Left) Trunk-only environment for training the HMM model for Trunk Category; (Middle) Leaf-only environment for training the HMM model for Leaf Category; (Right) Combined environment for testing*

extensive training data of equal sample-length to classify specific objects [30]. In our current study, we address these shortfalls by implementing an online categorization scheme using HMMs which can deal with time-series data of varied length. Some of the previous studies on online categorization used explicit exploration movements for object identification [115] and shape identification [116]. Soh et al. [115] created a spatio-temporal online recursive kernel gaussian process to perform online object classification during gripping movements by a robot hand. They found that they could identify between objects based on signature tactile features. The tactile features were measured with a specific hand closing movement. Liu et al. [116] used a naive Bayesian process to perform online classification of shape and pose of objects during an explicit exploration movement by a robot finger. They used an off-the-shelf tactile sensor array mounted on a robot finger and were able to rapidly identify object shape after exploration of the object by the finger. The objects were smaller than the sensor array, so complete exploration before identification was possible. Chitta et al. [117] created a hybrid velocity-force controller that allows a robot gripper to hold objects and gather tactile and deformation data from the interaction. Using their gathered tactile and deformation data, they were able to distinguish between states of the objects (e.g. empty, full, open, closed) with recognition rates comparable to that of a human. Jamali and Sammut [118] used several machine learning algorithms to perform material classification based on surface texture during explicit exploration movements by a

bio-inspired artificial finger. Vibrations measured by the tactile sensors in the finger while being run across the textured surface at a specified speed could be used to identify the material with some accuracy after minimal training data.

Work on online categorization has been performed in other fields as well, such as in 3D scene analysis, handwritten character recognition, human gait recognition, and in monitoring of bearings for abnormal behavior in industrial machinery. Hu et al. [119] categorized 3D scenes into different object types from range data for use in robotics. They described the tradeoff between precise categorization at the cost of speed and fast categorization at the cost of increased misclassifications and used a simple but imprecise scene representation method to address the problem. Hu and Zanibbi [120] performed online recognition of handwritten mathematical symbols by creating an HMM for each symbol class and a segmental K-means to initialize the gaussian mixture models parameters. Garain and Chaudhuri [121] combines a nearest-neighbor classifier with an HMM to perform online recognition of handwritten mathematical symbols. Kale et al. [122] used a continuous HMM to perform online identification of humans by gait. Starner et al. [123] presented two real-time HMM systems to recognize continuous, sentence-level American sign language while Yamato et al. [124] proposed a HMM-based method for recognizing human actions from a series of time-sequential images. Cartella et al. [125] assessed bearing condition in industrial machinery using online adaptive learning of left-right continuous HMM. These studies use HMMs as a tool for rapid identification of object characteristics.

3.4 Categorization Method

For our problem, the robot must classify each region of contact, R_i, according to the type of object, c_i, that resulted in the contact region. We assume that the robot is operating in a known environment, E, composed of T object types and that each contact region, R_i, results from one of these T object types or results from an anomalous object type that is not typically found in the environment, E. In this paper, we use hidden Markov models

(HMMs) to perform the classification problem, and focus on the problem of an environment with different object types.

Hidden Markov model is a statistical tool to model systems using a state-based approach such that the current state is dependent only on the previous state. The states are hidden and are not directly observable. Instead, they are stochastically dependent on observations. The elements which constitute an HMM are (1) N, the number of states in the model; (2) M, the number of distinct observation symbols per state; (3) A = $\{a_{ij}\}$, the state transition probability distribution; (4) B = $\{b_j\,(k)\}$, the observation symbol probability distribution; and (5) P = $\{\pi_i\}$, the initial state distribution [65, 126]. The model is represented as given in eq. (3.1), where the parameter λ describes the HMM model.

$$\lambda = (A, B, \pi) \tag{3.1}$$

For classification using HMMs, we need to train the HMM models first. We had different HMM models which we trained on environments composed of single object categories. We trained the HMMs by choosing the λ which locally maximizes $P\,(O|\lambda)$ iteratively using expectation-maximization (EM) techniques [65]. After training the models for the different categories, we evaluate a new observation sequence $O = \{O_1, O_2, ...O_n\}$ according to eq. (3.2) which gives us the model which best matches the observation sequence. The third step in eq. (3.2) leads to the fourth step, if all the models are equally likely, as is the case for the first part of this study.

$$
\begin{aligned}
c^* &= \arg\max_{c \in [C]} P\left(\lambda_c | O\right) \\
&= \arg\max_{c \in [C]} \frac{P\left(O|\lambda_c\right) P\left(\lambda_c\right)}{P\left(O\right)} \\
&= \arg\max_{c \in [C]} P\left(O|\lambda_c\right) P\left(\lambda_c\right) \\
&= \arg\max_{c \in [C]} P\left(O|\lambda_c\right)
\end{aligned}
\tag{3.2}
$$

Later, we use HMMs to identify an outlier in the environment for which all the models are not equally likely. In this case, the conditional probability is given by eq. (3.3).

$$
c^* = \arg\max_{c \in [C]} P\left(O|\lambda_c\right) P\left(\lambda_c\right) \tag{3.3}
$$

3.5 Experimental Procedure

For our experiments, we used a mobile humanoid robot Cody to reach into artificially created reconfigurable cluttered environments while rapidly classifying into various categories objects encountered through incidental contact. The details are given in the following subsections.

3.5.1 Experimental Setup

Cody, as shown in Fig. 3.1, is a mobile humanoid robot weighing approximately 160 kg. It has two Meka A1 arms, a Segway omni-directional base and a Festo 1 DoF (degree of freedom) vertical linear actuator for changing its height. The two 7 DoF anthropomorphic arms contain series elastic actuators for compliance and torque control ability. When we control these arms, each joint simulates a low-stiffness, visco-elastic, torsional spring. We control the robot's arms by changing the equilibrium angles of these simulated springs over

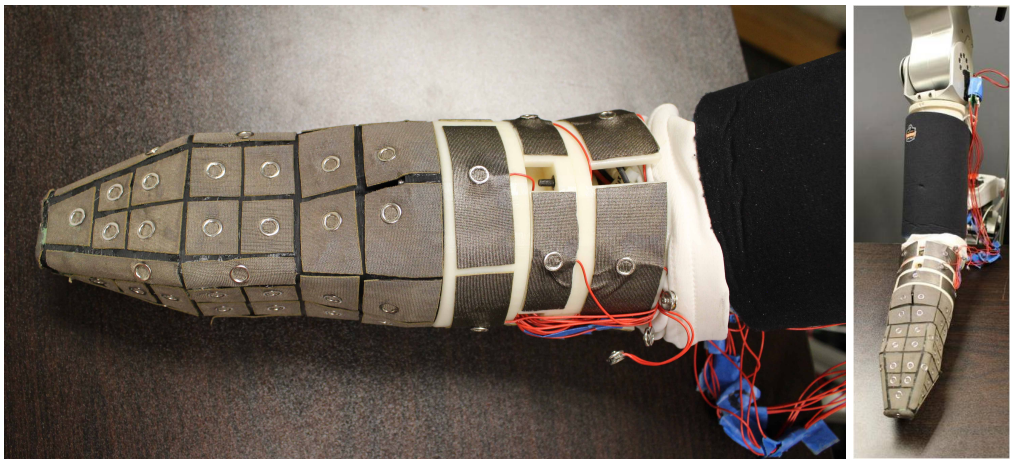

Figure 3.3: *A flipper with tactile sensing based on fabric based sensing technology. It has 69 taxels in total. It is used to navigate clutter.*

time [30].

Cody has a force-sensitive high-resolution skin across its forearm. Meka Robotics and the Georgia Tech Healthcare Robotics Lab developed the forearm tactile skin sensor, which is based on Stanford's capacitive sensing technology, as described by Ulmen et al. [27]. This skin has a capacitive pressure-sensor array and each sensing element is called a taxel (tactile pixel). The skin has 384 taxels in total arranged in a 24 X 16 pattern. Each taxel is of 9 mm X 9 mm size and it can measure applied force at 100 Hz. [30].

We created an artificial cluttered foliage environment using leaf and trunk objects as shown in Fig. 3.2. The clutter is reconfigurable so we can create a large set of environments by rearranging the relative position of the leaf and the trunks. It is made reconfigurable by a ground platform made of a combination of wet and dry foams as shown in Fig. 3.2. The leaves can be stuck stably inside these foams and can be removed at will. The trunks are fixed to the table beneath the foam platform with flanges to provide stability. Each foam block is a 25 cm X 10 cm sized rectangular block. We can move the foam blocks and the trunks and we can place leaves in different relative positions to reconfigure the environment and create a variety of cluttered environments with which the robot can interact.

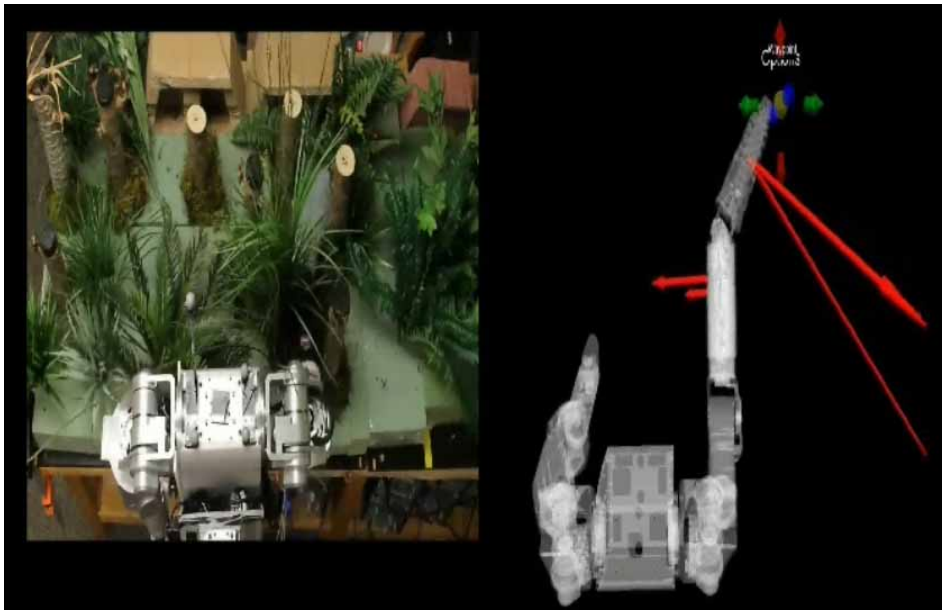

Figure 3.4: *(Left) Cody reaching into clutter while making contact with multiple objects on forearm and flipper; (Right) The contact forces on the forearm and flipper skins are shown in Rviz with the goal provided by the interactive marker*

Whole-Arm Tactile Sensing with Flipper

While reaching into clutter, contact can occur at any point of the arm including the end-effector. By using only the forearm skin sensor, we would lose contact information used for haptic navigation. Without an end-effector, we would also lose the degrees of freedom afforded by Cody's wrist joint. Hence, we created a wedge-shaped end-effector (referred to as a 'flipper', see Fig. 3.3) for Cody, on which we mounted tactile sensors based on our fabric-based tactile sensor technology [127]. We put 69 taxels ranging from 1 cm^2 to 15 cm^2 in a pattern fixed to the 25 cm long flipper's surface. We used haptic signals from the flipper to navigate in the foliage environment.

3.5.2 Collecting Training Data

The purpose of our classification is to categorize between leaf and trunk in a foliage environment. Hence, we need a model for the trunk and the leaf categories. To train the model for the trunk category, we made the robot reach into a trunk-only environment as shown

in Fig. 3.2 (Left). To train another model for the leaf category, we made the robot reach into a leaf-only environment as shown in Fig. 3.2 (Middle). The test environment was a combination of trunk and leaf objects as shown in Fig. 3.2 (Right).

To collect training data, we made Cody reach into the leaf training environment and into the trunk training environment multiple times. For each of these reaches, we commanded multiple goal positions for the robot end-effector using the interactive markers in Rviz as shown in Fig. 3.4. The 7 DoF robot arm moves towards the goal using model predictive control [114] while limiting contact forces across its whole arm. Fig. 3.4 shows the sensed forces from the forearm and flipper skin sensors while the robot is making contact with the environment. During each of the reaching attempts, we provided multiple goals to make the arm contact various parts of the clutter with various configurations. Between each reach, we changed the configuration of the environment using our reconfigurable cluttered environment setup to create multiple environment situations. We used both the forearm and flipper tactile sensors for haptic navigation and used the data from the forearm for object classification. The next two subsections detail the methods for extracting features from the data collected during the experiments.

3.5.3 Connected Component based Categorization

Our first method of extracting features relies on connected components. We represented the data from the forearm skin sensor as a gray-scale image with a 24 X 16 array pattern. We converted this image to a binary image representing the taxels in contact by applying a threshold to each taxel. We computed connected components on this array pattern to segment the contact regions. For each of these connected components, we computed the maximum force and the contact motion at every time-instant. We expected these two features to be informative about the characteristics which distinguishes a leaf from a trunk because we would expect the 3D position of the contact area to travel more when the robot is bending a soft leaf and the maximum force to rise faster when making contact with a

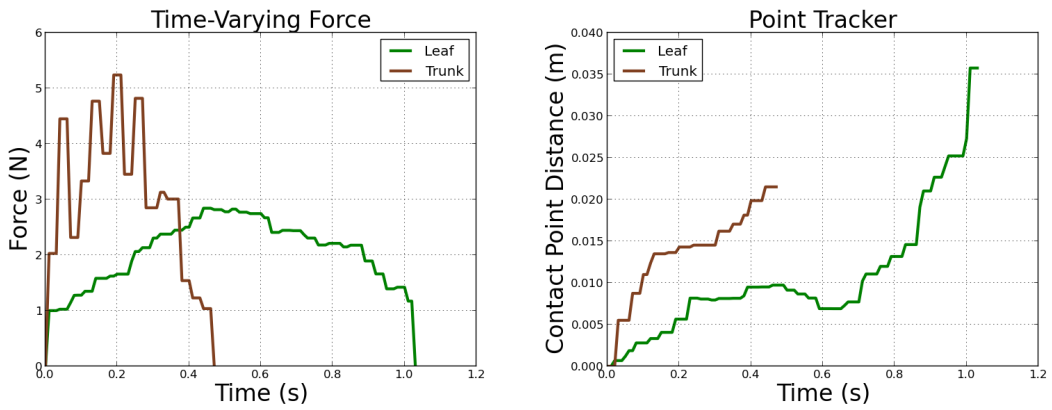

Figure 3.5: *The force (Left) and motion (Right) features collected from a taxel using taxel-based approach while the robot was reaching into a clutter. The figure shows a trial in which the robot came into contact with leaf (in green) and another trial in which it came into contact with a trunk (in brown). The left figure shows that as the robot pushes against the object, the force increases at first and then the MPC controller tries to decrease it while moving towards the goal. The right figure shows the motion of the taxel in contact. Clearly, the rate of increase of force as well the magnitude is higher for trunk contact. Also, the motion is larger for leaf as the robot can push and bend the leaf easily.*

trunk.

During each of the reaching attempts in the cluttered environments, the robot frequently came into contact with multiple objects simultaneously. We tracked the motion for each of these connected components using their estimated 3D positions in the world frame. We assumed that the robot's torso did not move throughout the trials and used the forward kinematics from the robot's torso to the center of each associated contact region to estimate these positions. We associated connected components between time steps based on the distances between their estimated 3D positions.

For data management purposes, we name each period between when the robot makes contact with an object and when the robot breaks contact with that object as one trial. There were varied numbers of trials during each reaching attempt depending on the number of times the robot initiated and broke contact with objects in the environment. Based on the connected component based segmentation, there were 288 such trials for the leaf environment over 10 reaches and 324 trials for the trunk environment over 25 reaches which

form our training data for this approach.

3.5.4 Taxel based Categorization

Our second method of extracting features is taxel-based. We consider data from each of the 384 taxels separately, nullifying the need for segmentation and tracking. This method is inherently high resolution but may contain redundant information when multiple taxels contacting the same object measure similar information content. We collect the same force and motion features as described in Section 3.5.3. In the taxel-based approach, the maximum force is the force acting on the taxel as there is only one force per taxel at each time-instant. In this approach, we name each period between when each taxel in the robot's forearm skin sensor makes contact with an object and when that taxel breaks contact as one trial. There were varied number of trials during each reaching attempt depending on the number of times each taxel initiated and broke contact with objects in the environment. Based on the taxel-based approach, there were 496 trials for the leaf environment over 10 reaches and 582 trials for the trunk environment over 25 reaches which form our training data for this approach. The features collected from a sample reaching experiment are shown in Fig. 3.5.

3.5.5 Results and Discussion

In this section, we present an experimental evaluation of algorithm using cross-validation, and present an assessment of online categorization performance.

Cross-Validation Performance of HMMs

We used two-fold cross-validation to characterize the performance of our HMM classifiers. The data was collected through various reaches in the leaf and trunk environments as discussed in Section 3.5.2. We applied both component-based (Section 3.5.3) and taxel-based (Section 3.5.4) categorization methods to the data to compare their performance. To

Table 3.1: Cross-Validation Performance.

Type	Features Used	5 Hidden States	10 Hidden States	20 Hidden States
Component-Based Categorization	Max. Force	61.76%	72.22%	70.75%
	Max. Force and Contact Motion	54.41%	55.55%	58.50%
Taxel-Based Categorization	Force	72.91%	**80.24%**	**81.40%**
	Force and Contact Motion	70.22%	**71.98%**	**73.47%**

analyze the effect of states and the effect of different features used in our algorithm, we compared the performance of our algorithm with varying numbers of hidden states (5, 10, and 20 states) and when using only force as a feature vs. both force and motion as features. The results are given in Table 3.1.

The taxel-based methods consistently performed better than component-based methods both for one-feature and for two-feature based classification methods, irrespective of the number of states used. This may be due to the presence of higher resolution data in taxel-based methods which captures the characteristics of dynamic interactions more effectively than in component-based methods: in a connected component, there are multiple taxels interacting with the same object that may each capture different aspects of the dynamic interaction when considered individually. The confusion matrices for the results of the cross-validation study for the taxel-based method with 20 states are shown in Fig. 3.6 with force as the sole feature and in Fig. 3.7 with both force and motion as features. Note that cross-validation results using force as the sole feature gives consistently equivalent or better results than using two features. It can be seen from Table 3.1 that our algorithm consistently performs better using 10 or 20 hidden states than using 5 states. This implies that 5 state transitions may be insufficient to characterize and distinguish models of leaf and trunk categories.

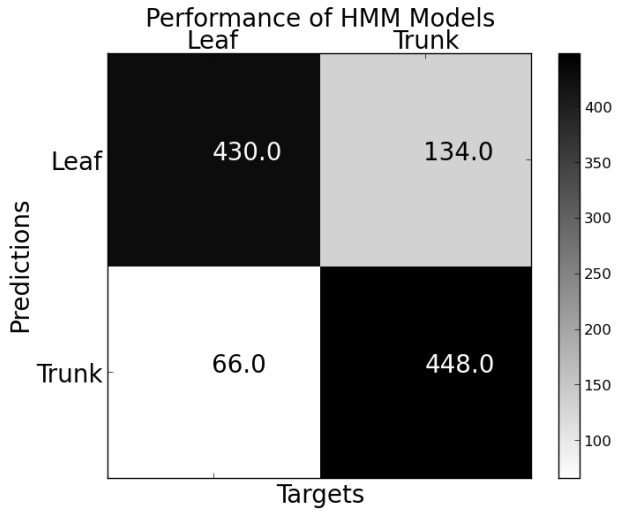

Figure 3.6: *Cross-validation performance of taxel-based categorization using a 20-state HMM with force as the feature.*

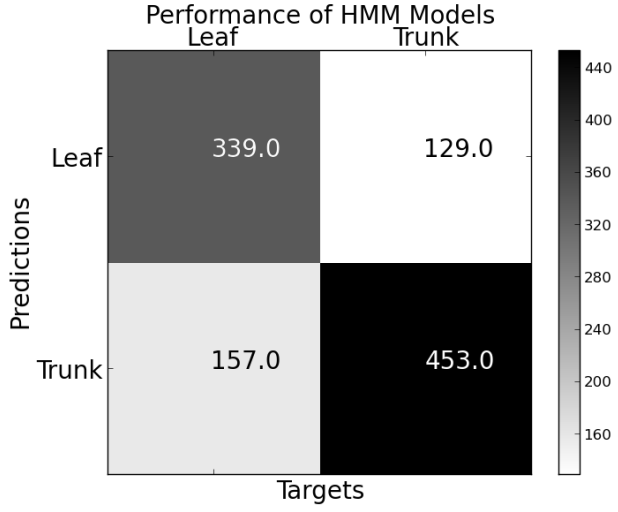

Figure 3.7: *Cross-validation performance of taxel-based categorization using a 20-state HMM with force and motion as the features.*

Online Categorization Performance

In this section, we describe the implementation of our algorithm for online rapid categorization as the robot reaches into clutter. Based on results from Section 3.5.5, we used taxel-based methods for categorization. The robot used both the forces sensed from forearm tactile sensing skin and flipper to reach into clutter by moving towards commanded goal while minimizing these forces using MPC [114]. We classified the taxels in contact into 3 categories: trunk, leaf and uncertain. The uncertain category was for those taxels which cannot be classified into either trunk or leaf with confidence. We implemented this classification scheme by using a threshold on the log-likelihood values of the HMM below which the taxel was categorized as uncertain. This helped in reducing the number of misclassifications and in improving the false-positive accuracy of our algorithm.

To analyze the performance of our algorithm, we computed metrics of computation time, and amount of data samples required for classification for one of the reaching tasks. The results are given in Figs. 3.8, 3.9, and 3.10. From Fig. 3.8, we see that the algorithm can categorize rapidly taking on average 0.83 s per 100 taxels in contact for inference using a 10-state univariate HMM. This computation was performed on a system which runs Ubuntu 12.04 32-bit OS with a 3.2.0-45-generic-pae linux kernel. It has 4 GB RAM and an Intel® Core™ i5-2410M CPU @ 2.30 GHz X 4 processor. The number of data-samples used for classification varies over time as seen in Fig. 3.9, with an average around 12 (exactly 11.9). Fig. 3.10 shows that the number of correctly classified taxels is higher than the misclassified taxels and the number of uncertain taxels is low.

To compare our results against ground-truth, we conducted 10 reaching experiments in the artificial foliage environment and designed them such that 5 of them contacted only leaves while the other 5 only trunks. The results are shown in Fig. 3.11. The results for the reaching trials in which the robot contacted only leaves, are shaded in green while the results for trunk contacts are shaded in brown. The number of mis-classifications was reduced, with the tradeoff that our algorithm is more conservative. We prefer a conservative

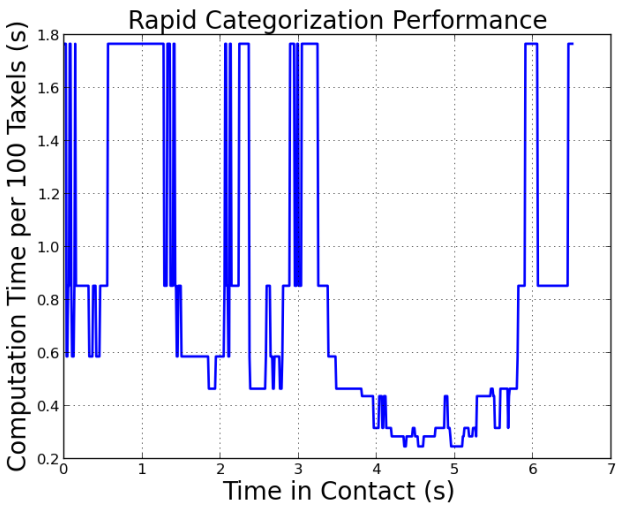

Figure 3.8: *Computation time per 100 taxels in contact during a reaching task for two category classification using 10-state univariate HMM.*

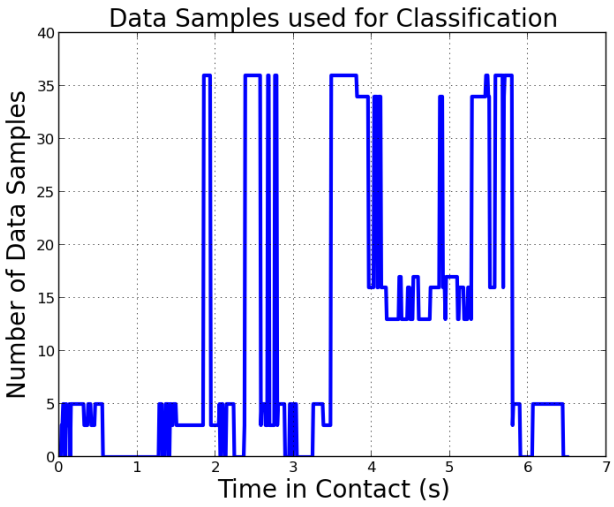

Figure 3.9: *Number of Data Samples used to classify the objects in clutter using HMMs during a reaching experiment. The data-samples are zero when the classification is uncertain. Please note that the number of data samples is proportional to time with the data-sample rate at 100 Hz.*

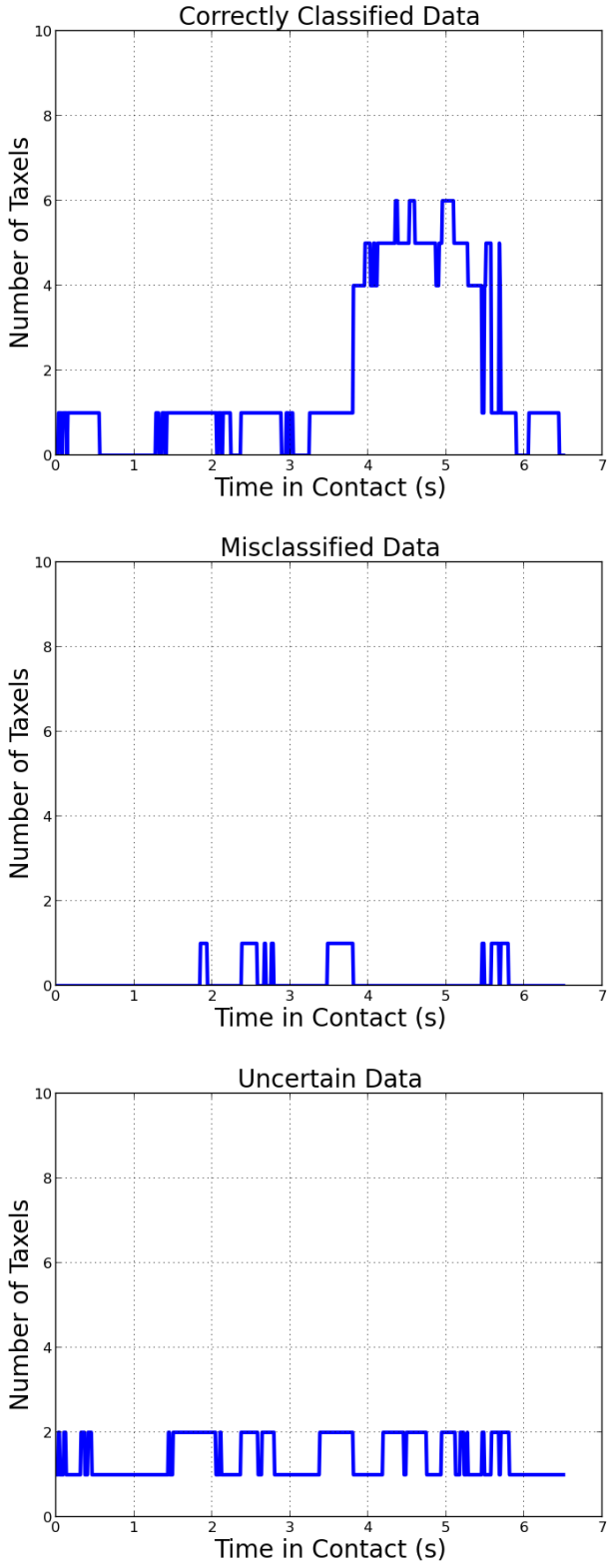

Figure 3.10: *(Top) Number of correctly classified taxels; (Middle) Number of misclassified taxels; (Bottom) Number of Taxels which are not strongly classified into one of the two categories, they are put into an uncertain category. We have this uncertain category to be able to reduce misclassifications while rapidly categorizing the environment*

approach as this allows us to choose environment-based manipulation strategies with higher confidence.

After these experiments, we did a general reaching experiment in which the robot reached into clutter while making contact with trunk and leaf at different times or simultaneously. *The video of the reaching trials is submitted along with this manuscript. It shows our approach for rapid categorization with simultaneous contacts and multiple objects.* Fig. 3.12 shows a snapshot of the robot reaching into the clutter while it is making contact with leaves. The rapid categorization algorithm classifies the taxels in contact as leaves and marks them with green dots as shown in Fig. 3.12. *Link to the video is given in [128]*

Effect of Data-Sample Length

Based on results from Fig. 3.9 in Section 3.5.5, we analyzed the effect of the data-sample length on the algorithm performance. We varied the training-data sample length by truncating the remaining data such that the maximum number of data samples varied from 200 to 50 in intervals of 50. We performed a two-fold cross-validation and the results are shown in Fig. 3.13. We do not see significant effect of the data sample length on the algorithm performance. This result encourages us to believe that we can achieve faster categorization without reduction in performance by using fewer training samples.

Identifying an Outlier in the Environment

We conducted an experiment to show that our algorithm can be used to identify an outlier object in the environment without explicitly modeling an outlier category. An outlier object is an object which does not normally belong to the environment in question and has distinct physical properties from the expected object types. If we had a model for the outlier category, we could use eq. (3.3) as is, for computing the conditional probability. However, in our implementation, without explicitly modeling the outlier, we identify an outlier by using a threshold on the log-likelihood values of HMM. We selected the threshold by considering

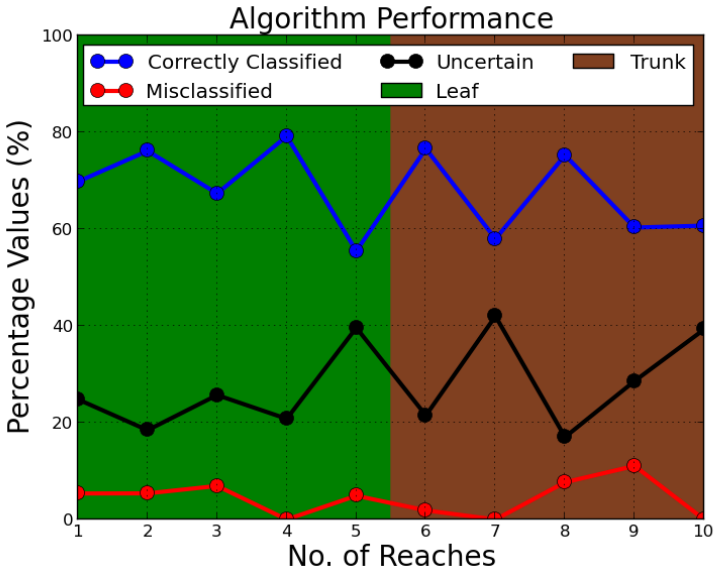

Figure 3.11: *Rapid categorization performance for 10 reaches in clutter. The figure shows the percentage of correctly classified, misclassified, and uncertain taxels. To compare the algorithm performance with ground truth, the first 5 reaches were engineered to have contacts only with leaves while the next 5 reaches had contacts only with trunks as represented by their respective colors.*

the likelihood of finding an outlier object in the environment.

Our setup consisted of a foam roll embedded in the artificial foliage environment as shown in Fig. 3.14. The experiment was designed to compare the algorithm performance against ground-truth. The robot would make contact with the outlier first and then would come into contact with leaf or trunk.

For our task, c^* (computed using eq. (3.3)) is the maximum of ${c^*}_T$ (for trunk) and ${c^*}_L$ (for leaf). We computed the difference between the log-likelihood values of ${c^*}_T$ and ${c^*}_L$ which is an indicator of how confident the model is in its inference. If the model (c^*) was either ${c^*}_T$ or ${c^*}_L$ and the difference was greater than a threshold chosen (80 for our task), we classified it as a trunk or a leaf respectively with high confidence. However, if the difference was between 80 and 15, we classified it as an outlier. Note that this is equivalent to having a model for an outlier in eq. (3.3) with a low prior. If the difference was less than 15, we classified it as uncertain because we do not have strong confidence in our inference.

Figure 3.12: *Successful categorization of leaves using taxel-based approach (green dots corresponding to the taxels in contact) as the robot reaches into clutter. The classification algorithm uses data from the forearm skin sensor only. The MPC controller uses the forces from both the forearm and flipper skin sensor to reach into clutter.*

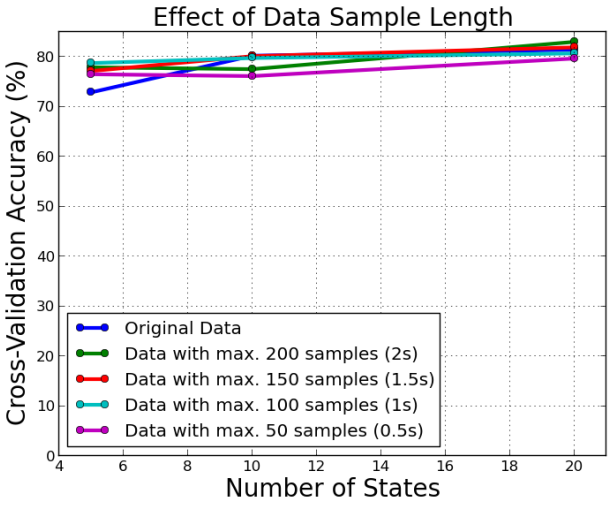

Figure 3.13: *Effect of changing the data-sample length. The original data has trials with variable length. To analyze the effect of data-sample length on the cross-validation performance, we truncated the remaining data such that the maximum number of data samples in the trials are varied from 200 to 50 in intervals of 50. The sampling rate was 100 Hz.*

Figure 3.14: *Experimental setup showing an outlier (foam roll) in an artificial foliage environment.*

The results are shown in Fig. 3.15. The algorithm successfully identified the outlier during both contact events, although there were some uncertain contact data as well. This method shows the potential of identifying outliers in the environment without the need of an explicit model.

One limitation of this algorithm is the need to choose a threshold to identify the outlier. A wiser choice of features might help in easily distinguishing the different object properties and make the algorithm more robust. Also, we used a specific artificial environment for testing and some carefully chosen environments for training which limits its practical usage. The information content in the haptic data is dense and visually promising but we might require more elaborate processing techniques to achieve more confident estimates about the categories. In addition, the recognition performance depends on the task chosen and the MPC controller used in this study, and it remains to be seen how well it can generalize to other controllers.

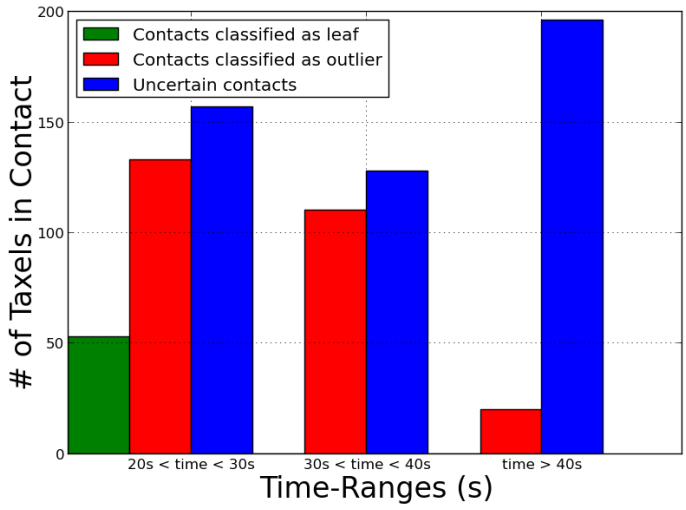

Figure 3.15: *Successful detection of the outlier object (red) during a reaching experiment. There were three distinct phases of contact, the first two were with the outlier object while the last was with leaves. The algorithm successfully detected the outlier in the first two phases of contact while some of the taxels were uncertain (blue). There were few misclassified taxels (green). For the last phase of the contact, the taxels were uncertain about the contact.*

3.6 A Manipulation System using Force Sensing based Mapping

In this section, we present an example of a system which uses haptic perception from a tactile sensor over an articulated joint that uses stretchable conductive and resistive fabrics.

3.6.1 A Fabric-based Resistive Stretchable Skin

Single Taxel

A single sensing element or taxel (short for tactile pixel) consists of five layers of fabric, illustrated in Fig. 3.16. The layer in the middle is resistive fabric, which is sandwiched between two layers of conductive fabric. The resistance between the two electrodes made of conductive fabric decreases given an applied force that compresses the layers.

The fabrics that we used to construct our sensor, follow:

- ***Stretchable conductive fabric:*** From Less EMF Inc., we purchased "Stretch Conductive Fabric (Cat. #321)", which is a silver-coated fabric made of 76% nylon and

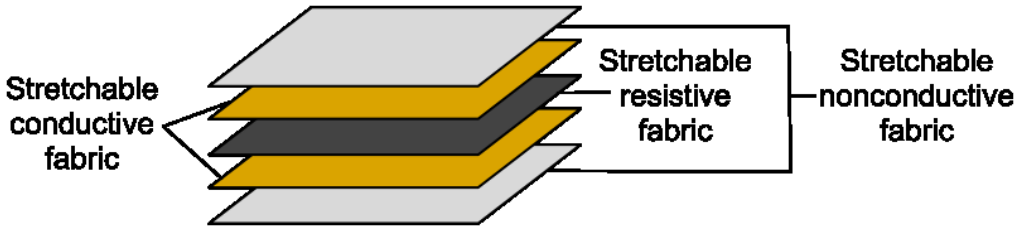

Figure 3.16: *Five layers of conductive, resistive and nonconductive fabric that make up our tactile sensor.*

24% elastic fiber.

- ***Stretchable resistive fabric:*** From Eeonyx, we purchased the EeonTex fabric named "LG-SLPA-16K" with a specified surface resistance of 16KΩ/sq. This is a a knitted nylon and spandex fabric with a proprietary conductive coating.

- ***Stretchable nonconductive fabric:*** We purchased a sleeveless compression shirt for athletes made by McDavid. The fabric is 80% nylon and 20% spandex.

Sleeve with an Array of Taxels

To make an array of tactile sensors, we laser cut one of the layers of conductive fabric to have multiple discrete conductive patches (electrodes) of the desired shapes and sizes. We then sew these electrodes to a layer of insulating fabric with space separating them so that they are insulated from one another (see Fig. 3.17). By having a separate wire go to each insulated electrode, we reduce the possibility of cross-talk that can occur during multi-contact conditions with grid-based wiring, as seen with the original rSkin design [129]. We leave the remaining conductive fabric layer as a single sheet in order to serve as a common ground for all the taxels, and we place a single sheet of resistive fabric between this common ground layer and the electrode layer. As with the single taxel design, we also have an insulating layer on the exposed side of the common ground layer.

For the humanoid robot Cody, we designed a single sleeve with 25 taxels that covers the end effector, 2 DoF wrist joint, and forearm (see Fig. 3.17). To fabricate the sensor,

we laser cut the fabrics and sewed them together. Due to the presence of 25 distinct taxels operating in parallel, the sleeve can detect multiple contacts simultaneously. The output of an individual taxel depends on the resistance between the taxel's discrete electrode and the common ground layer, R_{tax}. Prior to analog to digital conversion, the only signal conditioning we perform is to put R_{tax} into a resistive voltage divider with R_{div}, where $R_{div} > 0\Omega$. The output voltage of this voltage divider is converted to a digital signal via the analog to digital converter of an Arduino Mega 2560 R3 board, which linearly converts the 0 to 5 volt analog signal to a 10-bit digital signal. We refer to a taxel's digital signal resulting from this analog to digital conversion as ADC. Since the input to the voltage divider is 5 V, $ADC = \lfloor \frac{1024}{5V} \frac{R_{tax}}{R_{tax}+R_{div}} 5V \rfloor = \lfloor \frac{1024\, R_{tax}}{R_{tax}+R_{div}} \rfloor$

The ends of the sleeve are anchored to the proximal end of the forearm and the distal end of the end effector. Otherwise, the sleeve is allowed to slide across the underlying 2 DoF wrist joint and the rigid surfaces of the forearm and end effector. With respect to our model of stretch in [127], $L1 = 250.7$ mm, $L2 = 200.9$ mm, $R = 75.6$ mm, and $\beta = 0.167$. Where $L1$ relates to the forearm length and $L2$ relates to the end effector length. Given the wrist's maximum angle from neutral, $\theta = 55°$, our model predicts that the tactile sleeve will need to stretch by 16%. Interestingly, the predicted stretch required for $\theta = 70°$, which is not achievable with Cody's wrist, would be 20%, which is very close to the 20.4% stretch estimated in [130] for human skin when a human wrist undergoes a $70°$ bend.

3.6.2 Experiments with Fabric-based Resistive Skin on a Real Robot

For our system using the stretchable tactile sleeve, we trained two HMM models (for trunk objects and leaf objects) using training data we collected using the robot Cody [131], on environments wholly composed of small tree trunks and artificial leaves. We used a previous controller from [132] for training in these cluttered environments.

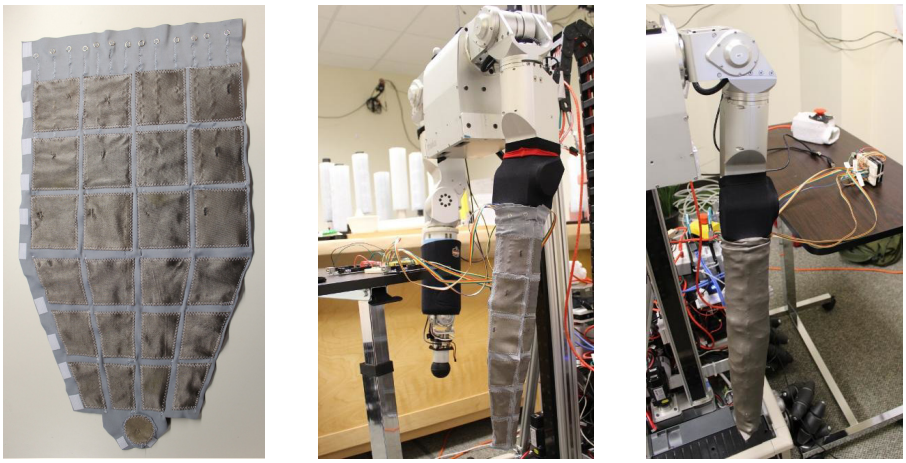

Figure 3.17: *Insulating fabric with 25 electrodes of conductive fabric (left) spread out, (middle) mounted on the robot, and (right) with the resistive layer and conductive layer added.*

3.6.3 Results and Discussion

Notably, even though Cody used a different controller and different tactile sensors, we found that the same HMM models worked well in practice for DARCI. DARCI and the environment are shown in Fig. 3.18. Our rapid categorization method classifies, online and in real-time, the contact force data for every taxel on the tactile sleeve.

We create a haptic map by mapping the leaf and trunk contacts encountered, as described in Sec. 3.6.3 for the planner. The visualization only shows the trunk contacts, in brown (Fig. 3.19).

The Haptic Map

We first construct a 3D cost map (haptic map). We represent the workspace of the robot as a 3D voxel grid with 0.01 m $\times$ 0.01 m $\times$ 0.01 m voxel size in Cartesian space. Each voxel includes a collision cost associated with the location. We define the collision-cost value as a scalar value between 0 to 100. Higher values indicate greater difficulty for traversal of the location by the robot's arm. The haptic classifier provides the 3D location and category of each detected contact while the robot moves. The system uses this information to continu-

Figure 3.18: *A robot reaches in dense clutter using our system.*

ously update its haptic map. It assigns collision costs of 50 and 100 for contacts classified as leaves or trunk, respectively. Open space has a collision cost of 0. Newly detected leaves and trunk contacts overwrite the current voxel values. For this implementation, voxels are never set back to 0. Implementations that allow the arm's volume to reduce voxel costs or that decay voxel costs over time might be valuable for dealing with dynamic environments and noisy sensing.

The total volume of the haptic map is a rectangular box, $0.6\,m \times 0.7\,m \times 0.6\,m$ in front of the robot. The system initially populates this volume with zeros, using the optimistic initial guess that the entire unobserved environment is easy to traverse. The map records the contact information using the Point Cloud Library's (PCL) Voxel Grid [133].

3.7 Conclusion

This chapter describes our approach for rapid categorization of objects conditioned on the environment. Our approach uses hidden Markov models to model the dynamic interactions of the objects with a robot-arm. Using our newly developed flipper with tactile skin and the forearm skin sensor, the robot can haptically navigate through a cluttered environment while rapidly categorizing objects encountered through incidental contact. We created an

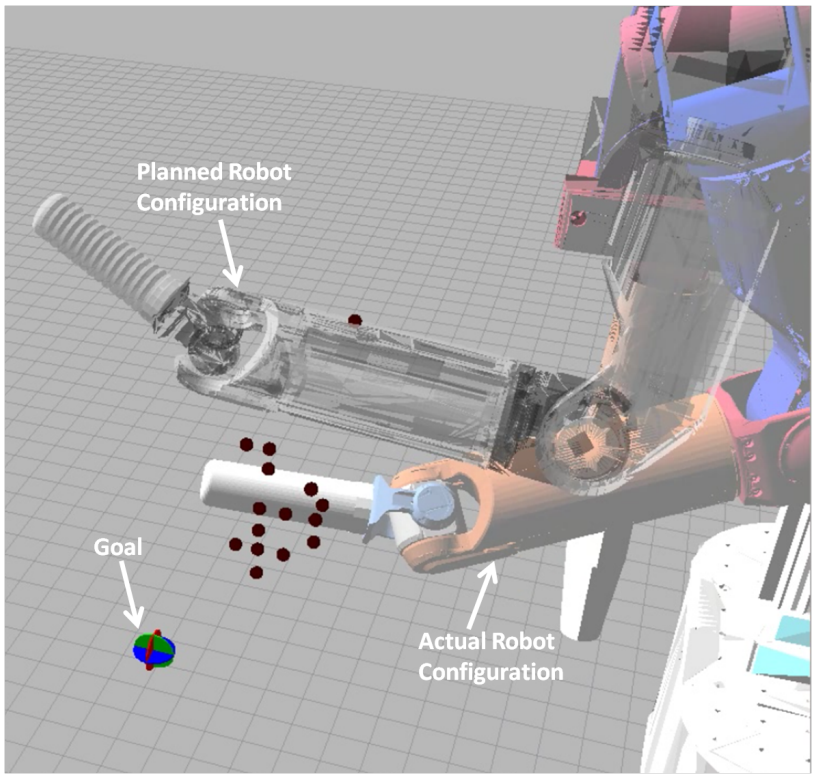

Figure 3.19: *Planned robot configuration with a visualization of trunk contacts in the associated haptic map.*

artificial foliage as a test environment and trained two HMM models for categorizing trunk vs. leaf. Our algorithm consistently performed with cross-validation accuracy as high as 81%. For our tests, the highest performance was achieved when the categorization was done on a taxel-by-taxel basis with force as the sole feature and using 20 states. The computation time and data sample length were appropriate for online categorization. Results showed that our algorithm can be used to classify multiple objects with multiple simultaneous contacts. In addition, our initial tests suggest that outlier detection may be achievable. We have also showed the feasibility of using this system with a resistive fabric-based skin in a cluttered foliage environment for rapid haptic mapping.

CHAPTER 4
MATERIAL RECOGNITION FROM HEAT TRANSFER GIVEN VARYING INITIAL CONDITIONS AND SHORT-DURATION CONTACT

4.1 Research Summary

When making contact with an object, a robot can use a tactile sensor consisting of a heating element and a temperature sensor to recognize the object's material based on conductive heat transfer from the tactile sensor to the object. When this type of tactile sensor has time to fully reheat prior to contact and the duration of contact is long enough to achieve a thermal steady state, numerous methods have been shown to perform well. In order to enable robots to more efficiently sense their environments and take advantage of brief contact events over which they lack control, we focus on the problem of material recognition from heat transfer given varying initial conditions and short-duration contact. We present both model-based and data-driven methods. For the model-based method, we modeled the thermodynamics of the sensor in contact with a material as contact between two semi-infinite solids. For the data-driven methods, we used three machine learning algorithms (SVM+PCA, k-NN+PCA, HMMs) with time series of raw temperature measurements and temperature change estimates. When recognizing 11 materials with varying initial conditions and 3-fold cross-validation, SVM+PCA outperformed all other methods, achieving 84% accuracy with 0.5 s of contact and 98% accuracy with 1.5 s of contact.

4.2 Introduction

When a robot's body makes physical contact with the world, it has a distinct opportunity to sense its surroundings. Multimodal tactile sensors can combine a variety of types of sensing, such as pressure, vibration, and temperature sensing, each with its own capabilities

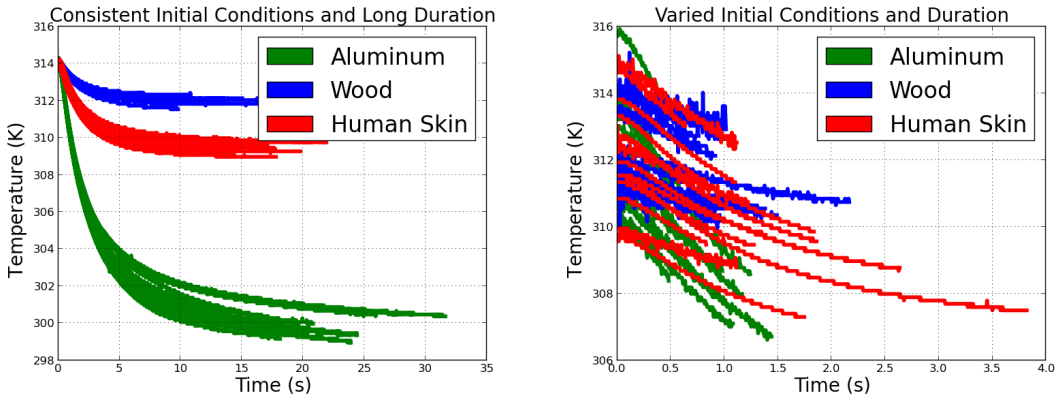

Figure 4.1: *Example temperature features for robot experiments with a) consistent initial conditions and long duration (top), b) varied initial conditions and duration (bottom).*

and limitations. Tactile sensing based on conductive heat transfer can be highly informative about materials in contact with the robot, but has temporal limitations. In order for heat to flow from the sensor to a material, the sensor is typically heated prior to contact and then held in contact with the material. The resulting temperature measurements over time can then be used to recognize the material. For example, touching an aluminum object results in a rapid drop in temperature as heat flows into the aluminum (see Fig. 4.1), which is related to the cold sensation a person feels upon touching aluminum at room temperature.

When a tactile sensor has time to achieve a consistent temperature well above the ambient temperature of the environment and stays in contact with an object until it reaches a thermal steady state, many methods can recognize the material with good performance. However, these requirements greatly decrease the temporal efficiency of tactile sensing, since they reduce the rate at which a sensor can make contact with the world and require that the sensor be held in contact for a substantial length of time. In this paper, we focus on the problem of recognizing materials given short-duration contact and varying initial conditions, which results in visibly different temperature time series, as seen in Fig. 4.1.

Many robotics applications would benefit from methods that recognize materials from short-duration contact with less time between contact events. In general, this would increase the speed at which a robot acquires information using touch. As we discuss later,

recent algorithm-centric research on heat-transfer-based sensing has used contact durations of 15 s or longer and consistent initial conditions. In contrast, we show the feasibility of acquiring useful information 30x faster with 0.5 s of contact, initial sensor temperatures varying from 26°C to 40°C in a room with an ambient temperature of 25°C, and materials that did not fully cool down to the ambient temperature between contact events. This is a markedly different level of efficiency and opens up the possibility of new uses for sensing based on heat transfer, such as helping a robot find metal keys in a bag.

The potential for robots to acquire information from incidental contact between their bodies and their surroundings has motivated our work. By *incidental contact*, we mean contact that is not central to the robot's current actions and may occur unexpectedly or unintentionally [31, 32]. In contrast to deliberate probing during which the robot controls contact to improve perception, sensing during incidental contact is opportunistic with the robot inferring what it can from contact as it occurs. For example, a robot reaching into a densely cluttered environment can use tactile sensing across its arm to better maneuver within the environment and map it [31, 32]. Likewise, an assistive robot reaching around a person with disabilities could potentially use tactile sensing to recognize contact between its arm and the person's body or wheelchair [34]. Similarly, tactile sensing across a robot's fingers might provide useful information during in-hand manipulation. All of these tasks could potentially benefit from tactile sensing based on heat transfer, but would be sensitive to the temporal limitations we address in this paper.

4.3 Related Work

Many researchers have used thermal sensing in studies with consistent initial conditions and long duration contact using specialized exploratory behaviors. In contrast to these studies, our work focuses on short-duration contact (without reaching steady-state) with varying initial conditions. Also, instead of investigating multiple sensory modalities, we focus on the performance of heat-transfer-based sensing in isolation. Unlike most previous

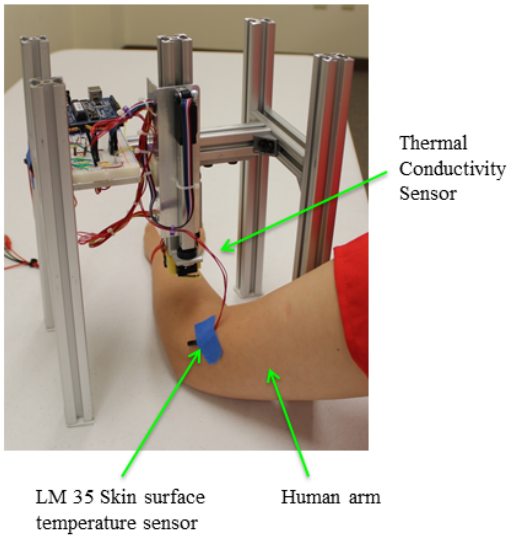

Figure 4.2: *Experimental setup with a 1-DOF linear actuator to measure thermal response of different materials in contact.*

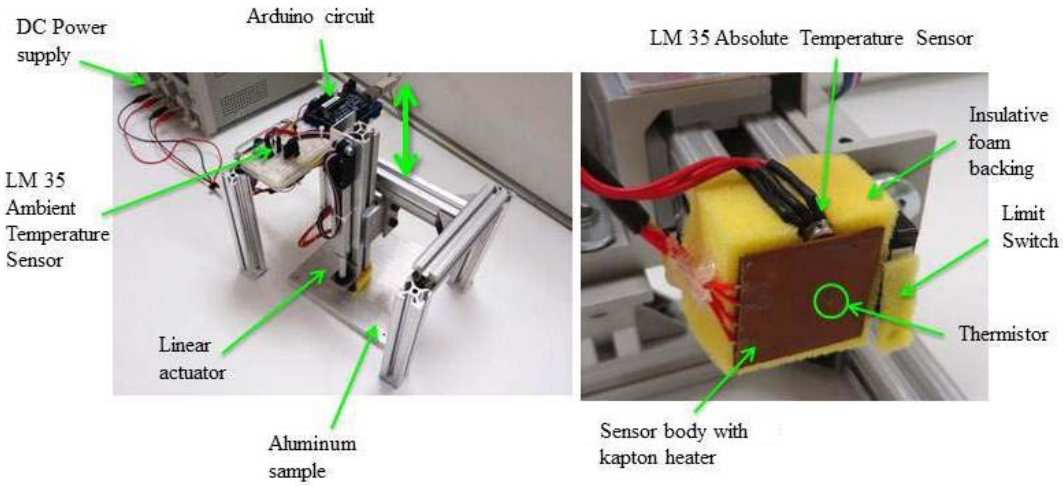

Figure 4.3: *Sensor test rig composed of a) linear actuator, Arduino circuit and sensor (left), b) Heat-transfer-based tactile sensor with a single-sided transient plane source technique (right).*

studies, we have developed a physics-based model for material recognition for increased understanding of the recognition problem and to provide a comparison with data-driven methods.

4.3.1 Short-duration Contact with Consistent Initial Conditions

Studies in this section focus on thermal sensing during short-duration contact. However, these studies are hardware-centric with limited evaluation. In addition, all of these studies use methods that assume consistent initial conditions.

Hardware-centric

Russell [134, 135] developed a thermal sensing array with which he compared the percent decrease in temperature from a uniform initial temperature after 3 s of contact. The array successfully recognized six distinct materials in a single trial [134, 135]. Siegal et al. [136] developed another sensor with a slower temporal response, according to Monkman and Taylor [137]. Monkman and Taylor [137] developed two methods of thermal sensing that they reported to be faster than Russell's or Siegal et al.'s . One sensor used a Peltier heating element, and the other used a pyrometer and a heating element. They evaluated the two sensors with respect to the recognition of four materials with distinct thermal properties given consistent initial conditions. Their figure showing sensor readings over time from a single trial with each material, suggests that recognition of these four materials could potentially be performed quickly (between 0 s and 3 s), but they did not report specific results. Engel et al. [138, 139] developed a flexible multimodal tactile sensing system that included a side-by-side gold heater and temperature sensor. Based on combined pressure and thermal sensing, their system recognized 5 materials with 90% accuracy over 50 trials with consistent initial conditions, but unreported contact duration. Our methods could potentially be used with these and other sensors that use heat transfer, and different hardware might result in improved performance.

4.3.2 Long-duration Contact with Consistent Initial Conditions

Studies in this section deal with thermal sensing under idealized scenarios with consistent initial conditions and long-duration contact.

Hardware-centric

Many researchers have included thermal sensing as a part of multimodal tactile sensing hardware, such as absolute temperature sensors [140], [141] and sensors that use heat transfer [142], [54], [143], [144], [145]. However, this body of work focuses on hardware development with little evaluation of material recognition performance.

Algorithm-centric

A number of researchers have performed algorithm-centric research using existing sensor hardware to perform tasks related to material recognition. Xu et al. [146] used a Syntouch BioTAC sensor to measure the temperature derivative during 15 s of contact using exploratory behaviors from Bayesian exploration coupled with Reinforcement Learning techniques. They used multimodal sensor data to identify 10 objects with 99% accuracy [146]. McMahon et al. [147] used HMMs to automatically assign adjectives to haptic signals collected from a BioTAC sensor using approximately 80 s of data. [147]. Takamuku et al. [148] constructed a soft anthropomorphic finger that included both tactile and thermal sensors. They achieved classification by recording the convergent temperatures of 5 materials after 35 s of contact [148]. Kerr et al. [149] also used a heated BioTAC sensor (allowed 15-20 minutes to reach a steady-state after it is powered on) to record the thermal response data of 6 material groups with varying thermal properties for 20 s. They used the static temperature (TAC) and dynamic thermal conductivity (TDC) data from 15 trials for each material and implemented ANN with 73% accuracy [149].

In summary, the above studies focus on long-duration contact with consistent initial conditions using specific exploratory behaviors. Hardware-centric studies have focused on

designing new thermal sensors with limited material recognition evaluation, while algorithm-centric studies have focused on data-driven algorithms such as HMMs, ANNs, and other ML-based methods. Most of the studies have used results from multimodal sensing devices, obscuring the role of thermal sensing.

4.4 Experiments

4.4.1 Experimental Setup

Figure 4.3 shows the test rig we used in our experiments. We constructed our sensor from the Thorlabs HT10K Foil Heater/Thermistor [150] which contains a 20 Ω heater and a 10 kΩ NTC thermistor. Our sensing technique is based on the single-sided transient plane source method that Mathis et al. [151] developed for characterizing samples of materials. This material characterization typically involves estimating material properties, such as thermal effusivity and thermal conductivity, for use in industrial applications, such as monitoring the quality of products, for which initial conditions can be controlled and the duration of contact can be long [142]. In contrast to previous transient plane source methods that required a sensor to be sandwiched between two samples of the material [152], [153], the single-sided approach [151] only requires that the sensor make frontal contact with a sample of the material, making it appropriate for tactile sensors that cover a robot. For this approach, the heater and temperature sensor are on a thermally insulating backing.

In general, a higher initial sensor temperature corresponds to better quality data. We chose a sensor heater supply voltage of 2.5 volts, so that a person can comfortably touch the sensor surface. We mounted the sensor on a layer of thermally insulating foam with the front face exposed as seen in Fig. 4.3. When the warmed sensor is brought into contact with an unknown surface, heat transfer from the sensor to the material occurs at a rate that depends on the material's temperature, thermal conductivity, density and specific heat capacity. We also installed a separate LM35 Precision Centigrade Temperature Sensor to measure the heater temperature and a limit switch to detect contact with the material and

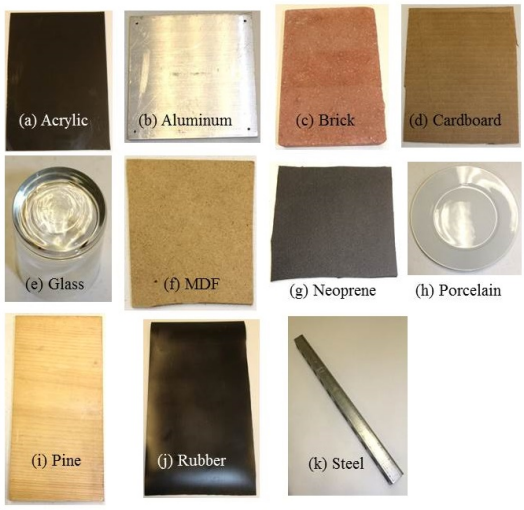

Figure 4.4: *Material test set consisting of a) Acrylic, b) Aluminum, c) Brick, d) Cardboard, e) Glass, f) Medium-density fiberboard (MDF), g) Neoprene, h) Porcelain, i) pine wood, j) Rubber, k) Steel. Please note that we have a separate subsection that analyzes the tests with a human forearm (Section 4.8.5).*

support autonomous data collection. To measure the ambient temperature of the room, we added a second LM35 temperature sensor on top of the test rig.

The test rig shown in Fig. 4.3 uses a 1-DOF linear actuator to move the heat-transfer-based tactile sensor. All sensors and actuators are connected to an Arduino Duemilanove. We used a DC power supply to run the linear actuator and sensor heater.

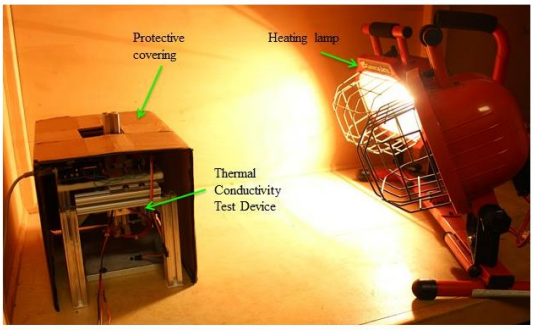

Figure 4.5: *Warm environment test configuration. We used a heating lamp as a heat source along with a protective covering to avoid direct thermal radiation from the lamp and provide an isolated environment for the experiments.*

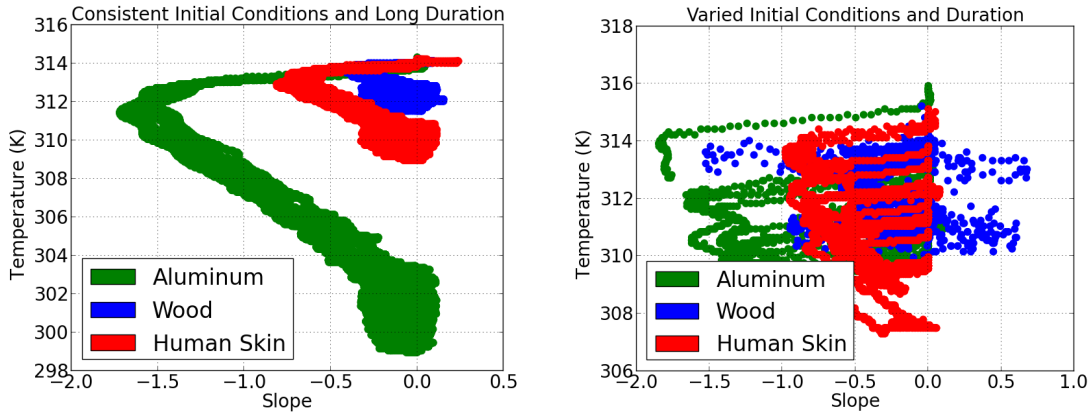

Figure 4.6: *Example temperature and slope features for experiments with a) consistent initial conditions and long duration (top), b) varied initial conditions and duration (bottom).*

4.4.2 Experimental Procedure

Figure 4.3 demonstrates the use of the test rig to sense an aluminum sample. We used a Python script running on a separate computer to control the device through a serial link with the Arduino. Before contacting the sample, the device waited with the linear actuator in the "Up" position and allowed the heating element to heat the sensor body. Once heated, the device lowered the linear actuator and brought the heat-transfer-based tactile sensor in contact with the unknown sample. As the two bodies came to a thermal steady state, the Arduino recorded the thermistor, ambient temperature sensor and absolute temperature sensor outputs at 200 Hz. We programmed the device to be in contact with the sample until the thermistor temperature maintained a constant value for 3 s or a total of 35 s passed. We truncated these trials in time to simulate different durations of contact. Once a trial was completed, the device raised the linear actuator and waited for the sensor body to reheat before making contact with the material again.

To gather data with varying initial conditions, we randomized the reheat time with each trial to be in the range of 2-60 s. After every 10 trials, the device waited for 10 minutes with the sensor in the "Up" position to allow the test sample to cool and the sensor to fully reheat. This method generated trials with the initial sensor temperatures distributed in the

range of 26-40°C in a room that was at 25°C.

4.4.3 Data Collection

Figure 4.1 shows the temperature data from various trials with samples of aluminum and wood, as well as a human forearm. As seen in the figure, materials with different thermal properties exhibit distinct temperature time series that vary based on the initial conditions. Despite this variation, features of the temperature time series remain similar for a given material.

Figure 5.5 shows the set of 11 test materials with various thermal properties that we used in our experiments. We collected 500 trials with random initial conditions for each material using the automated test rig shown in Fig. 4.3, giving a total of 5500 trials. During the experiment, we maintained the room temperature at 25°C throughout the day. The sensor temperature during this set of experiments varied from 26°C minimum to 40°C maximum with an average of 30°C across all the trials just before contact. To investigate the role of ambient temperature on performance, we conducted a second set of experiments in a warm environment of 35°C as shown in Fig. 4.5. We used a heating lamp to heat the surroundings to 35°C and a protective covering to isolate the sample. For this set, the sensor temperature varied from 35°C minimum to 43°C maximum with an average of 37°C across all the trials just before contact. We collected an additional 500 trials with random initial conditions for both aluminum and pine wood in the warm environment, resulting in 1000 total trials. We also collected two more data sets that we describe in Sections 4.8.2 and 4.8.5.

4.4.4 Data Preprocessing and Feature Extraction

For each trial in an experiment, we collected the thermistor raw analog values at 200 Hz. We truncated the data at the onset of contact and obtained time-series vectors until steady-state was reached. To simulate varying contact duration, we used the first 0.5-2.5 s of

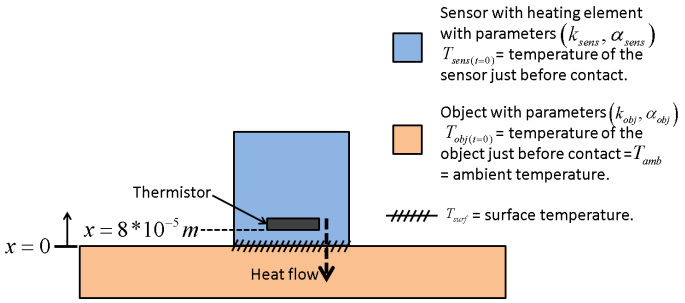

Figure 4.7: *Diagram representing our model of the sensor in contact with a material. We model both bodies as semi-infinite solids.*

data after the onset of contact. Fig. 4.1 shows the raw temperature time series for three example materials. In addition to the raw temperatures, our methods used estimates of the the derivative (slope) of the temperature with respect to time by taking the first difference of the raw signals and then using a causal filter. The filter was an 8th-order digital low-pass Butterworth filter with Nyquist frequency of 100 Hz and cutoff frequency of 2 Hz. Fig. 4.6 shows the slope features.

4.5 Modeling Heat Transfer

We modeled the heat transfer between the heat-transfer-based tactile sensor and a block of material as contact between two semi-infinite solids, which we refer to as the sensor body and the object body [142, 154]. Fig. 6.4 shows a diagram representing the model. A semi-infinite solid is an idealized body for which the temperature change in a part of the body is due to thermal conditions on a single surface [154]. In an analogous manner, [154] has modeled a finger touching a material as a contact between two semi-infinite bodies.

First, we assume that the initial temperature of the object body, $T_{obj(t=0)}$, is constant throughout its extent and equal to the ambient temperature, T_{amb}.

Second, we find the initial temperature of the sensor body, $T_{sens(t=0)}$. The input to the sensor body is the heat flux, $\dot{q}_x$, from the electrical heating element given by

$$\dot{q}_x = \frac{V^2}{R} \tag{4.1}$$

where V is the supply voltage, and R is the resistance of the heating element. $T_{sens(t=0)}$ is constant across the entire sensor body and results from the heating element heating the sensor body before it comes into contact with the object body (i.e., the material sample). We find $T_{sens(t=0)}$ using Fourier's law of Heat Conduction [154],

$$\frac{\dot{q}_x}{A} = k_{sens}\frac{T_{sens(t=0)} - T_{amb}}{l} \tag{4.2}$$

where A is the cross-sectional area of the heating element, l is the height of the sensor body (i.e., length in x dimension), T_{amb} is the ambient temperature, k_{sens} is the coefficient of thermal conductivity of the sensor body, and $\frac{\dot{q}_x}{A}$ is the magnitude of heat flux per unit cross-sectional area.

Once the sensor body comes into contact with the object body, heat begins to flow from the sensor body to the object body and the temperature varies with time and position. When the bodies come into contact with one another, the surface between them at $x = 0$ (see Fig. 6.4) attains a temperature, T_{surf}, that remains constant throughout the duration of contact and is given by

$$T_{surf} = \frac{\left(T_{sens(t=0)}\frac{k_{sens}}{\sqrt{\alpha_{sens}}} + T_{obj(t=0)}\frac{k_{obj}}{\sqrt{\alpha_{obj}}}\right)}{\left(\frac{k_{sens}}{\sqrt{\alpha_{sens}}} + \frac{k_{obj}}{\sqrt{\alpha_{obj}}}\right)} \tag{4.3}$$

where α_{obj} and k_{obj} are the coefficients of thermal diffusivity and thermal conductivity of the object body, and α_{sens} and k_{sens} are the coefficients of thermal diffusivity and thermal conductivity of the sensor body.

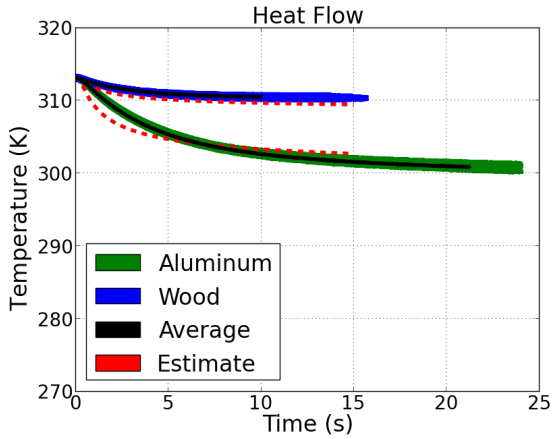

Figure 4.8: *Forward simulation results for pine wood and aluminum with temperature values.*

Once we have found $T_{sens(t=0)}$ and T_{surf}, we can find the temperature in the sensor body at any time, $t >= 0$, using the following partial differential equation from [154]:

$$\frac{\partial^2 T_{sens}}{\partial x^2} = \frac{1}{\alpha_{sens}} \frac{\partial T_{sens}}{\partial t} \tag{4.4}$$

where $T_{sens}(x,t)$ is the temperature at time t of the sensor body at distance x from the surface between the two bodies. The thermistor, which is inside the sensor body, measures the temperature $T_{sens}(x = 8 * 10^{-5}, t)$ (see Fig. 6.4). Using our boundary conditions, $T_{sens}(x = 0, t) = T_{surf}$and $T_{sens}(x, t = 0) = T_{sens(t=0)}$ we can solve for $T_{sens}(x,t)$.

$$\begin{aligned} T_{sens}\,(x,t) = T_{sens(t=0)} + \left(T_{surf} - T_{sens(t=0)}\right) \\ *erfc\left(\frac{x}{2\sqrt{\alpha_{sens} t}}\right) \end{aligned} \tag{4.5}$$

where $erfc()$ is the complementary error function given by

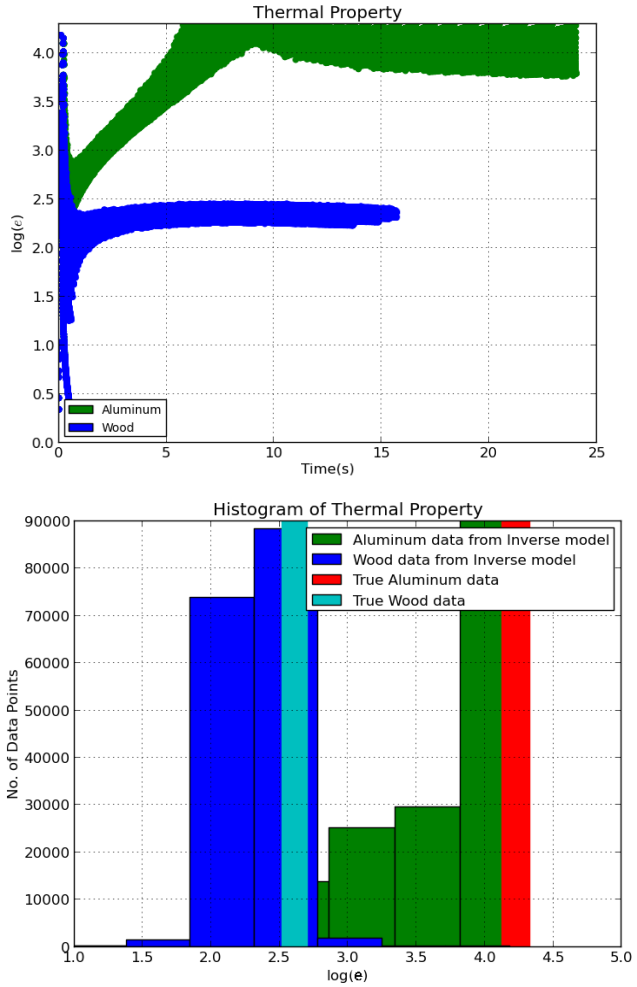

Figure 4.9: *Inverse Simulation of the heat-transfer data (top), Histogram of the thermal property (bottom). Shaded regions in the histogram show the true values.*

$$erfc(z) = \frac{2}{\sqrt{\pi}} \int_{z}^{\infty} e^{-r^2} dr \tag{4.6}$$

With this forward model we can predict the sensor readings, $T_{sens}(x = 8 * 10^{-5}, t)$, that would result from the heat-transfer-based tactile sensor coming into contact with a material with coefficient of thermal diffusivity α_{obj} and thermal conductivity k_{obj}.

4.6 Simulation Results

4.6.1 Forward Simulation

We used the heat-transfer model from Section 4.5 to simulate the temperature measurements, $T_{sens}(x = 8 * 10^{-5}, t)$, that would result from our sensor coming into contact with a known object, specifically a block of pine wood or a block of aluminum. We used the coefficients of thermal conductivity and diffusivity, $k_{obj}$and α_{obj}, for pine wood and aluminum from the CES materials database [92]. For aluminum, $\alpha_{obj} = 3.55 * 10^{-5}\ m^2/s$ and $k_{obj} = 80\ W/(mK)$ and for pine wood, $\alpha_{obj} = 2.05{*}10^{-7}\ m^2/s$ and $k_{obj} = 0.15\ W/(mK)$. We obtained the cross-sectional area of the heating element $A = 1.5625 * 10^{-4}\ m^2$, the height $l = 2.4 * 10^{-4}\ m$ and the thermistor location at a distance $x = 8 * 10^{-5}\ m$ from the sensor data sheet [150]. We calculated the heat flux using eq. (4.1) with $V = 2.5$ volt and $R = 19.7\ \Omega$. We set the initial temperature of the material $T_{obj(t=0)}$ to be the ambient temperature, $25\ ^{\circ}\mathrm{C}$.

We calibrated the tactile sensor's thermistor using a simplified version of the standard Steinhart-Hart equation [155],

$$T = \frac{1}{C_1 ln(R_{th}) + C_0}, \tag{4.7}$$

which relates the absolute temperature, T, to the resistance across the thermistor, R_{th}. Our calibration resulted in $C_0 = 9.5594 * 10^{-4}$ and $C_1 = 2.6181 * 10^{-4}$. A resistive voltage divider with the thermistor, R_{th}, and a resistor, R_{REF}, performed the only signal conditioning prior to analog-to-digital (A/D) conversion by an Arduino Duemilanove board. The A/D converter linearly converted a 0-1.1 volt analog signal to a 10-bit digital signal, A_{in}.

$$R_{th} = R_{REF}[\frac{V^+}{\frac{A_{in}}{1023}V_{REF}} - 1] \tag{4.8}$$

relates R_{th} to A_{in} with $R_{REF} = 668\ \Omega$, $V^+ = 5.06$ volts, and $V_{REF} = 1.1$ volts.

The only other parameters needed for the simulation were α_{sens} and k_{sens} for our tactile sensor, which we estimated using a recursive least squares method implemented in SciPy [156]. For this estimation, we used actual measurements from one trial with a pine wood block, resulting in $\alpha_{sens} = 2.796 * 10^{-9}\ m^2/s$ and $k_{sens} = 0.0349\ W/(mK)$.

To perform the simulation, we found the initial temperature of the sensor $T_{sens(t=0)}$ using eq. (4.2) and the surface temperature T_{surf} using eq. (4.3). We then computed $T_{sens(x=8*10^{-5},t)}$ using eq. (4.5). When compared with the average measurements from 60 real trials with wood and 60 real trials with aluminum, the pine wood simulation had an RMSE of 0.77°C, and the aluminum simulation had an RMSE of 1.08°C (see Fig. 4.8).

4.6.2 Model-based Inference

In this section, we use the model from Section 4.5 to recognize an unknown material given consistent initial conditions based on a time-series of real temperature measurements from our tactile sensor, $T_{sens}(x = 8 * 10^{-5}, t)$. We use the model to estimate the material's thermal effusivity, e, at each point in time, where $e = \frac{k_{obj}}{\sqrt{\alpha_{obj}}}$. These estimates tend to improve with a longer duration of contact (see Fig. 4.9). To estimate e, we first find the sensor temperature just before contact, $T_{sens(t=0)}$.

$$T_{sens(t=0)} = \frac{\left(\frac{\dot{q}_x}{A}l + T_{amb}\right)}{k_{sens}} \tag{4.9}$$

based on eq. (4.9) with T_{amb} set to the currently measured ambient temperature and the other parameters set to the values described in Section 4.6.1. We then combine eqs. (4.5)

and (4.3) to find

$$e = \frac{T_{surf}\frac{k_{sens}}{\sqrt{\alpha_{sens}}} - T_{sens(t=0)}\frac{k_{sens}}{\sqrt{\alpha_{sens}}}}{T_{obj(t=0)} - T_{surf}} \tag{4.10}$$

where

$$T_{surf} = \frac{T_{sens}(x = 8 * 10^{-5}, t) - T_{sens(t=0)}}{erfc\left(\frac{8*10^{-5}}{2\sqrt{\alpha_{sens}t}}\right)} + T_{sens(t=0)}. \tag{4.11}$$

Notably, all of the terms in the resulting equation are constants, except for t and $T_{sens}(x = 8 * 10^{-5}, t)$. Consequently, we can use this equation to estimate the material's thermal effusivity, e, at each point in time using only the current time, t, and the current sensor temperature, $T_{sens}(x = 8 * 10^{-5}, t)$. To recognize a material, our algorithm compares these thermal effusivity estimates to values from the CES materials database [92]. For this paper, our algorithm used a 10-bin histogram of $\log_{10}(e)$ from the estimates made during a trial. It then found the bin containing the largest number of estimates and compared the range associated with this bin to the ranges associated with the candidate materials, as determined by the materials database. It then classifies the material as being the candidate material with the most similar range of values.

We evaluated this model-based method of material recognition using time series of raw temperature measurements from 60 trials with aluminum and 60 trials with pine wood using consistent initial conditions with substantial time between trials. Fig. 4.9 shows the results of plotting $\log_{10}(e)$ for all the estimates of e from these 120 trials. The top figure illustrates how the estimates change with duration of contact. The bottom figure shows a histogram produced from these values along with the ranges for aluminum and pine wood from the materials database. When using this method to recognize whether each of the 120 trials was pine wood versus aluminum, it had no errors and achieved 100% accuracy. However, this performance must be considered with caution, given the consistent initial conditions,

the long duration of contact, and the very distinct thermal properties of aluminum and pine wood.

Given these results, model-based methods for material classification based on heat transfer merit further research. Perhaps more importantly, this model can potentially provide intuition for the estimation problem, inform feature selection, inform sensor design, and be used to generate synthetic data for evaluation and training. A clear benefit of this model-based method is that it can directly use information from materials databases. A potential limitation of this particular model-based method is that it is deterministic and does not represent various sources of uncertainty that could be relevant to the estimation.

4.7 Data-driven Inference

In addition to our model-based method for inference, we evaluated three data-driven machine-learning algorithms that categorize materials based on the raw temperature and estimated slope over time. We chose these algorithms based on their wide usage and suitability for time series.

4.7.1 k-Nearest Neighbors and Support-Vector Machines

We implemented both k-nearest neighbors (k-NN) and support vector machines (SVMs) using the scikit-learn package [109] in Python. For k-NN we used k=3. For the SVMs, we used the svm.SVC() function, which performs multiclass classification using SVMs. This function implements multiclass classification via pairwise coupling as described in [157]. We used a linear kernel after trying other kernels, such as radial basis functions.

To produce feature vectors for training, we truncated the raw temperature time series to 500 samples, starting from the onset of contact, to produce a 500-dimensional feature vector. Due to the 200 Hz sampling rate, this resulted in approximately 2.5 s of data. When using both the raw temperature and the estimated slope, we truncated each time series to 500 samples from the onset of contact and concatenated them into a 1000-dimensional fea-

ture vector. To reduce the effect of noise and overfitting, we computed a low-dimensional representation of the training data with principal component analysis (PCA) before classification with k-NN or SVMs. In our classification experiments, we used 10 principal components for dimensionality reduction. 10 principal components could account for 95% of the variance of the 1000-dimensional feature vectors resulting from 5500 trials.

4.7.2 Hidden Markov Model

We used a hidden Markov model (HMM) for each candidate material. We used multivariate continuous left-right HMMs with 25 hidden states and either 1 or 2 dimensional Gaussian emissions. We implemented them using the GHMM toolkit [106] in Python. We decided on these specifications based on results with preliminary data. We trained these HMMs with the standard Baum-Welch algorithm. For testing, we ran the Viterbi algorithm to find the HMM with the most probable state sequence given the observations and classified the material as being the material associated with this HMM [65].

4.8 Experimental Results

In this section, we present our results from evaluating the three data-driven methods.

4.8.1 Consolidated Results

Fig. 4.10 shows the range of values of $\log(e)$ for the materials in our experiments based on the CES materials database [92]. As seen from the figure, some of the materials have overlapping ranges, while others are quite different.

Table 4.1 shows the consolidated results from our evaluation of the three data-driven algorithms using 3-fold cross-validation with 5500 trials (500 trials for each of the 11 materials). SVM+PCA outperformed the other algorithms. HMMs had the worst performance, confusing neoprene with pine wood and aluminum with steel.

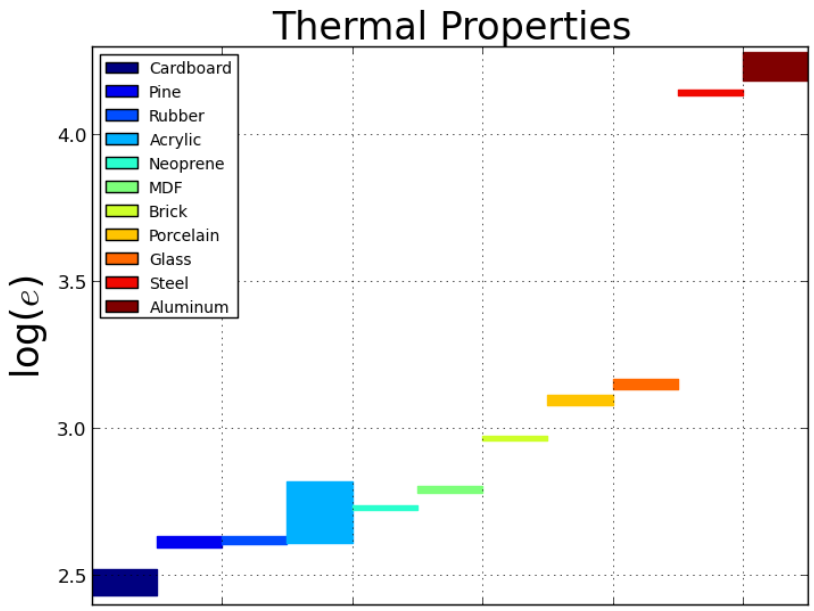

Figure 4.10: *Thermal properties of materials used for experiments. Each material has a minimum and maximum value for* $\log(e)$. *The values are taken from CES materials database [92].*

Table 4.1: Performance Summary.

Experimental Conditions	Features	HMMs	k-NN + PCA	SVM + PCA
Varied Initial Conditions and Contact Duration	One Feature	59.55%	82%	99%
	Two Features	53.2%	86%	99%

4.8.2 Effect of Initial Conditions

We conducted another evaluation using 60 trials each for aluminum and pine wood with similar initial conditions. We extracted the features and ran all the algorithms for these 120 trials. Table 4.2 shows the results. The overall results are much better than with the randomized initial conditions. SVM+PCA, k-NN+PCA, and the model-based inference method (Section 4.6.2) outperformed HMMs.

Table 4.2: Effect of Initial Conditions.

Experimental Conditions	Data-driven Approach				Model based Approach
	Features	HMMs	k-NN + PCA	SVM + PCA	
Same Initial Conditions	One Feature	100%	100%	100%	100%
	Two Features	68.12%	100%	100%	

Table 4.3: Effect of Contact Duration.

Experimental Conditions	Time (s)	HMMs	k-NN + PCA	SVM + PCA
Varied Initial Conditions	0.5	22.35%	63%	84%
	1.5	25.67%	77%	98%
	2.5	31.25%	82%	99%

4.8.3 Effect of Contact Duration

To analyze the effect of contact duration on classification performance, we truncated the data at different time lengths and ran the algorithms. Table 4.3 shows the results (500 trials for each of the 11 materials). As expected, with increased length of the time, the performance of the algorithms improves. With 2.5 s of random and uncertain data, SVM+PCA reached an accuracy of 99%. When the input was reduced to 0.5 s of data, SVM+PCA achieved 84% accuracy.

4.8.4 Effect of Ambient Temperature

We also conducted a set of experiments wherein we varied the ambient temperature to see if our results would generalize. We performed this set of experiments in a similar manner to the first set of experiments with short-duration contact and varying initial conditions. Table 4.4 shows the results (500 trials for aluminum and for pine wood). The overall trend remains the same and SVM+PCA shows the best cross-validation results with raw

Table 4.4: Effect of Ambient Temperature.

Experimental Conditions	Ambient Temperature	HMMs	k-NN + PCA	SVM + PCA
Varied Initial Conditions and Contact Duration	25°C	83.2%	100%	100%
	35°C	66.4%	94%	91%

temperatures. However, the performance at higher temperature degrades when compared to the results at 25°C due to the smaller difference between the sensor's temperature and the material's temperature.

4.8.5 A Heat Generating Material (Human Skin)

We recruited 1 able-bodied participant via word of mouth. We obtained written informed consent from the participant according to our experimental protocol that was approved by the Institutional Review Board of the Georgia Institute of Technology. We collected 35 random initial condition trials on the forearm of the participant as shown in Fig. 4.2. The skin was at approximately 30°C and the ambient temperature was 26°C. The sensor was at 2° to 6°C above the forearm skin temperature just before contact. The experimental data presented in [158] indicates that the thermal conductivity of human skin is around $0.37 W/mK$. According to [92], out of the 11 materials we used in our other trials, MDF has the closest thermal conductivity to that of human-arm skin. We evaluated how well our best performing algorithm (SVM+PCA) could distinguish them. The algorithm successfully classified the two materials with 99% accuracy using raw temperatures and with 100% accuracy using both raw temperatures and slope estimates.

4.9 Conclusion

We investigated the classification of different materials based on heat transfer with short-duration contact and varying initial conditions. We conducted five sets of experiments using our 1-DOF experimental setup and implemented both model-based and data-driven meth-

ods for classification. We modeled the heat transfer between the sensor and the material as contact between two semi-infinite solids and used this model to categorize materials from temperature data. In addition to this model-based approach, we compared three data-driven algorithms for classification performance and found that SVM+PCA gave the best results. We also investigated the effect of initial conditions, contact duration, and ambient temperature on the classification algorithms' performance. Our results provide evidence for the feasibility of material classification by robots based on measurements acquired during short-duration contact with varying initial conditions. The performance of these methods during real-world tasks for which the contact between the sensor and the object is more varied, and there are greater numbers and varieties of objects, merits further inquiry.

CHAPTER 5
DATA-DRIVEN THERMAL RECOGNITION OF CONTACT WITH PEOPLE AND OBJECTS

5.1 Research Summary

Many tactile sensors can readily detect physical contact with an object, but tactile recognition of the type of object remains challenging. In this paper, we provide evidence that data-driven thermal tactile sensing can be used to recognize contact with people and objects in real-world settings. We created a portable handheld device with three tactile sensing modalities: a heat-transfer sensor that is actively heated, a small thermally-isolated temperature sensor, and a force sensor to detect the onset of contact. Using this device, we collected data from contact with the arms of 10 people (3 locations on the right arm) and contact with 80 objects relevant to robotic assistance (8 object types in 10 residential bathrooms). We then used support vector machines (SVMs) to perform binary classifications relevant to assistive robots. When classifying contact as person vs. object, classifiers that only used the temperature sensor performed best (average accuracy of 98.75% for 3.65 s of contact, 93.13% for 1.0 s, and 82.13% for 0.5 s). When classifying contact into two task-relevant object types (e.g., towel vs. towel rack), classifiers that used the heat-transfer sensor together with the temperature sensor performed best. Performance was good when generalizing to new contact locations in the same environment (average accuracy of 92.14% for 3.65 s of contact, 91.43% for 1.0 s, and 84.29% for 0.5 s), but weaker when generalizing to new environments (average accuracy of 84% for 3.65 s of contact, 71% for 1.0 s, and 65% for 0.5 s).

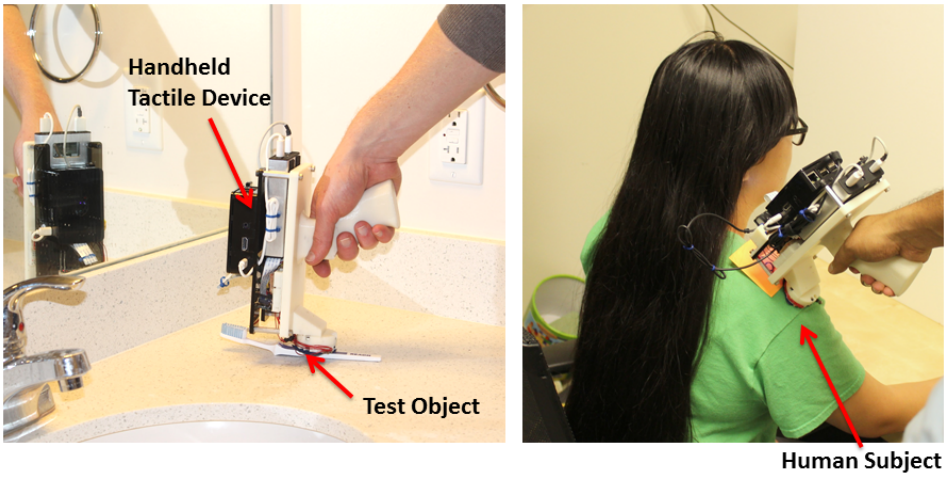

Figure 5.1: *A person using a handheld device to make contact with a toothbrush on counter in a bathroom (left), and a human participant's shoulder (right).*

5.2 Introduction

In this paper, we provide evidence that data-driven thermal tactile sensing can be used to recognize contact with people and objects in real-world settings. Unlike approaches that attempt to classify objects into a large number of categories, we focus on task-relevant binary classification. Robots operating in human environments would benefit from the ability to recognize when contact has occurred with a person versus objects in the environment. For example, a robot might regulate the force it applies to a person or monitor contact with a person for communicative signals. When manipulating objects, distinguishing between contact with an object of interest and a nearby object could also be useful. For example, a robot might use this capability to better maneuver its end effector to grasp a target object. In general, we expect that the task being performed by the robot and observations of the local environment can be used to reduce the tactile recognition problem to one of categorizing contact into a small number of categories.

We train support vector machines (SVMs) to classify time series from a temperature sensor and a heat-transfer sensor. As we demonstrate, temperature sensing is useful for detecting contact with a person's body versus the environment. Temperature sensing is well matched to this classification problem, since the human body actively generates heat, while

most objects in the environment are thermally passive and close to the ambient temperature. We also show that heat-transfer sensing can be informative for distinguishing between task-relevant objects. This is in part due to heat-transfer sensing being able to distinguish materials with different thermal effusivities, such as metal and plastic.

Data-driven approaches for tactile perception have shown promise [31], but suitable training data is lacking. To help address this challenge, we developed a portable handheld device (see Fig. 5.1) [159] for the efficient acquisition of heat-transfer and temperature sensing data from objects in their natural settings. Robot vision and audition, including face detection and speech recognition, have benefited greatly from large labeled data sets of pictures, videos, and audio collected by people. One of our motivations for creating this device is to enable people to efficiently acquire tactile training data for robots, so that tactile perception systems for robots can similarly benefit. Our data-driven recognition algorithm uses this data to train the classifiers for thermal recognition of contact with people and objects.

Thermal recognition of objects in situ entails distinct challenges from material recognition and laboratory-based studies. In contrast to recognition of material samples, objects will often be composed of multiple materials with distinct thermal properties, such as different thermal effusivities. Objects will also have geometries that affect heat transfer, such as by altering the contact area between thermal sensors and the object. Also, different objects in the same object category can be made of thermally distinct materials, such as a plastic fork and a metal fork. In contrast to laboratory-based studies, objects in their natural settings and thermal sensors making contact with them will be influenced by more varied thermal phenomena. These include sunlight through windows, heating, ventilating, and air conditioning (HVAC), body heat, and complex connections between objects and the interiors and exteriors of buildings.

To evaluate our approach, we collected two data sets. For the first, we collected data from contact with 3 different locations on the right arms of 10 human participants. For

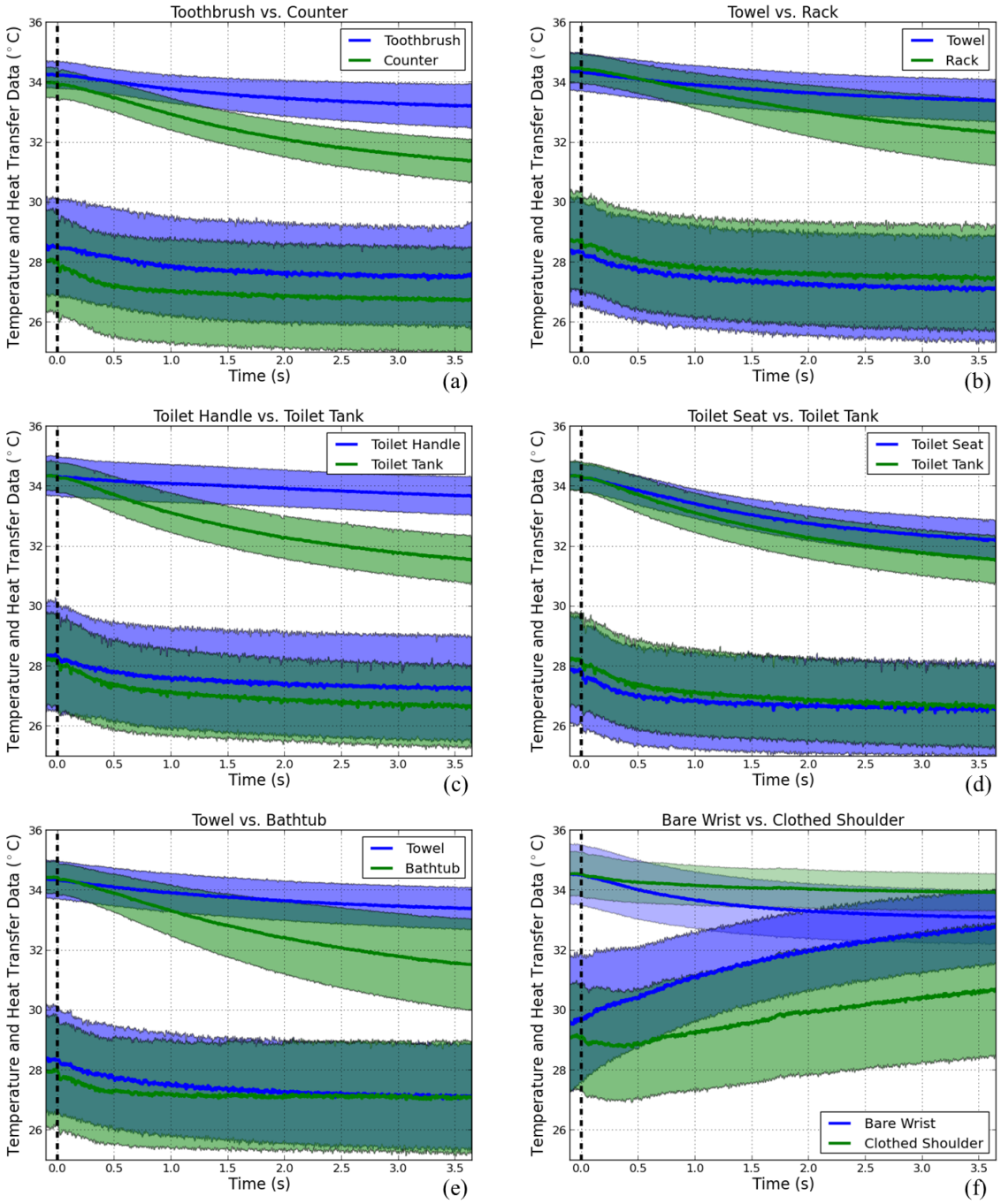

Figure 5.2: *Tactile sensor response with average (solid lines) and standard deviation (shaded) values for both heat-transfer (top two regions in each graph) and temperature (bottom two regions in each graph) sensors for contact with task-relevant objects and locations on human arm. Black dashed lines show the onset of contact.*

the second, we collected data from contact with 80 objects, consisting of 8 object types from 10 residential bathrooms. We considered objects in the bathroom because many activities of daily living (ADLs) with which robots might provide valuable assistance take

place in bathrooms, such as hygiene, grooming, bathing, showering, toileting, transfers, and dressing [160–162]. We selected these objects because they are related to ADLs and are commonly found within residential bathrooms in the United States.

In our evaluation, we only consider binary classification problems. Due to the existence of only two categories (i.e., two object types or two contact types), we use terms like 'distinguishing', 'classifying', and 'recognizing' nearly interchangeably.

Our evaluation of human vs. object recognition focuses on distinguishing contact with a human arm from contact with task-relevant objects associated with ADLs. This recognition problem has additional challenges due to factors such as clothing, the location of contact on the person's body, and physiological differences among people (See Fig. 5.2(f)).

Our evaluation of task-relevant object recognition focuses on distinguishing a target object, which we refer to as the tactile foreground, from an object in its immediate surrounding, which we refer to as the tactile background. Each foreground/background pair corresponds with two objects relevant to a specific task. For example, the task of placing a towel on a towel rack and the task of picking up a toothbrush from a counter (See Fig. 5.2).

5.3 Related Work

Most previous tactile recognition studies focus on data taken from material samples or objects in a controlled laboratory setting. However, our work focuses on task-relevant object recognition using data gathered from in situ objects in homes. Also, contact based material recognition studies in the literature have often focused on deliberate exploratory contact behaviors. These behaviors help in controlling the sensing to maximize the information retrieval for material recognition. Our work uses a single instance of sustained contact.

5.3.1 Human vs. Object Recognition

Humans represent an important class of object in the world that merits special consideration by machines. Research communities devoted to other perceptual modalities, such as

audio and video, have emphasized machine perception of signals resulting from people, such as face detection [163]. In contrast, detecting when tactile signals result from human contact has been relatively unexplored [164]. In [165], we used heat flow to classify contact with medium-density fiberboard versus a persons bare forearm. The closest other work of which we are aware investigated multimodal tactile sensing for affective interaction with the Huggable, a small robotic teddy bear for companionship [166, 167]. The Huggable used distributed electric field, temperature, and force sensors [167] to categorize gestures based on 200 examples from a single person using his/her hand to make communicative contact. In contrast, we focus on discriminating contact between objects and people under varying conditions, such as location and presence of clothing, and investigate the relevance of these capabilities for tasks related to ADLs. [168] uses SVMs and carefully designed features to detect collisions from physical interactions between a robot and a human. Kerr et al. [169] used the BioTAC^{TM} sensor to infer properties of a human body by detecting pulse, classifying the heart rate and analyzing pulse-to-pulse intervals.

There have also been studies on detecting people using non-contact thermal sensors such as thermal cameras [170]. This body of work generally relies on the fact that there is a temperature difference between a heat-generating object like the human body and surrounding objects. Researchers have also used other non-contact thermal sensors such as pyrometers to measure skin temperature [171]. [172] gives an overview of the temperature of the human body, explains the source of heat generation, and discusses its variability depending on the location on the body.

5.3.2 Object vs. Object Recognition

Thermal Sensing Only

There have been many studies on material recognition using only thermal sensing. For an overview of such material recognition studies, please refer to [134, 135, 137, 165, 173, 174].

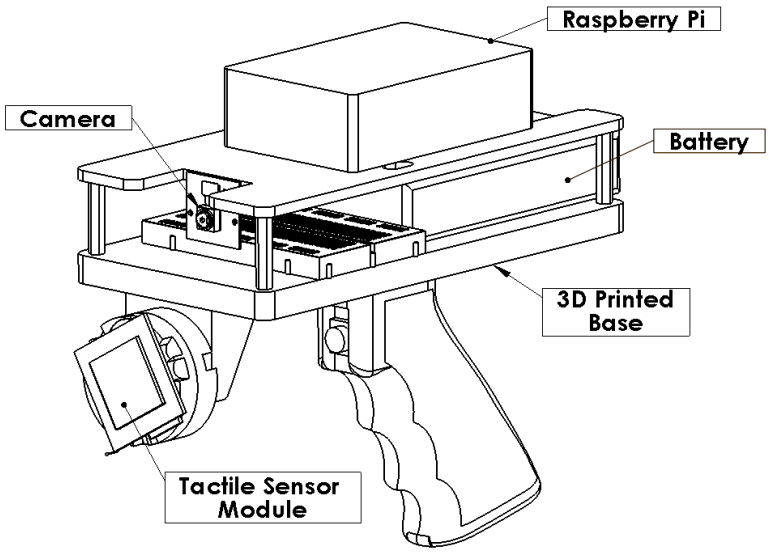

Figure 5.3: *Design of handheld haptic data acquisition device.*

There have also been studies in which researchers have used thermal sensing in conjunction with other sensory modalities for material recognition purposes.

Thermal and Force Sensing Modality

Engel et al. [138, 139] developed a flexible multimodal tactile sensing system using pressure and thermal sensing and achieved 90% accuracy over 50 trials for recognizing 5 materials. Siegal et al. [136] developed a multimodal sensor consisting of an 8 x 8 array of capacitive tactile sensors with a 4 x 4 array of thermal sensors. Takamuku et al. [148] designed an anthropomorphic finger consisting of 3 strain gauges and 4 thermistors with a heating element arranged in a layered format. They successfully classified 5 materials using a combination of strain gauge information and thermal sensing. Yang et al. [140] constructed a 32 x 32 array of conductive rubber based force sensors and absolute temperature measurement chips mounted on both sides of a flexible substrate.

Yuji et al. [145] developed a tactile and thermal sensor using a single pressure-conductive rubber sheet with unequally spaced electrodes to infer both temperature and contact force. They used a common heating element to warm a 2x2 array of sensing modules to 36°C and performed tests with two materials. Caldwell et al. [143] developed a multimodal

tactile sensor to measure contact force and thermal response. They measured the contact force and robot position during specific exploratory behaviors to infer texture, stiffness and object profile, temperature and thermal properties. The thermal sensor used a temperature controlled heat source at a constant 40°C and a Peltier Effect sensor to identify 7 materials with different thermal properties. Castelli [141] developed an 8x8 array of capacitive-based tactile sensors using temperature-dependent semiconductors for absolute temperature measurement. Dario et al. [175] developed a polymer-based tactile and thermal sensor inspired by dermal and epidermal layers of human skin.

Thermal and Other Sensing Modalities

Taddeucci et al. [176] used a multimodal haptic sensing finger with thermal and vibration feedback and a high resolution array of tactile sensors to identify 14 objects during idealized sliding contact using neural networks. [146, 149, 177] used the BioTAC^{TM} sensor with thermal feedback to classify objects using Bayesian learning techniques, ANNs and HMMs.

Mittendorfer et al. [144] developed hexagonal multimodal sensing modules with optical proximity, thermal and acceleration-vibration modalities combined to form an array on a robot arm. In [178], the authors developed a prosthetic skin that used strain, pressure, temperature, and humidity sensors, along with electroresistive heaters.

5.4 Description of the handheld device

Figure 5.3 shows the design of the complete handheld data acquisition device. Figure 5.4 shows the tactile sensor module that mounts to the front of the handheld device and comes into contact with objects. The tactile sensor includes a sensor for measuring heat transfer, a fast response thermistor for temperature sensing and a fabric-based force sensor for force estimation. The heat-transfer and temperature sensing modalities are used for recognition purposes. The force sensing modality is only used to detect the onset of contact and is not

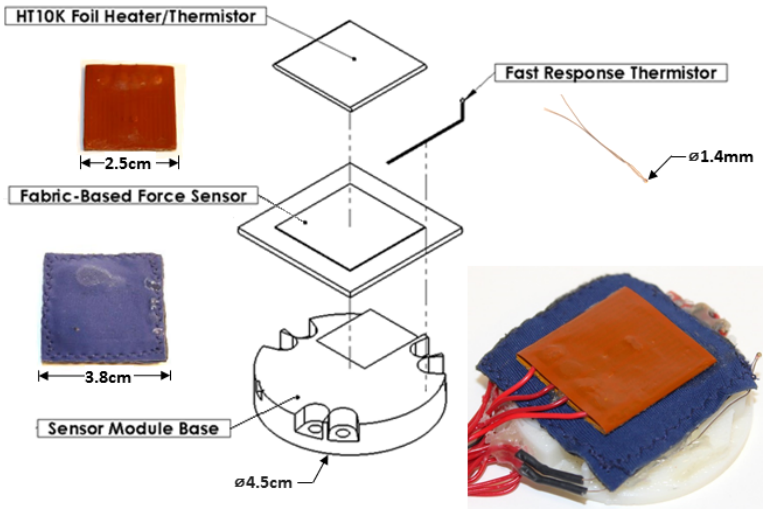

Figure 5.4: *Exploded view of tactile sensor module.*

used for recognition.

The handheld device uses an onboard camera to save a picture of each object for documentation. The onboard Raspberry Pi 2 and 8 channel 12 bit ADS7828 analog-to-digital converter (ADC) record data to a USB flash drive from the force sensor at approximately 550 Hz and from the heat-transfer sensor and temperature sensor at approximately 110 Hz. To simplify analysis, we upsampled the data from the heat-transfer and temperature sensors to 550 Hz using zero-order hold interpolation in order to match the sample rate of the force sensor.

5.4.1 Design Assembly of the Sensor Module

Figure 5.4 shows the complete sensor with a 3D printed base. We used Surebonder 727 Hot Glue [179] to attach the passive fast response thermistor, and heat-transfer sensor on top of the force sensor, which is mounted on the 3D printed base. The heat-transfer sensor and fast response thermistor sit beside one another and form the outer-most sensing layer. They come into direct contact with the object, which allows for faster response times.

5.4.2 Heat-Transfer Sensor

We based the sensor for measuring heat transfer on our work in [165]. The sensor uses a Thorlabs HT10K - Flexible Polyimide Foil Heater with a 10 kOhm Thermistor [150]. This sensor uses the modified transient plane source technique for thermal property estimation [151]. In this technique, a resistive heater heats the sensor up before bringing it into contact with a uniform material sample at room temperature. With good contact and a large sample, the material's thermal effusivity [165] primarily determines the heat transfer from the sensor to the sample. This results in a characteristic temperature change measured by the HT10K's thermistor. We converted the raw ADC output from the thermistor in the heat-transfer sensor to degrees Celsius using a third-order polynomial fit ($R^2 = 0.994$) based on calibration data.

5.4.3 Temperature Sensor

Unlike our previous work in [165], we also used a small, passive EPCOS fast response 10K NTC thermistor to measure the approximate air temperature before contact and the object's temperature during contact. Though heat from the heat-transfer sensor's heater and other onboard electronics, as well as other environment factors tend to raise the temperature of the surrounding air, it is still possible to estimate the ambient temperature of the environment within approximately 1°C by recording the temperature sensor value prior to contact. We implemented a third-order polynomial fit ($R^2 = 0.994$) based on calibration data to convert the raw ADC output from the fast response thermistor to degrees Celsius (See [165] for details).

5.4.4 Fabric-Based Force Sensor

The force sensing modality uses a single 2.5 cm square taxel of piezoresistive fabric in a voltage divider circuit based on the stretchable fabric-based force sensor described in [180]. We converted the raw ADC output from the taxel to force in newtons, assuming a uniform

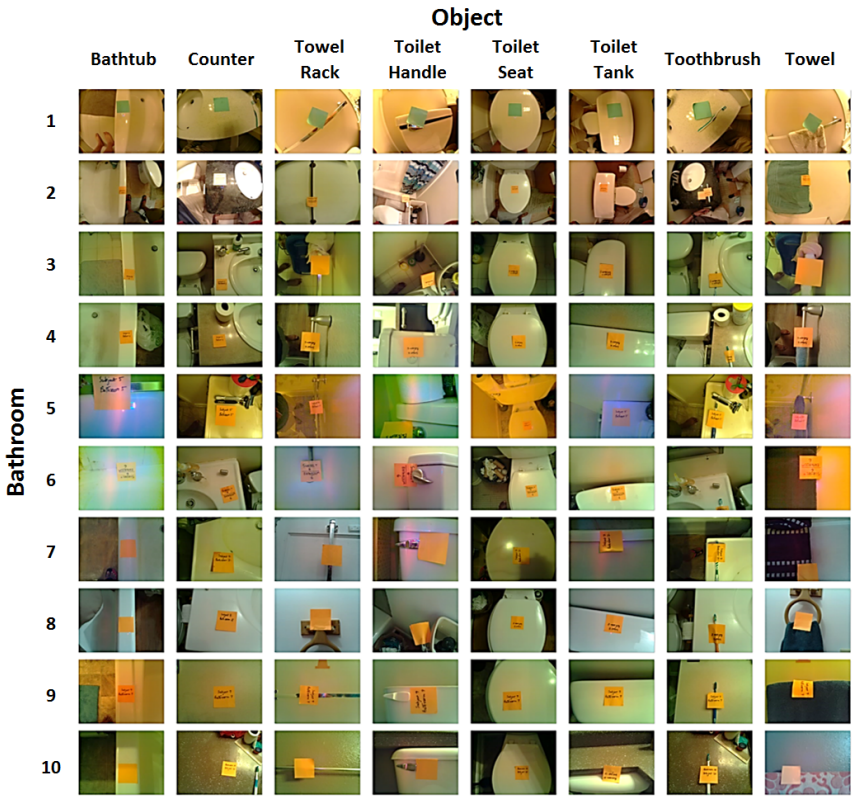

Figure 5.5: *Test set consisting of 10 sets of common items found in a bathroom associated with activities of daily living (ADLs): bathtub, sink counter, empty towel rack, toilet handle, toilet seat, toilet tank, toothbrush and towel on towel rack.*

pressure distribution over the taxel, using a third-order polynomial fit ($R^2 = 0.984$) with calibration data collected using an ATI Mini45 Force/Torque sensor.

5.5 Experiments

We performed two sets of experiments to evaluate our device and methods.

5.5.1 Experimental Procedure

For both the experiments with humans and objects, we performed the following procedure for data collection.

- We identified the object or the location on the human arm and attached a sticky note adjacent to it identifying the object / location.

- Before a trial with any object or any location on the human arm, we allowed the heat-transfer sensor to heat for 3 minutes to allow it to reach a thermal steady state. This reduces variability in the sensor's initial conditions.
- We took a picture of the object/location using the camera mounted on the device.
- We attempted to move the device in a linear motion normal to the surface of the object with constant velocity.
- We maintained contact with approximately constant pressure for 5 s and waited for a beep from the device to break contact.

5.5.2 Experiments with human participants

For these trials, we used the handheld device to make contact with three locations on the human arm, namely the wrist, the forearm and the shoulder (covered by the sleeve of an article of clothing) as shown in Fig. 5.6. Each participant wore his/her own shoulder-covering clothing for the study. We recruited 10 participants via word of mouth. We had 3 female and 7 male participants from 21 to 49 years of age. We obtained informed consent from each participant. Our study was approved by the Institutional Review Board of the Georgia Institute of Technology. For each experiment, we asked the participant to keep his / her arm on a table-like surface while we applied the handheld device to three points on his / her arm.

We chose locations on the wrist, forearm and elbow of a human arm to be anatomically consistent across different participants in our controlled experiments (Fig. 5.6). For the wrist, we chose a location 1cm away from the triquetral bone towards the sagittal plane. For the forearm, we chose a location on the bulk of the flexor muscle, 5cm away (towards the wrist) from the line connecting the elbow pit and elbow bone. For the shoulder, we chose the location of the acromion scapula. We conducted 1 trial per location, thus collecting a total of 30 trials (3 locations X 10 participants). Figure 5.2(f) shows 3.65 s of the data from

all trials on the wrist and shoulder of human participants. As seen in the figure, the heat-transfer rate is higher for the bare wrist (and forearm) locations compared to the clothed shoulder potentially due to the thermal insulation provided by the clothing. Unlike the experiments with household objects, the temperature sensor warms up slightly after contact because it is in contact with a heat-generating object (human body). The temperature sensor is close to ambient temperature (within 1°C) before contact.

5.5.3 Experiments with household objects

Figure 5.5 shows the common household objects found in a bathroom from which we collected data. Our objective was to analyze recognition performance for the following task-relevant tactile foreground versus tactile background recognition problems: toothbrush vs. counter; towel vs. towel rack; toilet handle vs. toilet tank; toilet seat vs. toilet tank; and towel vs. bathtub.

Objects in the same bathroom

We used the handheld device to make contact with each of the 8 objects in the same bathroom. We collected 10 trials from 10 different locations on the same object while waiting for 3 minutes between each trial. After collecting the data, for each sensing modality, we subtracted the starting temperature of a trial from all subsequent measurements in the trial. We did this to avoid bias from spatially varying temperatures in the bathroom.

Objects from different bathrooms

We used the handheld device to make contact with each of the 8 objects once each in 10 different bathrooms for a total of 10 trials with each object. Figure 5.2 shows 3.65 s of the sensor data from all trials with different objects. As seen in the figure, the heat-transfer rate is higher for the counter when compared to the toothbrush. Also from the figure we see that the average room temperature measured by the temperature sensor before contact

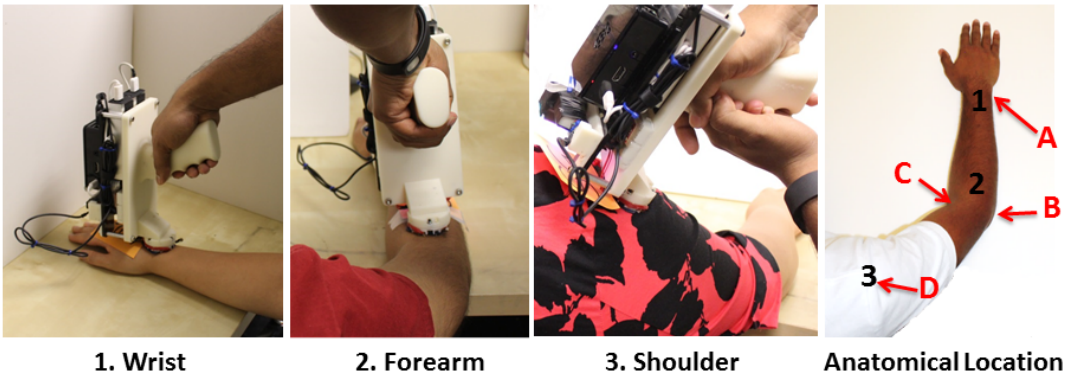

Figure 5.6: *The three images on the left show data collection from three locations on the dominant arm of 3 different participants using the handheld device. The image on the right shows the test locations (black) [1-Wrist, 2-Forearm, 3-Shoulder] and the anatomical key points (red) [A-Triquetral bone, B-Elbow bone, C-Elbow pit, and D-Acromion Scapula].*

varies slightly between trials with toothbrushes and counters potentially due to variations in the temperature of the room while the data was recorded. After contact, the temperature sensor cools slightly for approximately the first 1s of contact before coming to thermal steady state with the object. Before contact the temperature sensor is heated approximately 1°C above the air temperature in the room, potentially due to heat generated in the heat-transfer sensor's heater and other onboard electronics.

5.5.4 Recognition algorithm

For each trial, we truncated the raw time series from the heat-transfer sensor and temperature sensor to include 2000 time samples from time of contact to approximately 3.65s after contact for each modality. To ensure accurate detection of contact, we checked each trial data visually and determined the time instant when contact occurred using the force sensor modality. We then used the same time instant for the thermal modalities in the same trial. Our methods also used estimates of the derivative (slope) of the heat-transfer data with respect to time by taking the first difference of the raw signals and then using a causal filter. The filter was an 8th-order digital low-pass Butterworth filter with Nyquist frequency of 100 Hz and cutoff frequency of 5 Hz.

We then normalized each modality by subtracting the mean and dividing by the variance

across all of the modality's data, after which we vectorized each modality and concatenated the resulting vectors into a single vector. We used a binary support vector machine (SVM) classifier with a linear kernel and 5-fold cross-validation to recognize each object-object and human-object pair.

5.6 Results and Discussion

5.6.1 Results with human participants

Effect of different modalities

Table 5.1 shows the results with different modalities and 30 trials across the human-participants experiment and 80 trials across the objects experiment. Results show that temperature is a valuable modality for distinguishing humans from their surroundings irrespective of location or clothing. This is intuitive as the human body generates heat which can be felt irrespective of clothing.

Effect of contact duration

For these analyses, we varied the duration of contact by truncating the data at different time intervals (0.5 s, 1.0 s, 2.0 s, and 3.65 s) to see how rapidly our algorithm could accurately classify. Table 5.2 shows the results for different contact durations. We chose passive temperature sensing because it gave the best results in Table 5.1. Results show the highest accuracy was with the longest contact duration of 3.65 s, as seen in Table 5.2. However, results with just 0.5 s of contact were above chance (82.13%) showing the potential of these methods for faster discrimination between humans and their surroundings.

5.6.2 Results with objects in the same bathroom

Table 5.3 shows the results for objects in the same bathroom. Using both heat-transfer and temperature sensing gave the best results. For this experiment, we used two different towel

Table 5.1: Human vs. Object recognition.

Tasks		Accuracy with Different Modalities		
		Two Modalities	Single Modality	
		H+T+ Slope of H	H+ Slope of H	T
Brushing Teeth				
Human	Toothbrush	88%	72%	**100%**
Hand on Counter				
Human	Counter	97%	95%	**100%**
Wiping Face				
Human	Towel	95%	75%	**100%**
Flushing Toilet				
Human	Toilet Handle	93%	72%	**100%**
Flushing Toilet				
Human	Toilet Tank	95%	88%	**100%**
Lifting Toilet Seat				
Human	Toilet Seat	95%	88%	**97%**
Taking a Bath				
Human	Bathtub	**93%**	90%	**93%**
Placing a Towel				
Human	Rack	93%	90%	**100%**
Average Performance		93.63%	83.75%	**98.75%**

*H = Heat-Transfer, T = Temperature Sensor Modality

conditions in dry and wet state as seen in Table 5.3. Note that the rack in this bathroom had a rectangular cross-section, thus allowing more contact with the heat-transfer sensor. Table 5.4 shows the effect of contact duration on the recognition problem. Even with just 0.5 s of contact, the accuracy results are good because of less variability in object conditions in the same bathroom, as mentioned above.

5.6.3 Results with objects from different bathrooms

Effect of different modalities

Table 5.5 shows the results with one trial for each object in each bathroom for different modalities thus totaling 80 (10 bathrooms x 8 objects x 1 trial) trials. Results (Table 5.5) show that heat-transfer with temperature sensing gave the best results, thus generalizing

Table 5.2: Human vs. Object recognition : Effect of contact duration.

Tasks		T Modality			
		0.5s	1.0s	2.0s	3.65s
Brushing Teeth					
Human	Toothbrush	80%	97%	97%	**100%**
Hand on Counter					
Human	Counter	85%	93%	97%	**100%**
Wiping Face					
Human	Towel	78%	97%	97%	**100%**
Flushing Toilet					
Human	Toilet Handle	85%	90%	97%	**100%**
Flushing Toilet					
Human	Toilet Tank	90%	90%	93%	**100%**
Lifting Toilet Seat					
Human	Toilet Seat	82%	93%	93%	**97%**
Taking a Bath					
Human	Bathtub	82%	88%	88%	**93%**
Placing a Towel					
Human	Rack	75%	97%	97%	**100%**
Average Performance		82.13%	93.13%	94.88%	**98.75%**

Table 5.3: Object recognition : Generalization to new locations.

Task Relevant Scenarios	Accuracy with Different Modalities		
	Two Modalities	Single Modality	
	H+T+ Slope of H	H+ Slope of H	T
Toothbrush on Counter	**95%**	90%	**95%**
Dry Towel on Rack	**100%**	**100%**	65%
Wet Towel on Rack	**100%**	**100%**	**100%**
Toilet Handle on Toilet Tank	**85%**	80%	**85%**
Toilet Seat on Toilet Tank	**75%**	65%	60%
Dry Towel on Bathtub	**95%**	**95%**	60%
Wet Towel on Bathtub	**95%**	**95%**	90%
Average Performance	**92.14%**	89.29%	79.29%

to different objects / bathrooms. Results in Table 5.5 are worse when compared with the results in Table 5.3 because 10 trials were taken from 10 different toothbrushes, counters, towels etc. that may be different in each of the 10 bathrooms. Results with towel and

Table 5.4: Object recognition : Effect of contact duration on generalization to new locations.

Task Relevant Scenarios	H+T+Slope of H Modalities			
	0.5s	1.0s	2.0s	3.65s
Toothbrush on Counter	90%	90%	**95%**	**95%**
Dry Towel on Rack	95%	**100%**	**100%**	**100%**
Wet Towel on Rack	95%	**100%**	**100%**	**100%**
Toilet Handle on Toilet Tank	65%	75%	**90%**	85%
Toilet Seat on Toilet Tank	75%	**90%**	**90%**	75%
Dry Towel on Bathtub	90%	90%	**95%**	**95%**
Wet Towel on Bathtub	80%	**95%**	90%	**95%**
Average Performance	84.29%	91.43%	**94.29%**	92.14%

rack are low, possibly because racks varied with rectangular and circular cross-sections which affects the contact area with the heat-transfer sensor. Segregating the data with the rectangular rack, which allows more contact area with the heat-transfer sensor, resulted in 93% accuracy for towel-rack recognition with heat-transfer and temperature data.

Effect of contact duration

Table 5.6 shows the results for different contact duration of 0.5 s, 1.0 s, 2.0 s, and 3.65 s. We used both the heat-transfer and temperature data because it gave the best overall results shown in Table 5.5. Our methods achieved highest accuracy with the longest contact duration of 3.65 s as seen in Table 5.6. With a duration of 1.0 s, the accuracies are high except for recognition of towel vs. rack, due to different shapes of cross-sections of racks (See Section 5.6.3). Recognition of towel vs. bathtub in such short intervals is also low, probably due to different wet and dry towel conditions.

Table 5.5: Object recognition : Generalization to new environments.

Task Relevant Scenarios	Accuracy with Different Modalities		
	Two Modalities	Single Modality	
	H+T+ Slope of H	H+ Slope of H	T
Toothbrush on Counter	**90%**	85%	70%
Towel on Rack	**65%**	**65%**	55%
Toilet Handle on Toilet Tank	**95%**	**95%**	55%
Toilet Seat on Toilet Tank	**80%**	60%	35%
Towel on Bathtub	**90%**	75%	55%
Average Performance	**84%**	76%	54%

Table 5.6: Object recognition : Effect of contact duration on generalization to new environments.

Task Relevant Scenarios	H+T+Slope of H Modalities			
	0.5s	1.0s	2.0s	3.65s
Toothbrush on Counter	70%	80%	85%	**90%**
Towel on Rack	55%	50%	60%	**65%**
Toilet Handle on Toilet Tank	75%	90%	90%	**95%**
Toilet Seat on Toilet Tank	70%	75%	75%	**80%**
Towel on Bathtub	55%	60%	70%	**90%**
Average Performance	65%	71%	76%	**84%**

5.6.4 Discussion

Throughout this paper, we have referred to the actively heated sensor as the heat-transfer sensor. However, both thermal sensors rely on heat transfer. For example, the unheated temperature sensor is cooler than the human body, resulting in a distinctive signal due to heat transfer from the human body to the sensor.

We conducted our research with robots in mind. We expect our results to be relevant to robots that operate in close proximity to people and manipulate objects, such as assistive robots. However, other devices could potentially use similar methods to sense their surroundings and human interaction. For robots, a number of open questions remain. For example, more varied conditions associated with a task might degrade performance. During

real-world use, we would expect greater variability in applied force, contact area, relative orientation of the sensor to the object's surface, reheat times, and other characteristics. Nonetheless, we expect data-driven thermal recognition to still be useful, given the strong performance of object vs. object classification when in a single environment and human vs. object classification.

5.7 Conclusions

We investigated data-driven thermal recognition of contact with people and objects. Using a portable handheld data acquisition device, we collected data from 3 different locations on the arms of 10 different human participants, and from 8 types of task-relevant objects found in 10 residential bathrooms. We implemented SVMs to distinguish between contact with humans and objects, and between task-relevant object pairs. In our tests, classifying contact as people versus object worked well with temperature sensing alone in spite of clothing, individual variation, and different locations on the arm. Classifying contact into two task-relevant object types worked well when restricted to a particular bathroom. Heat-transfer sensing and temperature sensing had complementary value for this type of recognition problem. Recognition performed using both modalities outperformed recognition performed with either modality alone. Classifying contact in a new bathroom based on training data only from other bathrooms did not work as well. However, the classifiers did generalize to new bathrooms to some extent, as evidenced by their improved performance with longer contact duration.

CHAPTER 6
A MODEL TO ESTIMATE MATERIAL RECOGNITION PERFORMANCE USING THERMAL SENSING

6.1 Research Summary

We demonstrate the feasibility of using heat-transfer based sensing for material recognition across a wide range of materials. We use a physics-based model with a statistical method to estimate the material recognition performance when a heated sensor touches two materials with flat surfaces. We used a semi-infinite solid based model for modeling the time-dependent heat transfer process. We added gaussian noise in the model and modeled the resulting time-series as a gaussian process. We developed a statistical method to calculate the F1-score of the binary material recognition performance given the sensor and material thermal properties. Using our model, we also analyzed the effect of variability in the initial temperature of the sensor, sensor and object thermal properties on the material recognition performance. We performed experiments with the simulated heat-transfer data from all 69 materials in the CES Edupack Level-1 Database [92] and predicted their binary material recognition performance for all different material combinations resulting in a total of 2346 comparisons. We then compared these results with the results obtained using Support Vector Machines (SVMs). Our model's predictions matched the SVM performance with 96% accuracy. Finally, we selected 12 representative real-world materials and performed real-world experiments with a robot and a heat-transfer sensor module touching the material samples. We identified the sensor and material thermal parameters using a system identification procedure and then predicted the material recognition performance (66 binary comparisons) using our physics-based model and statistical method. We compared the results with results obtained using SVMs with the real-world data. Our model

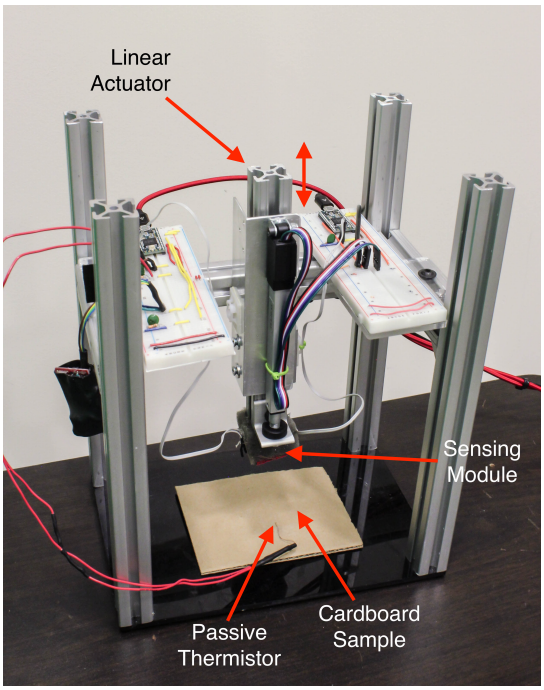

Figure 6.1: *A 1-DoF Robot with an active thermal sensing module reaching to touch a cardboard material sample*

successfully predicted the real-world results with 92% accuracy for fixed initial conditions and 91% accuracy for varied initial conditions.

6.2 Introduction

Material recognition using thermal sensing is relatively unexplored in robotics when compared with other haptic sensing modalities such as force sensing. However, different materials have different thermal properties [165] and it remains to be seen how robots can use this sensing modality to differentiate between different materials. Knowing the material when a robot touches an object can help in devising intelligent manipulation strategies in cluttered and uncertain environments as well as in assistive scenarios. For example, a robot might come in contact with a bed or a mattress while assisting a disabled person lying on bed. Knowing that the object in contact is 'wood' might help the robot infer that it is in contact with the bed frame instead of the human body or the mattress and thus, the robot might want to avoid it.

Previously, we have shown the relevance of recognizing 'tactile foreground' vs. 'tactile background' for task-specific manipulation tasks [181], where 'tactile foreground' is the target object and 'tactile background' is any other object in its vicinity that the robot might come in contact with during the manipulation task. This involves the robot touching two objects made of different materials. In this paper, we focus on binary material recognition tasks for various combinations of material comparisons. For each of these binary material comparisons, our objective is to analyze how well the robot can recognize these two materials using the thermal sensing modality.

For this paper, we focus on heat-transfer based thermal sensing, where we have a tactile sensor with a heating element and a temperature sensor touch an object. We call this 'active' thermal sensing modality compared to 'passive' thermal sensing which is just a temperature sensor touching an object to measure its temperature. During active thermal sensing, when the tactile sensor, which is heated above room temperature, comes in contact with an object at room temperature, heat transfers away from the sensor into the object. This heat-transfer is dependent on the sensor and object thermal properties, the initial temperature conditions of the sensor and the object, as well as the noise due to various sensor and environmental conditions. A robot could potentially use the difference in this heat transfer for different materials to distinguish them. Figure 6.1 shows a 1-DoF robot with an active sensor module reaching to touch a cardboard material sample.

We developed a physics-based model using a semi-infinite solid assumption for modeling heat-transfer from the heated sensor to the object. We added gaussian i.i.d noise to model the effect of noise. This model can account for the variability in the initial conditions of the sensor and the object, the sensor and object thermal properties, as well as noise. Using this model, we can generate simulated time-series heat-transfer data given sensor and object parameters as well as their initial temperature conditions. We modeled this time-series as gaussian process and developed a statistical method to calculate the F1-score of the material recognition performance. Using this model and the statistical method,

we analyzed the effect of material thermal effusivities, initial temperatures, and noise on the material recognition performance. We also estimated the binary material recognition performance for all materials in the CES Edupack Level-1 Database [92] resulting in a total of 2346 binary material recognition tasks and compared the results with that of Support Vector Machines (SVMs). We also collected data from 12 real-world representative materials using a 1-DOF robot with a linear actuator and a tactile sensor attached at its end. We estimated their material recognition performance (66 binary comparisons) using the identified parameters from the real-world data, the physics-based model and the statistical method. Our objective is to see if our model can predict the results obtained using SVMs.

6.3 Related Work

6.3.1 Passive Thermal Sensing

A passive thermal sensor detects the temperature of a target object without introducing additional heat transfer. Related work on passive thermal sensors are more hardware-centric with limited applications in material detection. In this section, we will discuss both contact based and non-contact based passive thermal sensors.

Contact Based Sensors

Researchers used different types of contact based thermal sensors to develop passive sensing devices. Contact based thermal sensors fall into three main categories: Resistance Temperature Detectors (RTDs), Thermistors and Thermocouples. RTDs and Thermistors measure temperature by the fact that the resistance of some materials changes as temperature changes. Thermocouples function by the Seebeck Effect [182], which states that the difference between temperatures of two electric junctions in a thermoelectric device creates a voltage. Of the three types of thermal sensors, thermocouples have the widest operating range of -200°C to 2000°C, with relatively low accuracy. RTDs have a high accuracy of

0.03°C with relatively long response time. Compared with RTDs, thermistors have a lower accuracy of 0.1°C but give faster thermal responses [183].

Many researchers [19, 140, 184–189] developed arrays of combined thermal and tactile sensors using RTDs and thermistors. Someya et al. [185] developed a flexible artificial electronic skin with a network of pressure and thermal sensors using organic diodes. They pointed out that the network can be applied on robot fingers, but they did not mention its application on material recognition. Ma et al. [189] fabricated a flexible thermal sensor array using Nickel-based RTDs to detect dynamic wave flow in hydrodynamic experiments. Bayindir et al. [190] developed a fiber device for large area thermal sensing, using long fiber thermistors that can sense heat along its entire length and generates electrical signal in response.

Non-Contact Based Sensors

An alternative type of passive thermal sensor is non-contact based, which detects the radiated energy out of the target object by applying the Plank's Law of Radiation. By avoiding contact, such sensors have the advantage of real-time non-destructive measurement. A common type of non-contact based thermal sensor is infrared thermal camera. Many researchers study complex heat transfer problems by taking the advantage of infrared thermal cameras [191–193]. Sarro et al. [194] developed an infrared thermal sensing linear array based on integrated silicon thermopiles, and Schaufelbhl et al. [195] fabricated a thermal imager consisting of a 10×10 array of infrared sensors. Both claim that their own designs have the advantage of low cost, low crosstalk and high yield, and can be applied to monochromatic radiation sensing.

In summary, studies on passive thermal sensing focus on the fabrication process of sensing hardware, with limited evaluation for inferring thermal properties of materials or objects.

6.3.2 Active Thermal Sensing

Active thermal sensors have a heating element to heat up the sensor above room temperature and a thermistor to measure the response over time. Thus, on contact with an object at room temperature, there is heat transfer away from the sensor into the object.

Contact Based Sensors

a. RTDs and Thermistors Many researchers use thermistors and RTDs to develop integrated thermal and tactile sensing systems [135, 136, 138, 139, 144, 145, 148, 175, 196–201]. Russell [135] developed an array of thermistors, with which he compared the percent decrease of different materials from a uniform initial temperature after 3 seconds of contact. The array is able to recognize six different materials in a single trial. Instead of comparing temperature at a specific time, our work compare the entire time series of temperature. Siegel et al. [136] developed an integrated tactile and thermal sensor, and compared the response of the thermistor on touching wood, nylon and steel over a 50 second period, with the initial temperature maintained by the heat generated by current flow on the conductive paint. However, Siegel et al.'s work does not involve any machine learning algorithm; material recognition is achieved by matching the sensor's response with existing library of response curves.

Engel et al. [138, 139] developed flexible multimodal tactile sensing systems with gold heaters and nickle RTDs. With consistent initial conditions and based on the combined pressure and temperature sensing, their system successfully recognized 5 materials with 90% accuracy over 50 trials and unreported contact duration. Takamuku et al. [148] developed an anthropomorphic finger with 3 strain gauges, 4 thermistors and a heating element arranged in a layered format. They used the outputs of thermal and tactile sensors to classify 5 different materials.

In the study of material recognition, some researchers use the SynTouch BioTAC sensor. The SynTouch BioTAC sensor is a multimodal tactile sensor which uses thermistors

for thermal sensing [202]. Xu et al. [146] used the BioTAC sensor to measure the temperature derivative and other multimodal sensor data during 15 s of contact. They used Bayesian Exploration and Reinforcement Learning techniques to identify 10 objects with 99% accuracy using the data. McMahon et al. [147] used the BioTAC sensor on PR2 robots to get the haptics data with each trial approximately 80 s. They then used HMMs to automatically assign adjectives to the collected haptic signals. Kerr et al. [149] used the BioTAC sensor to record the thermal response data of 6 material groups with varying thermal properties for 20 s with 15 trials. They used the derivative of the temperature (TAC) as well as the dynamic thermal conductivity (TDC) data and got 73% accuracy with the ANN they implemented.

b. Thermocouples Of the three types of contact-based thermal sensors, thermocouples have faster response, wide range but relatively low accuracy [183]. Monkman and Taylor [137] developed a method of using the response drive current of the thermocouple in performing material recognition, which they reported to be faster than Russell [135]'s and Siegel et al. [136]'s. They evaluated the sensor by the recognition of four materials with distinct thermal properties under consistent initial conditions. Their figure of sensor readings over time of a single trial suggests that the recognition of the four materials could potentially be performed more quickly (between 0 and 3 s), but they did not report specific results.

Caldwell and Gray [143] developed a method of using the response output voltage of thermocouple in material recognition, while maintaining the temperature of the sensor at 40 $\pm$ 0.5 °C. They collected the data of testing 7 typical materials 20 trials each, and showed a graph of the probability densities of the 7 materials on steady-state thermocouple output voltage. However, they did not apply the sensor data to any classifier algorithm to get the performance of this method on material recognition. Caldwell et al. [203] also proposed a multi-functional tactile sensor, in which they used thermocouple to acquire temperature

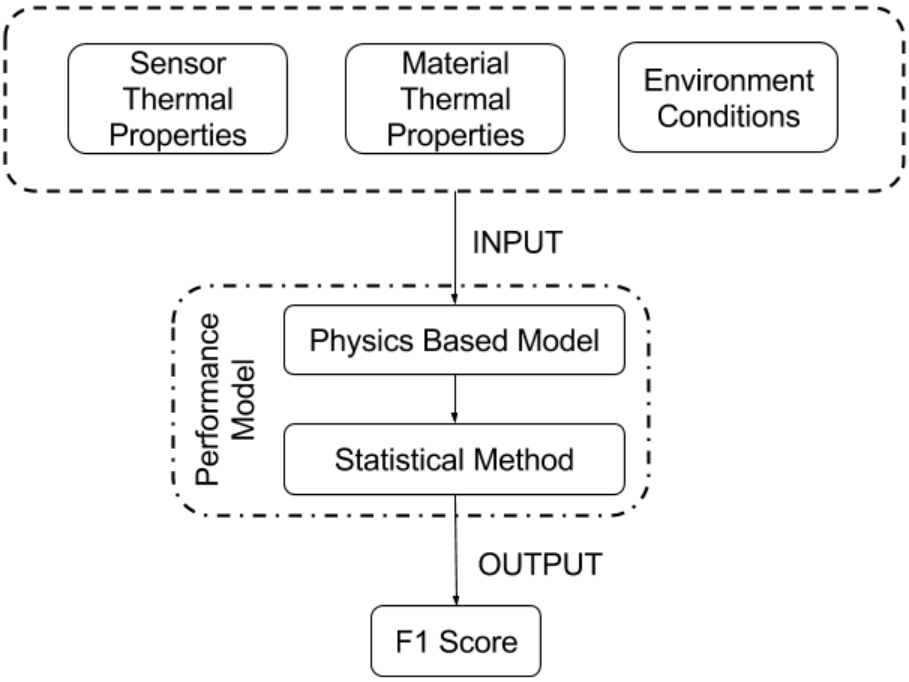

Figure 6.2: *Schematic of our Performance model*

gradient information through induced output voltage. They reported high accuracy for classifying 5 materials using the thermal sensing modality, but they did not report the specific classification method used.

Jackson W. proposed a paper sensing system that identifies physical properties of papers. The system includes a heater and two thermocouples for the purpose of detecting the thermal diffusivity of different papers. [204]. Shao et al. [205] developed a tactile sensation measurement system, using thermocouples in the thermal module. The system served to quantify human sensory perceptions by studying the correlation of collected sensor data and human subject self report. A similar attempt to quantify human haptic perception [206] also uses thermocouples to simulate human contact of materials and register the thermal process.

6.3.3 Non-Contact Based Sensors

Though not often used in material recognition, non-contact based thermal sensors also have application in active thermal sensing. An example is the method of Infrared Non-

destructive Testing (IRNDT) [207] to find defects in laminar materials. The method injects controlled thermal energy into the test sample, and uses infrared cameras to observe the response. Mulaveesala et al. [208] applied different non-stationary thermal excitation schemes to perform IRNDT on fiber-reinforced plastic materials. VanDamme et al. [209] performed IRNDT on different laminate materials and electric circuits to detect flaws using infrared lamp and low-power CO_2 laser heat source.

In summary, related studies on material detection from active thermal sensing did material recognition on a small set of materials using contact-based active thermal sensors and specific machine learning algorithms. However, none of them developed a generalized model that is able to evaluate the expected recognition performance of a given active thermal sensor with a specific thermal property for recognizing two materials.

6.4 A Model for Performance Estimation

In our attempt to better understand material recognition using thermal sensing, we derived a performance model that, given a set of sensor and environmental conditions, evaluates the expected performance of the material recognition task. In general, our model calculates the probability of successfully distinguishing two materials, given sensor and environment conditions.

Figure 6.2 shows our approach for the performance model. It consists of a physics-based model [165] that takes sensor and material thermal properties as well as environment conditions as inputs and outputs a time-series heat-transfer data. This heat-transfer data is then fed into a statistical method which helps quantify the difference between the heat-transfer data from two materials. We express this difference in terms of F1-score values.

We evaluate our performance model using a three-part evaluation. First we compare the prediction of our performance model with the performance of SVM, which is a widely used data-driven algorithm, in classifying simulated sensor time-series data for two different thermal effusivities. We use a wide range of thermal effusivities to compare the perfor-

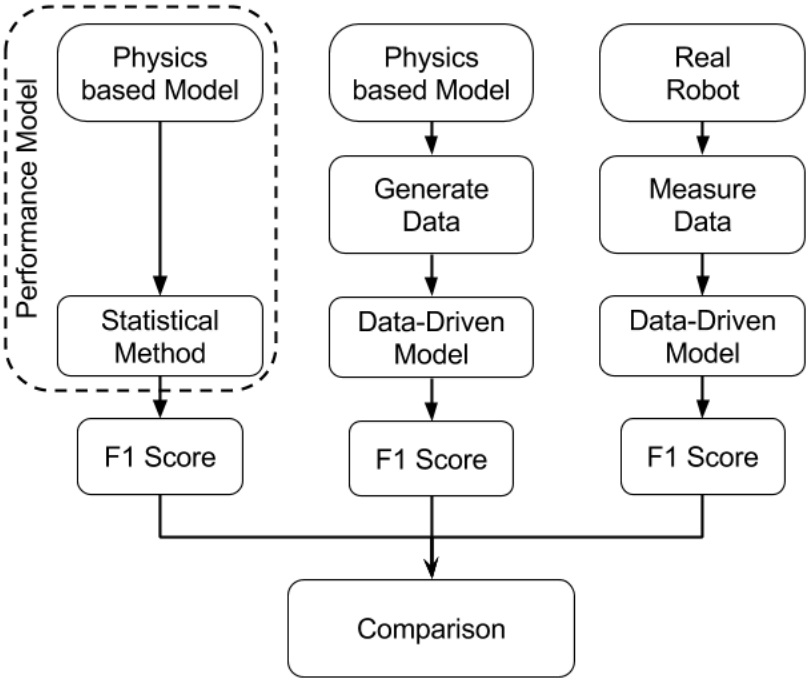

Figure 6.3: *Evaluation of our Performance Model.*

mance and analyze the effect of noise and sensor initial condition on the performance.

Second, we compare the prediction of the performance model in binary material recognition tasks for simulated time-series heat-transfer data from all materials in the CES-Edupack Level 1 Database [92] with that of SVM under consistent sensor initial conditions.

Third, we compare the prediction of the performance model in binary material recognition tasks for real-world time-series heat-transfer data collected using a 1-DoF robot from 12 different materials under both consistent and varied sensor initial conditions.

We use F_1 Scores as a metric to compare the performances for all three cases. Figure 6.3 shows a schematic of the evaluation method.

6.5 Physics-based Model

Here we present the physics model that help us understand the heat transfer process between a heated sensor and a material.

6.5.1 Semi-infinite Solid Model

A semi-infinite solid is an idealized body in which a temperature change in any part of the body is due to thermal conditions on a single surface [154]. [154] has modeled a finger touching a material as a contact between two semi-infinite bodies. In an analogous manner, we modeled the heat transfer process between a heated thermal sensor and a block of material as heat conduction between two semi-infinite solids [142, 154]. Fig. 6.4 shows the diagram that represents this model.

In the model, we first assume that the initial temperature of the object body, $T_{obj(t=0)}$, is equal to the ambient temperature, T_{amb}. The initial temperature of the sensor body, $T_{sens}(t=0)$, is higher than T_{amb}.

Once the sensor body comes into contact with the object body, heat begins to transfer from the sensor to the object, resulting in temperature change over time. In the sensor body, let x be the distance of the thermistor from the contact surface (Fig. 6.4). The contact surface at $x=0$ has a temperature T_{surf} that remains constant and is given by

$$\begin{aligned} T_{surf} &= \frac{(T_{sens}(t=0)e_{sens} + T_{obj}(t=0)e_{obj})}{(e_{sens}+e_{obj})} \\ where \quad e_{sens} &= \frac{k_{sens}}{\sqrt{\alpha_{sens}}} \quad and \quad e_{obj} = \frac{k_{obj}}{\sqrt{\alpha_{obj}}} \end{aligned} \tag{6.1}$$

where α_{obj} and k_{obj} are the coefficients of thermal diffusivity and thermal conductivity of the object body, and α_{sens} and k_{sens} are the coefficients of thermal diffusivity and thermal conductivity of the sensor body. Given $T_{sens}(t=0)$ and T_{surf}, we can find the temperature in the sensor body at any time, $t \geq 0$, using the following partial differential equation from [154]:

$$\frac{\partial^2 T_{sens}}{\partial x^2} = \frac{1}{\alpha_{sens}} \frac{\partial T_{sens}}{\partial t} \tag{6.2}$$

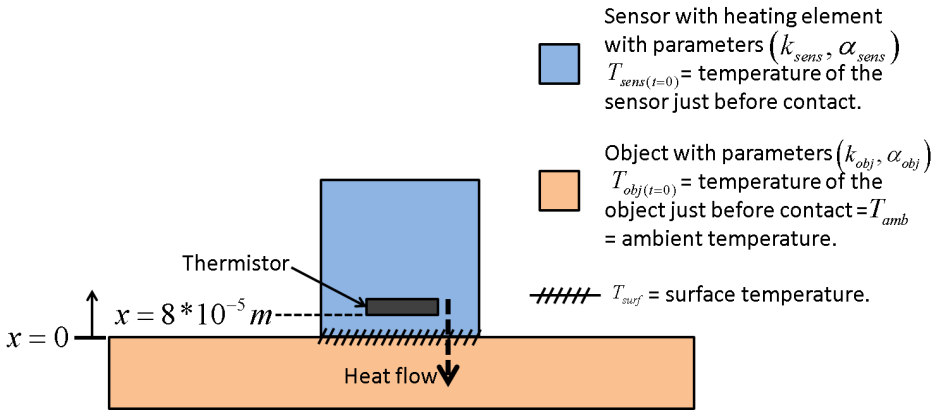

Figure 6.4: *Diagram representing our model of the sensor in contact with a material. We model both the sensor and the material as semi-infinite solids.*

where $T_{sens}(x,t)$ is the temperature at time t of the sensor body at distance x from the contact surface. The thermistor, which is inside the sensor body, measures the temperature at $x = 8 * 10^{-5}$ (obtained from manufacturer) as shown in Fig. 6.4. Using the boundary conditions, $T_{sens}(x = 0, t) = T_{surf}$ and $T_{sens}(x, t = 0) = T_{sens}(t = 0)$, we can solve for $T_{sens}(x,t)$.

$$T_{sens}(x,t) = T_{sens}(t=0) + (T_{surf} - T_{sens}(t=0)) \times erfc\left(\frac{x}{2\sqrt{\alpha_{sens} t}}\right) \tag{6.3}$$

where $erfc$ is the complimentary error function given by

$$erfc(z) = \frac{2}{\sqrt{\pi}} \int_z^\infty e^{-r^2} dr \tag{6.4}$$

With the physics based model we can predict the sensor readings, $T_{sens}(x = 8 \times 10^{-5}, t)$, that would result from the heat-transfer-based tactile sensor coming into contact with a material with thermal effusivity e_{obj}.

6.5.2 Noise Model

Note that during each temperature measurement, the measurement of the sensor also includes noise and other sources of uncertainty. In order to account for the noise and uncertainty in sensor reading, we introduce an additive Gaussian noise, Z_i, with zero mean and variance σ^2 to each temperature measurement. The underlying assumption is that, the deviation of each sensor reading from the actual sensor temperature, caused by the uncertainty due to sensor and environment conditions, can be modeled as an independent normal random variable.

With noise taken into consideration, the complete sensor model is given by

$$\begin{aligned} T_{sens}\left(x,t\right) = T_{sens}(t=0) + \left(T_{surf} - T_{sens}(t=0)\right) \\ *erfc\left(\frac{x}{2\sqrt{\alpha_{sens}t}}\right) + Z \sim \mathcal{N}\left(0,\sigma^2\right) \end{aligned} \tag{6.5}$$

This modified model can help us analyze the effect of noise on the performance of material recognition.

6.6 Statistical Method

In this section, we derive a performance model to evaluate a given sensor under specific environmental conditions and noise.

6.6.1 Gaussian Process

In order to account for the effect of noise, we introduce the concept of Gaussian Process (GP). In a Gaussian process, every point in some continuous input space is associated with a normally distributed random variable [210]. In our case, the continuous domain is time, and at any time instant, the associated normal random variable is the noisy sensor reading at that instant. Moreover, every finite collection of those random variables has a multivariate

normal distribution. The distribution of a Gaussian process is the joint distribution of all those (infinitely many) random variables, and as such, it is a distribution over functions in a continuous domain [210].

In our model, let T_{sens} be the random function (given by eq. 6.5, with x fixed) from which every observation $T_{sens}(t_i)$ can be sampled. We have

$$T_{sens}(t_i) = f(t_i) + \epsilon_i \sim i.i.d. \mathcal{N}\left(0, \sigma^2\right) \tag{6.6}$$

where $f(t)$ is the mean function (given by eq. 6.3) and ϵ_i is a random normal variable.

Thus, we can express T_{sens} as Gaussian process $GP(f, K)$, meaning the random function T_{sens} is distributed as a GP with mean function f and covariance function K [211]. The covariance for any two given samples is given by K as

$$\begin{aligned}
&K(T_{sens}(t_i), T_{sens}(t_j)) \\
&= COV(T_{sens}(t_i), T_{sens}(t_j)) \\
&= \mathbb{E}\big[T_{sens}(t_i) - \mathbb{E}[T_{sens}(t_i)]\big] * \\
&\quad \mathbb{E}\big[T_{sens}(t_j) - \mathbb{E}[T_{sens}(t_j)]\big] \\
&= \mathbb{E}\big[f(t_i) + \epsilon_i - f(t_i)\big] * \\
&\quad \mathbb{E}\big[f(t_j) + \epsilon_j - f(t_j)\big] \\
&= \mathbb{E}\big[\epsilon_i\big]\mathbb{E}\big[\epsilon_j\big]
\end{aligned} \tag{6.7}$$

Since $\epsilon_i, \epsilon_j \sim i.i.d. \mathcal{N}(0, \sigma^2)$,

$$K(T_{sens}(t_i), T_{sens}(t_j)) = \mathbb{E}\big[\epsilon_i \epsilon_j\big] \tag{6.8}$$

6.6.2 Multivariate Normal Distribution

The multivariate normal distribution $\boldsymbol{\mathcal{N}}(\boldsymbol{\mu}, \boldsymbol{\Sigma})$ is a generalization of the one-dimensional (univariate) normal distribution to higher dimensions, given as

$$P(\boldsymbol{x}|\boldsymbol{\mu}, \boldsymbol{\Sigma}) = \frac{1}{\sqrt{(2\pi)^n|\boldsymbol{\Sigma}|}} \exp\left(-\frac{1}{2}(\boldsymbol{x}-\boldsymbol{\mu})^T\boldsymbol{\Sigma}^{-1}(\boldsymbol{x}-\boldsymbol{\mu})\right) \tag{6.9}$$

where $\boldsymbol{x}$ is an n dimensional random vector, $\boldsymbol{\mu}$ is the n dimensional mean vector given by $\mathbb{E}\big[\boldsymbol{x}\big] = \{f(t_i)|i \in (1, n)\}$ (f being the mean function), and $\boldsymbol{\Sigma}$ is the $n \times n$ covariance matrix.

Every set of finite samples $\boldsymbol{x} = \{T_{sens}(t_i)|i \in (1, n)\}$ drawn from $T_{sens} = GP(f, K)$ can be viewed as a random vector corresponded to a multivariate normal distribution, meaning we can calculate the probability of observing a specific random vector $\boldsymbol{x}$ given prior knowledge of the mean function and the covariance matrix.

Further more, the covariance function K is a spherical covariance matrix for the random vector $\boldsymbol{x}$:

$$\boldsymbol{\Sigma}_{ij} = \mathbb{E}\big[\epsilon_i\epsilon_j\big] = \begin{cases} \sigma^2 & i = j \\ 0 & i \neq j \end{cases} \tag{6.10}$$

As a result, $\boldsymbol{\Sigma}$ is a diagonal matrix in which the main diagonal entries are all σ^2. Thus, we have the determinant of $\boldsymbol{\Sigma}$ equal to the product of all main diagonal entries

$$|\boldsymbol{\Sigma}| = (\sigma^2)^n \tag{6.11}$$

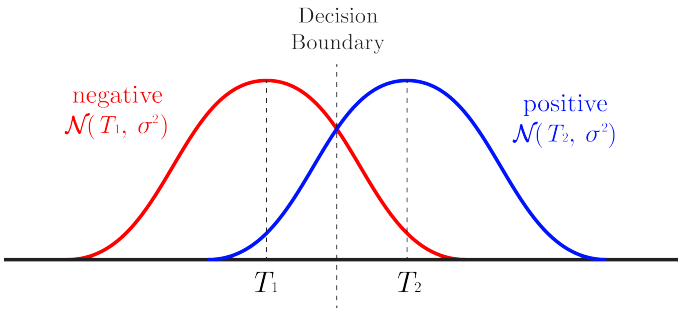

Figure 6.5: *Gaussian Decision Boundary illustrated in 1 Dimension*

Rewriting the probability distribution function, we have

$$P(\boldsymbol{x}|\boldsymbol{\mu}, \boldsymbol{\Sigma}) = \frac{1}{\sqrt{(2\pi\sigma^2)^n}} \exp\left(-\frac{1}{2}(\boldsymbol{x}-\boldsymbol{\mu})^T(\boldsymbol{x}-\boldsymbol{\mu})/\sigma^2\right) \tag{6.12}$$

The above equation represents the probability distribution of observed measured time series $\boldsymbol{x}$, given the mean vector $\boldsymbol{\mu}$ and covariance matrix $\boldsymbol{\Sigma}$ associated with the underlying Gaussian process $T_{sens} = GP(f, K)$.

6.6.3 F_1 Score and F_1 Score Matrix

We determine whether a given material pair is distinguishable by modeling the performance of a binary classifier given a random time series sample from the underlying multivariate normal distribution associated with each of the two materials. In other words, if the labeling accuracy of the binary classifier is higher than a certain threshold, we decide that the material pair is distinguishable. For consistency, we use F_1 Score as the accuracy measurement and 0.9 as the threshold.

We model the decision process of binary classifiers with a Gaussian decision boundary. Consider two underlying distributions of random vector variables (time series) $\boldsymbol{\mathcal{N}}(\boldsymbol{T}_1, \boldsymbol{\Sigma})$ and $\boldsymbol{\mathcal{N}}(\boldsymbol{T}_2, \boldsymbol{\Sigma})$ each associated with a material. At any instant, we obtain a sensor measured time series vector $\boldsymbol{x}'$, and we want to label it with its corresponding material la-

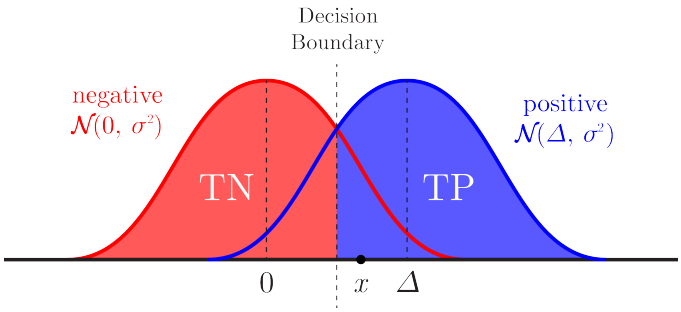

Figure 6.6: *True Negative Rate and True Positive Rate*

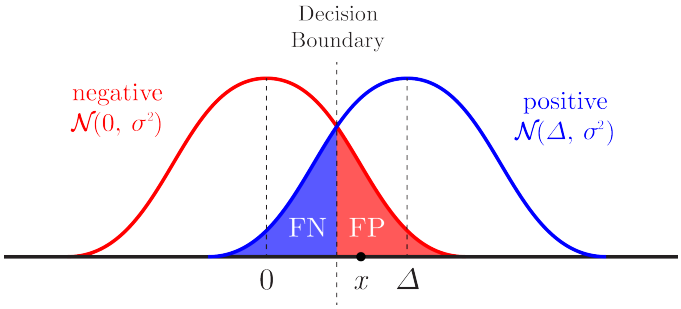

Figure 6.7: *False Negative Rate and False Positive Rate*

bel. Since we actually do not know which material the sensor is currently in contact with, we naively label $\boldsymbol{x}'$ with the more probable distribution by comparing $P(\boldsymbol{x}'|\boldsymbol{T}_1, \boldsymbol{\Sigma})$ and $P(\boldsymbol{x}'|\boldsymbol{T}_2, \boldsymbol{\Sigma})$, and assign the more probable label. This leads to the formation of a decision boundary as illustrated in Fig. 6.5, which is a hyperplane in the n dimensional space associated with the two distributions. To simplify the calculation, we translate both distributions by $-\boldsymbol{T}_1$, and define $\boldsymbol{x} = \boldsymbol{x}' - \boldsymbol{T}_1$, $\boldsymbol{\Delta} = \boldsymbol{T}_2 - \boldsymbol{T}_1$.

We can then express the translated distributions as $\boldsymbol{\mathcal{N}}(\boldsymbol{0}, \boldsymbol{\Sigma}) = \boldsymbol{\mathcal{N}}(\boldsymbol{T}_1 - \boldsymbol{T}_1, \boldsymbol{\Sigma})$ and $\boldsymbol{\mathcal{N}}(\boldsymbol{\Delta}, \boldsymbol{\Sigma}) = \boldsymbol{\mathcal{N}}(\boldsymbol{T}_2 - \boldsymbol{T}_1, \boldsymbol{\Sigma})$. As a result, $P(\boldsymbol{x}'|\boldsymbol{T}_1, \boldsymbol{\Sigma}) = P(\boldsymbol{x}|\boldsymbol{0}, \boldsymbol{\Sigma})$, and $P(\boldsymbol{x}'|\boldsymbol{T}_2, \boldsymbol{\Sigma}) = P(\boldsymbol{x}|\boldsymbol{\Delta}, \boldsymbol{\Sigma})$. We can calculate the likelihood of the measured time series belonging to each distribution using the translated distributions and get the same result.

To derive an expression of F_1 Score specific to our model, we start from the definition

$$F_1 = \frac{2TP}{2TP + FN + FP} \tag{6.13}$$

where 'TP' is the true positive rate, 'FP' is the false positive rate, and 'FN' is the false negative rate. Let $\boldsymbol{\Delta}$ be the positive label and $\mathbf{0}$ be the negative label. Then, we can define true positive rate as, the probability of assigning a positive label to a sample that belongs to the positive distribution $\boldsymbol{\mathcal{N}}(\boldsymbol{\Delta}, \boldsymbol{\Sigma})$. As illustrated in Fig. 6.6, all samples that belong to $\boldsymbol{\mathcal{N}}(\boldsymbol{\Delta}, \boldsymbol{\Sigma})$ and fall on the right side of the decision boundary, in other words, closer to the $\boldsymbol{\mathcal{N}}(\boldsymbol{\Delta}, \boldsymbol{\Sigma})$ distribution, will be correctly labeled positive. This proximity, as we will elaborate later, can be measured using the Mahalanobis Distance [212].

We then define the mathematical expression for true positive rate, false negative rate, true negative rate, and false positive rate as follows,

$$\begin{aligned}
TP &= P\Big[P(\boldsymbol{x}|\mathbf{0}, \boldsymbol{\Sigma}) < P(\boldsymbol{x}|\boldsymbol{\Delta}, \boldsymbol{\Sigma})\Big|\boldsymbol{x} \sim \boldsymbol{\mathcal{N}}(\boldsymbol{\Delta}, \boldsymbol{\Sigma})\Big] \\
FN &= P\Big[P(\boldsymbol{x}|\mathbf{0}, \boldsymbol{\Sigma}) > P(\boldsymbol{x}|\boldsymbol{\Delta}, \boldsymbol{\Sigma})\Big|\boldsymbol{x} \sim \boldsymbol{\mathcal{N}}(\boldsymbol{\Delta}, \boldsymbol{\Sigma})\Big] \\
TN &= P\Big[P(\boldsymbol{x}|\mathbf{0}, \boldsymbol{\Sigma}) > P(\boldsymbol{x}|\boldsymbol{\Delta}, \boldsymbol{\Sigma})\Big|\boldsymbol{x} \sim \boldsymbol{\mathcal{N}}(\mathbf{0}, \boldsymbol{\Sigma})\Big] \\
FP &= P\Big[P(\boldsymbol{x}|\mathbf{0}, \boldsymbol{\Sigma}) < P(\boldsymbol{x}|\boldsymbol{\Delta}, \boldsymbol{\Sigma})\Big|\boldsymbol{x} \sim \boldsymbol{\mathcal{N}}(\mathbf{0}, \boldsymbol{\Sigma})\Big]
\end{aligned} \tag{6.14}$$

Note, the two distributions $\boldsymbol{\mathcal{N}}(\mathbf{0}, \boldsymbol{\Sigma})$ and $\boldsymbol{\mathcal{N}}(\boldsymbol{\Delta}, \boldsymbol{\Sigma})$ have identical spherical covariance matrix, so we have $TP = TN$, and $FN = FP$. Therefore, the expression for F_1 Score can be simplified as follows

$$\begin{aligned}
F_1 &= \frac{2TP}{2TP + FN + FP} \\
&= \frac{TP}{TP + FN} \\
&= TP/1 = 1 - FP
\end{aligned} \tag{6.15}$$

Now we derive the expression for FP, where we assume $\boldsymbol{x} \sim \boldsymbol{\mathcal{N}}(\mathbf{0}, \boldsymbol{\Sigma})$

$$FP = P\Big[P(\boldsymbol{x}|\mathbf{0}, \boldsymbol{\Sigma}) < P(\boldsymbol{x}|\boldsymbol{\Delta}, \boldsymbol{\Sigma})\Big] \tag{6.16}$$

Using the Square of Mahalanobis distance, which is proportional to the negative log likelihood [212], we have

$$\begin{aligned} FP &= P\Big[(\boldsymbol{x}-\mathbf{0})^T\boldsymbol{\Sigma}^{-1}(\boldsymbol{x}-\mathbf{0}) > (\boldsymbol{x}-\boldsymbol{\Delta})^T\boldsymbol{\Sigma}^{-1}(\boldsymbol{x}-\boldsymbol{\Delta})\Big] \\ &= P\Big[\sum_{i=1}^{n} x_i^2 \Big/ \sigma^2 > \sum_{i=1}^{n}(x_i-\Delta_i)^2 \Big/ \sigma^2\Big] \\ &= P\left[\frac{\sum_{i=1}^{n}(x_i-\Delta_i)^2 \Big/ \sigma^2}{\sum_{i=1}^{n} x_i^2 \Big/ \sigma^2} < 1\right] \end{aligned} \tag{6.17}$$

Let $X = \sum_{i=1}^{n}(x_i-\Delta_i)^2 \Big/ \sigma^2$, $Y = \sum_{i=1}^{n} x_i^2 \Big/ \sigma^2$, and $F = (Y/n)/(X/n)$, we have

$$FP = P\left[\frac{X}{Y} < 1\right] = P\left[\frac{X/n}{Y/n} < 1\right] = P(F < 1) \tag{6.18}$$

Note that $x_i \sim i.i.d.\mathcal{N}(0, \sigma^2)$ and $(x_i - \Delta_i) \sim i.i.d.\mathcal{N}(-\Delta_i, \sigma^2)$. It follows that X is a noncentral chi-squared random variable with n degrees of freedom and noncentrality parameter $\lambda = \sum_{i=1}^{n} \Delta_i^2 \Big/ \sigma^2$. Y is a central chi-squared random variable with n degrees of freedom. As a result, random variable F falls under a noncentral F-distribution. Then, we can calculate $P(F < 1)$ by evaluating the cumulative distribution function of F, which we will refer as CDF_F, at 1 [213]. We used the implementation from Pav et al. [214] in 'R' language to calculate $CDF_F(1)$.

The expression for F_1 Score is

$$
\begin{aligned}
F_1 &= 1 - FP = 1 - CDF_F(1) \\
F_1 &= 1 - \sum_{j=0}^{\infty} \left(\frac{(\frac{1}{2}\lambda)^2}{j!} e^{-\frac{\lambda}{2}} \right) I\left(\frac{1}{2} \middle| \frac{n}{2} + j, \frac{n}{2} \right) \\
where\ \lambda &= \frac{1}{\sigma^2} ||\mathbf{\Delta}||_2^2 = \frac{1}{\sigma^2} \sum_{i=1}^{n} \Delta_i^2
\end{aligned}
\tag{6.19}
$$

λ is the noncentrality parameter, I is the regularized incomplete beta function [215], and

$$
\Delta_i = (T_{surf1} - T_{surf2}) * erfc\left(\frac{x}{2\sqrt{\alpha_{sens} t_i}} \right) \tag{6.20}
$$

where T_{surf1} and T_{surf2} can be calculated by eq. 6.1. Thus, we have

$$
\begin{aligned}
\lambda &= \frac{1}{\sigma^2} \sum_{i=1}^{n} (T_{surf1} - T_{surf2})^2 * erfc^2\left(\frac{x}{2\sqrt{\alpha_{sens} t_i}} \right) \\
&= \frac{(T_{surf1} - T_{surf2})^2}{\sigma^2} \sum_{i=1}^{n} erfc^2\left(\frac{x}{2\sqrt{\alpha_{sens} t_i}} \right)
\end{aligned}
\tag{6.21}
$$

Let $\Delta t = t_{i+1} - t_i$ represent the sample time. We have,

$$
\lambda = \frac{(T_{surf1} - T_{surf2})^2}{\sigma^2 * \Delta t} \sum_{i=1}^{n} erfc^2\left(\frac{x}{2\sqrt{\alpha_{sens} t_i}} \right) * \Delta t \tag{6.22}
$$

We assume that sample time Δt is small, so that $\sum_{i=1}^{n} erfc^2\left(\frac{x}{2\sqrt{\alpha_{sens} t_i}} \right) * \Delta t$ can be approximated with $\int_0^{t_{contact}} erfc^2\left(\frac{x}{2\sqrt{\alpha_{sens} t}} \right) dt$.

Therefore, the resulting final expression for F_1 Score and λ is given by,

$$F_1 = 1 - \sum_{j=0}^{\infty} \left(\frac{(\frac{1}{2}\lambda)^2}{j!} e^{-\frac{\lambda}{2}} \right) I\left(\frac{1}{2} \middle| \frac{n}{2} + j, \frac{n}{2} \right)$$

$$where \quad \lambda = \frac{(T_{surf1} - T_{surf2})^2}{\sigma^2 * \Delta t} * \int_0^{t_{contact}} erfc^2 \left(\frac{x}{2\sqrt{\alpha_{sens} t}} \right) dt \tag{6.23}$$

6.7 Experiments with Different Thermal Effusivities

In this section, we evaluate our performance model by comparing its F_1 Score for classifying two different thermal effusivities with the F_1 Score obtained with SVMs and simulated time-series data. We use SVMs as our data-driven method given its best performance in our previous work [165, 181].

Given a reference thermal effusivity value, we are interested in comparing the performance model result and the SVM result for the minimum effusivity difference required to obtain a binary classification F_1 Score greater than or equal to a desired performance (Φ). In this paper, we set $\Phi = 0.9$. This means we consider any effusivity pair with $F_1 \geq 0.9$ classification score as distinguishable.

6.7.1 Minimum Distinguishable Difference $\delta(e)$

For a given thermal effusivity value e, let $\delta(e)$ be the smallest value such that either $F_1(e, e+\delta(e))$ or $F_1(e, e-\delta(e))$ is greater than Φ. We then define the minimum distinguishable difference of the given effusivity value e to be $\delta(e)$. Intuitively, the calculated $\delta(e)$ for a given e provides us with a quantitative evaluation of what materials can be distinguished from a specific material with effusivity e under the current sensor and environmental conditions.

6.7.2 Evaluation Procedure

We are interested in finding the effect of the following parameters on the F_1 Score obtained with our model as well as with SVMs.

- Noise $Z \sim \mathcal{N}(0, \sigma^2)$: $\sigma = 0.01$, $\sigma = 0.05$ and $\sigma = 0.10$
- Initial Sensor Temperature $T_{sens}(t = 0)$: 30°C and 35°C
- Contact Duration $t_{contact}$: 1.00s, 2.00s, 3.00s, and 4.00s

We estimate the minimum distinguishable difference $\delta(e)$ for every effusivity value e for the above conditions with the model and with SVMs and compare the results. For our performance model, we use the statistical method to calculate the F_1 Score under the given sensor and material thermal properties using Eq. 6.23. For SVMs, we generate noisy data using the physics-based model and performed a 3-fold cross-validation over each unique effusivity value pair and report the F_1 Score.

We used the implementation of binary support vector machines (SVMs) provided by the scikit-learn package [109] in Python. We used a linear kernel for the classification task. To produce feature vectors for training, we use both the raw temperature and the estimated local slope from each trial of experiment, and concatenate them into a single feature vector.

6.7.3 Data Collection

In order to account for a sufficiently large thermal effusivity range, we refer to the CES EduPack 2016 [216] Level 1 material database. Of all the included materials, Rigid Polymer Foam (LD) has the minimum effusivity value of $3.05 \times 10^1 J/(s^{\frac{1}{2}} \cdot K \cdot m^2)$, and Copper Alloy has the maximum effusivity value of $3.68 \times 10^4 J/(s^{\frac{1}{2}} \cdot K \cdot m^2)$. Therefore, we sample effusivity values in the range $(0, 4.00 \times 10^4]\ J/(s^{\frac{1}{2}} \cdot K \cdot m^2)$. We discretize the range to 500 equal intervals. We can think of each interval as a material category, and an instance of the material category can take on any effusivity value within the interval.

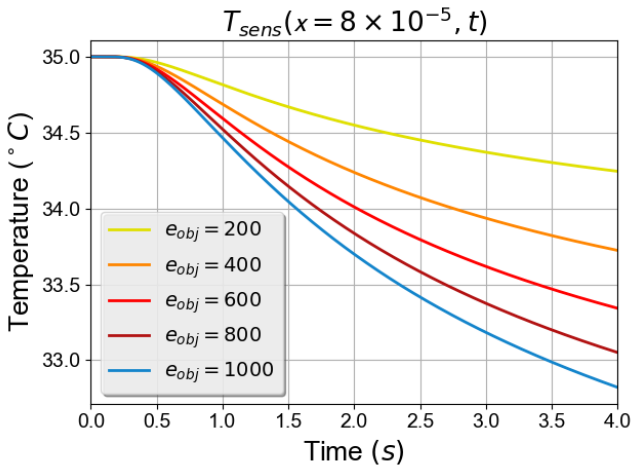

Figure 6.8: *Examples of generated time-series heat-transfer data from our physics-based model for some example effusivity values.*

Given an effusivity value e, we construct the time series heat-transfer data based on the semi-infinite solid model defined in 6.5.1. We use $e_{sens} = 892$ $(J \cdot s^{-\frac{1}{2}} \cdot K^{-1} \cdot m^{-2})$, and $\alpha_{sens} = 1.19 \times 10^{-9}$ $(m^2 \cdot s^{-1})$ similar to our real-world sensor parameters. We set T_{amb} to 25°C. We set the sampling rate to be 200 Hz, similar to our real-world sensor sampling rate. Figure 6.8 shows examples of data generated using our physics-based model with these parameters and some example object effusivity values.

We generated 50 trials for each effusivity interval by uniformly sampling from the effusivity interval and performed simulations with the sampled effusivity. We performed all simulations using a 2015 MacBook Pro equipped with Intel Core i7 CPU at 3.1 GHz running OS X El Capitan Version 10.11.6.

6.7.4 Results and Discussion

In this section, we present and compare the results of our performance model based evaluation and SVM based evaluation. Figure 6.9 shows the F_1 Score Matrix with pairwise F_1 Scores for all effusivity values using our performance model and SVMs. We obtained this matrix using $t_{contact} = 2s$, $T_{sens}(t = 0)$ = 35°C, and $\sigma = 0.05$. Table 6.1 shows the percentage of indistinguishable effusivity combinations calculated based on the F_1 Score

matrices with $\Phi = 0.9$. The results show that the evaluation using our performance model matches well with the evaluation using SVMs.

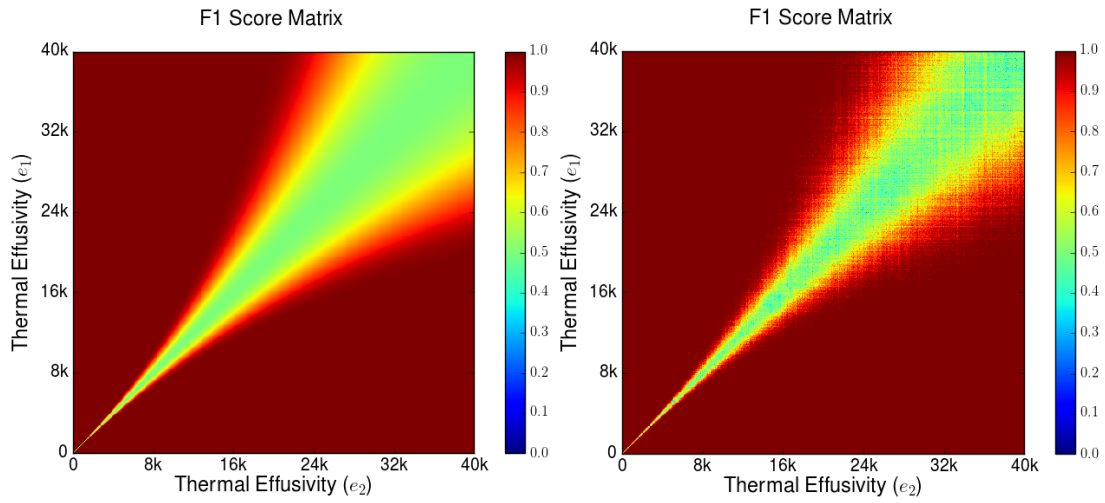

Figure 6.9: *Example F_1 Score Matrix with our performance model (left) and SVM (right) (T_{sens} = 35°C, σ = 0.05, $t_{contact}$ = 2.00s)*

Table 6.1: Percentage of Indistinguishable Effusivity Combinations, $t_{contact} = 2.00$ s

Experimental Conditions		Performance Model		SVM	
		Temperature Difference		Temperature Difference	
		5°C	10°C	5°C	10°C
Noise	0.1	62.97%	45.96%	55.54%	38.61%
	0.05	45.96%	30.00%	38.62%	24.41%
	0.01	14.69%	7.89%	23.30%	13.26%

We compare the F_1 Score matrix predicted by the performance model and the F_1 Score matrix produced by SVM for binary classification of the experiment data by calculating the L_1 distance between the two matrices. Before, we calculate the L_1 distance, we convert the F_1 Score matrix into a binary map where any score greater than 0.9 (our threshold for determining whether a material is distinguishable) is converted to 1 and the any score less than 0.9 is converted to 0. This gives us a sense of which materials are distinguishable under the given scheme with thermal sensing. The L_1 distance [217] between two $n \times n$ converted matrices $\mathbf{A}$ and $\mathbf{B}$ is defined as:

$$||\mathbf{A} - \mathbf{B}||_1 = \sum_{i=1}^{n}\sum_{j=1}^{n}|a_{ij} - b_{ij}| \tag{6.24}$$

Since F_1 Score matrix is symmetrical, and the diagonal values in the matrix are trivial (a material's recognition performance with itself is not meaningful), we only consider the upper diagonal matrix in the following accuracy metric,

$$d(\mathbf{A}, \mathbf{B}) = \left(1 - \sum_{i=1}^{n-1}\sum_{j=i+1}^{n}|a_{ij} - b_{ij}| * \frac{2}{n(n-1)}\right) * 100\% \tag{6.25}$$

This gives a measure of the difference between two F_1 Score matrices. We use this metric to compare the difference between our performance model F_1 Score matrix and the F_1 Score matrix obtained with SVMs running on both simulation and experimental data. Table 6.2 shows that the F_1 Score matrices predicted by our performance model match well with the F_1 Score matrices produced by SVM.

Table 6.2: Percent Matching Between Performance Model Predictions and SVM Results of Indistinguishable Effusivity Combinations, $t_{contact} = 2.00s$

Experimental Conditions		Temperature Difference	
		5°C	10°C
Noise	0.1	92.60%	92.65%
	0.05	92.63%	94.38%
	0.01	91.45%	94.65%

In order to capture the impact of initial condition $T_{sens}(t = 0)$ and noise Z, we calculate minimum distinguishable difference $\delta(e)$ for all values of e for each of the conditions. Figs. 6.10 and 6.11 show the results.

Effect of Contact Duration

To analyze the effect of contact duration on classification performance, we truncated the time series data at different time lengths and ran our performance model and SVMs on the truncated data. Fig. 6.10 shows the minimum distinguishable difference $\delta(e)$ curves calculated based on the performance model results (left graphs). As expected, in each plot, with increased length of the time, the expected performance of the algorithm improves. Fig. 6.10 also shows the results from SVMs and it follows the same trend (right graphs). The more the contact duration, the better is the performance of material recognition.

Effect of Initial Condition

Fig. 6.10 shows the results with our performance model (left-graphs) and SVMs (right-graphs) for both $T_{sens}(t = 0) = 30°\text{C}$ and $T_{sens}(t = 0) = 35°\text{C}$ initial conditions. By comparing the ($T_{sens}(t = 0) = 35°\text{C}$) graphs with the ($T_{sens}(t = 0) = 30°\text{C}$) graphs in Fig.6.10, we observe that larger initial temperature difference ($T_{sens}(t = 0) = 35°C$) between sensor and ambient environment produces a lower $\delta(e)$ curve. In other words, the classification algorithm works better with larger initial temperature difference between sensor and measured object, which generates more distinguishable heat transfer data for materials.

Also, the graphs generated by the performance model are visually similar with the ones generated by SVMs across different initial sensor temperature conditions. Observe that SVM actually performs slightly better than the performance model for each specified $t_{contact}$, with $\delta(e)$ curves just below that of the performance model. This is probably because SVMs are less susceptible to the additive gaussian noise in the data than the performance model.

Effect of Noise

Fig. 6.11 shows the results with our performance model (top graphs) and SVMs (bottom graphs) for different levels of noise. By comparing the left plot ($\sigma = 0.01$) with the middle

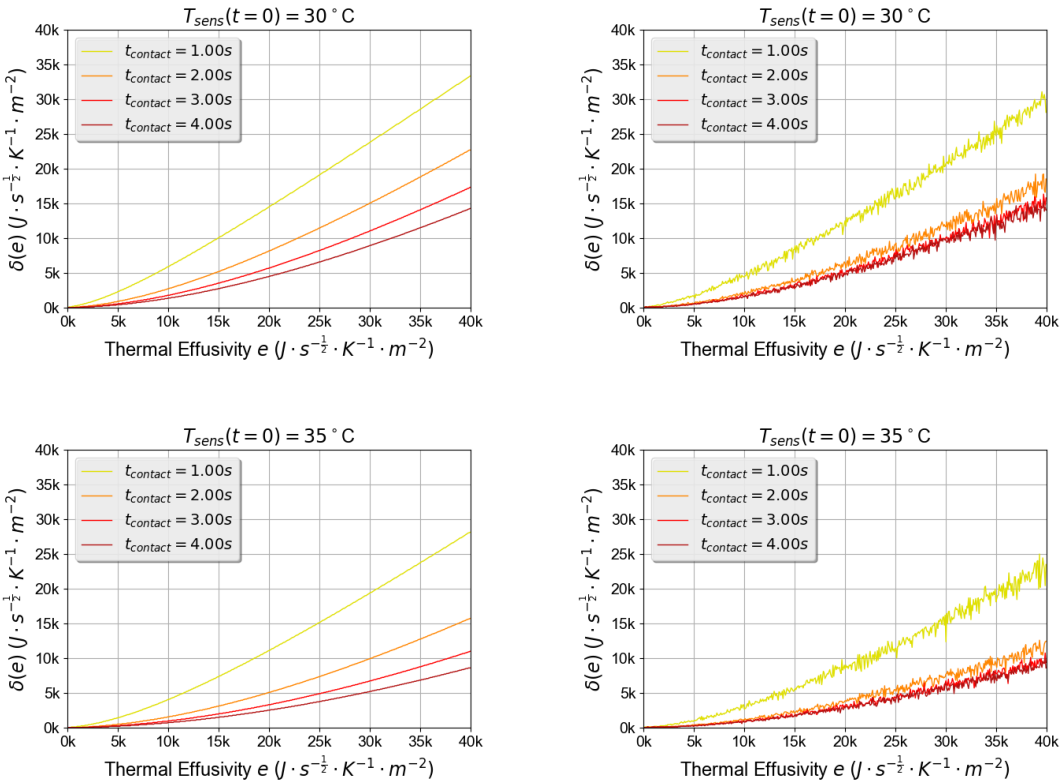

Figure 6.10: *Effect of Initial Condition on $\delta(e)$ with fixed noise $\sigma = 0.05$: Performance Model and $T_{sens}(t = 0)$ = 30°C (Top-left), SVM and $T_{sens}(t = 0)$ = 30°C (Top-Right), Performance Model and $T_{sens}(t = 0)$ = 35°C (Bottom-left), and SVM and $T_{sens}(t = 0)$ = 35°C (Bottom-Right)*

plot ($\sigma = 0.05$) and the right plot ($\sigma = 0.10$) in Fig. 6.11, we observe the impact of noise on the algorithm performance. As expected, simulations with a noise level $\sigma = 0.10$ produce the highest $\delta(e)$ values. Again, the graphs generated by our performance model are similar to the ones generated by SVMs.

6.8 Experiments with Simulated Data from Material Database

In this set of experiments, we map the previous results obtained using different thermal effusivity values to actual material effusivity values. Our objective here is to evaluate our performance model using actual material effusivity values. We take thermal effusivity values of all 69 materials from CES EduPack Level 1 database [92]. Figure 6.12 shows the effusivity ranges of all the 69 materials. We looked up binary material classification re-

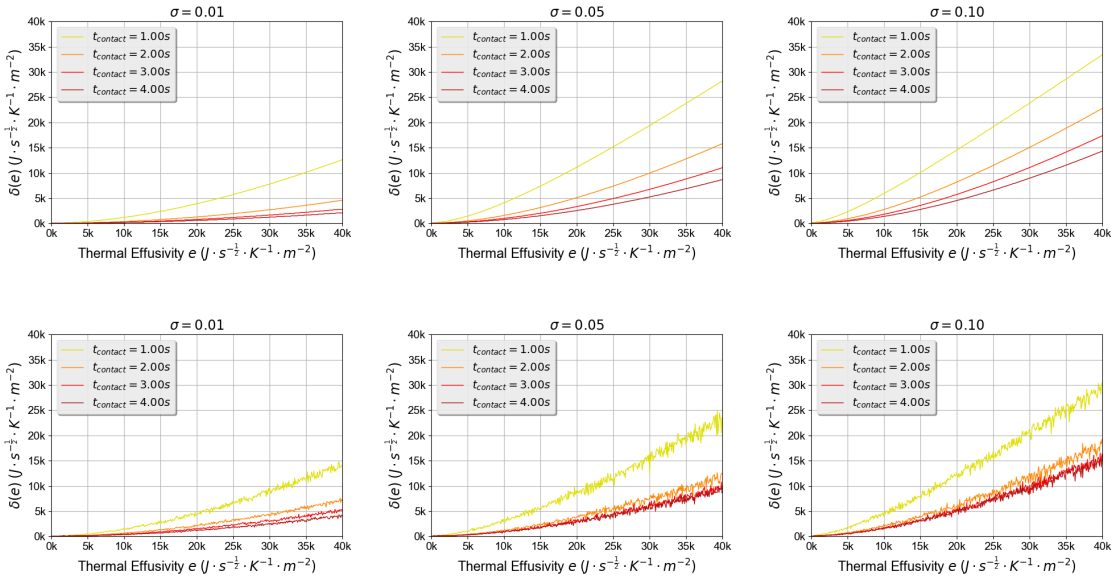

Figure 6.11: *Effect of Noise on $\delta(e)$ with fixed initial condition $T_{sens}(t = 0) = 35°C$: Top graphs show the results from the performance model whereas the bottom graphs show the results from SVMs. The noise levels increase from ($\sigma = 0.01$) in the left graphs to ($\sigma = 0.05$) in the middle graphs, and finally ($\sigma = 0.1$) in the right graphs.*

sults for all possible pairs of effusivity values corresponding to 69 materials (2346 material pairs) from our previous results in Section 6.7.4 to find out what materials are distinguishable with F_1 Score greater than 0.9. We compare the results of our performance model with that of SVMs. We present the F_1 Score matrices in terms of node graphs of distinguishable and indistinguishable pairs.

6.8.1 Node Graphs of Material Pairs

To visualize whether any two materials from the CES EduPack Level 1 database [92] is distinguishable, we generate a node-graph based on their F_1 Scores where each node represents a material. The node-graph has the following characteristics:

- An edge between two material nodes represent that they are indistinguishable. Note $\Phi = 0.9$.
- The radius of a material node is proportional to its thermal effusivity. So, metals with larger effusivities are represented by larger circles.

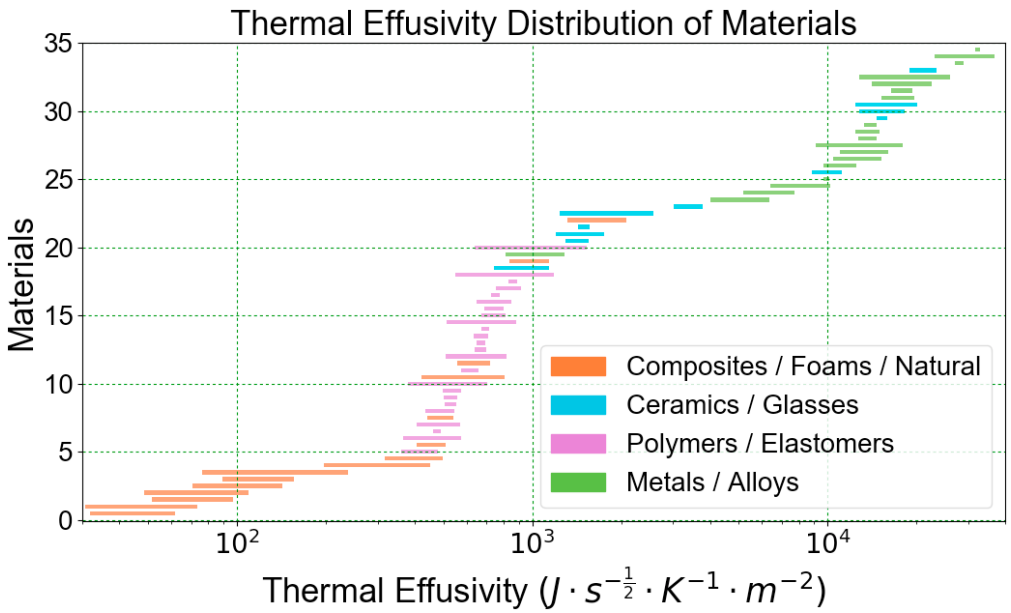

Figure 6.12: *Effusivity Distribution of the 69 Materials in CES Edupack Level 1 [92] in Logarithmic Scale*

- CES Edupack divides all materials into four large categories such as Metals / Alloys, Ceramics / Glasses, Polymers / Elastomers, and Composites / Foams / Natural. A material node's color signifies which category the material belongs to.

- The thickness of the edge connecting two materials is inversely proportional to their F_1 Score. This means that the thicker the edge, the more difficult it is to distinguish the material nodes that are at its ends.

- The relative position of the nodes has no relation with any physical property. It is purely for visualization purposes.

Note, each material in the CES Edupack database [92] has a range of thermal effusivity values that it can have. So, to calculate a single F_1 Score for the range of effusivity values for a single material pair, we use the average F_1 Score ≥ 0.9. To find the average F_1 Score, for example, for gold and silver, we find the average of F_1 Scores for the binary classification between all possible combinations of gold effusivities and silver effusivities. In our case, the average F_1 Score can be calculated based on the F_1 Score Matrix, as shown

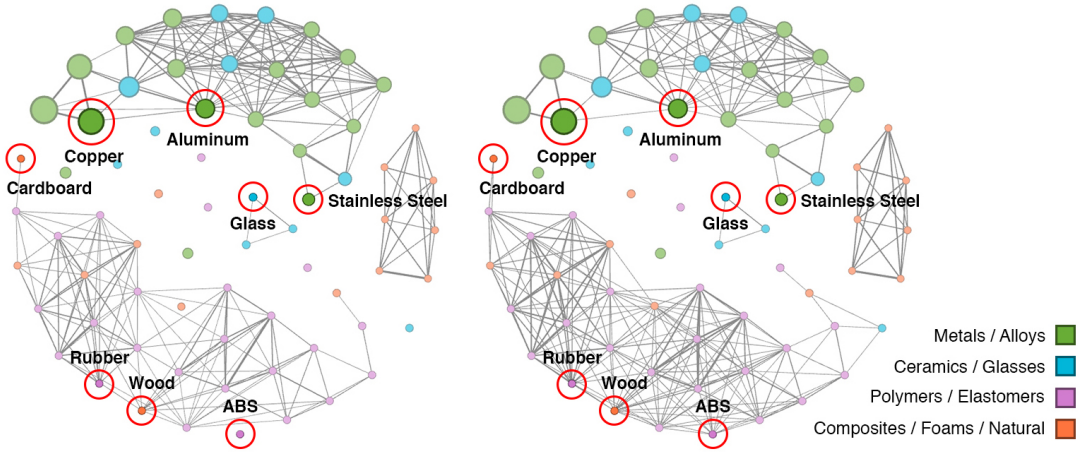

Figure 6.13: *Node Graphs of Material Pairs using Performance Model (left) and SVMs on the simulated data (right). A link between two nodes means that they are indistinguishable with F1 Score > 0.9*

in Fig. 6.9, by taking the average of all F_1 Scores within a rectangular area, bounded by all possible effusivity values ($e1$) (inside effusivity range of gold), and all possible effusivity values ($e2$) (inside effusivity range of silver).

Fig. 6.13 shows the results with $T_{sens}(t = 0) = 35°\text{C}$ and $N = 0.05$ noise. We see that the results with our performance model match well with the results with SVMs. From the figure, we note that there are three to four connected components in each node-graph and these connected components tend to have majority of the material nodes in a particular category such as Metals / Alloys, Ceramics / Glasses, Polymers / Elastomers, and Composites / Foams / Natural. This further means that a material belonging to one of these categories has a higher probability of being distinguished from a material in another category than in its own category. For example, it would be easier to distinguish a Ceramic from a Metal than another Ceramic. We can also see some densely connected components in the graph. For example, Metals are densely connected together, which agrees with our observation in Fig. 6.10, as rising $\delta(e)$ makes it harder to distinguish materials with larger effusivity. The Metals are more densely connected in the performance model, while Polymers / Elastomers are more densely connected in SVM result. The intuition behind this observation is that the performance model finds it difficult to distinguish among materials with larger

effusivity values, such as Metals / Alloys, while the SVM finds it difficult to distinguish among materials with smaller effusivity values, such as Polymers / Elastomers.

The observed connected components also agree well when compared with the effusivity ranges provided in Fig. 6.12. Metals, with large effusivity values, are generally difficult to distinguish amongst themselves because their effusivity values are so large that they dominate T_{surf} (eq. 6.1) to a value very close to the ambient temperature, rendering the T_{sens} curves indistinguishable.

While our performance model predicts better $\delta(e)$ for smaller effusivity values, Polymers / Elastomers and Composites / Foams / Natural materials still form many edges, because the effusivity values of materials are so close that their difference is smaller than the minimum distinguishable distance $\delta(e)$.

Table 6.3: Percentage of Indistinguishable Pairs for Experiments with Simulated Data, $t_{contact} = 2.00s$

Experimental Conditions		Performance Model		SVM	
		Temperature Difference		Temperature Difference	
		5°C	10°C	5°C	10°C
Noise	0.1	22.42%	14.54%	21.14%	15.77%
	0.05	14.54%	10.61%	14.96%	12.53%
	0.01	7.08%	5.16%	11.94%	8.35%

Table 6.4: Percent Matching Between Performance Model Predictions and SVM Results of Indistinguishable Material Pairs for Experiments with Simulated Data, $t_{contact} = 2.00s$

Experimental Conditions		Temperature Difference	
		5°C	10°C
Noise	0.1	98.55%	96.63%
	0.05	97.53%	96.63%
	0.01	95.14%	96.80%

As shown in Table. 6.3, the number of edges present in the graph is consistent with the observation we made in Fig. 6.10, that a larger initial temperature difference between sensor and material and less noise leads to more distinguishable material pairs. Also, the

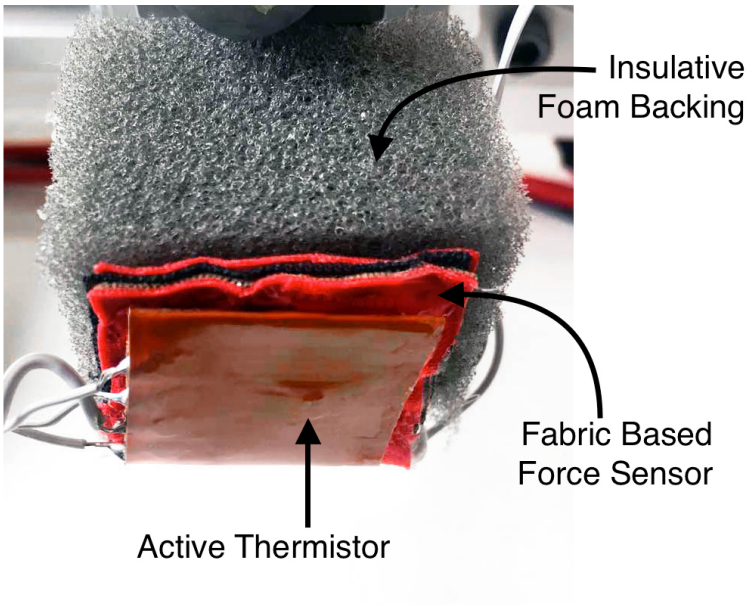

Figure 6.14: *The sensing module with fabric-based force sensor and an active thermal sensor*

quantitative values using the performance model match well with that of SVMs. As shown in Table 6.4 the indistinguishable material pairs predicted by our performance model match with the SVM results with 99.6% accuracy across all experimental conditions.

6.9 Experiments with a Real-Robot

6.9.1 Experimental Setup

Figure 6.1 shows the 1-DoF robot used in our experiments. The robot consists of a linear actuator, two Teensy 3.2 microcontrollers, a passive sensing thermistor, and an active sensing module. The active sensing module consists of the Thorlabs HT10K Flexible Polyimide Foil Heater with 10 kOhm Thermistor [150] (heating element and a temperature sensor) on a fabric based force sensor [180] which is backed by thermal insulation foam. The passive sensing thermistor uses the fast-response $10k\Omega$ NTC thermistor (EPCOS B57541G1103F) [218].

Figure 6.15 shows the list of materials used for this set of experiments. We selected these materials in order to have uniform representation of materials from all the four cat-

Figure 6.15: *Twelve selected materials for real-world experiments with the 1-DoF robot*

egories (Metals, Ceramics, Polymers, and Composites) from the CES Edupack database [92]. We included 3 materials from each category. We selected 12 materials such that it has both distinguishable and indistinguishable material pairs between them. We estimated this by running our performance model using the mid-point of the effusivity range of these materials.

6.9.2 Experimental Procedure

Figure 6.1 shows an example of the 1-DoF robot reaching to touch a cardboard sample. We used a Python script on a separate Dell Optiplex 9010 Computer equipped with Intel(R) Core(TM) i7-3770 CPU at 3.40 GHz running 32-bit Ubuntu 12.04.2 LTS system with Linux Ubuntu 3.5.0-54-generic kernel to control the device through a serial link with the Teensy 3.2 microcontrollers. Before contacting the sample, the device waits at 15 mm above the sample, to allow a voltage supply to generate heat based on an integral controller such that

the active sensing thermistor maintains a desired temperature. Then the integral controller stops so as not to interfere with the natural heat-transfer from the sensor to the material and the robot lowers the sensing module. Upon contact (detected by the fabric-based force sensor when the force that the actuator exerts on the material exceeds $5N$), the micro-controllers record the active sensing thermistor and the passive sensing thermistor readings at 200 Hz for 10 s. Note, we do not use the passive thermistor data for any material recognition purposes. The robot then raises the sensing module and waits for 20 seconds before starting the next trial. Using the FLIR Tau 2 324 7.5mm Thermal Imaging Camera Core (46324007H-FRNLX), we found that 20 s was enough for the materials to come back to their initial state. This is to ensure that the material is at a consistent initial condition before the robot touches it at any trial.

We performed two sets of experiments with the real-robot. The first set consisted of 10 trials each with fixed initial sensor temperature conditions for each material. The second set consisted of 50 trials each with uniformly varied initial sensor temperature conditions for each material. We uniformly varied the initial sensor conditions between $T_{sens}(t = 0) = 30°\text{C}$ to $T_{sens}(t = 0) = 35°\text{C}$. We performed this set of experiments to simulate contact situations when a robot incidentally touches objects in its environment without the opportunity to adjust its sensor conditions. This is a common scenario in manipulation in cluttered and unstructured environments or in assistive scenarios working in close contact with a human body [219].

6.9.3 Finding Sensor and Material Parameters

To get sensor parameter values (sensor effusivity e_{sens} and sensor diffusivity α_{sens}), we collected 10 trials data with fixed initial conditions from each of the materials in Figure 6.15. We identified the sensor parameter values based on the sum of squared error between experiment temperature data and the ideal temperature data based on the semi-infinite solid

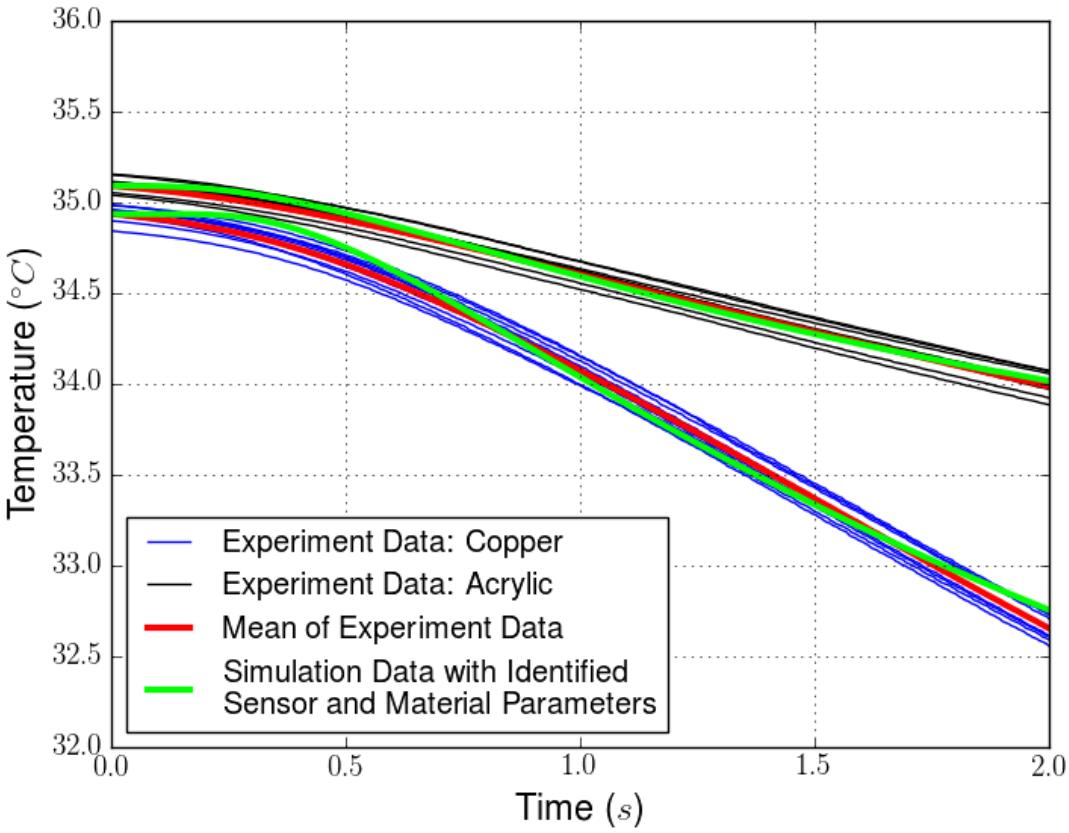

Figure 6.16: *Example Real-world data from Copper and Acrylic under fixed sensor initial conditions. The graphs also show the simulated data using the identified sensor and material parameters.*

model defined in Section 6.5.1. For each material, we use the Limited-memory BFGS with boundary constraints (L-BFGS-B) [156] algorithm to find its optimal effusivity value, with the boundary constraints given by the thermal effusivity values of materials in CES EduPack database [92]. We identified the sensor effusivity as $e_{sens} = 892\ (J \cdot s^{-\frac{1}{2}} \cdot K^{-1} \cdot m^{-2})$, and sensor diffusivity as $\alpha_{sens} = 1.19 \times 10^{-9}\ (m^2 \cdot s^{-1})$. The resultant effusivity value of each material is given in Table 6.5.

Table 6.5: Thermal Effusivity Values of Materials in the Experiment

Material	Thermal effusivity identified $(J \cdot s^{-\frac{1}{2}} \cdot K^{-1} \cdot m^{-2})$	Maximum thermal effusivity from database $(J \cdot s^{-\frac{1}{2}} \cdot K^{-1} \cdot m^{-2})$	Minimum thermal effusivity from database $(J \cdot s^{-\frac{1}{2}} \cdot K^{-1} \cdot m^{-2})$
Cardboard	336.90	196.67	452.23
Wood	400.95	331.00	506.46
ABS	514.15	514.15	882.58
Rubber	570.81	407.00	570.81
MDF	544.63	618.47	733.93
Acrylic	635.49	380.35	702.15
Porcelain	1276.59	1162.69	1334.07
Glass	1433.31	1433.31	1560.39
Granite	2749.87	2252.32	2749.87
Stainless Steel	10184.17	6388.35	10184.17
Aluminum	17530.03	12767.69	25972.02
Copper	23049.18	23049.18	36761.16

Figure 6.16 shows some examples of the experimental data as well as the simulated data using the identified sensor and material thermal parameters. As seen from the figure, using the identified parameters, the simulated data matches the experimental data well.

6.9.4 Results

Fixed Initial Conditions

With fixed initial conditions, SVMs achieved an average F_1 Score of 0.985 for binary material recognition across all 66 material pair comparisons. Our performance model result successfully achieved a 92.42% match with the SVM results, using the metric defined in eq. 6.25. While the performance model predicted that MDF vs. Acrylic can only be distinguished with 0.62 F_1 Score, SVMs were able to achieve an F_1 Score of 0.92.

Varied Initial Conditions

In order to test the accuracy of the performance model under varied initial conditions, we collect 50 trials of data for each material with varied sensor initial conditions by uniformly sampling $T_{sens}(t = 0)$ from 30°C to 35°C before contact. SVMs were able to achieve an average F_1 Score of 0.976 for binary material recognition across all 66 material pair comparisons.

However, to apply our performance model to trials collected with varied initial conditions, we need to transform the data to fixed initial conditions. We achieve this by transforming the data as follows.

By using eq. 6.5 and substituting T_{surf} with eq. 6.2, we have the following relation,

$$\begin{aligned} &\frac{T_{sens}(x,t) - T_{obj}(t=0)}{T_{sens}(t=0) - T_{obj}(t=0)} = \\ 1 - &\frac{e_{obj}}{e_{obj} + e_{sens}} erfc\left(\frac{x}{2\sqrt{\alpha_{sens} t}}\right) \\ &+ \frac{Z \sim \mathcal{N}(0, \sigma^2)}{T_{sens}(t=0) - T_{obj}(t=0)} \end{aligned} \tag{6.26}$$

where all initial conditions are transformed to 1, and the expected noise level Z' of the transformed data becomes,

$$\begin{aligned} Z' &= \frac{1}{35 - 30} * \int_{T \in [30,35]} \frac{Z}{T - T_{obj}(t=0)} dT \\ &= \frac{ln35 - ln30}{35 - 30} * Z \end{aligned} \tag{6.27}$$

Using the above transformation, our performance model prediction successfully achieved a 90.91% match with the real-world data performance obtained with SVMs. The performance model successfully predicted the majority of distinguishable material pairs. It also successfully predicted that ABS and Rubber, and MDF and Rubber would be indistinguish-

able under the given sensor and environment conditions. Interestingly, our performance model predicted that Copper vs. Aluminum would be indistinguishable but SVMs could distinguish them. Out of the four pairs of materials (ABS vs. MDF, Copper vs. Stainless Steel, ABS vs. Wood, and Aluminum vs. Stainless Steel) that the performance model expected to distinguish, SVM achieved F_1 Score ≤ 0.9, but managed to achieve an average F_1 Score of 0.83.

6.10 Limitations

Our performance model is based on a semi-infinite solid model assumption, which assumes heat transfer from the active thermal sensor to the material in one direction only. In reality, however, none of the materials are perfectly semi-infinite though its a widely used model in these scenarios. Note that this semi-infinite solid model assumption is generally valid for a short duration which is characterized by the Fourier Number of the material [220] [221]. Also, the thermal properties of a material change with temperature which we did not account for in our physics-based model.

In our performance model, we modeled the sensor time series data as a gaussian process, wherein there is an underlying 'mean temperature vector', and a multivariate gaussian distribution from which each trial of the noisy sensor temperature vector is sampled. As a result, the discrepancy between the distribution of actual temperature time series data and the assumed multivariate gaussian distribution can cause inaccuracy in the prediction of the performance model. For example, if we obtain a sample population of time-series data where the initial condition is varied by sampling $T_{sens}(t = 0)$ for each trial uniformly from $30°$C to $35°$C, the expected resulting distribution is a high dimensional "plateau" shaped multivariate generalized normal distribution [222], which our statistical method cannot directly account for. Although it is possible through affine transformation of the variable initial condition time-series data to consistent initial condition time-series data (See Section 6.9.4). While our performance model is only suitable for estimating the performance

of binary classification, we can transform a multiclass classification problem to binary classification problems using the one-vs-one strategy or the one-vs-rest strategy [223] and predict the performance for classifiers similar to the scikit-learn implementation of multiclass SVMs [109].

Finally, note that in this paper, we used the active thermal sensor similar to the one used in [165]. However, we also performed all these three evaluations with another 'point' thermal sensor used in [224]. For experiments with fixed initial conditions, our model predicted the performance well using the point sensor. The model performance matched the SVM performance with 92.29% accuracy using the metric (See eq. 6.25) for effusivity combinations, 99.94% for simulated data from material database, and 86.36% for real-world data with fixed initial conditions. However, the model predictions matched the real-world data with varied initial conditions with only 46.97% accuracy for the 'point' sensor. Basically, the model predicted that a lot of the binary material pairs are distinguishable but the SVMs running on the real-world data collected using the 'point' sensor could distinguish only 22 out of the 66 material pairs. This is probably because the sensor is a 'point' sensor whose contact area during heat-transfer is low and thus the differences in the heat-transfer between materials is less prominent than the 'flat area' sensor used in this paper and in [165]. This relates to the fact that heat-transfer is dependent on the contact area and geometry as well how well two surfaces are in contact. Thus, depending upon the compliance in the sensor, application of larger force might result in a better contact area or contact between two flat surfaces may result in more prominent heat-transfer than contact between a flat surface and a spherical surface ('point' sensor) or between two spherical surfaces. This is compounded by the fact that the point sensors were also in contact with the fabric, thus adding more uncertainty to the heat-transfer data. Also, the 'point' sensor parameters may be more susceptible to temperature changes i.e. the thermal effusivity and diffusivity of the 'point' sensor may have changed significantly with temperature changes in the sensor and thus, during varied initial conditions, the heat-transfer data was more unpredictable

than obtained using a fixed sensor parameter in our physics-based model. Accounting for the sensor parameter dependence on temperature, the effect of contact area, as well the force applied during physical contact, in the heat-transfer data using the semi-infinite model needs further investigation.

6.11 Conclusion

We investigated the binary classification of material pairs across a wide range of materials using heat transfer based sensing. We derived a physics-based model with a statistical method to calculate the binary material recognition performance when a heated sensor touches two materials with flat surfaces. We conducted a three part evaluation of the performance model. First, we evaluated the accuracy of performance model prediction with different thermal effusivity values by calculating and comparing $\delta(e)$ vs. e curves. Based on the evaluation result, we investigated the effect of initial conditions, contact duration, and noise on the classification algorithms expected performance. We then performed evaluation using simulated data from 69 materials provided in CES EduPack Level 1 database. In the third part of our evaluation, we collected real world data using a 1-DoF robot and compared the classification performance with the model prediction. Our results provide evidence for the feasibility of using the performance model to evaluate the binary material classification performance given sensor and material thermal properties. The accuracy of our performance model during real-world tasks, for which the contact between the sensor and the material is more varied and there are greater numbers and varieties of objects and material compositions, merits further investigation.

CHAPTER 7

CAN ROBOTS OVERCOME HUMAN LIMITS OF THERMAL SENSING?-ROLE OF MULTIPLE INITIAL CONDITIONS.

7.1 Research Summary

During touch, people use thermal sensing cues to identify material properties [225–229]. Similarly, robots can use thermal sensing for material recognition [53, 138, 148, 149, 181, 230–232]. The perception of warmth and cold when humans touch a material depends on various factors such as object temperature and material properties, skin temperature and properties, as well as area and geometry of contact [233–240]. Skin temperature, in turn, affects other haptic perception modalities [241–243]. Researchers working on tactile thermal displays use these factors to create realistic thermal sensations [244–249]. Using psychophysics experiments, researchers have found that material discrimination with thermal sensing is possible only if large differences in certain material properties exist [228, 245, 249]. However, these results are conservative for data-driven material recognition by robots [231]. Here we develop a non-conservative mathematical condition under which thermal sensing ambiguities arise and provide empirical evidence for ambiguity. This can provide insights into the related phenomenon of the cold feeling of metals to touch. We then develop conditions under which such thermal ambiguities can be removed and show that robots can overcome these human thermal sensing limitations by actively using sensors with multiple thermal initial conditions.

7.2 Research Overview and Results

Thermal sensing in robotics is becoming more common but fundamental ambiguity has not been extensively explored yet. When a robot with an actively heated thermal sensor

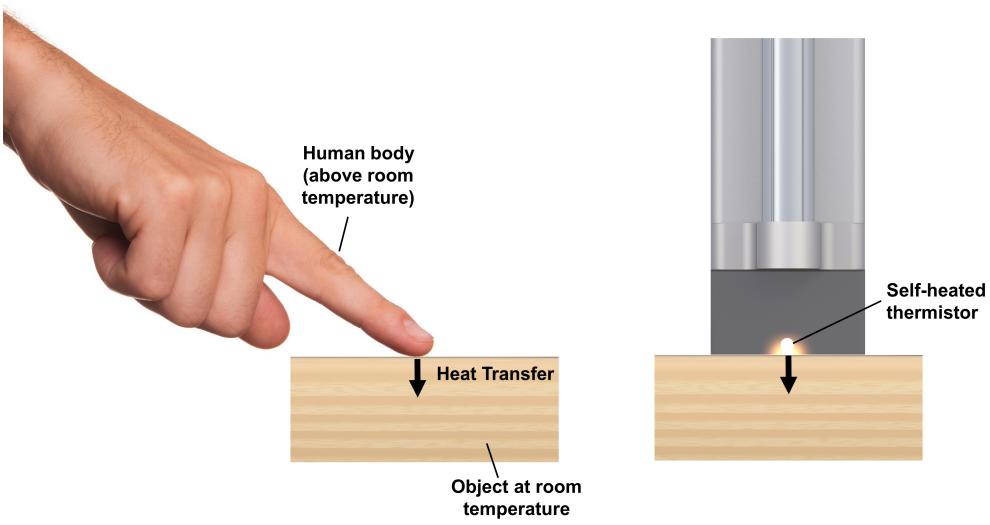

Figure 7.1: *When the human body makes contact with an object at ambient temperature, heat flows from the body into the object, creating the sensation of coldness that is more or less pronounced based on the thermal properties of the object. Similarly a robot with an actively heated thermal sensor such as a self-heated thermistor can use this sensing modality to distinguish materials with different thermal properties. We model the heat transfer from the robot's sensor to the object as contact between two semi-infinite solids, an approach also used to approximate human thermal touch [225, 231, 245, 248].*

(containing a heater and a temperature sensor) comes in contact with an object at ambient temperature (usually lower than the heated sensor), heat flows out of the sensor at a rate that depends on the initial contact conditions as well as material properties of sensor and object (See Fig. 7.1). Given consistent initial conditions, the heat-transfer rate will differ only according to the material properties and thus, we can employ data-driven or model-based methods to identify different materials [231].

Researchers have modeled heat transfer based interaction between a human finger and an object using contact between two semi-infinite solids [225, 231, 245, 248]. Using this model, the thermistor temperature (inside the heated sensor module) at a distance x from the contact surface and at any point of time, t, is given by

$$T_{\mathrm{s}}(x,t) = T_{\mathrm{s}} + (T_{\mathrm{surf}} - T_s) * \operatorname{erfc}\left(\frac{x}{2\sqrt{\alpha_s t}}\right) \tag{7.1}$$

where $T_s = T_s(t=0)$ is the sensor initial temperature, T_{surf} is the surface temperature

when the sensor touches the object, $\mathrm{erfc}()$ is the complimentary error function, and α_s is the coefficient of thermal diffusivity of the sensor.

The common phenomenon that metals usually feel colder than wood or plastic at same temperature when we touch them, is related to their material properties being different as evident from eq. (7.1). However, note that in addition to the material properties, the heat transfer also depends on the initial temperature of the object and the sensor (or human finger). Therefore, it is possible that two different materials with different material properties (eg. wood and metal) might feel the same if the initial conditions are different. We define this phenomenon as 'thermal ambiguity'.

To find out the thermally ambiguous conditions when a thermal sensor touches two objects $O1$ and $O2$ made of different materials, we have,

$$\begin{aligned} T_{\mathrm{s}}(x,t) &= T_{\mathrm{s}} + (T_{\mathrm{surf\_O1}} - T_{\mathrm{s}}) * \mathrm{erfc}\left(\frac{x}{2\sqrt{\alpha_{\mathrm{s}} t}}\right) \\ &= T_{\mathrm{s}} + (T_{\mathrm{surf\_O2}} - T_{\mathrm{s}}) * \mathrm{erfc}\left(\frac{x}{2\sqrt{\alpha_{\mathrm{s}} t}}\right), \end{aligned} \tag{7.2}$$

where $T_{\mathrm{surf\_O1}}$ and $T_{\mathrm{surf\_O2}}$ are the contact surface temperatures when the sensor touches the objects $O1$ and $O2$ respectively. Let e, e_1, and e_2 be the thermal effusivities of sensor, object $O1$, and object $O2$ respectively and T_{O1}, T_{O2} are the initial temperatures of objects $O1$ and $O2$ respectively. From eq. 7.2, we have,

$$T_{\mathrm{surf\_O1}} = T_{\mathrm{surf\_O2}} \tag{7.3}$$

which implies

$$\frac{T_{\mathrm{s}} e + T_{\mathrm{O1}} e_1}{e + e_1} = \frac{T_{\mathrm{s}} e + T_{\mathrm{O2}} e_2}{e + e_2}, \tag{7.4}$$

By rearranging eq. (7.4) and using a mathematical identity, we have the relation between the initial temperatures of the objects and the sensor and their thermal effusivities

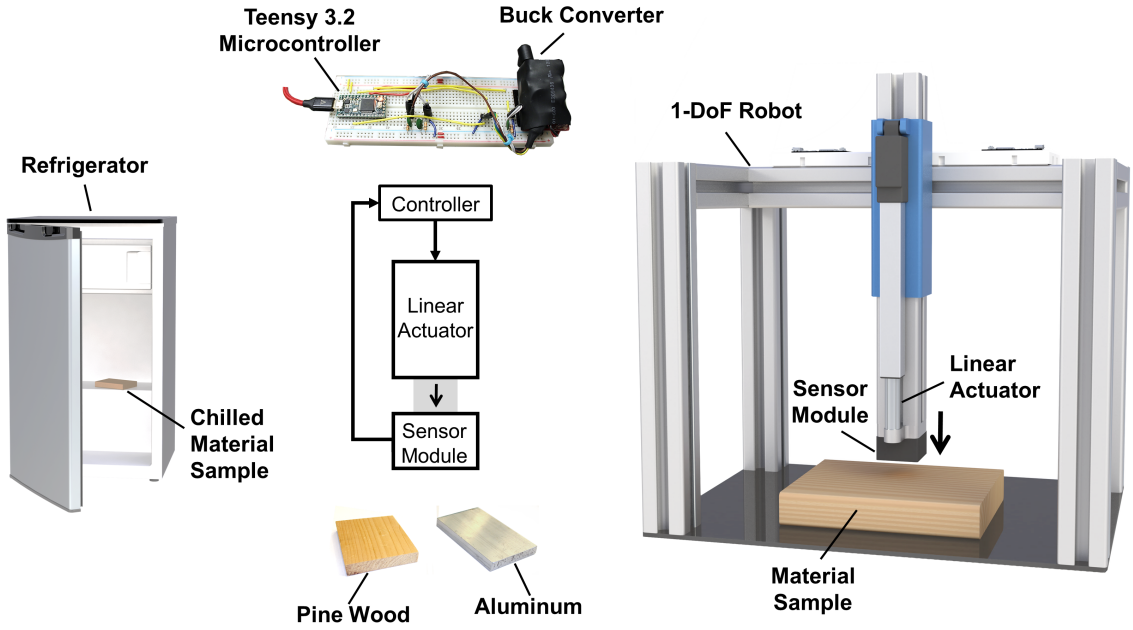

Figure 7.2: *We used a simple 1-DoF robot with interchangeable thermal sensing modules to test samples of aluminum and pine wood at room temperature and pine wood chilled in a refrigerator. The robot's Teensy 3.2 microcontroller lowers the linear actuator to bring the sensor module into contact with the material sample and uses an internal analog-to-digital converter to record sensor values.*

as,

$$\frac{(T_{\mathrm{s}} - T_{\mathrm{O1}})}{(T_{\mathrm{s}} - T_{\mathrm{O2}})} = \left(\frac{e_2}{e_1}\right)\left(\frac{e + e_1}{e + e_2}\right). \tag{7.5}$$

Given the thermal effusivities of the objects and the sensor and the sensor initial temperature, the above equation lets us find the conditions (initial temperatures of two objects) in which it is impossible to distinguish them using the model even if they have very different thermal effusivities. We performed experiments with two materials (See Fig. 7.2) to show this result (See Fig. 7.3). We selected a pine wood block ($O1$) and an aluminum block ($O2$) for comparison purposes because pine wood and aluminum are two of the most common materials of objects found in homes. Fig. 7.2 shows our experimental setup consisting of a 1-DoF (degree-of-freedom) robot with a sensor module, two material samples, and a refrigerator to change the temperature of the pine wood block.

It is a common occurrence that an object made of aluminum feels much colder com-

pared a similar object made of wood, when touched in the same normal ambient conditions. And, through experiments, we see that a block of aluminum and a block of pine wood under same ambient temperature conditions generate very different heat transfer data shown in Fig. 7.3, and can thus, be easily distinguished. Figure 7.3 also shows the actively heated sensor in the sensor module which the robot used to collect the data. We obtained the thermal effusivity of the pine wood block ($e_1 = 331\ \mathrm{J}/(\mathrm{m}^2\mathrm{s}^{0.5}\mathrm{K})$, the aluminum block ($e_2 = 23664\ \mathrm{J}/(\mathrm{m}^2\mathrm{s}^{0.5}\mathrm{K})$) and the sensor ($e = 225\ \mathrm{J}/(\mathrm{m}^2\mathrm{s}^{0.5}\mathrm{K})$) by using a quasi-Newton constrained nonlinear optimization method on the empirical data. The material blocks were initially at $T_{\mathrm{O1}} = 23.4°\mathrm{C}$ and the sensor was at $T_{\mathrm{s}} = 40.0°\mathrm{C}$.

Under certain conditions as derived from eq. (7.5), the same aluminum and pine wood blocks can generate very similar heat transfer data which might make the task of distinguishing them difficult. What this means, is that the same wooden block will feel thermally similar to the aluminum block when touched, if they are kept at certain ambient temperatures. Using eq. 7.5 and the estimated thermal effusivities of the materials and the initial temperatures of the aluminum block and the sensor, we estimate the temperature at which the pine wood block should generate similar heat-transfer data as that of the aluminum block to be $\hat{T}_{\mathrm{O2}} = 12.4°\mathrm{C}$. We used a refrigerator (See Fig. 7.2) to cool the pine wood block and collected data at various cold temperatures ranging from $10°\mathrm{C}$ to $15°\mathrm{C}$ at $0.5°\mathrm{C}$ intervals. We found that the data collected at $T_{\mathrm{O2}} = 12.5°\mathrm{C}$ is very similar (and thus, thermally ambiguous) to the original data collected from aluminum (See Fig. 7.3). We computed a histogram of the temperature difference of the empirical data and found the temperature difference to be less than given by histogram of the sensor noise, thus showing the evidence of ambiguity. This also provides evidence that the conditions derived from the model match well with real experimental conditions and thus, the model was predictive ($\hat{T}_{\mathrm{O2}} \approx T_{\mathrm{O2}}$) of the thermal ambiguity conditions. Figure 7.3 also shows the histogram of temperature difference between the heat-transfer data using the model based on semi-infinite solid assumption and the empirical data. We see from Fig. 7.3 that the difference

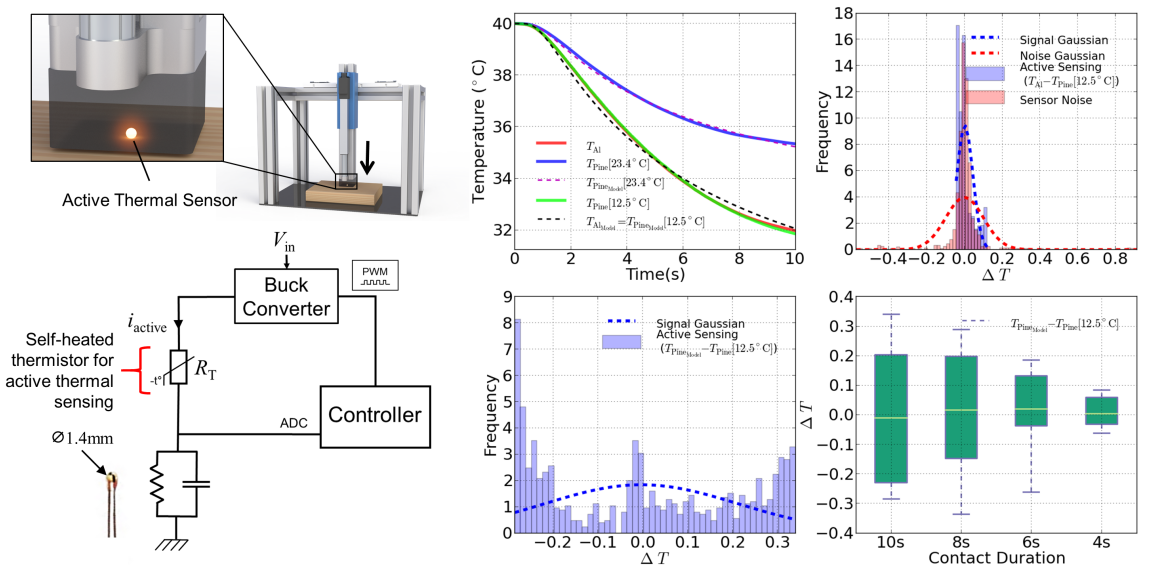

Figure 7.3: *Using an active thermal sensor in the form of a self-heated thermistor can distinguish between pine wood and aluminum when both samples are at room temperature (*23.4°C*). However, when the pine wood is cooled to* 12.5°C *the signal from the active thermal sensor is very similar to aluminum at* 23.4°C*.*

decreases with smaller time windows which could be due to the fact that the semi-infinite solid assumption is valid for small contact time durations [249].

We, as humans, cannot actively control the skin temperature in normal circumstances and thus, this poses a potential limitation to human material recognition capabilities using thermal sensing. This may in part explain human interpretation of metal as generally cold to touch at normal room temperatures. However, we devise a solution that robots could potentially use to overcome these challenges. Our solution relies on the fact that robots could actively control the sensor temperature by using a simple PID based feedback control and thus use multiple sensor initial conditions to overcome the thermal ambiguity. Therefore, we propose a thermal sensor module design in which we have two adjacent thermal sensors, one actively heated and one passive (unheated), which are at two different initial conditions. The actively heated sensor can control its temperature using a simple closed loop PID controller. Fig. 7.4 shows the sensor module with the two adjacent sensors. During a contact event, using the new sensor design, when the robot comes in contact with the object, it collects data using the two adjacent sensors at different initial conditions and thus, can re-

solve the ambiguous heat-conduction data arising out of certain temperature conditions of the objects.

Mathematically, from eq. (7.5), we derive the sensor initial temperature T_s for ambiguous situations to be

$$T_{\mathrm{s}} = \frac{T_{\mathrm{O1}} e_1 (e + e_2) - T_{\mathrm{O2}} e_2 (e + e_1)}{e_1 (e + e_2) - e_2 (e + e_1)}. \tag{7.6}$$

Let us assume that there is another sensor initial temperature T_s' for which thermal ambiguity exists given all other thermal conditions $(T_{\mathrm{O1}}, T_{\mathrm{O2}}, e, e_1, e_2)$ are the same. Therefore,

$$T_{\mathrm{s}}' = \frac{T_{\mathrm{O1}} e_1 (e + e_2) - T_{\mathrm{O2}} e_2 (e + e_1)}{e_1 (e + e_2) - e_2 (e + e_1)}. \tag{7.7}$$

Given all the other conditions are same, for eqs. (7.6) and (7.7) to be same, the required condition is $T_{\mathrm{s}} = T_{\mathrm{s}}'$. So, if everything else is same such as the temperature of objects and material properties of sensor and object, then there is only one sensor initial condition for which thermal ambiguity can exist. Therefore, if the sensor can be heated to a different initial condition $T_{\mathrm{s}}' \neq T_{\mathrm{s}}$, then

$$\frac{T_{\mathrm{s}}' e + T_{\mathrm{O1}} e_1}{e + e_1} \neq \frac{T_{\mathrm{s}}' e + T_{\mathrm{O2}} e_2}{e + e_2}, \tag{7.8}$$

which implies

$$T_{\mathrm{surf\_O1}} \neq T_{\mathrm{surf\_O2}} \tag{7.9}$$

and hence, they are no longer ambiguous. Fig. 7.4 shows the results with the new sensor design using two different initial conditions. It is evident that using the passive temperature sensor, the data is significantly different and the robot can overcome the ambiguity. We computed the histogram of the temperature difference of the passive sensor data under the previous found ambiguous conditions in Fig. 7.3 and compared it with the histogram of

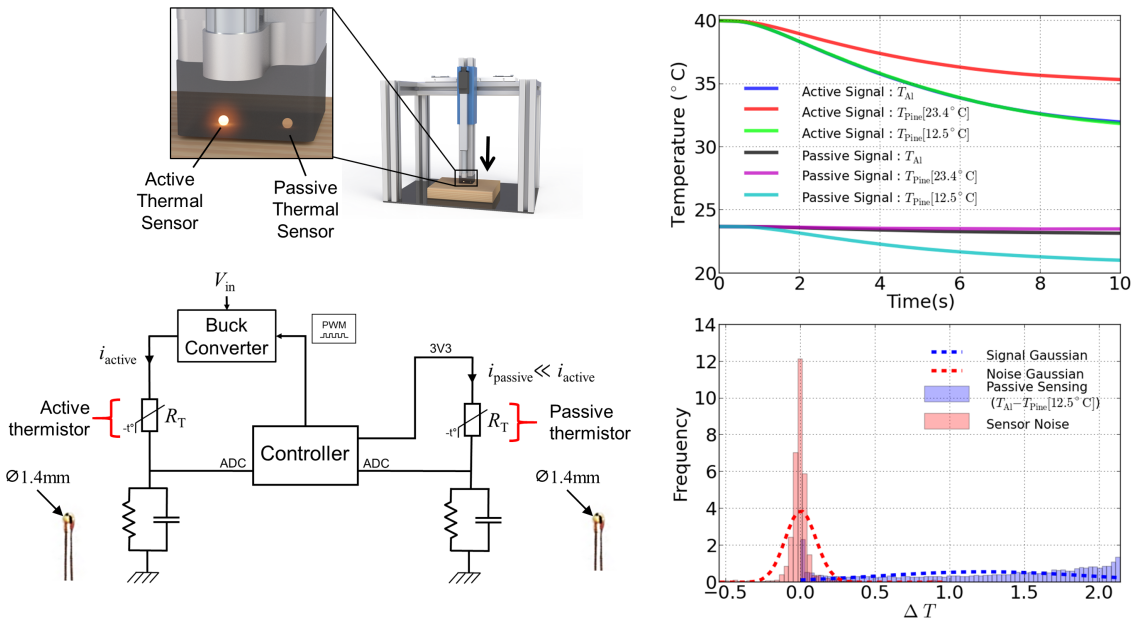

Figure 7.4: *Using two thermal sensors at two different initial temperatures (such as active and passive) robots can overcome the thermal ambiguity by inferring both the temperature and thermal properties of the material. The active thermal sensor is useful for recognizing pine wood and aluminum at room temperature but an additional passive sensor is required to distinguish between aluminum at* 23.4°C *pine wood at* 12.5°C.

sensor noise and found it to be significantly higher, thus overcoming the issue of thermal ambiguity as shown in Fig. 7.4. Note that though we have provided empirical evidence of overcoming ambiguity using an active and a passive sensor simultaneously, the method should work with two active sensors as well, so long they are at sufficiently different initial conditions.

7.3 Methods

7.3.1 Experimental Setup.

Figure 7.2 shows the 1-DoF robot used to collect thermal sensor data from samples of pine wood and aluminum. We used a Teensy 3.2 microcontroller to control the Firgelli L12 linear actuator and read data from the sensor module on the robot's end-effector and a separate passive thermistor mounted to the material sample during the experiment.

Figure 7.5 shows a circuit diagram of a self-heated thermistor powered by a buck con-

verter for active thermal sensing. We used an EPCOS B57541G1103F thermistor as a combined heat source and temperature sensor and measured its resistance using a voltage divider circuit and the microcontroller's internal 12-bit analog-to-digital converter. This resistance value is then converted to temperature in Celsius using calibration constants provided by the thermistor manufacturer. A closed-loop PID controller adjusts the duty cycle of the pulse-width modulated signal (V_{pwm}) to vary the DC output voltage from the buck converter based on the feedback voltage (V_{FB}) and the temperature of the thermistor.

Figure 7.4 shows the circuit used for combined active and passive thermal sensing. This circuit uses two identical thermistors similar to the circuit shown in Figure 7.3 except that the passive thermistor is powered by a constant $3.3\,\mathrm{V}$ input from the microcontroller and has a larger reference resistor ($10\,\mathrm{k}\Omega$ instead of $1\,\mathrm{k}\Omega$) to limit the current passing through the passive thermistor and greatly reduce the heat generation. For both the active and passive thermistors we included a physical $.022\,\mu\mathrm{F}$ capacitor in parallel with the reference resistor and 2nd order software Butterworth filter with a cutoff frequency of $10\,Hz$ to filter noise.

7.3.2 Experimental Procedure.

To achieve the thermally ambiguous temperature condition for the pine wood material sample, we used an ELBA RF80RCRW2 refrigerator with thermostat set at 50% (See Fig. 7.2) to cool the material to 8.0°C. before placing it in the 1-DoF robot in a room at 23.4 ± 0.1°C. We embedded a temperature sensor inside the wooden block to measure its temperature as it slowly warmed. When the block reached the desired temperature the robot automatically lowered the linear actuator and sensor module to make contact with the sample. We tested the pine wood at temperatures from 10°C to 15°C at 0.5°C intervals and found that the data collected at 12.5°C was most similar to the data collected from aluminum 23.4°C (See Fig. 7.3).

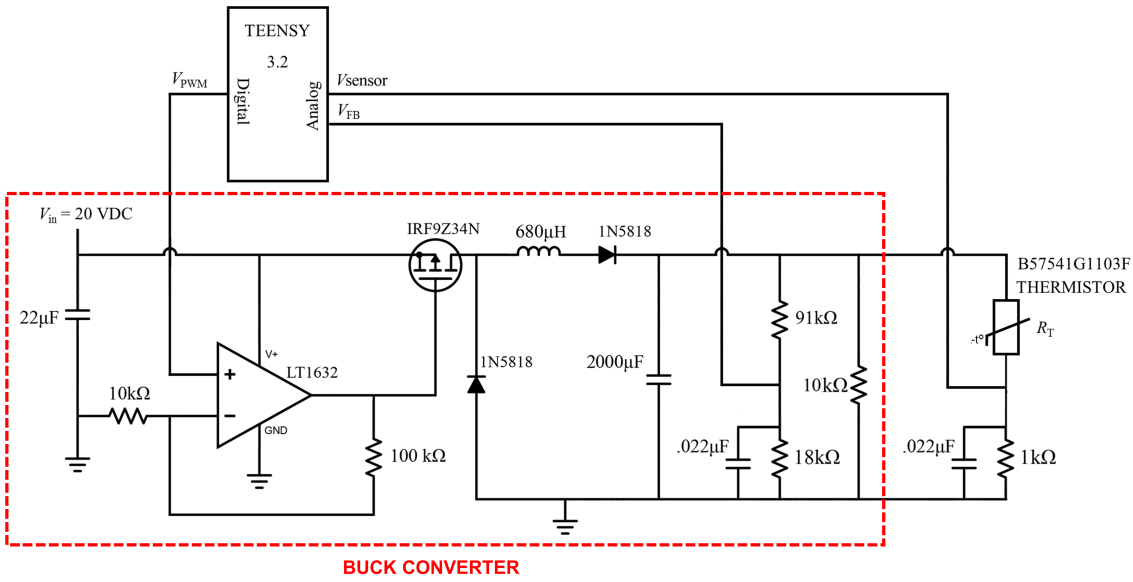

Figure 7.5: *We used a Teensy 3.2 microcontroller, buck converter and self-heated thermistor for active thermal sensing. By amplifying and smoothing a PWM signal from the microcontroller, buck converter provides a variable DC voltage source to the thermistor to heat it to* $40.0°\mathrm{C}$*. The system uses voltage divider circuit and the microcontrollers internal analog-to-digital converter to measure the resistance of the thermistor.*

CHAPTER 8
GENERALIZING IN-SITU MULTIMODAL HAPTIC PERCEPTION PERFORMANCE DURING RAPID CONTACT

8.1 Research Summary

The final part of our work focuses on combining the force, motion, and thermal modalities and analyzing if we can extend the results obtained above to real-world in-situ conditions. For this part, we focus on haptic perception using multiple modalities such force and thermal sensing with a rapid first contact between a robot and an object without using any exploratory behaviors. Robot arm velocity affects the forces that are sensed when touching an object. Time of the day affects the temperature conditions of an object. We focus on generalizing the performance of haptic perception across two robot velocities and two different times of the day. For data collection, we used a mobile robot with a telescopic arm attached to a vertical lift into a house and collected data over three days from 47 in-situ objects with a total of 67 object parts relevant to ADLs and IADLs in the bedroom, kitchen and bathroom. We used various data-driven methods such as k-NNs, SVMs, HMMs, and LSTMs to analyze the performance of categorizing objects into various compliance, mobility, material as well as object based haptic labels. Results show the importance of using multiple sensing modalities for generalizing the performance. They also show the feasibility of using data-driven methods for generalizing the performance across different robot and environment conditions.

8.2 Introduction

Inferring properties of objects or distinguishing objects by touch has many interesting challenges because sensing depends on action. Robots generally use exploratory behaviors to

maximize the sensing for inferring the object properties [30]. However, during manipulation in cluttered and uncertain environments [132] or while assisting humans during activities of daily living (ADLs) or instrumental activities of daily living (IADLs) [250], contact can happen anywhere across the robot-arm and the robot might not have the opportunity to carefully explore the object in contact. Therefore, in this paper, our objective is to analyze if a robot can perceive an object through a rapid first normal contact.

Our focus in this work is on generalizing the haptic perception performance across various robot and environment parameters using multiple sensing modalities. In our previous work, we used force sensing modality to infer properties of the objects [30], to distinguish between different object types when conditioned on an environment [31, 32], and also showed some preliminary results on generalizing the performance across various robot stiffnesses and velocities [219]. Previously, we also used thermal sensing to infer material properties and generalize the performance across various environments [251], and to distinguish object types by simplifying the problem to distinguishing between tactile foreground (target object) vs. tactile background [181].

In this work, we focus on combining the force and thermal modalities and use these to generalize the haptic perception performance across various robot and environment conditions. For haptic perception, we use various widely used and state-of-the-art data-driven methods such as k-Nearest Neighbors (k-NNs), Support Vector Machines (SVMs), hidden Markov models (HMMs), as well as Long short-term memory networks (LSTMs).

To use data-driven methods, we need data. However, collecting haptic data from objects in controlled laboratory settings might not be representative of the data in real-world environments. Note, many ADLs and IADLs take place in the bedroom, kitchen and bathroom of a common household. Collecting data from in-situ objects in these environments can give us a wide range of realistic and varying environment conditions which is otherwise difficult to obtain in a controlled laboratory setting. For our data collection we used a mobile robot with a multimodal sensor module attached at the end of a horizontal telescopic

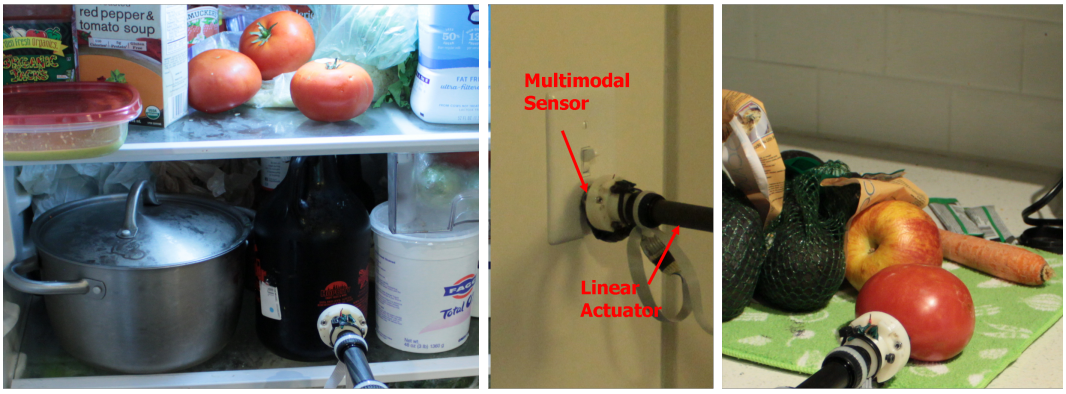

Figure 8.1: *A mobile robot with a linear actuator and a multimodal tactile sensor attached at its end touching objects such as a bottle inside refrigerator, a light switch, and a fruit.*

arm to touch various objects in the bedroom, kitchen, and bathroom of a household using a rapid first normal contact without using any exploratory behaviors.

Using the collected data, our focus is to infer various properties of an object as well as to distinguish between various object types. Knowing whether an object is soft or hard, or if the object moved during manipulation can help devise manipulation strategies such as, avoiding a hard object but pushing through a soft object which moved, to reach a goal [252]. Therefore, we focus on compliance and mobility based haptic labels. We are also interested in material based haptic labels because knowing the material of an object is also informative [251].

To distinguish object types, we identified various tasks relevant to ADLs and IADLs in which two objects are involved (such as 'putting a *towel* on *rack*', 'fetching a *bottle* from *refrigerator*', 'pushing a *door handle* on a *door surface*' to open the door etc.). Thus, knowing the task, we also focus on distinguishing between tactile foreground and tactile background.

We are also interested in analyzing if we can distinguish different object parts given an object (such as 'chair cushion' given chair, or 'chair handle' given chair).

8.3 Related Work

Most of the related work on haptic perception has focused on using exploratory probing behaviors to extract information from contact with objects. In addition, few related works have looked into generalizing the haptic perception performance across various robot and environment conditions. The following sub-sections describe some of the work on haptic perception using both single as well as multiple modalities which are the most relevant to our work presented in this paper. For this paper, we will focus on related work with force and thermal sensing modalities.

8.3.1 Single Modalities

Researchers have extensively used force and thermal sensing modalities separately to perform various object categorization tasks.

Force Sensing

Researchers have used force sensing to classify objects based on their material property, shape property, functional property etc. [30] using specific exploratory behaviors. In this sub-section, we focus on related work on material property based classification. For a more detailed survey ~~please~~ refer to [30, 219].

Drimus et al. used a novel tactile sensor comprised of a flexible, piezo-resistive rubber to classify hard and deformable objects [4] using a palpation procedure. They used a k-nearest-neighbor (k-NN) classifier to categorize the objects. Jain et al. used data-driven object centric models to haptically recognize specific doors as well as classes of doors (refrigerator vs. kitchen cabinet) [63]. Sukhoy et al. used a vibro-tactile sensor and an SVM classifier for surface texture recognition [5]. Kim and Kesavadas estimated the material properties of objects using an active tapping procedure [7] while Takamuku et al. used both tapping and squeezing behaviors [8]. Hosoda and Iwase used a recurrent neural network to

classify objects based on haptic cues learned from dynamic interactions between a bionic hand and objects during grasping behaviors [9]. Nizar et al. developed a sensor that used a lightweight plunger probe and used the optical mouse sensor to obtain surface images and implemented a radial basis function neural network to classify material type and surface properties [13]. Liarokapis et al. used force sensors on an underactuated robotic hand to classify objects with a single force closure grasp. They used random forests for classification [56]. Kiwatthana and Kaitwanidvilai used K-means clustering techniques to classify different cans using proprioceptive feedback [58]. Hoelscher et al. used BioTAC sensors [202] and Schunk F/T sensors with multiple classifiers and feature extraction methods for object recognition. They concluded that simple, dimensionally-reduced features performed better than more elaborate features [59].

Thermal Sensing

There have been many studies on material recognition using only thermal sensing. For a detailed overview of such material recognition studies, please refer to [165, 173, 174]. In this sub-section, we focus on related work on material property based classification.

Russell [134, 135] developed a thermal sensing array with which he compared the percent decrease in temperature of materials in contact and recognized six distinct materials with one trial. Monkman and Taylor [137] developed two methods of thermal sensing that they reported to be faster than Russell's [134, 135] or Siegal et al.'s [136]. One sensor used a Peltier heating element, and the other used a pyrometer and a heating element. They used the two sensors to recognize four materials with distinct thermal properties.

Other Sensing Modality

Vision modality has also been used for texture recognition [253, 254]. Recent work has shown that vision can also be used for material recognition tasks [255–259]. Bell et al. [257] introduced a large scale database, Materials in Context Database (MINC), that has 23

material categories. They also introduced a framework that combines a convolutional neural network with a fully connected conditional random field to produce pixel level material labeling of the scene with 73.1% mean class accuracy. Researchers have also used CRFs in vision problems to simultaneously segment and assign labels to each pixel in multi-class labeling problems [260–262]. Arnab et al. [259] used a joint dense CRF model to augment dense visual cues with sparse auditory cues to estimate dense object and material labels. While a basic CRF uses a pairwise potential term that incorporates local smoothing term, a dense CRF incorporates a pairwise potential between each individual pair of pixels, which enables long range interaction between pixels.

8.3.2 Multiple Modalities : Force and Thermal

Engel et al. [138, 139] achieved 90% accuracy over 50 trials for recognizing 5 materials using pressure and thermal sensing. Siegal et al. [136] developed a multimodal sensor consisting of capacitive and thermal sensors. Takamuku et al. [148] classified 5 materials using a combination of strain gauge information and thermal sensing on an anthropomorphic finger. Yang et al. [140] developed an array of conductive rubber based force sensors and temperature sensors mounted on both sides of a flexible substrate. Dario et al. [175] developed a polymer-based tactile and thermal sensor inspired by dermal and epidermal layers of human skin. Castelli [141] developed an array of capacitive tactile sensors using temperature-dependent semiconductors for absolute temperature measurement. Yuji et al. [145] developed a tactile and thermal sensor using a single pressure-conductive rubber sheet to infer both temperature and contact force. Caldwell et al. [143] developed a multimodal tactile sensor to measure contact force and thermal response during specific exploratory behaviors to infer texture, stiffness and object profile, temperature and thermal properties of 7 materials. Xu et al. used multimodal sensor feedback to identify various materials with a BioTAC sensor [202] attached to the finger of a robotic hand [146]. Chu et al. attached two BioTAC sensors [202] to the gripper of a PR2 robot and performed four

deliberate exploratory procedures on 60 objects. They used discrete HMMs to construct a feature vector of likelihoods and used binary SVM classifiers on the feature vector to assign 24 adjectives to those objects [53]. Schmitz et al. used power grasping of objects and multiple modalities for object recognition with deep learning [57].

8.3.3 Other Multiple Sensing Modalities

Taddeucci et al. [176] used a multimodal haptic sensing finger with thermal and vibration feedback and a high resolution array of tactile sensors to identify 14 objects during idealized sliding contact using neural networks. Some researchers used the BioTAC^{TM} sensor with thermal feedback to classify objects using Bayesian learning techniques, ANNs and HMMs [146, 149, 177].

Mittendorfer et al. [144] developed hexagonal multimodal sensing modules with optical proximity, thermal and acceleration-vibration modalities combined to form an array on a robot arm. In [178], the authors developed a prosthetic skin that used strain, pressure, temperature, and humidity sensors, along with electroresistive heaters.

Many studies on human multisensory perception focus on cognitive and neurological aspects, such as the binding problem [263] in cross-modal interactions [264]. Others have investigated the psychophysical aspects of combined perception with vision and haptics [265–267] using the concept of temporal synchrony and spatial coincidence. Studies have shown that, under some conditions, humans can be modeled as combining visual and haptic information using a maximum-likelihood integrator [268]. The researchers proposed that humans integrate estimates of an environmental property through each individual sensory modality by performing a maximum likelihood estimator. Some early work in integrating vision and haptics [269–271] integrated information from the two modalities to build models of objects. Researchers have also worked on various aspects of the role of multiple sensory modalities such as haptics and vision in day-to-day manipulation tasks for both humans and robots. Research on multisensor fusion has often focused on combining over-

lapping information to obtain a reliable estimate of the environment [272], and other work has focused on using modalities sequentially to guide each other, such as vision providing guidance for tactile exploration [269].

There are many studies that deal with haptic and visual perception of virtual objects [273–275] or real remote objects [276] by a human operator. Researchers have also investigated haptic and visual perception to support object perception for robot autonomy. Stansfield [269] used vision to segment an object and estimate its position and then used haptics to actively explore and perceive the object. Allen [270] used vision to obtain sparse 3-D data about regions of interest and then used haptics to actively explore regions for object recognition. Researchers have also extracted object attributes such as rheological properties [61], mass and elasticity [277], friction [278], and such by exerting known forces with haptics and observing responses with vision.

Researchers have also worked on active vision and associated information from vision to various physical interactions [279–282]. Coelho et al. [283] used vision to determine appropriate grasping strategies and then used haptics to grasp the objects. Using tasks such as flipping a light switch and operating a drawer, Nguyen and Kemp implemented SVMs with vision as input to predict if a manipulation behavior is likely to succeed at a particular 3D location [284]. Sukhoy and Stoytchev developed a framework for pressing buttons using a robot's visual and auditory percepts [285]. van Hoof et al. used vision in cluttered environments to predict an action with the highest information gain [286].

Allen [270] used vision to first determine objects of interest which the robot then explored using tactile sensing. The data from the two modalities were integrated to build a model that was compared with a model database to recognize the object. Stansfield [269] presented a robotic perceptual system that used vision to segment objects, and then haptically explored them to build a model of the object. Hosoda et al. [287] used a Hebbian network to learn consistency between data from a camera and tactile sensors to identify slip. Zytkow and Pachowicz [271] used vision and touch to learn object manipulation

tasks. Luo et al. [288] combined vision and tactile sensing to localize the local point of contact by matching tactile feature with the visual map. In this work, we propose the use of dense CRFs to integrate the material classification predictions from tactile sensing and those made using vision to generate labels for the entire scene.

Kroemer et al. autonomously inferred low-dimensional representations from contact vibration tactile data by sliding a tactile sensor on 26 rich multi-scale surfaces of 17 different materials. They used both tactile and vision data in the training phase and created a mapping matrix, which they used in the testing phase with only tactile data [289]. Ueda et al. [12] used vision to observe the deformation of an object after interacting with it and used this information to extract rheological properties of the object. Charniya and Dudul [290], used a lightweight plunger and an optical mouse to take the surface image to classify the material. Zheng et al. [291] used deep learning for surface material classification using surface texture images and time-series of acceleration data measured from scratching the surface. They used multiple convolutional neural networks, one with images as inputs and the other with spectrograms of acceleration signals as inputs and used a fully-connected layer to combine information from both.

Gao et al. [292] trained two CNNs for haptic and vision data and combined their output using a fusion layer to assign up to 24 haptic adjectives to an object. To use the highest-performing version of their algorithm, a robot would obtain images of the object from multiple views, and record tactile signals while touching the object with four exploratory behaviors (*hold*, *squeeze*, *slow slide*, and *fast slide*). This work is strongly related to ours. For example, their haptic adjectives could be considered a type of haptic label, and they make use of the same material recognition CNN from Bell et al. [257] that we do. However, they focus on assigning multiple haptic labels to a single isolated object that the robot has haptically explored. In contrast, we focus on assigning haptic labels to locations all around the robot to produce a haptic map. Our current algorithm assigns a single haptic label to each location with the notion that the haptic label could be inferred by touching the

location.

Researchers have also looked at using haptics for mapping tasks. Haptic maps generated via active exploration [293–295] and incidental contact [32] tend to be sparse due to the local nature of tactile sensing. Relatively few studies have looked at mapping using both haptics and vision modalities. However, researchers have studied various ways of haptically mapping the environment by assigning physical properties to objects using only tactile sensors. Some studies focused on presenting haptic information using a 'haptograph' that uses frequency and spatial analysis to represent contact information [296, 297]. Schaeffer and Okamura [293] used various probabilistic methods to simultaneously localize the movement of a robotic fingertip while haptically mapping the surface. Rui et al. used Gelsight tactile sensing to localize the pose of small parts grasped using a robot hand [298]. Alt and Steinbach developed a visuo-haptic sensor which uses vision to monitor the deformation of a plastic foam in contact to attribute haptic properties to objects in the environment [294]. Fox et al. [295] used data from a whiskered robot for grid-based Tactile SLAM to generate an occupancy grid. All these studies focus on building the haptic map based on tactile data alone, and thus, the maps are local and limited to the area of active exploration.

8.4 Approach

8.4.1 Relevant Haptic Labels

We have adopted various data-driven approaches to address the problem of generalizing the performance of haptic perception to various situations. For haptic perception, we are interested in compliance-based, mobility-based, material-based, and object-based haptic labels. For generalization, we are interested in generalization across time, velocity and instance as described in Section 8.4.2. In addition to inferring compliance, mobility, and material properties of an object, we have also focused on distinguishing between different object types.

Compliance and Mobility

To infer compliance and mobility based properties, we are interested in inferring if an object is 'hard' or 'soft', of if the object 'moved' during the physical interaction between robot and object. Specifically, we perform three kinds of classification tasks :

- 'Hard' vs. 'Soft',
- 'Moved' vs. 'Unmoved',
- 'Hard-Unmoved' vs. 'Soft-Unmoved' vs. 'Hard-Moved' vs. 'Soft-Moved'.

Tactile Foreground vs. Tactile Background

In our previous paper, we introduced the notion of 'tactile foreground' and 'tactile background' [181]. During a task-driven manipulation task while manipulating a target object (tactile foreground), a robot might come in contact with another object (tactile background) in its immediate vicinity. Therefore, instead of doing an all-inclusive multiclass classification, we could simplify the problem to the problem of classification between 'tactile foreground' and 'tactile background'. We have identified 50 such comparisons for the objects relevant to ADLs and IADLs in a household environment, such as 'rack vs. towel', 'bottle vs. refrigerator', 'book cover vs. book spine', 'TV vs. TV remote', 'fruits vs. kitchen countertop', 'kitchen faucet vs. kitchen backsplash', 'chair cushion vs. chair frame', 'socket vs dry wall', 'door handle vs. door frame' etc. The training data had 10 trials (collected with one velocity or at one time depending upon the generalization scheme) from one of the objects in each foreground-background pair and the testing data had 10 trials from the other object (collected with the other velocity or at another time depending upon the generalization scheme) in the pair. We repeated this classification method for 50 such foreground-background pairs.

Material

We are also interested in material property based haptic labels. We sampled 67 object parts relevant to ADLs and IADLs in the bedroom, kitchen and bathroom of a household. We noted the materials of each of these object parts and found that there are 14 materials that the object parts are made of. Our objective is to perform binary classification between every combination of these 14 materials (inspired by 'tactile foreground' and 'tactile background') thus leading to 91 such comparisons. The 14 materials are 'Foam', 'Aluminum', 'Wood', 'Steel', 'Dry Wall', 'Plastic', 'Glass', 'Paper', 'Porcelain', 'Granite', 'Cardboard', 'Fiberglass', 'Vegetable Matter', and 'Fabric'.

Object Parts given Object

Finally, we also focus on analyzing whether using multiple modalities, we could classify between different object parts given an object. This could be useful in assistive manipulation scenarios such as assisting a human sitting on a chair or lying in a bed. Knowing whether the robot made contact with 'chair cushion or chair frame given its manipulating near a chair' could be useful in devising manipulation or control strategies used by the robot. Similarly, knowing if the robot is in 'contact with bed frame or the mattress or pillow on the bed given its performing a task near the bed' could provide relevant and useful information to the robot's manipulation task. We have identified 13 such comparisons involving two to three object parts given an object in the bedroom, kitchen, and bathroom of a household.

8.4.2 Generalization Tasks

For generalizing the haptic performance, we focus on generalizing the classification results using force and thermal sensing modalities across time, velocity and instance. This is because force signals depend on the impact velocity [219] whereas thermal signals might depend on the time of the day because temperature can be different at different times of the

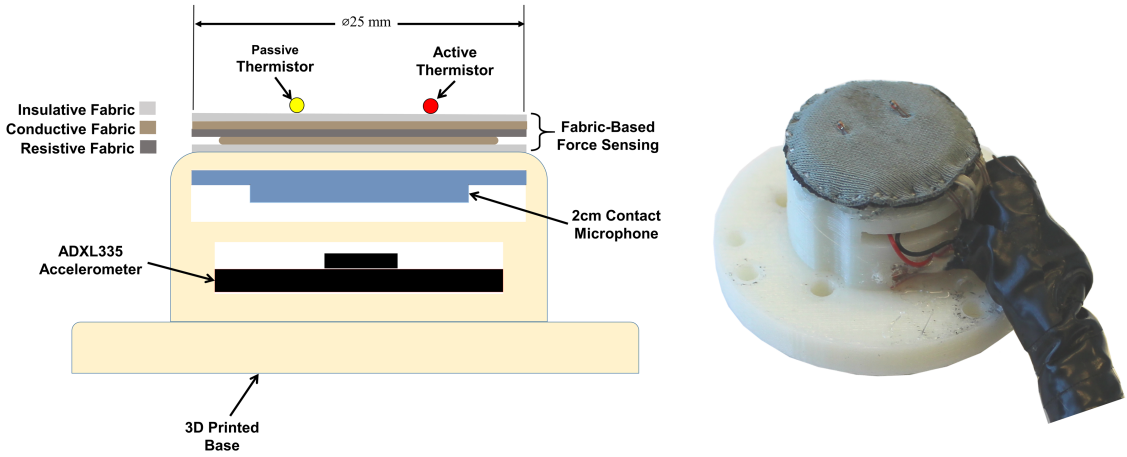

Figure 8.2: *Multimodal sensor module.*

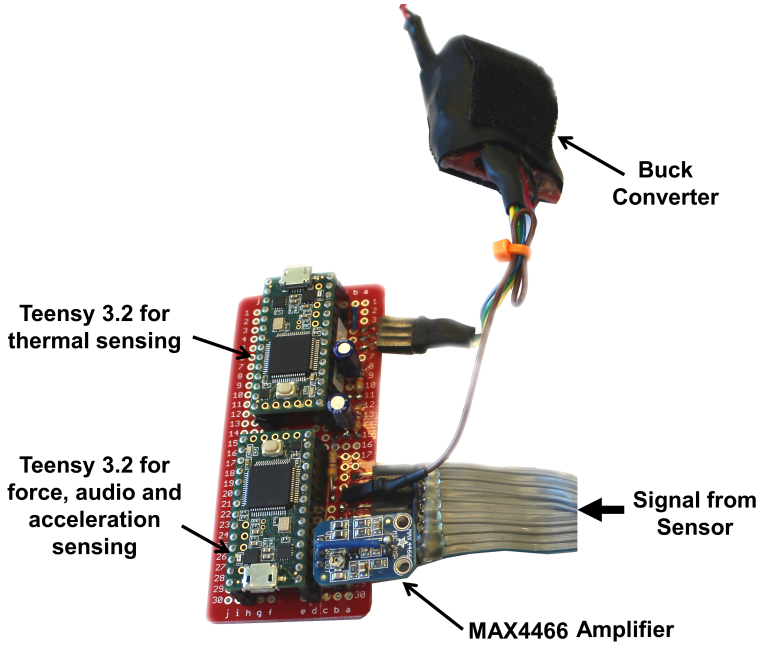

Figure 8.3: *Teensy 3.2 microcontrollers Hardware for analog-to-digital conversion (ADC) and buck converter to power active thermal sensor.*

day or on different days.

Generalizing Across velocity

For this generalization experiment, we varied the robot-arm velocity to two distinct velocities. The 'slow' velocity was half the 'fast' velocity. We were interested to see if the results obtained using data-driven methods trained on data collected at one velocity from various objects through multiple trials can generalize to data collected from the same set of objects through multiple trials at another velocity.

Generalizing Across Time

For this experiment, we wanted to see if the results obtained using data-driven methods trained on data collected at one time of a day can generalize to data collected at another time on another day. This is challenging because at different times of the day, the ambient temperature conditions are different due to various HVAC, daylight, and other conditions (temperature in a bathroom is different before and after a hot shower, temperature in a kitchen near the oven is different before cooking in the morning and after cooking in the afternoon). This changes the temperature of objects in the house, which in turn affect the heat-transfer data. Therefore, we collected the data from the same set of objects with multiple trials at two different times over a period of three days.

Generalizing Across Instance

For this experiment, we wanted to see if the results obtained using data-driven methods trained on a set of objects in one specific category with a particular velocity can generalize to another object in the same category with the same velocity. We focused this analysis on the 'Hard vs. Soft' and 'Moved vs. Unmoved' classification problems. We used 'Leave-one-object-out' crossvalidation scheme for testing the generalizing scheme, which means that data from the same object is not in both the training and testing set.

8.4.3 Experiments with a Mobile Robot

Experimental Setup

Our experimental setup consists of a multimodal sensor attached at the end of a linear actuator on a mobile robot, and the environment which includes the objects.

The Multimodal Sensor Figure 8.2 shows the mulitmodal tactile sensor module with force, audio, acceleration, active and passive thermal sensing modalities. We did not perform any analysis with the audio sensing modality in this paper. As shown in the figure, the individual sensors are attached to a 3D printed base. Figure 8.3 shows the system separate circuit module with two Teensy 3.2 microcontrollers and a buck converter to provide power to and read data from the various sensors using the microcontrollers' built in analog-to-digital converters (ADCs).

The fabric-based force sensor is based on the design in [180]. It reads force data at 1kHz. We used a voltage divider reference resistor, $R_{\text{ref}} = 1\,\text{k}\Omega$. Because the fabric-based electrodes are comparatively small compared to the touched objects, we assumed the contact would cover the entire sensor's area. We also assumed the curvature of the contact surface be small with respect to the sensor size, approximating the surface as flat. In this work we used the fabric-based force sensor to detect the start of contact with a force threshold of 0.1 N. We used a 2 cm contact microphone and a MAX4466 amplifier with the gain set at 25 to measure audio signals resulting from contact. The Teensy 3.2 microcontroller shown in Fig. 8.3 measures the signals from the contact microphone at 10 kHz. We used an ADXL335 Accelerometer with a bandwidth of 500 Hz to measure acceleration normal to the surface of the sensor. Similarly to the force sensor, we sampled the acceleration signals at 1 kHz.

The active thermal sensor uses a self-heated 10 kΩ B57541G1103F NTC thermistor [218]. It reads data at 100 Hz. The active thermal sensor is self-heated with an adjustable voltage input from a digitally-controlled buck converter (see Fig. 8.3). We use a closed-

loop temperature controller to heat the thermistor to $55\,^{\circ}\mathrm{C}$ prior to contact with the object. Once the fabric-based force sensor detects contact, this closed-loop temperature controller turns off by holding the desired buck converter voltage, V_{des}, constant. This is necessary to ensure that the temperature controller does not cancel potentially-informative temperature changes resulting from contact.

The passive thermal sensor uses a second $10\,\mathrm{k}\Omega$ B57541G1103F NTC thermistor [218] similar to the active thermal sensor and also reads data at 100 Hz. However, the passive thermal sensor is powered by a constant 3.3 V input from the microcontroller rather than a higher voltage buck converter.

The Environment The environment was the household of Joshua Wade, who worked with me actively on this experiment. It consisted of 12 objects with 22 object parts in the bedroom (See Fig. 8.4), 9 objects with 15 object parts in the bathroom (See Fig. 8.5), and 26 objects with 30 object parts in the kitchen (See Fig. 8.6). We chose all these objects because they are relevant to various ADLs and IADLs in a common household. Figure 8.7 shows a close-up shot from each of these object parts in the three rooms.

Experimental Procedure

Our experimental procedure consisted of manually placing the mobile robot to a location in a room using a joystick controller from which a specific object could be reached. In the experimental trial, the robot then autonomously reached towards the object to make a rapid first contact with the object. We set the robot-arm linear actuator to move at a specific velocity ('slow : 3 cm/s' or 'fast : 6 cm/s') until it came in contact with the object and the force threshold of 5 N is not exceeded. We detected contact using the fabric-based force sensor on the multimodal sensor module. We programed the robot-arm to be in contact with the object for 5 seconds or till the robot arm pushes into the object for 2 cm, whichever is earlier. However, note that for this work, we used only 2 seconds of data after onset of

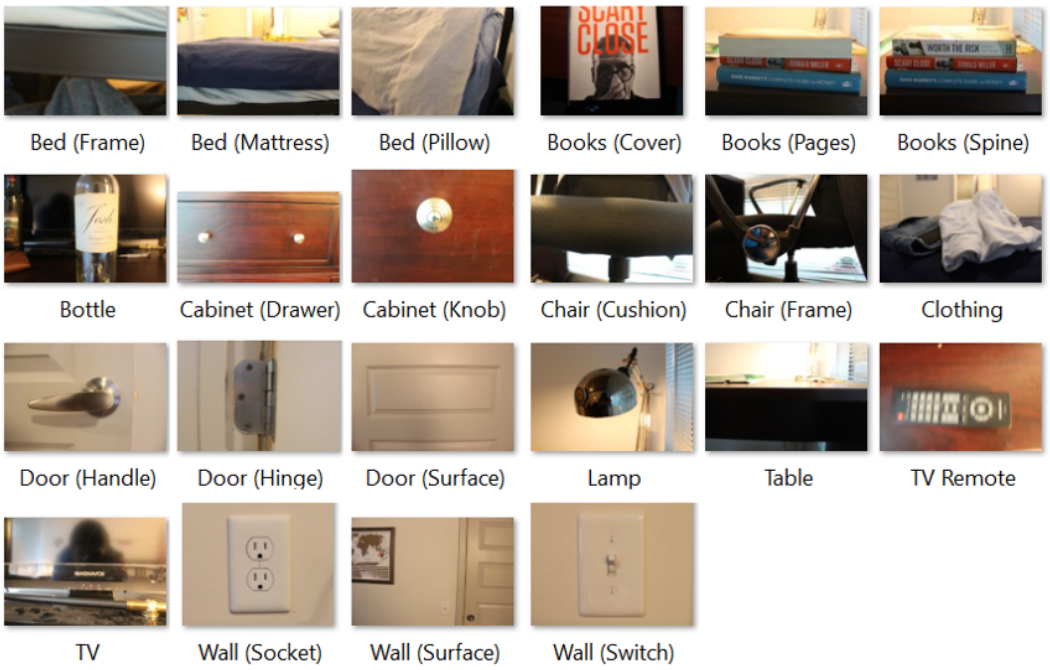

Figure 8.4: *Objects touched in bedroom.*

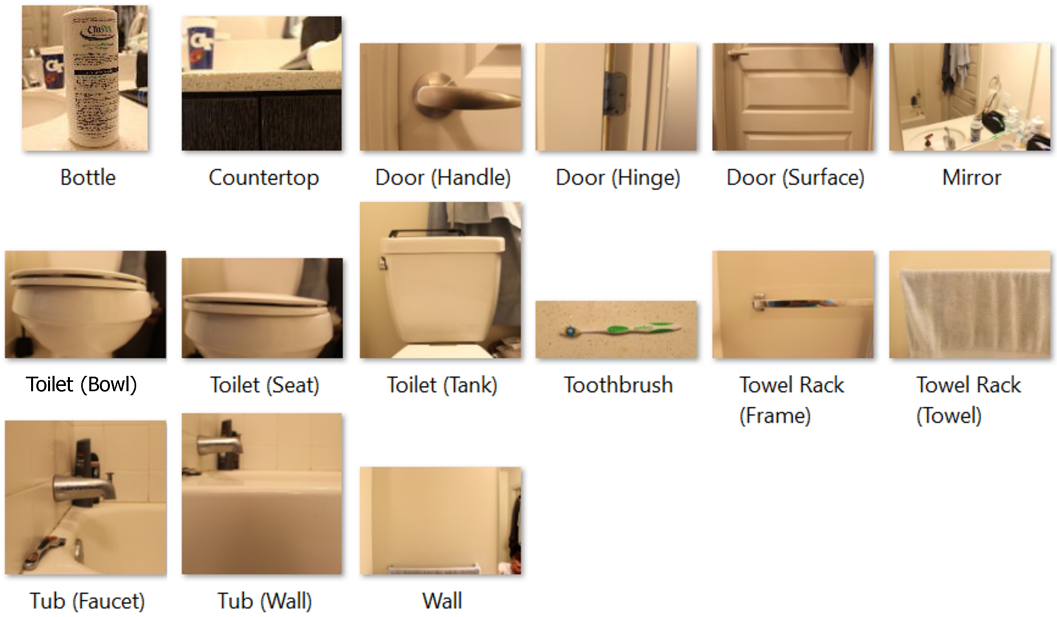

Figure 8.5: *Objects touched in bathroom.*

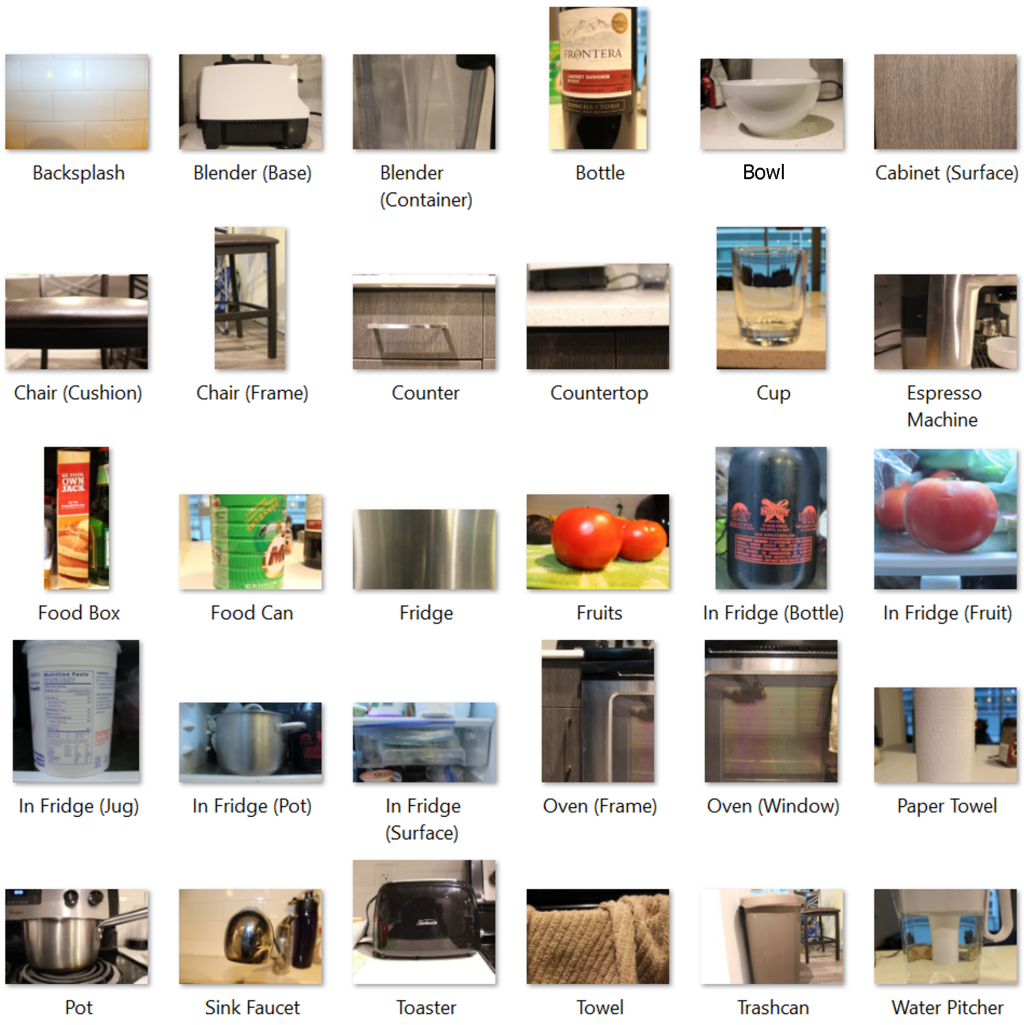

Figure 8.6: *Objects touched in kitchen.*

contact for all data analysis purposes. 2 seconds of data was present for all robot-object interaction cases. After the contact duration, the linear actuator retracted fully and waited at that position for 20 seconds for the thermal sensors in the multimodal sensor module to reach a consistent initial condition before the next trial. Note that for objects with large surface area, we sampled the space such that at every trial, the robot collected data from a different part of the object surface. For objects with small surface area, we collected data from the same spot over multiple trials. The waiting period of 20 seconds also ensured that the object was at the same initial temperature for the next trial. This is because the small amount of heat transferred to the object from the contact sensor would dissipate in a small amount of time. We repeated this procedure for multiple trials across various objects in the three rooms over a period of three days.

Data Collection and Preprocessing

We collected data from all the objects over a period of three days. The first day, we required around three hours in the morning to transfer the robot from the lab to the house and then set it up there for data collection. Our first day's data collection started from 11.50 AM and continued till 6.50 PM. Our second day's data collection started from 9 AM and continued till 10.45 PM. Our third and final day's data collection started from 9.40 AM and continued till 10.40 PM. During the data collection, we ensured that we collected data from the same object at different times of the day (either 'Morning - early Afternoon' or 'Afternoon - late Night'). For each object part at one specific time, once we manually position the robot's mobile base at a particular location using the joystick controller, the robot autonomously reaches and touches the object 10 times, 5 times with 'slow' velocity (3 cm/s) and then, 5 times with 'fast' velocity (6 cm/s). After 5 trials with 'slow' velocity, we reset the object back to the original position before the next 5 trials with 'fast' velocity, if the object moved during the trials. We do this to ensure the robot initially touches the object at the same condition for the first trial in each of the 'slow' and 'fast' group of trials. We collected 20

Figure 8.7: *Some examples of the robot with the multimodal tactile sensor touching various objects such as kitchen towel, wall socket, revolving chair cushion, trash can, door handle, door hinge, book spine, light switch, utensil, bottle inside refrigerator, box in cabinet, clothing, heated lamp, cabinet handle, fixed chair cushion, bathroom mirror, fruit inside refrigerator, pillow, cabinet knob, fruit, toilet seat, sink faucet, toothbrush, bowl, towel on rack, etc.*

trials (5 trials x 2 velocitys x 2 times) for each of the 67 object parts, thus collecting a total of 1340 trials. For each of these trials, we collected time-series vectors of force (f), motion (relative position of the robot arm after onset of contact) (m), active thermal (h), and passive thermal (t) modalities. We sampled the high frequency force and motion signals (1000 Hz.) to match the frequency of active and passive thermal signals (100 Hz.). Note, when we used combinations of features, we scaled each feature (ft) to a scaled feature (S_{ft}) according to eq. (8.1) to normalize the values.

$$S_{ft} = (ft - \text{mean}(ft)) / \text{std}(ft) \tag{8.1}$$

For labeling the objects, we used independent labeling from two experimenters and then convened after the experiments to match the labels for material-based labels, 'hard' or 'soft' labels, and 'moved' or 'unmoved' labels. We did not have any disagreements and our independent labeling matched unanimously. We also noted down the 'surface material' and the 'dominant material' for each object (some objects can have a different surface material than the dominant material such as a 'paper label' on a 'glass bottle'). However, we used the dominant material as the material label for these sets of analyses. We also measured the stiffness of the objects using a compression spring. For very hard objects, we could not measure the stiffness accurately as the deformation is minimal. For those objects, we just put it as stiffness greater than $100,000$ N/m which is the highest stiffness measurable by the device. At the end of the experiment, we found that both the experimenters tended to classify objects with stiffness lower than $10,000$ N/m as 'soft' and objects with stiffness greater than $10,000$ N/m as 'hard'. We also noted the labels were highly skewed as the ratio of number of trials with hard objects to soft objects was around 83%. Also, to label objects as 'moved' or 'unmoved', we assigned the labels in real-time because during some of the manipulation tasks, the object moved for some trials but did not for some others (e.g. an object could move till it hits a background wall). Again, the labels were skewed towards unmoved objects and the ratio of the number of trials of unmoved objects to that of

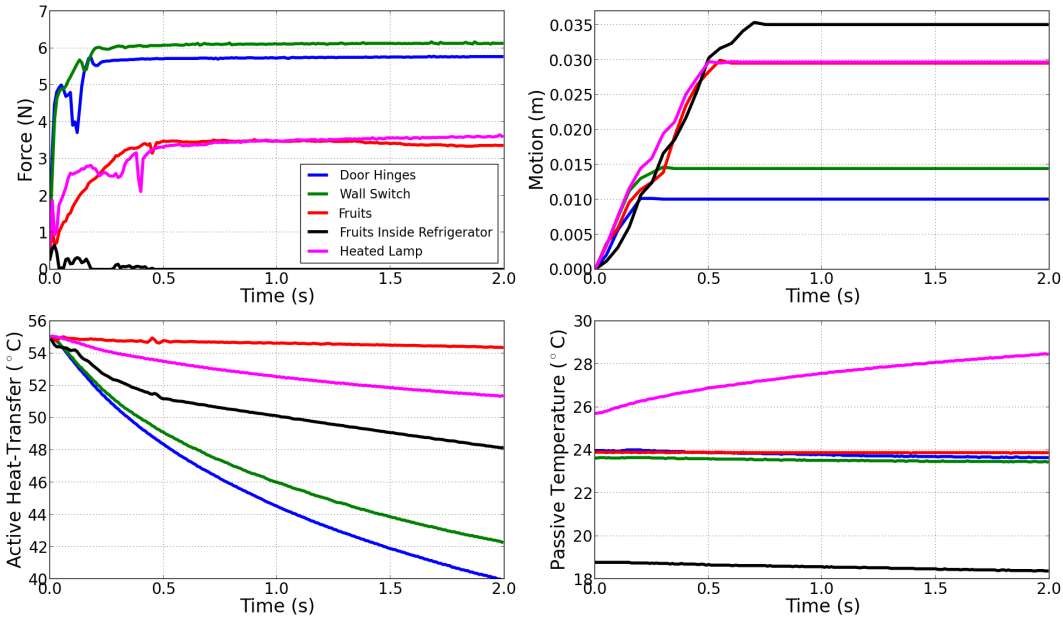

Figure 8.8: *This figure shows force, motion, active heat, and passive temperature data from five examples of objects. From the graph, we see that for hard and unmoved objects, the magnitude of forces go up higher than softer objects or objects which moved. Note, the fruit inside refrigerator rolled and moved significantly such that interaction forces decreased and eventually the fruit broke contact with the sensor. Also, interestingly, the heat-transfer from fruit is different when outside vs. when inside refrigerator. This is probably because the fruit inside the refrigerator is at a lower temperature initially and that changes the heat-transfer between the sensor and the fruit. Also, similarly note that the heated lamp (made of Aluminum) is at a higher temperature initially, and hence the heat-transfer data is different from that of an aluminum block at normal room temperature [251].*

moved objects was around 75%. Figure 8.9 shows image sequences of the robot touching and pushing objects and Figure 8.8 shows examples of multimodal data from the robot touching some objects.

8.4.4 Data-driven Methods

We used four data-driven algorithms to compare their generalization performance in classifying the objects into their various haptic labels. We selected these data-driven machine-learning algorithms based on their wide usage and suitability for time series. We used various combinations of the force, motion, active and passive thermal time-series vectors as the features for analyzing the performance. Note for each algorithm, we used the same

set of corresponding parameters with which we found success after exhaustive grid search in their corresponding parameter space in Chapters 2 and 4.

Support Vector Machines

We implemented binary support vector machines (SVMs) using the scikit-learn package [109] in Python. We used a linear kernel. To produce feature vectors for training, we truncated each feature to 2.0 seconds after the onset of contact (detected using the fabric-based force sensor). For the active thermal modality, we also estimated the slope of the raw temperature data using first central difference. We concatenate the features to obtain a $200 * (n + 1)$-dimensional feature vector where 'n' is the number of sensing modalities.

k-Nearest Neighbors

We also implemented 1-nearest neighbor (k-NN with k=1) using the scikit-learn package [109] in Python. We used the same concatenated feature vector. However, we have previously seen that k-NNs tend to get affected by the noise in haptic data [30] and therefore, to reduce the effect of noise and overfitting, we computed a low-dimensional representation of the training data with principal component analysis (PCA) before classification with 1-NN. In our classification experiments, we used 3 principal components for dimensionality reduction similar to our implementation with force sensing in Chapter 2. Note, 3 principal components could account for more than 95% of the variance of the 400-dimensional feature vector.

Hidden Markov Models

We used a hidden Markov model (HMM) for each candidate category. We used multivariate continuous left-right HMMs with 10 hidden states and $n + 1$ dimensional Gaussian emissions. We set a uniform prior to all the states. We used a spherical covariance matrix structure for initialization. We implemented them using the GHMM toolkit [106] in

Python. We decided on these specifications based on our previous results [31, 252]. We trained these HMMs with the standard Baum-Welch algorithm. For testing, we ran the Viterbi algorithm to find the HMM with the most probable state sequence given the observations and classified the category as being the category associated with this HMM [65].

Long Short-term Memory Networks

Finally, we also implemented long short-term memory (LSTM) networks [69] which have shown promise in modeling time-series in many applications [66–68, 70–73].

In this paper, we used an LSTM structure where each memory cell has an input gate, a forget gate, and an output gate. We implemented a stacked-LSTM structure of 2 layers with 50 cells each. We also added a dropout layer in between the two layers, which helps in regularization. We added an dense output layer which was fully connected. The LSTM has a total of 31,004 parameters. We initialized the parameters with uniform distribution, used 'softsign' activation functions for the hidden layers, and 'softmax' activation function [107] for the fully connected output layer. Our dropout probability was 0.2. We used 'RMSprop' [107] as the optimizer and 'categorical_crossentropy' [107] as our loss function because our task is a classification task. We used 'MinMaxScaler' function [107] to scale multivariate features for LSTMs. These parameters and choice of functions are similar to our implementation in Chapter 2 with which we found the best results after an exhaustive search in the parameter space.

8.5 Results and Discussion

We describe our haptic perception results based on haptic labels given below in the following sub-sections. For each of the haptic label based classification, we present results with different combinations of force (f), motion (m), active thermal (h), and passive thermal (t) features. For generalization across velocity, we trained on one velocity and tested on another velocity (across both the times) and vice-versa and reported the average percentage

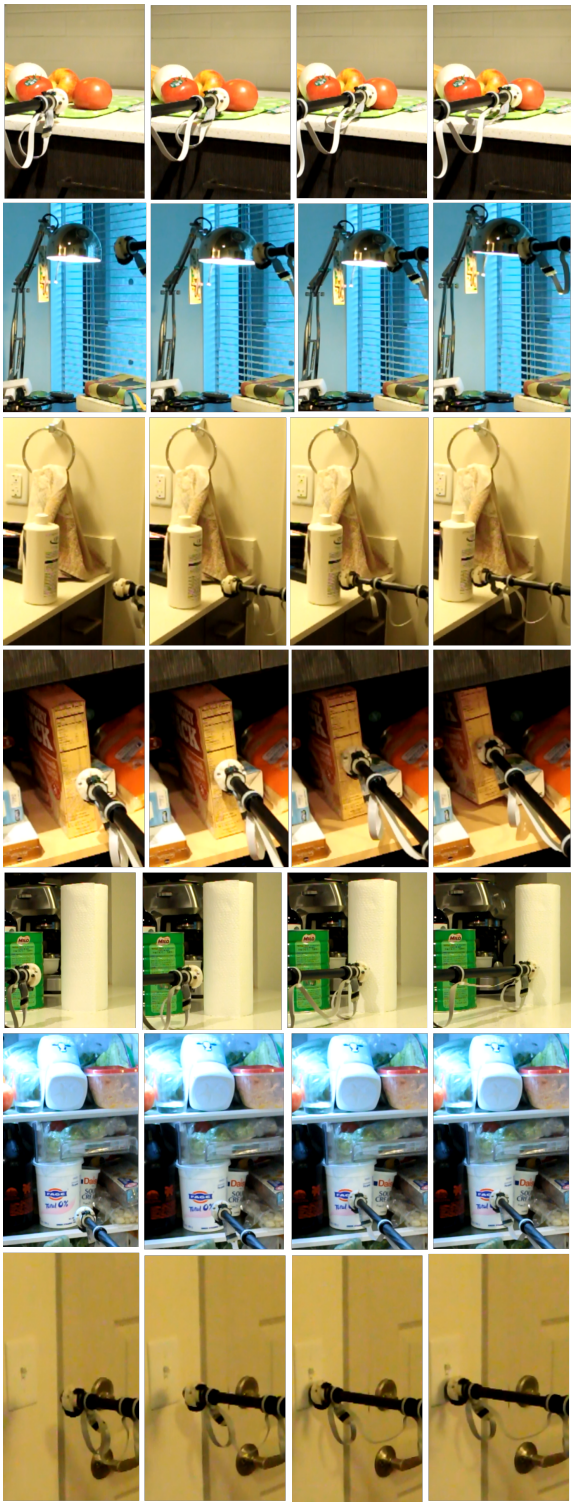

Figure 8.9: *Image sequences (left-to-right) showing the experimental procedure of the linear actuator with the multimodal tactile sensor touching various objects such as a tomato, a heated lamp, a plastic bottle, a cardboard box, a kitchen towel roll, a bottle inside refrigerator, a light switch and pushing them. Note the cardboard box tipped at the end of its motion, the tomato rolled slightly, while some of the other objects just slid away, and some objects were unmoved. Also note, some objects were hard whereas some were soft.*

accuracy. For generalization across time, we trained on one time and tested on another time (across both the velocities) and vice-versa and reported the average percentage accuracy.

8.5.1 Compliance and Mobility based Labels

For compliance and mobility based categories, we performed three kinds of classification tasks - 'Hard' vs. 'Soft', 'Unmoved' vs. 'Moved', and 'Hard-Unmoved' vs. 'Hard-Moved' vs. 'Soft-Unmoved' vs. 'Soft-Moved'. Note that this categorization task is highly skewed because of the objects we have collected data from, and a majority classifier can do very well on these tasks as well.

Generalizing Across velocity

The top row in Tables 8.1, 8.2, and 8.3 shows the results for haptic perception when trained in one velocity but tested on another velocity. Irrespective of the type of categorization for the compliance and mobility based haptic labels, multivariate HMMs usually show the best results whereas 1-NN with single features show the worst results. Univariate HMMs with temperature feature also show the worst result as temperature modality alone does not inform much about the compliance or mobility of an object.

Generalizing Across Time

The middle row in Tables 8.1, 8.2, and 8.3 show the results for haptic perception when trained in one time but tested on another time. Irrespective of the type of categorization for compliance and mobility based haptic labels, SVMs with both force and motion features give the best results. Similar to the generalization results for velocity, the worst results are for 1-NN with single features. Univariate HMMs with heat-transfer feature also performs the worst in two cases. Again, this is intuitive because we do not expect heat-transfer feature to be informative about the compliance or mobility of an object.

Table 8.1: Hard vs. Soft

Summary of Algorithm Performance for Hard vs. Soft Categorization with 2 seconds of contact. Note 'f' = force, 'm' = motion, 'h' = active thermal (heat-transfer), and 't' = passive thermal (temperature) feature. Also, generalization across instance means 'leave-one-object-out' cross-validation where data from the same object is not in both training and testing sets.

Generalize Across	Best and Worst	Algorithm	Features	Accuracy (%)
Velocity	Best	HMM	f+m+h+t	**86**
	Worst	1-NN	f	61
Time	Best	SVM	f+m	**87**
	Worst	HMM	h	50
Instance	Best	HMM	f+m+h+t	**92**
	Worst	1-NN	h+t	67
		Majority Classifier		83
		Random Guess		50

Table 8.2: Moved vs. Unmoved

Summary of Algorithm Performance for Moved vs. Unmoved Categorization with 2 seconds of contact. Note 'f' = force, 'm' = motion, 'h' = active thermal (heat-transfer), and 't' = passive thermal (temperature) feature. Also, generalization across instance means 'leave-one-object-out' cross-validation where data from the same object is not in both training and testing sets.

Generalize Across	Best and Worst	Algorithm	Features	Accuracy (%)
Velocity	Best	HMM	f+m+h+t	**93**
	Worst	1-NN	f	23
Time	Best	SVM	f+m	**94**
	Worst	1-NN	h	54
Instance	Best	HMM	f+m	**100**
	Worst	LSTM	m	53
		Majority Classifier		76
		Random Guess		50

Table 8.3: Hard-Unmoved vs. Hard-Moved vs. Soft-Unmoved vs. Soft-Moved

Summary of Algorithm Performance for Hard-Unmoved vs. Soft-Unmoved vs. Hard-Moved vs. Soft-Moved Categorization with 2 seconds of contact. Note 'f' = force, 'm' = motion, 'h' = active thermal (heat-transfer), and 't' = passive thermal (temperature) feature.

Generalize Across	Best and Worst	Algorithm	Features	Accuracy (%)
Velocity	Best	HMM	f+m+h+t	**83**
	Worst	HMM	t	13
Time	Best	SVM	f+m	**84**
	Worst	1-NN	h	27
		Majority Classifier		66
		Random Guess		25

Generalizing Across Instance

For the generalization across instance tasks, we performed a 'Leave-One-Object-Out' cross-validation for only 'Hard' vs. 'Soft' and 'Unmoved' vs. 'Moved' categorization tasks with fixed velocity across time. This means that data from the same object was not present in both the training and testing sets. We report average accuracy across both the velocities. The bottom row in Tables 8.1, and 8.2 show the results. Again, irrespective of whether its the 'Hard vs. Soft' or 'Moved vs. Unmoved' categorization, multivariate HMMs perform the best and 1-NNs perform the worst. In one case, LSTMs perform the worst as well. This is probably because the amount of training data is not significantly more than the testing data.

Overall Results

Figure 8.10 shows the overall results. From the charts we note that, irrespective of algorithms used, on average, force and motion features are especially important for classifying compliance and mobility based haptic labels and generalizing the results to different conditions.

8.5.2 Material based Labels

Table 8.4 shows the results for binary material recognition. Note, we did not implement LSTMs for this categorization task as the amount of training data is less.

Generalizing Across velocity

The top four rows in Table 8.4 show the generalization results across velocities. SVMs with all the features of force, motion, heat-transfer, and temperature show the best results. This shows that all these modalities with complimentary information are important for getting material specific information. The worst results are given by univariate HMMs with force or temperature features as these features alone cannot extract relevant information for material recognition. Forces, in addition to the mechanics of contact, depend on the stiffness of an object and its a combination of material as well as structural property. Thus, having only forces might confuse the system about material specific features. Similarly, passive thermal sensing measures the temperature of an object and this is a function of the ambient temperature rather than just the object characteristics. Thus, temperature alone can also not give useful information for material recognition tasks.

Generalizing Across Time

The bottom four rows in Table 8.4 show the generalization results across time. Again, SVM with all the features give the best results which shows the importance of all the features for material recognition problems. And again, univariate HMMs and 1-NNs give the worst performance with just force and temperature features, probably because of similar reasons outlined above.

Overall Results

Figure 8.10 shows the overall results. From the charts we note that, irrespective of algorithms used, on average, all four features (force, motion, heat, and temperature) features

Table 8.4: Binary Material Recognition

Summary of Algorithm Performance for Binary Material Recognition with 2 *seconds of contact. Note 'f' = force, 'm' = motion, 'h' = active thermal (heat-transfer), and 't' = passive thermal (temperature) feature.*

Generalize Across	Best and Worst	Algorithm	Features	Accuracy (%)
Velocity	Best	SVM	f+m+h+t	**82**
	Worst	HMM	t	60
Time	Best	SVM	f+m+h+t	**86**
	Worst	1-NN	t	56
		Majority Classifier		50
		Random Guess		50

are important for classifying material based haptic labels and generalizing the results to different conditions. However, passive temperature modality does not seem to be very informative for this task.

8.5.3 Tactile Foreground vs. Tactile Background : Object based Labels

Table 8.5 shows the results for tactile foreground vs. tactile background classification. Note, we did not implement LSTMs for this categorization task as the amount of training data is less.

Generalizing Across velocity

The top four rows in Table 8.5 show the results for generalization across two velocities. SVMs with all features show the best results for this recognition task. Similar to the binary material recognition results in Section 8.5.2, these show the importance of all the features in recognizing two objects. The worst results are for 1-NN with temperature feature alone or with HMMs with force and motion features. Again, this could be because passive temperature sensing is a function of the ambient temperature rather than the object alone. Also, this shows that heat-transfer modality (active thermal sensing) is an important feature for

Table 8.5: Distinguish Two Objects (Tactile Foreground vs. Tactile Background)

Summary of Algorithm Performance for Distinguishing two Objects with 2 *seconds of contact. Note 'f' = force, 'm' = motion, 'h' = active thermal (heat-transfer), and 't' = passive thermal (temperature) feature.*

Generalize Across	Best and Worst	Algorithm	Features	Accuracy (%)
Velocity	Best	SVM	f+m+h+t	**91**
	Worst	1-NN	t	55
Time	Best	SVM	f+m+h+t	**83**
	Worst	1-NN	t	55
		Majority Classifier		50
		Random Guess		50

object categorization task. This agrees with our previous result in [181].

Generalizing Across Time

The bottom four rows in Table 8.5 show the results for generalization across two time. Here, again SVMs with all the features give the best results whereas 1-NNs with temperature feature and HMMs with force and motion features perform the worst, probably because of the same reasons outlined above. This result is exactly same as that for results of generalization across velocities.

Overall Results

Figure 8.10 shows the overall results. From the charts we note that, irrespective of algorithms used, on average, all four features (force, motion, heat, and temperature) features are important for distinguishing objects (tactile foreground vs. tactile background) and generalizing the results to different conditions. However, passive temperature modality does not seem to be very informative for this task.

8.5.4 Object Parts given Object : Object based Labels

Table 8.6 shows the results for object part categorization given an object. Note, we did not implement LSTMs for this categorization task as well because of less training data. Also, depending upon the object, some objects had three object parts whereas others had two that we were interested in classifying relevant to ADLs and IADLs. Therefore, the majority and random guess classifiers in Table 8.6 have two numbers each.

Generalizing Across velocity

The top four rows in Table 8.6 show the generalization results across two velocities. Again, SVMs with all the features show the best results showing the importance of all the features to recognize an object. Univariate HMMs with motion feature as well as 1-NN with heat-transfer and temperature feature show the worst results probably because without using the complementary modalities of force and thermal sensing together, it is difficult to extract useful information.

Generalizing Across Time

The bottom four rows in Table 8.6 show the generalization results across two time. Again, SVMs with all the features or using features that capture the complementarity of force and thermal sensing performed the best, whereas 1-NNs and univariate HMMs with just the force and motion features or only passive temperature feature gave the worst results.

Overall Results

Figure 8.10 shows the overall results. From the charts we note that, irrespective of algorithms used, on average, all four features (force, motion, heat, and temperature) features are important for distinguishing objects (object parts given object) and generalizing the results to different conditions. However, passive temperature modality does not seem to be very informative for this task.

Table 8.6: Distinguishing Object Parts given Object

Summary of Algorithm Performance for Object Part Classification given Object with 2 *seconds of contact. Note 'f' = force, 'm' = motion, 'h' = active thermal (heat-transfer), and 't' = passive thermal (temperature) feature.*

Generalize Across	Best and Worst	Algorithm	Features	Accuracy (%)
Velocity	Best	SVM	f+m+h+t	**78**
	Worst	1-NN	h+t	47
Time	Best	SVM	f+h+t	**71**
	Worst	1-NN	f+m	44
		Majority Classifier		42
		Random Guess		42

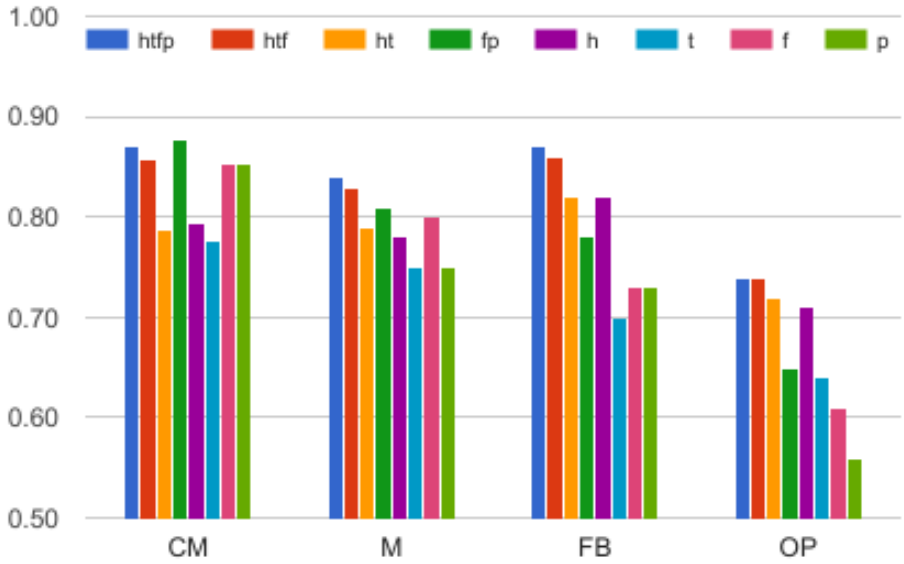

Figure 8.10: *This figure shows the performance of various feature combinations irrespective of data-driven algorithms used for different haptic label based classification schemes. Here, 'CM' = Compliance and Mobility based haptic labels ('Moved vs. Unmoved', 'Hard vs. Soft', and 'Hard-Unmoved vs. Soft-Unmoved vs. Hard-Moved vs. Soft-Moved'), 'M' = Material-based haptic labels (Binary Material Recognition), 'FB' = Distinguishing Objects (Tactile Foreground vs. Tactile Background), and 'OP' = Distinguishing Object Parts given Object. Each bar in the chart represents the average best performance using a particular feature combination across all data-driven algorithms and across all generalization schemes (time, velocity, and instance (if available)). For the features, 'f' = force data, 'p' = position data, 'h' = active heat-transfer data, and 't' = passive temperature data.*

8.6 Conclusions

In this paper, we demonstrated the usefulness of the complimentary capabilities of force and thermal sensing modalities in various haptic perception related categorization tasks. Specifically, we were interested in inferring compliance and mobility based haptic labels, material based haptic labels as well as distinguishing between objects in simplified scenarios such as tactile foreground vs. tactile background or object parts given object. We were interested in analyzing if the haptic perception results can generalize to different speeds (which might affect the force sensing modality) or different times (which might affect the thermal sensing modality) or even across different instances. We collected data using a mobile robot with a multimodal sensor module attached at the end of a linear actuator from 67 object parts in the bedroom, bathroom, and kitchen of a house over a period of three days. We implemented widely used and state-of-the-art data-driven algorithms such as 1-NNs, SVMs, HMMs, and LSTMs for generalization tasks. Our results show the importance of using multiple features in distinguishing objects or inferring haptic properties of objects rather than using single features. SVMs and HMMs show the best results for generalization for different haptic label based classification tasks whereas 1-NN fails to generalize. LSTMs show promise for our problem but need a lot of data to give meaningful results.

CHAPTER 9

LESSONS LEARNED AND IMPLICATIONS FOR FUTURE WORK

9.1 Lessons Learned

9.1.1 Force Sensing

From the overall results on force sensing, we learned that:

- Force sensing is sensitive to the mechanics of contact and therefore, haptic perception with force sensing has its own challenges such as varying robot stiffnesses and velocities, which makes generalizing the results to new situations difficult,
- It is feasible to use data-driven methods to infer object properties from contact during a reaching motion and the results can generalize across varying robot stiffnesses and velocities,
- Classification results with a combination of multiple features can generalize better than with single features,
- Classification results using LSTMs (with sufficient data availability) and multivariate HMMs can generalize well to different robot parameters such as robot-arm stiffnesses and arm velocities,
- Using a simple physics-based model, it is possible to generate data which are similar to real-world data. This can help us test our methods with a wide variety of simulated objects,
- We can also use simplified robots and custom and cheap fabric-based sensors to collect relevant haptic data,

- Inferring compliance and mobility based properties is limited by the resolution of the force sensors and the encoders on the robot.

9.1.2 Thermal Sensing

From the overall results on thermal sensing, we learned that:

- Haptic perception with thermal sensing has its own challenges such as varying initial conditions and duration of contact, which makes generalizing the results to new situations difficult,
- It is feasible to use data-driven methods to infer object material properties from contact during a reaching motion and the results can generalize across varying initial conditions, time of the day (which affects temperature of the object), and environments with different HVAC conditions,
- Classification results with active thermal sensing features work better for object recognition, but passive thermal sensing is especially relevant for distinguishing humans,
- Classification results using SVMs can generalize well to different initial and environment conditions and can infer object properties and distinguish object types with short-duration contact,
- Using a simple physics-based model, it is possible to generate data which are similar to real-world data. This can help us test our methods with a wide variety of simulated objects,
- We can also use simplified robots, sensors, and portable data-acquisition devices to collect relevant haptic data,
- Using the physics-based model, it is also possible to predict binary material recognition performance of data-driven methods,

- The prediction results using the physics-based models match well with the results using SVMs with both simulated and real-world data,

- The physics-based model can also help us guide the choice of sensors with required specifications (sensor noise, sensor initial temperature) for a desired level of material classification performance,

- Using the physics-based model, we can also estimate environment conditions when the thermal data from two different materials might look ambiguous and suggest ways to resolve the ambiguity using both active and passive thermal sensing modality,

- Thermal sensing is less sensitive to the mechanics of contact compared to force sensing, but we found empirically that it depends on the contact area (a derivative of object shape / contact geometry). And, depending on the amount of force applied, or whether the robot is interacting with a hard or soft object, the contact area might change which could affect the heat transfer. The semi-infinite solid model does not directly account for the effect of contact shape or area, however, while generating data using the model, we perform system identification for the sensor parameters from the real-world data and the identified parameters takes into account these effects indirectly,

- Haptic perception using thermal sensing is a function of thermal effusivities. The sensing is dependent on sensor noise, sensor initial conditions, as well as object initial conditions. However, it is limited by the time constant of the sensor.

9.2 Implications for Future Work

Based on the above discussions, here are some recommendations on directions for future work:

9.2.1 Robust Sensor Design

Through the investigations done in this work, we found that haptic perception using large-area force-sensors is dependent on the temporal and spatial resolution of force sensors. We also learned that haptic perception using thermal sensors is dependent on the time constant and contact area of the thermal sensors. Another important factor is the availability of a large amount of haptic data and thus, we need sensors that are robust enough to be used repetitively for extensive data collection without continuous human supervision.

Therefore, a future direction could be to design robust multimodal tactile sensors that address the issues raised above. However, increasing the spatial and temporal resolution of a force sensor simultaneously is challenging and may increase the resultant circuitry. It is also challenging to lower the time constant and increase the contact area simultaneously. A larger contact surface area reduces the time constant if we follow a lumped capacitance based model [299]. But, it may have many surface irregularities which may decrease the effective contact area and thus, increase the thermal contact resistance. This may make the time constant larger. This is because the time constant of a thermal sensor is proportional to the product of thermal contact resistance and thermal capacitance of a sensor [300, 301]. On the other hand, choosing a sensor of smaller size may lower the thermal capacitance thus lowering the time constant [300] but can also increase the thermal contact resistance (e.g. a sensor with spherical shape) due to smaller contact area. Also an important factor is the shape and compliance of the surface with which the sensor is making contact. For example, a compliant material (human skin) may wrap around a thermal sensor when force is applied, thus effectively increasing the contact surface area and this can affect heat transfer. Also, a smooth metal sphere would result in an approximate point contact with a large flat surface. So, there is a tradeoff in thermal sensor design and various factors such as its mass, volume, surface contact area, and surface finish affect the time constant. Also, object shape and compliance affect heat transfer. Note that designing a sensor of smaller size may make the sensor more fragile and protective layers might be needed [139, 300]. In addition, to

make the sensors robust, we also need design solutions that do not require frequent sensor recalibration as it could restrict large amounts of autonomous data collection.

9.2.2 Analyze Human Perception

Through this work, we found that force and kinematic (motion) sensing modalities are informative to infer the compliance and mobility based haptic labels, but all the force, motion, and thermal modalities were informative to infer the material properties of objects as well as to distinguish object types. To understand the role of the individual sensing modalities, one approach could be to analyze how humans use these different modalities for haptic perception. One way to achieve this would be to look at the psychophysics literature and understand the human perception mechanisms [302, 303] and design and conduct human participant studies to find out how humans combine these different sensory modalities for haptic perception [304]. This could help us understand the role of these different sensory modalities in inferring properties of objects through touch. This can in turn provide us guidelines for designing multimodal sensors to be used with robots for haptic perception.

9.2.3 Other Cases of Incidental Contact

Through this body of work, we have provided results of rapid haptic perception using simple robotic motions with normal contact between a sensor and an object. In real world manipulation scenarios, especially for robots with whole-arm tactile sensing moving in cluttered and unstructured environments, there could be various cases of incidental contact such as non-normal, sliding as well as partial contact. A non-normal contact, sliding contact or partial contact may affect force and thermal sensing. Therefore, extending the results of this work to these cases of incidental contact scenarios merit further investigation.

9.2.4 Role of Other Sensory Modalities

In addition to using these multiple sensory modalities such as force and thermal modalities, it would likely be informative to use the vibration modality [48, 305]. In Chapter 2, we found that using force and motion sensing modalities, our algorithms had difficulty in disambiguating between motion due to deformation of a soft object and motion due to sliding of a hard object. Having vibration modality, could help in identifying the subtle vibrations due to the sliding motion of an object.

Distinguishing objects can be a much harder problem when compared to inferring a specific property of an object such as its compliance, mobility, or material. This is because an object can have various properties that identifies it. In Chapters 3, 5 and 8, we devised strategies to simplify the problem of distinguishing objects by focusing on the task and classifying objects that are relevant to the task such as classification based on conditioning the environment, tactile foreground vs. tactile background, object parts given object etc. However, these simplified strategies assumed that the algorithm knows the task. In real-world manipulation scenarios, to be able to identify the context or the task is not trivial and using non-contact modalities such as vision (Is the robot near the door or bed ?) and IR-based thermal (Is the robot near a human ?) can help identify the immediate environment or the task / context. In addition, vision can also be used to identify properties of an object such as its material [306, 307].

9.3 Conclusion

To conclude, this work developed and analyzed different methods for rapid haptic perception using force and thermal sensing using simple motions. Haptic perception is unique as sensing depends on action. This work showed the feasibility of generalizing the haptic perception results to situations and actions which are different from those used when collecting training data. We achieved this using proper choice of features as well as using

both data-driven methods and physics-based models. We used the physics-based models to generate data similar to real-world experiments (for both force and thermal sensing) to be used by the data-driven methods. We also used the physics-based models to predict the performance of data-driven methods (for thermal sensing). We also analyzed limitations of these sensing modalities and suggested solutions. And finally, we identified research directions that merit further investigation.

Appendices

APPENDIX A

OPEN ACCESS HAPTIC DATABASE (OAHD)

All the relevant data, code, models, as well as design files are available publicly as a part of our 'Open-Access-Haptic-Database (OAHD)'. The link is given below:

http://www.oahd.gatech.edu/

REFERENCES

[1] D. Katz and O. Brock. "Manipulating Articulated Objects with Interactive Perception". In: *International Conference on Robotics and Automation (ICRA)*. 2008, pp. 272–277.

[2] J. Sun et al. "Learning Visual Object Categories for Robot Affordance Prediction". In: *The International Journal of Robotics Research* 29.2-3 (2010), pp. 174–197. eprint: `http://ijr.sagepub.com/content/29/2-3/174.full.pdf+html`.

[3] A. Petrovskaya et al. "Touch Based Perception for Object Manipulation". In: *Robotics Science and Systems Conference*. Atlanta, GA: Robot Manipulation Workshop, 2007.

[4] A. Drimus et al. "Classification of Rigid and Deformable Objects Using a Novel Tactile Sensor". In: *in Proceedings of 15th International Conference on Advanced Robotics (ICAR)*. 2011, pp. 427–434.

[5] V. Sukhoy et al. "Vibrotactile Recognition of Surface Textures by a Humanoid Robot". In: *Proceedings of the 2009 Humanoids Workshop: Tactile Sensing in Humanoids Tactile Sensors and Beyond*. 2009.

[6] H. Ho and L. A. Jones. "Material Identification using Real and Simulated Thermal Cues". In: *Proceedings of the 26th Annual International Conference of the IEEE EMBS*. 2004, pp. 2462–2465.

[7] Y. S. Kim and T. Kesavadas. "Material Property Recognition by Active Tapping for Fingertip Digitizing". In: *Proceedings of the Symposium on Haptic Interfaces for Virtual Environment and Teleoperator Systems*. 2006, pp. 133–139.

[8] S. Takamuku et al. "Haptic Discrimination of Material Properties by a Robotic Hand". In: *Proceedings of IEEE 6th International Conference on Development and Learning (ICDL)*. 2007, pp. 1–6.

[9] K. Hosoda and T. Iwase. "Robust Haptic Recognition by Anthropomorphic Bionic Hand through Dynamic Interaction". In: *Proceedings of International Conference on Intelligent Robots and Systems (IROS)*. 2010, pp. 1236–1241.

[10] B. Frank et al. "Learning the Elasticity Parameters of Deformable Objects with a Manipulation Robot". In: *Proceedings of International Conference on Intelligent Robots and Systems(IROS)*. 2010, pp. 1877–1883.

[11] B. Frank et al. “Learning Deformable Object Models for Mobile Robot Navigation using Depth Cameras and a Manipulation Robot”. In: *Proceedings of the Workshop on Advanced Reasoning with Depth Cameras at Robotics, Science and Systems Conference (RSS)*. 2010.

[12] Naoki Ueda, Shin-iti Hirai, and Hiromi T Tanaka. “Extracting rheological properties of deformable objects with haptic vision”. In: *Robotics and Automation, 2004. Proceedings. ICRA'04. 2004 IEEE International Conference on*. Vol. 4. IEEE. 2004, pp. 3902–3907.

[13] N. N. A. Charniya and S. V. Dudul. “Sensor for Classification of Material Type and its Surface Properties using Radial Basis Networks”. In: *IEEE Sensors Journal* 8.12 (2008), pp. 1981–1991.

[14] R. Platt Jr, F. Permenter, and J. Pfeiffer. “Using Bayesian Filtering to Interpret Tactile Data During Flexible Materials Manipulation”. In: *IEEE Transactions on Robotics, Special Issue on A Robotic Sense of Touch* 27.3 (2011), pp. 586–598.

[15] Kayla Matheus and Aaron M Dollar. “Benchmarking grasping and manipulation: Properties of the objects of daily living”. In: *Intelligent Robots and Systems (IROS), 2010 IEEE/RSJ International Conference on*. IEEE. 2010, pp. 5020–5027.

[16] R. Kikuuwe and T. Yoshikawa. “Recognizing Object Surface Properties Using Impedance Perception”. In: *Proceedings of International Symposium on Micromechatronics and Human Science*. 2003.

[17] A. Schneider, J. Sturm, and C. Stachniss. “Object Identification with Tactile Sensors using Bag-of-Features”. In: *Proceedings of International Conference on Intelligent Robots and Systems (IROS)*. 2009, pp. 243–248.

[18] P. K. Allen and K. S. Roberts. “Haptic Object Recognition Using a Multi-Fingered Dexterous Hand”. In: *Proceedings of International Conference on robotics and Automation (ICRA)*. 1989, pp. 342–347.

[19] S. Caselli, C. Magnanini, and F. Zanichelli. “Haptic Object Recognition with a Dexterous Hand Based on Volumetric Shape Representations”. In: *Proceedings of the 1994 International Conference on Multisensor Fusion and Integration for Intelligent Systems*. 1994, pp. 280–287.

[20] E. Faldella et al. “A Neural Approach to Robotic Haptic Recognition of 3-D Objects Based on Kohonen Self-Organizing Feature Map”. In: *IEEE Transactions on Industrial Electronics* 44.2 (1997), pp. 267–269.

[21] Z. Pezzementi et al. “Tactile Object Recognition from Appearance Information”. In: *IEEE Transactions on Robotics* 27.3 (2011), pp. 473–486.

[22] N. Gorges et al. “Haptic Object Recognition using Passive Joints and Haptic Key Features”. In: *Proceedings of IEEE International Conference on Robotics and Automation (ICRA)*. 2010, pp. 2349–2355.

[23] J. Sinapov, M. Weimer, and A. Stoytchev. “Interactive Learning of the Acoustic Properties of Household Objects”. In: *Proceedings of the 2009 IEEE International Conference on Robotics and Automation (ICRA)*. 2009, pp. 2518–2524.

[24] T. Berquist et al. “Interactive object Recognition using Proprioceptive Feedback”. In: *Proceedings of the 2009 IROS Workshop on Semantic Perception for Mobile Manipulation (IROS)*. 2009.

[25] S. Griffith et al. “A Behavior Grounded Approach to Forming Object Categories: Separating Containers from Non-Containers”. In: *to appear in IEEE Transactions on Autonomous Mental Development* (2011).

[26] J. Sinapov et al. “Interactive Object Recognition Using Proprioceptive and Auditory Feedback”. In: *International Journal of Robotics Research* 30.10 (2011), pp. 1250–1262.

[27] J. Ulmen, A. Edsinger, and M. Cutkosky. “A Highly Sensitive, Manufacturable, Low-Cost Tactile Sensor for Responsive Robots”. In: *submitted to IEEE International Conference on Robotics and Automation (ICRA)*. 2012.

[28] I. Guyon and A. Elisseeff. “An Introduction to Variable and Feature Selection”. In: *JOurnal of Machine Learning Research* 3 (2003), pp. 1157–1182.

[29] Advait Jain et al. “Reaching in clutter with whole-arm tactile sensing”. In: *The International Journal of Robotics Research* 32.4 (2013), pp. 458–482.

[30] T. Bhattacharjee, J. M. Rehg, and C. C. Kemp. “Haptic Classification and Recognition of Objects Using a Tactile Sensing Forearm”. In: *IEEE International Conference on Intelligent Robots and Systems (IROS)*. 2012, pp. 4090 –4097.

[31] T. Bhattacharjee et al. “Rapid Categorization of Object Properties from Incidental Contact with a Tactile Sensing Robot Arm”. In: *IEEE-RAS International Conference on Humanoid Robots (Humanoids)*. 2013.

[32] T. Bhattacharjee et al. “A Robotic System for Reaching in Dense Clutter that Integrates Model Predictive Control, Learning, Haptic Mapping, and Planning”. In: *Proceedings of the 3rd IEEE/RSJ International Conference on Intelligent Robots and Systems (IROS) Workshop on Robots in Clutter: Perception and Interaction in Clutter*. 2014.

[33] Tapomayukh Bhattacharjee et al. “Tactile Sensing over Articulated Joints with Stretchable Sensors”. In: *IEEE World Haptics Conference (WHC)*. 2013.

[34] P. M. Grice et al. “Whole-arm Tactile Sensing for Beneficial and Acceptable Contact During Robotic Assistance”. In: *13th International Conference on Rehabilitation Robotics (ICORR)*. 2013.

[35] Susan J Lederman et al. “Perceiving surface roughness via a rigid probe: Effects of exploration speed and mode of touch”. In: (1999).

[36] Susan J Lederman et al. “Perceiving surface roughness through a probe: Effects of applied force and probe diameter”. In: *Proceedings of the ASME DSCD-IMECE*. 2000.

[37] Susan J Lederman and Roberta L Klatzky. “Extracting object properties through haptic exploration”. In: *Acta psychologica* 84.1 (1993), pp. 29–40.

[38] David Silvera-Tawil, David Rye, and Mari Velonaki. “Artificial skin and tactile sensing for socially interactive robots: A review”. In: *Robotics and Autonomous Systems* 63 (2015), pp. 230–243.

[39] Haoying Wu, Hongbin Liu, and Dikai Liu. “Two-Dimensional Direction Recognition Using Uniaxial Tactile Arrays”. In: *Sensors Journal, IEEE* 13.12 (2013), pp. 4897–4903.

[40] Luca Muscari et al. “Real-time reconstruction of contact shapes for large area robot skin”. In: *Robotics and Automation (ICRA), 2013 IEEE International Conference on*. IEEE. 2013, pp. 2360–2366.

[41] Dana Hughes and Nikolaus Correll. “Texture recognition and localization in amorphous robotic skin”. In: *Bioinspiration & biomimetics* 10.5 (2015), p. 055002.

[42] Maria Javaid, Milos Zefran, and Andrey Yavolovsky. “Using pressure sensors to identify manipulation actions during human physical interaction”. In: *Robot and Human Interactive Communication (RO-MAN), 2015 24th IEEE International Symposium on*. IEEE. 2015, pp. 670–675.

[43] Pasu Boonvisut and M Cenk Çavusoglu. “Identification and active exploration of deformable object boundary constraints through robotic manipulation”. In: *The International journal of robotics research* 33.11 (2014), pp. 1446–1461.

[44] Barrett Heyneman and Mark R Cutkosky. “Slip classification for dynamic tactile array sensors”. In: *The International Journal of Robotics Research* (2015), p. 0278364914564703.

[45] Carsten Schürmann et al. “A high-speed tactile sensor for slip detection”. In: *Towards service robots for everyday environments*. Springer, 2012, pp. 403–415.

[46] Anh-Van Ho and Shinichi Hirai. “Slip Perception via Soft Robotic Skin Made of Electroconductive Yarn”. In: *Mechanics of Localized Slippage in Tactile Sensing*. Springer, 2014, pp. 113–154.

[47] Mohsen Kaboli, Rich Walker, Gordon Cheng, et al. “In-hand object recognition via texture properties with robotic hands, artificial skin, and novel tactile descriptors”. In: *Humanoid Robots (Humanoids), 2015 IEEE-RAS 15th International Conference on*. IEEE. 2015, pp. 1155–1160.

[48] Robert D Howe and Mark R Cutkosky. “Dynamic tactile sensing: Perception of fine surface features with stress rate sensing”. In: *IEEE transactions on robotics and automation* 9.2 (1993), pp. 140–151.

[49] Qiang Li et al. “A control framework for tactile servoing”. In: (2013).

[50] Uriel Martinez-Hernandez et al. “Active contour following to explore object shape with robot touch”. In: *World Haptics Conference (WHC), 2013*. IEEE. 2013, pp. 341–346.

[51] Don Joven Agravante et al. “Collaborative human-humanoid carrying using vision and haptic sensing”. In: *Robotics and Automation (ICRA), 2014 IEEE International Conference on*. IEEE. 2014, pp. 607–612.

[52] Sylvain Calinon et al. “Learning collaborative manipulation tasks by demonstration using a haptic interface”. In: *Advanced Robotics, 2009. ICAR 2009. International Conference on*. IEEE. 2009, pp. 1–6.

[53] Vivian Chu et al. “Robotic learning of haptic adjectives through physical interaction”. In: *Robotics and Autonomous Systems* 63 (2015), pp. 279–292.

[54] Chia-Hsien Lin et al. “Signal processing and fabrication of a biomimetic tactile sensor array with thermal, force and microvibration modalities.” In: *IEEE International Conference on Robotics and Biomimetics (ROBIO)*. IEEE, 2009, pp. 129–134.

[55] Mohsen Kaboli et al. “Humanoids learn object properties from robust tactile feature descriptors via multi-modal artificial skin”. In: *Humanoid Robots (Humanoids), 2014 14th IEEE-RAS International Conference on*. IEEE. 2014, pp. 187–192.

[56] Minas V Liarokapis et al. “Unplanned, model-free, single grasp object classification with underactuated hands and force sensors”. In: *Intelligent Robots and Sys-*

tems (IROS), 2015 IEEE/RSJ International Conference on. IEEE. 2015, pp. 5073–5080.

[57] Alexander Schmitz et al. "Tactile object recognition using deep learning and dropout". In: *Humanoid Robots (Humanoids), 2014 14th IEEE-RAS International Conference on*. IEEE. 2014, pp. 1044–1050.

[58] Nisit Kiwatthana and Somyot Kaitwanidvilai. "Development of smart gripper for identification of grasped objects". In: *Asia-Pacific Signal and Information Processing Association, 2014 Annual Summit and Conference (APSIPA)*. IEEE. 2014, pp. 1–5.

[59] Janine Hoelscher, Jan Peters, and Tucker Hermans. "Evaluation of tactile feature extraction for interactive object recognition". In: *Humanoid Robots (Humanoids), 2015 IEEE-RAS 15th International Conference on*. IEEE. 2015, pp. 310–317.

[60] Dennis Babu et al. "Machine Learning Based Shape Classification Using Tactile Sensor Array". In: *Advanced Computing, Networking and Informatics, Volume 1: Advanced Computing and Informatics Proceedings of the Second International Conference on Advanced Computing, Networking and Informatics (Icacni-2014)*. Vol. 27. Springer. 2014, p. 47.

[61] N. Ueda, S. Hirai, and H. T. Tanaka. "Extracting Rheological Properties of Deformable Objects with Haptic Vision". In: *Proceedings of the 2004 IEEE International Conference on Robotics and Automation*. 2004.

[62] Marten Bjorkman et al. "Enhancing visual perception of shape through tactile glances". In: *Intelligent Robots and Systems (IROS), 2013 IEEE/RSJ International Conference on*. IEEE. 2013, pp. 3180–3186.

[63] A. Jain and C. C. Kemp. "Improving robot manipulation with data-driven object-centric models of everyday forces". In: *Autonomous Robots* 35.2-3 (2013), pp. 143–159.

[64] Jivko Sinapov and Alexander Stoytchev. "Grounded object individuation by a humanoid robot". In: *Robotics and Automation (ICRA), 2013 IEEE International Conference on*. IEEE. 2013, pp. 4981–4988.

[65] L. R. Rabiner. "A Tutorial on Hidden Markov Models and Selected Applications in SPeech Recognition". In: *Readings in Speech Recognition*. Ed. by A. Waibel and K. F. Lee. Kaufmann, San Mateo, CA, 1990, pp. 267–296.

[66] Ilya Sutskever, Oriol Vinyals, and Quoc V Le. "Sequence to sequence learning with neural networks". In: *Advances in neural information processing systems*. 2014, pp. 3104–3112.

[67] Alex Graves. “Generating sequences with recurrent neural networks”. In: *arXiv preprint arXiv:1308.0850* (2013).

[68] Alex Graves, Abdel-rahman Mohamed, and Geoffrey Hinton. “Speech recognition with deep recurrent neural networks”. In: *Acoustics, speech and signal processing (icassp), 2013 ieee international conference on*. IEEE. 2013, pp. 6645–6649.

[69] Sepp Hochreiter and Jürgen Schmidhuber. “Long short-term memory”. In: *Neural computation* 9.8 (1997), pp. 1735–1780.

[70] Zackory Erickson et al. “What does the person feel? Learning to infer applied forces during robot-assisted dressing”. In: *Robotics and Automation (ICRA), 2017 IEEE International Conference on,* in print.

[71] Angelica I Aviles et al. “Exploring the effects of dimensionality reduction in deep networks for force estimation in robotic-assisted surgery”. In: *SPIE Medical Imaging*. International Society for Optics and Photonics. 2016, pp. 97861X–97861X.

[72] Yang Gao et al. “Deep learning for tactile understanding from visual and haptic data”. In: *Robotics and Automation (ICRA), 2016 IEEE International Conference on*. IEEE. 2016, pp. 536–543.

[73] Felix A Gers, Jürgen Schmidhuber, and Fred Cummins. “Learning to forget: Continual prediction with LSTM”. In: *Neural computation* 12.10 (2000), pp. 2451–2471.

[74] Vu Pham et al. “Dropout improves recurrent neural networks for handwriting recognition”. In: *Frontiers in Handwriting Recognition (ICFHR), 2014 14th International Conference on*. IEEE. 2014, pp. 285–290.

[75] Reza Shadmehr. “The equilibrium point hypothesis for control of movement”. In: *Baltimore, MD: Department of Biomedical Engineering, Johns Hopkins University* (1998).

[76] Harold Malcolm Westergaard. *Theory of elasticity and plasticity*. Vol. 367. Harvard University Press Cambridge, 1952.

[77] *Poisson’s ratio*. `https://en.wikipedia.org/wiki/Poisson%27s_ratio`.

[78] *Coefficients of Friction*. `http://www.roymech.co.uk/Useful_Tables/Tribology/co_of_frict.htm`.

[79] *Friction and Coefficients of Friction*. `http://www.engineeringtoolbox.com/friction-coefficients-d_778.html`.

[80] *Coefficient of Friction, Rolling Resistance and Aerodynamics*. http://www.tribology-abc.com/abc/cof.htm.

[81] *Coefficient of Friction Reference Table*. http://www.engineershandbook.com/Tables/frictioncoefficients.htm.

[82] IS Grigoriev and EZ Meilikhov. "Handbook of Physical Quantities CRC". In: *Boca Raton, FL* (1997), p. 1548.

[83] John W Jewett and Raymond A Serway. *Physics for scientists and engineers with modern physics*. Cengage Learning EMEA, 2008.

[84] ASM International. Handbook Committee. *Friction, lubrication, and wear technology*. Vol. 18. ASM International, 1992.

[85] Peter J Blau. *Friction science and technology: from concepts to applications*. CRC press, 2008.

[86] PJ Blau. "Appendix: Static and kinetic friction coefficients for selected materials". In: *ASM Handbook, 4th ed., ASM International, Materials Park, OH* 18 (2002).

[87] PA Hasgall et al. *ITIS Database for thermal and electromagnetic parameters of biological tissues*. http://www.itis.ethz.ch/database.

[88] MS Farvid et al. "Association of adiponectin and resistin with adipose tissue compartments, insulin resistance and dyslipidaemia". In: *Diabetes, obesity and metabolism* 7.4 (2005), pp. 406–413.

[89] J Mendez and A Keys. "Density and composition of mammalian muscle". In: *Metabolism-Clinical and Experimental* 9.2 (1960), pp. 184–188.

[90] S Derler and L-C Gerhardt. "Tribology of skin: review and analysis of experimental results for the friction coefficient of human skin". In: *Tribology Letters* 45.1 (2012), pp. 1–27.

[91] Noor Veijgen. "Skin Friction - A Novel Approach to Measuring in vivo human skin". PhD thesis. 2013.

[92] M. F. Ashby. *The CES EduPack database of natural and man-made materials*. 2008.

[93] *Wood Densities*. http://www.engineeringtoolbox.com/wood-density-d_40.html.

[94] *Seats & Cushions*. http://www.usafoam.com/seat&cushion/seat&cushion.html.

[95] *Glass_Fibre_Reinforced_Products*. http://www.amiantit.com/media/pdf/brochures/Glass_Fibre_Reinforced_Products/files/Glass_Fibre_Reinforced_Products.pdf.

[96] Wit Witkiewicz and Andrzej Zieliński. "Properties of the polyurethane (PU) light foams". In: *Advances in Materials Science* 6.2 (2006), pp. 35–51.

[97] *CES EduPack database of natural and man-made materials*. Granta Design. 2016.

[98] Jarkko T Iivarinen et al. "Experimental and computational analysis of soft tissue stiffness in forearm using a manual indentation device". In: *Medical engineering & physics* 33.10 (2011), pp. 1245–1253.

[99] Brian Chin Wing Kot et al. "Elastic modulus of muscle and tendon with shear wave ultrasound elastography: variations with different technical settings". In: *PloS one* 7.8 (2012), e44348.

[100] MJ Birch and PD Srodon. "Biomechanical properties of the human soft palate". In: *The Cleft Palate-Craniofacial Journal* 46.3 (2009), pp. 268–274.

[101] Beth A Todd and John G Thacker. "Three-dimensional computer model of the human buttocks, in vivo." In: *Journal of rehabilitation research and development* 31.2 (1994), p. 111.

[102] L. Daneshmend, V. Hayward, and M. Pelletier. "Adaptation to environment stiffness in the control of manipulators". In: *Experimental Robotics I*. Springer. 1990, pp. 150–165.

[103] Tiffany L Chen et al. "Evaluation by Expert Dancers of a Robot That Performs Partnered Stepping via Haptic Interaction". In: (2015).

[104] Singiresu S Rao. *Vibration of continuous systems*. John Wiley & Sons, 2007.

[105] *Choose a Solver - MATLAB & Simulink*. http://www.mathworks.com/help/simulink/ug/types-of-solvers.html.

[106] *General Hidden Markov Model Library*. http://ghmm.org/.

[107] François Chollet. *Keras*. https://github.com/fchollet/keras. 2015.

[108] Theano Development Team. "Theano: A Python framework for fast computation of mathematical expressions". In: *arXiv e-prints* abs/1605.02688 (May 2016).

[109] F. Pedregosa et al. “Scikit-learn: Machine Learning in Python”. In: *Journal of Machine Learning Research* 12 (2011), pp. 2825–2830.

[110] *Elastic Compute Cloud (EC2) Cloud Server & Hosting*. `https://aws.amazon.com/ec2/`.

[111] Morgan Quigley et al. “ROS: an open-source Robot Operating System”. In: *ICRA workshop on open source software*. Vol. 3. 3.2. 2009.

[112] David Tabor. *The hardness of metals*. Oxford university press, 2000.

[113] Warren Carl Oliver and George Mathews Pharr. “An improved technique for determining hardness and elastic modulus using load and displacement sensing indentation experiments”. In: *Journal of materials research* 7.6 (1992), pp. 1564–1583.

[114] A. Jain et al. “Reaching in Clutter with Whole-Arm Tactile Sensing”. In: *International Journal of Robotics Research (IJRR)* 32.4 (2013), pp. 458–482.

[115] H. Soh, Yanyu Su, and Y. Demiris. “Online spatio-temporal Gaussian process experts with application to tactile classification”. In: *IEEE/RSJ International Conference on Intelligent Robots and Systems (IROS)*. 2012, pp. 4489–4496.

[116] Hongbin Liu et al. “A computationally fast algorithm for local contact shape and pose classification using a tactile array sensor”. In: *IEEE International Conference on Robotics and Automation (ICRA)*. 2012, pp. 1410–1415.

[117] S. Chitta et al. “Tactile Sensing for Mobile Manipulation”. In: *IEEE Transactions on Robotics* 27.3 (2011), pp. 558–568.

[118] N. Jamali and C. Sammut. “Majority Voting: Material Classification by Tactile Sensing Using Surface Texture”. In: *IEEE Transactions on Robotics* 27.3 (2011), pp. 508–521.

[119] Hanzhang Hu et al. “Efficient 3-D Scene Analysis from Streaming Data”. In: *IEEE International Conference on Robotics and Automation (ICRA)*. 2013.

[120] Lei Hu and R. Zanibbi. “HMM-Based Recognition of Online Handwritten Mathematical Symbols Using Segmental K-Means Initialization and a Modified Pen-Up/Down Feature”. In: *International Conference on Document Analysis and Recognition (ICDAR)*. 2011, pp. 457–462.

[121] U. Garain and B.B. Chaudhuri. “Recognition of online handwritten mathematical expressions”. In: *IEEE Transactions on Systems, Man, and Cybernetics, Part B: Cybernetics* 34.6 (2004), pp. 2366–2376.

[122] A. Kale et al. “Gait-based recognition of humans using continuous HMMs”. In: *in Proceedings of 5th IEEE International Conference onAutomatic Face and Gesture Recognition*. 2002, pp. 336–341.

[123] T. Starner, J. Weaver, and A. Pentland. “Real-time American sign language recognition using desk and wearable computer based video”. In: *IEEE Transactions on Pattern Analysis and Machine Intelligence* 20.12 (1998), pp. 1371–1375.

[124] J. Yamato, Jun Ohya, and K. Ishii. “Recognizing human action in time-sequential images using hidden Markov model”. In: *in Proceedings of IEEE Computer Society Conference on Computer Vision and Pattern Recognition (CVPR)*. 1992, pp. 379–385.

[125] F Cartella et al. “Online adaptive learning of Left-Right Continuous HMM for bearings condition assessment”. In: *Journal of Physics: Conference Series* 364.1 (2012), pp. 12–31.

[126] Wei Chai and Barry Vercoe. “Folk music classification using hidden Markov models”. In: *Proceedings of International Conference on Artificial Intelligence*. Vol. 6. 6.4. Citeseer. 2001.

[127] T. Bhattacharjee et al. “Tactile Sensing over Articulated Joints with Stretchable Sensors”. In: *IEEE World Haptics Conference (WHC), The 5th Joint EuroHaptics Conference and IEEE Haptics Symposium*. 2013.

[128] *Rapid Categorization Online Video*. `http://youtu.be/AvuKeXXpP1U`.

[129] Hannah Perner-Wilson and Ian Danforth. *rSkin – Open Source Robot Skin*. `http://www.instructables.com/id/rSkin-Open-Source-Robot-Skin/`.

[130] F.W.J. Cody et al. “Tactile spatial acuity is reduced by skin stretch at the human wrist”. In: *Neuroscience Letters* 484 (2010), pp. 71–75.

[131] Tapomayukh Bhattacharjee et al. “Rapid Categorization of Object Properties from Incidental Contact with a Tactile Sensing Robot Arm”. In: *Humanoid Robots, IEEE-RAS International Conference on*. Atlanta, GA, USA, Oct. 2013.

[132] A. Jain et al. “Reaching in Clutter with Whole-Arm Tactile Sensing”. In: *International Journal of Robotics Research (IJRR)* 32.4 (2013), pp. 458–482.

[133] Radu Bogdan Rusu and Steve Cousins. “3D is here: Point Cloud Library (PCL)”. In: *IEEE International Conference on Robotics and Automation (ICRA)*. Shanghai, China, 2011.

[134] R. A. Russell. “Thermal sensor for object shape and material constitution”. In: *Robotica* 6.01 (1988), pp. 31–34.

[135] R. A. Russell. “A thermal sensor array to provide tactile feedback for robots”. In: *The International journal of robotics research* 4.3 (1985), pp. 35–39.

[136] D. Siegel, I. Garabieta, and J. M. Hollerbach. “An integrated tactile and thermal sensor”. In: *IEEE International Conference on Robotics and Automation (ICRA)*. Vol. 3. IEEE. 1986, pp. 1286–1291.

[137] G. J. Monkman and P. M. Taylor. “Thermal tactile sensing”. In: *IEEE Transactions on Robotics and Automation* 9.3 (1993), pp. 313–318.

[138] J. Engel et al. “Flexible multimodal tactile sensing system for object identification”. In: *5th IEEE Conference on Sensors*. IEEE. 2006, pp. 563–566.

[139] J. Engel et al. “Polymer micromachined multimodal tactile sensors”. In: *Sensors and Actuators A: Physical* 117.1 (2005), pp. 50–61.

[140] Y. J. Yang et al. “A 32x32 temperature and tactile sensing array using PI-copper films”. In: *The International Journal of Advanced Manufacturing Technology* 46.9-12 (2010), pp. 945–956.

[141] F. Castelli. “An integrated tactile-thermal robot sensor with capacitive tactile array”. In: *IEEE Industry Applications Conference*. Vol. 3. IEEE. 1995, pp. 1970–1975.

[142] N. E. Mathis. “New Transient Non-Destructive Technique Measures Thermal Effusivity and Diffusivity”. In: *Thermal Conductivity* 25 (2000), pp. 3–14.

[143] D. G. Caldwell and J. O. Gray. “Dynamic multi-functional tactile sensing”. In: *RoManSy 9*. Springer, 1993, pp. 187–198.

[144] Philipp Mittendorfer and Gordon Cheng. “Humanoid multimodal tactile-sensing modules”. In: *IEEE Transactions on robotics* 27.3 (2011), pp. 401–410.

[145] J. I. Yuji and K. Shida. “A new multifunctional tactile sensing technique by selective data processing”. In: *IEEE Transactions on Instrumentation and Measurement* 49.5 (2000), pp. 1091–1094.

[146] D. Xu, G. E. Loeb, and J. A. Fishel. “Tactile identification of objects using Bayesian exploration”. In: *IEEE International Conference on Robotics and Automation (ICRA)*. IEEE. 2013, pp. 3056–3061.

[147] I. McMahon et al. “Robotic Learning of Haptic Adjectives through Physical Interaction”. In: *Proceedings of the 2012 Second Workshop on Advances in Tactile Sensing and Touch-based Human-Robot Interaction*. 2012.

[148] S. Takamuku, T. Iwase, and K. Hosoda. “Robust material discrimination by a soft anthropomorphic finger with tactile and thermal sense”. In: *IEEE/RSJ International Conference on Intelligent Robots and Systems (IROS)*. IEEE. 2008, pp. 3977–3982.

[149] E. Kerr, T. M. McGinnity, and S. Coleman. “Material classification based on thermal properties-A robot and human evaluation”. In: *IEEE International Conference on Robotics and Biomimetics (ROBIO)*. IEEE. 2013, pp. 1048–1053.

[150] *Flexible Polyimide Foil Heater with 10 kOhm Thermistor*. `https://www.thorlabs.com/thorproduct.cfm?partnumber=HT10K`.

[151] N. Mathis and C. Chandler. *Direct thermal conductivity measurement technique*. US Patent 6,676,287. 2004.

[152] A. Maqsood et al. “Simultaneous measurements of thermal conductivity and thermal diffusivity of insulators, fluids and conductors using the transient plane source (tps) technique”. In: *International journal of energy research* 18.9 (1994), pp. 777–782.

[153] Y. He. “Rapid thermal conductivity measurement with a hot disk sensor: Part 1. Theoretical considerations”. In: *Thermochimica Acta* 436.1 (2005), pp. 122–129.

[154] Yunus C. and Afshin G. “Transient Heat Conduction”. In: *Heat and Mass Transfer: Fundamentals and Applications*. New York, NY: McGraw-Hill, 2010. Chap. 4, pp. 245–246.

[155] J. S. Steinhart and S. R. Hart. “Calibration curves for thermistors”. In: *Deep Sea Research and Oceanographic Abstracts*. Vol. 15. 4. Elsevier. 1968, pp. 497–503.

[156] E. Jones, T. Oliphant, and P. Peterson. “SciPy: Open source scientific tools for Python”. In: *http://www. scipy. org/* (2001).

[157] Ting-Fan Wu, Chih-Jen Lin, and Ruby C Weng. “Probability estimates for multi-class classification by pairwise coupling”. In: *The Journal of Machine Learning Research* 5 (2004), pp. 975–1005.

[158] PA Hasgall et al. “ITIS Database for thermal and electromagnetic parameters of biological tissues”. In: *Version 3.0* (2015).

[159] Joshua Wade, Tapomayukh Bhattacharjee, and Charles C Kemp. “A handheld device for the in situ acquisition of multimodal tactile sensing data”. In: *See and*

Touch: 1st Workshop on multimodal sensor-based robot control for HRI and soft manipulation, IEEE/RSJ International Conference on Intelligent Robots and Systems (IROS). 2015.

[160] Tracy L Mitzner et al. "Identifying the Potential for Robotics to Assist Older Adults in Different Living Environments". In: *International journal of social robotics* 6.2 (2014), pp. 213–227.

[161] Sidney Katz et al. "Studies of illness in the aged: the index of ADL: a standardized measure of biological and psychosocial function". In: *Jama* 185.12 (1963), pp. 914–919.

[162] *Activities of Daily Living*. `https://en.wikipedia.org/wiki/Activities_of_daily_living`.

[163] Wenyi Zhao et al. "Face recognition: A literature survey". In: *ACM computing surveys (CSUR)* 35.4 (2003), pp. 399–458.

[164] Brenna D Argall and Aude G Billard. "A survey of tactile human–robot interactions". In: *Robotics and Autonomous Systems* 58.10 (2010), pp. 1159–1176.

[165] Tapomayukh Bhattacharjee, Joshua Wade, and Charles C Kemp. "Material Recognition from Heat Transfer given Varying Initial Conditions and Short-Duration Contact". In: *Robotics: Science and Systems (RSS)*.

[166] Walter Dan Stiehl et al. "Design of a therapeutic robotic companion for relational, affective touch". In: *Robot and Human Interactive Communication, 2005. ROMAN 2005. IEEE International Workshop on*. IEEE. 2005, pp. 408–415.

[167] Walter Dan Stiehl and Cynthia Breazeal. "A sensitive skin for robotic companions featuring temperature, force, and electric field sensors". In: *Intelligent Robots and Systems, 2006 IEEE/RSJ International Conference on*. IEEE. 2006, pp. 1952–1959.

[168] Saskia Golz, Christian Osendorfer, and Sami Haddadin. "Using tactile sensation for learning contact knowledge: Discriminate collision from physical interaction". In: *Robotics and Automation (ICRA), 2015 IEEE International Conference on*. IEEE. 2015, pp. 3788–3794.

[169] Emmett Kerr et al. "Towards pulse detection and rhythm analysis using a biomimetic fingertip". In: *Neural Networks (IJCNN), 2015 International Joint Conference on*. IEEE. 2015, pp. 1–8.

[170] James W Davis and Vinay Sharma. "Robust detection of people in thermal imagery". In: *Pattern Recognition, 2004. ICPR 2004. Proceedings of the 17th International Conference on*. Vol. 4. IEEE. 2004, pp. 713–716.

[171] M Leandri et al. “Measurement of skin temperature after infrared laser stimulation”. In: *Neurophysiologie Clinique/Clinical Neurophysiology* 36.4 (2006), pp. 207–218.

[172] Yvon Houdas and EFJ Ring. *Human body temperature*. Springer Science & Business Media, 1982.

[173] Howard R Nicholls and Mark H Lee. “A survey of robot tactile sensing technology”. In: *The International Journal of Robotics Research* 8.3 (1989), pp. 3–30.

[174] Mark H Lee and Howard R Nicholls. “Review Article Tactile sensing for mechatronicsa state of the art survey”. In: *Mechatronics* 9.1 (1999), pp. 1–31.

[175] P. Dario et al. “Ferroelectric polymer tactile sensors with anthropomorphic features”. In: *IEEE International Conference on Robotics and Automation*. Vol. 1. IEEE. 1984, pp. 332–340.

[176] Davide Taddeucci et al. “An approach to integrated tactile perception”. In: *IEEE International Conference on Robotics and Automation (ICRA)*. Vol. 4. IEEE. 1997, pp. 3100–3105.

[177] V. Chu et al. “Using Robotic Exploratory Procedures to Learn the Meaning of Haptic Adjectives”. In: *Proceedings of International Conference on Robotics and Automation*. 2013.

[178] Jaemin Kim et al. “Stretchable silicon nanoribbon electronics for skin prosthesis”. In: *Nature communications* 5 (2014).

[179] *Surebonder 727 Adhesive Specifications*. `http://www.surebonder.com/products.asp?Choice=VD4&sbonder_glue_stick_prod_id=61`.

[180] Tapomayukh Bhattacharjee et al. “Tactile sensing over articulated joints with stretchable sensors”. In: *World Haptics Conference (WHC), 2013*. IEEE. 2013, pp. 103–108.

[181] Tapomayukh Bhattacharjee et al. “Data-driven thermal recognition of contact with people and objects”. In: *IEEE Haptics Symposium (HAPTICS)*. IEEE. 2016, pp. 297–304.

[182] A.W. Van Herwaarden and P.M. Sarro. “Thermal sensors based on the seebeck effect”. In: *Sensors and Actuators* 10.3 (1986), pp. 321 –346.

[183] Alan Tong. “Improving the accuracy of temperature measurements”. In: *Sensor Review* 21.3 (2001), pp. 193–198. eprint: `http://dx.doi.org/10.1108/02602280110398044`.

[184] Y.-J. Yang et al. “An integrated flexible temperature and tactile sensing array using PI-copper films”. In: *Sensors and Actuators A: Physical* 143.1 (2008). Micromechanics Section of Sensors and Actuators (SAMM), based on contributions revised from the Technical Digest of the {IEEE} 20th International Conference on Micro Electro Mechanical Systems (MEMS 2007)MEMS 2007IEEE 20th International Conference on Micro Electro Mechanical Systems, pp. 143 –153.

[185] Takao Someya et al. “Conformable, flexible, large-area networks of pressure and thermal sensors with organic transistor active matrixes”. In: *Proc. Natl. Acad. Sci. U.S.A* 102.2 (2005), pp. 12321 –12325.

[186] F. Castelli. “An integrated tactile-thermal robot sensor with capacitive tactile array”. In: *Industry Applications Conference, 1995. Thirtieth IAS Annual Meeting, IAS’95., Conference Record of the 1995 IEEE*. Vol. 3. IEEE. 1995, pp. 1970–1975.

[187] K.H.V. Hedengren et al. *Thermal sensor array and methods of fabrication and use*. US Patent 6,180,867. 2001.

[188] Wen-Pin Shih et al. “Flexible Temperature Sensor Array Based on a Graphite-Polydimethylsiloxane Composite”. In: *Sensors* 10.4 (2010), pp. 3597–3610.

[189] B. Ma et al. “Flexible thermal sensor array on PI film substrate for underwater applications”. In: *2010 IEEE 23rd International Conference on Micro Electro Mechanical Systems (MEMS)*. 2010, pp. 679–682.

[190] Mehmet Bayindir et al. “Thermal-Sensing Fiber Devices by Multimaterial Codrawing”. In: *Advanced Materials* 18.7 (2006), pp. 845–849.

[191] O.A. Kabov and I.V. Marchuk. “Thermal Imaging Study of the Liquid Film Flowing on Vertical Surface with Local Heat Source”. In: *Russian Journal of Engineering Thermophysics* 6(2) (1996), pp. 105–138.

[192] M. Matian, A.J. Marquis, and N.P. Brandon. “Application of thermal imaging to validate a heat transfer model for polymer electrolyte fuel cells”. In: *International Journal of Hydrogen Energy* 35.22 (2010). Bio-Ethanol and Other Renewable Sources and Reforming Process for Sustainable Hydrogen Production, pp. 12308 –12316.

[193] R. Boukhanouf et al. “Experimental investigation of a flat plate heat pipe performance using {IR} thermal imaging camera”. In: *Applied Thermal Engineering* 26.1718 (2006), pp. 2148 –2156.

[194] P.M. Sarro et al. “An integrated thermal infrared sensing array”. In: *Sensors and Actuators* 14.2 (1988), pp. 191 –201.

[195] A. Schaufelbuhl et al. “Uncooled low-cost thermal imager based on micromachined CMOS integrated sensor array”. In: *Journal of Microelectromechanical Systems* 10.4 (2001), pp. 503–510.

[196] C. Liu, J. Chen, and J. Engel. *Sensor chip and apparatus for tactile and/or flow sensing*. US Patent 7,357,035. 2008.

[197] P. Mansky and J. Bennett. *Method for conducting sensor array-based rapid materials characterization*. US Patent 6,438,497. 2002.

[198] P. Mansky and J. Bennett. *Sensor array-based system and method for rapid materials characterization*. US Patent 6,535,824. 2003.

[199] P. Dario and D.E. De Rossi. *Composite, multifunctional tactile sensor*. US Patent 4,555,953. 1985.

[200] D. Taddeucci et al. “An approach to integrated tactile perception”. In: *Proceedings of International Conference on Robotics and Automation*. Vol. 4. 1997, 3100–3105 vol.4.

[201] Jaemin Kim et al. “Stretchable silicon nanoribbon electronics for skin prosthesis”. In: *Nature Communications* 5 (2014). Article, 5747 EP –.

[202] *Syntouch BioTac Sensor*. Syntouch Inc.

[203] Darwin G Caldwell and Clarence Gosney. “Enhanced tactile feedback (tele-taction) using a multi-functional sensory system”. In: *Robotics and Automation, 1993. Proceedings., 1993 IEEE International Conference on*. IEEE. 1993, pp. 955–960.

[204] W.B. Jackson et al. *Paper property sensing system*. US Patent 5,934,140. 1999.

[205] Fei Shao et al. “A novel tactile sensation measurement system for qualifying touch perception”. In: *Proceedings of the Institution of Mechanical Engineers, Part H: Journal of Engineering in Medicine* 224.1 (2010), pp. 97–105.

[206] Xiaojuan Chen et al. “Exploring relationships between touch perception and surface physical properties”. In: *International Journal of Design* 3.2 (2009), pp. 67–76.

[207] Herbert Kaplan. *Practical Applications of Infrared Thermal Sensing and Imaging Equipment*. 3rd ed. The address: SPIE Press, Mar. 2007. ISBN: 9780819467232.

[208] R. Mulaveesala, V. S. Ghali, and V. Arora. “Applications of non-stationary thermal wave imaging methods for characterisation of fibre-reinforced plastic materials”. In: *Electronics Letters* 49.2 (2013), pp. 118–119.

[209] G. E. VanDamme and J. W. McGarvey. *Infrared Nondestructive Testing of Laminated Structures and Electrical Circuits*. Tech. rep. June 1972.

[210] R Frigola-Alcade. "Bayesian Time Series Learning with Gaussian Processes". PhD thesis. PhD thesis, University of Cambridge, 2015.

[211] Carl Edward Rasmussen. "Gaussian processes in machine learning". In: *Advanced lectures on machine learning*. Springer, 2004, pp. 63–71.

[212] Roy De Maesschalck, Delphine Jouan-Rimbaud, and Désiré L Massart. "The mahalanobis distance". In: *Chemometrics and intelligent laboratory systems* 50.1 (2000), pp. 1–18.

[213] NL Johnson. *S. Kotz Distributions in statistics: continuous multivariate distributions*. 1972.

[214] Steven E. Pav. *sadists: Some Additional Distributions*. R package version 0.2.3. 2017.

[215] PB Patnaik. "The non-central χ2-and F-distributions and their applications". In: *Biometrika* 36.1-2 (1949), pp. 202–232.

[216] Granta Design Ltd., Cambridge, UK. *CES EduPack (2016)*. 2016.

[217] Mary L Crowley and Eugene F Krause. *Taxicab Geometry, an Adventure in Non-Euclidean Geometry (P, L, S)*. 1988.

[218] *EPCOS (TDK) B57541G1103F NTC Thermistor 10k Bead, Glass*. `http://www.digikey.com/product-detail/en/epcos-tdk/B57541G1103F/495-4599-ND/3712554`. Accessed: 2016-10-01. 2016.

[219] T. Bhattacharjee, J. M. Rehg, and C. C. Kemp. "Inferring Object Properties from Incidental Contact with a Tactile Sensing Forearm". In: *arXiv preprint arXiv:1409.4972* (2014).

[220] Hsin-Ni Ho and Lynette A Jones. "Development and evaluation of a thermal display for material identification and discrimination". In: *ACM Transactions on Applied Perception (TAP)* 4.2 (2007), p. 13.

[221] Gi-Hun Yang, Lynette A Jones, and Dong-Soo Kwon. "Use of simulated thermal cues for material discrimination and identification with a multi-fingered display". In: *Presence: Teleoperators and Virtual Environments* 17.1 (2008), pp. 29–42.

[222] Saralees Nadarajah. "A generalized normal distribution". In: *Journal of Applied Statistics* 32.7 (2005), pp. 685–694.

[223] C. M. Bishop et al. *Pattern recognition and machine learning*. Vol. 1. springer New York, 2006.

[224] Joshua Wade, Tapomayukh Bhattacharjee, and Charles C Kemp. "Force and Thermal Sensing with a Fabric-based Skin". In: *See, Touch and Hear: 2nd Workshop on multimodal sensor-based robot control for HRI and soft manipulation, IEEE/RSJ International Conference on Intelligent Robots and Systems (IROS)*. 2016.

[225] Hsin-Ni Ho and Lynette A Jones. "Contribution of thermal cues to material discrimination and localization". In: *Attention, Perception, & Psychophysics* 68.1 (2006), pp. 118–128.

[226] Lynette A Jones and Michal Berris. "Material discrimination and thermal perception". In: *Haptic Interfaces for Virtual Environment and Teleoperator Systems, 2003. HAPTICS 2003. Proceedings. 11th Symposium on*. IEEE. 2003, pp. 171–178.

[227] Wouter M Bergmann Tiest. "Tactual perception of material properties". In: *Vision research* 50.24 (2010), pp. 2775–2782.

[228] Wouter M Bergmann Tiest and Astrid ML Kappers. "Tactile perception of thermal diffusivity". In: *Attention, perception, & psychophysics* 71.3 (2009), pp. 481–489.

[229] Peter James Dyck et al. "Description of Minnesota Thermal Disks and normal values of cutaneous thermal discrimination in man". In: *Neurology* 24.4 (1974), pp. 325–325.

[230] Alexander Kron and Günther Schmidt. "Multi-fingered tactile feedback from virtual and remote environments". In: *Haptic Interfaces for Virtual Environment and Teleoperator Systems, 2003. HAPTICS 2003. Proceedings. 11th Symposium on*. IEEE. 2003, pp. 16–23.

[231] Tapomayukh Bhattacharjee, Joshua Wade, and Charles C Kemp. "Material recognition from heat transfer given varying initial conditions and short-duration contact". In: *Proceedings of Robotics: Science and Systems, Rome, Italy* (2015).

[232] K Katoh et al. "Material discrimination by heat flow sensing". In: *TRANSDUCERS 2009-2009 International Solid-State Sensors, Actuators and Microsystems Conference*. IEEE. 2009, pp. 1549–1552.

[233] Ernst Heinrich Weber. *EH Weber: The sense of touch*. Academic Pr, 1978.

[234] Herbert Hensel. "Cutaneous thermoreceptors". In: *Somatosensory System*. Springer, 1973, pp. 79–110.

[235] Wouter M Bergmann Tiest. "An Experimentally Verified Model of the Perceived'Coldness' of Objects". In: *Second Joint EuroHaptics Conference and Symposium on Haptic Interfaces for Virtual Environment and Teleoperator Systems (WHC'07)*. IEEE. 2007, pp. 61–65.

[236] Newton C Burnett and Karl M Dallenbach. "The experience of heat". In: *The American Journal of Psychology* 38.3 (1927), pp. 418–431.

[237] Joseph C Stevens and Stanley Smith Stevens. "Warmth and cold: dynamics of sensory intensity." In: *Journal of Experimental Psychology* 60.3 (1960), p. 183.

[238] Mark F Tritsch. "The veridical perception of object temperature with varying skin temperature". In: *Perception & psychophysics* 43.6 (1988), pp. 531–540.

[239] Wouter M Bergmann Tiest and Astrid ML Kappers. "Thermosensory reversal effect quantified". In: *Acta psychologica* 127.1 (2008), pp. 46–50.

[240] Barry G Green. "Temperature perception and nociception". In: *Journal of neurobiology* 61.1 (2004), pp. 13–29.

[241] Barry G Green. "The effect of skin temperature on vibrotactile sensitivity". In: *Perception & Psychophysics* 21.3 (1977), pp. 243–248.

[242] Barry G Green, Susan J Lederman, and Joseph C Stevens. "The effect of skin temperature on the perception of roughness". In: *Sensory processes* 3 (1979), pp. 327–333.

[243] Joseph C Stevens and Janet E Hooper. "How skin and object temperature influence touch sensation". In: *Perception & psychophysics* 32.3 (1982), pp. 282–285.

[244] Mohamed Guiatni and Abderrahmane Kheddar. "Theoretical and experimental study of a heat transfer model for thermal feedback in virtual environments". In: *2008 IEEE/RSJ International Conference on Intelligent Robots and Systems*. IEEE. 2008, pp. 2996–3001.

[245] Lynette A Jones and Hsin-Ni Ho. "Warm or cool, large or small? The challenge of thermal displays". In: *IEEE Transactions on Haptics* 1.1 (2008), pp. 53–70.

[246] Gi-Hun Yang, Dong-Soo Kwon, and Lynette A Jones. "Spatial acuity and summation on the hand: The role of thermal cues in material discrimination". In: *Perception & Psychophysics* 71.1 (2009), pp. 156–163.

[247] Shuichi Ino et al. "A tactile display for presenting quality of materials by changing the temperature of skin surface". In: *Robot and Human Communication, 1993. Proceedings., 2nd IEEE International Workshop on*. IEEE. 1993, pp. 220–224.

[248] Akio Yamamoto et al. “Control of thermal tactile display based on prediction of contact temperature”. In: *Robotics and Automation, 2004. Proceedings. ICRA’04. 2004 IEEE International Conference on*. Vol. 2. IEEE. 2004, pp. 1536–1541.

[249] H Ho and LA Jones. “Material identification using real and simulated thermal cues”. In: *Engineering in Medicine and Biology Society, 2004. IEMBS’04. 26th Annual International Conference of the IEEE*. Vol. 1. IEEE. 2004, pp. 2462–2465.

[250] Phillip M Grice et al. “Whole-arm tactile sensing for beneficial and acceptable contact during robotic assistance”. In: *IEEE International Conference on Rehabilitation Robotics (ICORR)*. IEEE. 2013, pp. 1–8.

[251] Tapomayukh Bhattacharjee, Joshua Wade, and Charles Kemp. “Material Recognition from Heat Transfer given Varying Initial Conditions and Short-Duration Contact”. In: *Proceedings of Robotics: Science and Systems*. Rome, Italy, 2015.

[252] Tapomayukh Bhattacharjee, James M Rehg, and Charles C Kemp. “Haptic classification and recognition of objects using a tactile sensing forearm”. In: *IEEE/RSJ International Conference on Intelligent Robots and Systems*. IEEE. 2012, pp. 4090–4097.

[253] Thomas Leung and Jitendra Malik. “Representing and recognizing the visual appearance of materials using three-dimensional textons”. In: *International journal of computer vision* 43.1 (2001), pp. 29–44.

[254] Manik Varma and Andrew Zisserman. “A statistical approach to material classification using image patch exemplars”. In: *Pattern Analysis and Machine Intelligence, IEEE Transactions on* 31.11 (2009), pp. 2032–2047.

[255] Ce Liu et al. “Exploring features in a bayesian framework for material recognition”. In: *Computer Vision and Pattern Recognition (CVPR), 2010 IEEE Conference on*. IEEE. 2010, pp. 239–246.

[256] Diane Hu and Liefeng Bo. “Toward Robust Material Recognition for Everyday Objects.” In: Citeseer.

[257] Sean Bell et al. “Material recognition in the wild with the materials in context database”. In: *arXiv preprint arXiv:1412.0623* (2014).

[258] Mircea Cimpoi, Subhransu Maji, and Andrea Vedaldi. “Deep filter banks for texture recognition and segmentation”. In: *Proceedings of the IEEE Conference on Computer Vision and Pattern Recognition*. 2015, pp. 3828–3836.

[259] Anurag Arnab et al. “Joint Object-Material Category Segmentation from Audio-Visual Cues”. In: *British Machine Vision Conference (BMVC)* (2015).

[260] Chris Russell, Pushmeet Kohli, Philip HS Torr, et al. “Associative hierarchical crfs for object class image segmentation”. In: *Computer Vision, 2009 IEEE 12th International Conference on*. IEEE. 2009, pp. 739–746.

[261] Jamie Shotton et al. “Textonboost for image understanding: Multi-class object recognition and segmentation by jointly modeling texture, layout, and context”. In: *International Journal of Computer Vision* 81.1 (2009), pp. 2–23.

[262] Brian Fulkerson, Andrea Vedaldi, Stefano Soatto, et al. “Class segmentation and object localization with superpixel neighborhoods.” In: *ICCV*. Vol. 9. Citeseer. 2009, pp. 670–677.

[263] Anne Treisman. “The binding problem”. In: *Current opinion in neurobiology* 6.2 (1996), pp. 171–178.

[264] Sergei Gepshtein et al. “The combination of vision and touch depends on spatial proximity”. In: *Journal of Vision* 5.11 (2005), p. 7.

[265] Roberta L Klatzky, Susan J Lederman, and Catherine Reed. “There’s more to touch than meets the eye: The salience of object attributes for haptics with and without vision.” In: *Journal of experimental psychology: general* 116.4 (1987), p. 356.

[266] Bill Jones and Sandra ONeil. “Combining vision and touch in texture perception”. In: *Perception & Psychophysics* 37.1 (1985), pp. 66–72.

[267] Hannah B Helbig and Marc O Ernst. “Knowledge about a common source can promote visual-haptic integration”. In: *Perception-London* 36.10 (2007), pp. 1523–1534.

[268] Marc O Ernst and Martin S Banks. “Humans integrate visual and haptic information in a statistically optimal fashion”. In: *Nature* 415.6870 (2002), pp. 429–433.

[269] Sharon A. Stansfield. “A robotic perceptual system utilizing passive vision and active touch”. In: *The International journal of robotics research* 7.6 (1988), pp. 138–161.

[270] Peter K Allen. “Integrating vision and touch for object recognition tasks”. In: *The International Journal of Robotics Research* 7.6 (1988), pp. 15–33.

[271] Jan M Zytkow and Peter W Pachowicz. “Fusion of vision and touch for spatio-temporal reasoning in learning manipulation tasks”. In: *1989 Advances in Intelligent Robotics Systems Conference*. International Society for Optics and Photonics. 1990, pp. 404–415.

[272] Jay K Hackett and Mubarak Shah. “Multi-sensor fusion: a perspective”. In: *Robotics and Automation, 1990. Proceedings., 1990 IEEE International Conference on*. IEEE. 1990, pp. 1324–1330.

[273] J Kenneth Salisbury and Mandayam A Srinivasan. “Phantom-based haptic interaction with virtual objects”. In: *Computer Graphics and Applications, IEEE* 17.5 (1997), pp. 6–10.

[274] Anatole Lécuyer. “Simulating haptic feedback using vision: A survey of research and applications of pseudo-haptic feedback”. In: *Presence: Teleoperators and Virtual Environments* 18.1 (2009), pp. 39–53.

[275] Yasuyoshi Yokokohji, Ralph L Hollis, and Takeo Kanade. “What you can see is what you can feel-development of a visual/haptic interface to virtual environment”. In: *Virtual Reality Annual International Symposium, 1996., Proceedings of the IEEE 1996*. IEEE. 1996, pp. 46–53.

[276] Christopher W Kennedy et al. “A novel approach to robotic cardiac surgery using haptics and vision”. In: *Cardiovascular Engineering: An International Journal* 2.1 (2002), pp. 15–22.

[277] Hiromi T Tanaka et al. “A vision-based haptic exploration”. In: *Robotics and Automation, 2003. Proceedings. ICRA’03. IEEE International Conference on*. Vol. 3. IEEE. 2003, pp. 3441–3448.

[278] Dai Yamashiro, Shiro Tanaka, and Hiromi T Tanaka. “Active estimation of friction properties with Haptic Vision”. In: *Control, Automation, Robotics and Vision, 2008. ICARCV 2008. 10th International Conference on*. IEEE. 2008, pp. 1329–1332.

[279] Luc Berthouze, Paul Bakker, and Yasuo Kuniyoshi. “Learning of oculo-motor control: a prelude to robotic imitation”. In: *Intelligent Robots and Systems’ 96, IROS 96, Proceedings of the 1996 IEEE/RSJ International Conference on*. Vol. 1. IEEE. 1996, pp. 376–381.

[280] Luc Berthouze and Yasuo Kuniyoshi. “Emergence and categorization of coordinated visual behavior through embodied interaction”. In: *Autonomous Robots* 5.3-4 (1998), pp. 369–379.

[281] Martin HUlse, Sebastian McBride, and Mark Lee. “Developmental robotics architecture for active vision and reaching”. In: *Development and Learning (ICDL), 2011 IEEE International Conference on*. Vol. 2. IEEE. 2011, pp. 1–6.

[282] Nicholas J Butko and Javier R Movellan. “Learning to look”. In: *Development and Learning (ICDL), 2010 IEEE 9th International Conference on*. IEEE. 2010, pp. 70–75.

[283] Jefferson Coelho, Justus Piater, and Roderic Grupen. “Developing haptic and visual perceptual categories for reaching and grasping with a humanoid robot”. In: *Robotics and Autonomous Systems* 37.2 (2001), pp. 195–218.

[284] Hai Nguyen and Charles C Kemp. “Autonomously learning to visually detect where manipulation will succeed”. In: *Autonomous Robots* 36.1-2 (2014), pp. 137–152.

[285] Vladimir Sukhoy and Alexander Stoytchev. “Learning to detect the functional components of doorbell buttons using active exploration and multimodal correlation”. In: *Humanoid Robots (Humanoids), 2010 10th IEEE-RAS International Conference on*. IEEE. 2010, pp. 572–579.

[286] Herke Van Hoof et al. “Maximally informative interaction learning for scene exploration”. In: *Intelligent Robots and Systems (IROS), 2012 IEEE/RSJ International Conference on*. IEEE. 2012, pp. 5152–5158.

[287] Koh Hosoda, Yasunori Tada, and Minoru Asada. “Internal representation of slip for a soft finger with vision and tactile sensors”. In: *Intelligent Robots and Systems, 2002. IEEE/RSJ International Conference on*. Vol. 1. IEEE. 2002, pp. 111–115.

[288] Shan Luo et al. “Localizing the object contact through matching tactile features with visual map”. In: *Robotics and Automation (ICRA), 2015 IEEE International Conference on*. IEEE. 2015, pp. 3903–3908.

[289] Oliver Kroemer, Christoph H Lampert, and Jan Peters. “Learning dynamic tactile sensing with robust vision-based training”. In: *IEEE transactions on robotics* 27.3 (2011), pp. 545–557.

[290] Nadir Nizar Ali Charniya and Sanjay Vasant Dudul. “Sensor for classification of material type and its surface properties using radial basis networks”. In: *Sensors Journal, IEEE* 8.12 (2008), pp. 1981–1991.

[291] Haitian Zheng et al. “Deep Learning for Surface Material Classification Using Haptic And Visual Information”. In: *arXiv preprint arXiv:1512.06658* (2015).

[292] Yang Gao et al. “Deep Learning for Tactile Understanding From Visual and Haptic Data”. In: *arXiv preprint arXiv:1511.06065* (2015).

[293] Monika A Schaeffer and Allison M Okamura. “Methods for intelligent localization and mapping during haptic exploration”. In: *Systems, Man and Cybernetics, 2003. IEEE International Conference on*. Vol. 4. IEEE. 2003, pp. 3438–3445.

[294] Nicolas Alt and Eckehard Steinbach. “Navigation and manipulation planning using a visuo-haptic sensor on a mobile platform”. In: (2014).

[295] Charles Fox et al. “Tactile SLAM with a biomimetic whiskered robot”. In: *Robotics and Automation (ICRA), 2012 IEEE International Conference on*. IEEE. 2012, pp. 4925–4930.

[296] Yuki Yokokura, Seiichiro Katsura, and Kiyoshi Ohishi. “Haptic recognition and mapping of driving road environment by haptograph”. In: *SICE, 2007 Annual Conference*. IEEE. 2007, pp. 2296–2301.

[297] Seiichiro Katsura, Yuki Yokokura, and Kiyoshi Ohishi. “Acquisition and visualization of personal characteristics by haptograph”. In: *Advanced Motion Control, 2008. AMC’08. 10th IEEE International Workshop on*. IEEE. 2008, pp. 434–439.

[298] Rui Li et al. “Localization and manipulation of small parts using gelsight tactile sensing”. In: *Intelligent Robots and Systems (IROS 2014), 2014 IEEE/RSJ International Conference on*. IEEE. 2014, pp. 3988–3993.

[299] *Time Constant*. `https://en.wikipedia.org/wiki/Time_constant`.

[300] Joshua Wade et al. “A Force and Thermal Sensing Skin for Robots in Human Environments”. In: *Robotics and Autonomous Systems: Special Issue on multimodal sensor-based robot control for interaction, soft manipulation and whole body control.* 2017.

[301] Theodore L Bergman et al. *Fundamentals of heat and mass transfer*. John Wiley & Sons, 2011.

[302] Lynette A Jones. “Perception of force and weight: Theory and research.” In: *Psychological bulletin* 100.1 (1986), p. 29.

[303] Lynette A Jones and Michal Berris. “The psychophysics of temperature perception and thermal-interface design”. In: *Haptic Interfaces for Virtual Environment and Teleoperator Systems, 2002. HAPTICS 2002. Proceedings. 10th Symposium on*. IEEE. 2002, pp. 137–142.

[304] Max Berniker and Konrad Kording. “Bayesian approaches to sensory integration for motor control”. In: *Wiley Interdisciplinary Reviews: Cognitive Science* 2.4 (2011), pp. 419–428.

[305] Yoji Yamada and Mark R Cutkosky. “Tactile sensor with 3-axis force and vibration sensing functions and its application to detect rotational slip”. In: *Robotics and Automation, 1994. Proceedings., 1994 IEEE International Conference on*. IEEE. 1994, pp. 3550–3557.

[306] Tapomayukh Bhattacharjee et al. “Combining Tactile Sensing and Vision for Rapid Haptic Mapping”. In: *Proceedings of IEEE/RSJ International Conference on Intelligent Robots and Systems (IROS)*. Hamburg, Germany, 2015.

[307] Ashwin A. Shenoi, Tapomayukh Bhattacharjee, and Charles C. Kemp. “A CRF that Combines Touch and Vision for Haptic Mapping”. In: *Proceedings of IEEE/RSJ International Conference on Intelligent Robots and Systems (IROS)*. Daejeon, South-Korea, 2016.